CHARLES UNIVERSITY IN PRAGUE
Faculty of Mathematics and Physics

HEIDELBERG UNIVERSITY
Faculty of Mathematics and Computer Sciences

DOCTORAL THESIS

by

Petra Pustějovská

Biochemical and mechanical processes in synovial fluid

—

modeling, analysis and computational simulations

Mathematical Institute, Charles University in Prague
Institute of Applied Mathematics, Heidelberg University

Supervisors of doctoral thesis: prof. RNDr. Josef Málek CSc., DSc.
                                    Prof. Dr. Dr. h.c. mult. Willi Jäger

Study branch: 4F11 – Mathematical and Computer Modelling

2012, Prague

Hereby, I would like to thank to both of my supervisors, prof. Josef Málek and Prof. Willi Jäger, for guiding me throughout my doctoral study, as a student, a human and a young inexperienced scientist. Their boundless will to help was always encouraging, always making the science topic number one. Last but not least, for the possibility taking a part in "Bi–nationally Supervised Doctoral Thesis" program between Heidelberg University and Charles University in Prague.

This thesis could not have been done even without the support of my mentors and co–advisers. My special and great thanks belong to dr. Jaroslav Hron, for the patient and structured advices in the field of numerical and computational mathematics, for the possibility to work with his computer code, uncountable helpful comments and corrections, and not least, for the mental support through the whole period of my study. To my mentor, dr. Maria Neuss–Radu, for giving me insight in the membrane modeling, the understanding of the real processes connected with membranes and for making my stay at Heidelberg University as pleasant as possible. And, to my third co–adviser, dr. Miroslav Bulíček, whose undoubtedly great knowledge in the field of mathematical analysis of partial differential equations for the non–Newtonian fluid problems was essential for my analytical work.

My thanks belong also to the following institutions for material, financial and scientific support, to Mathematical Institute of the Charles University, Nečas Center for Mathematical Modeling, Institute of Applied Mathematics of the Heidelberg University, Interdisciplinary Center for Scientific Computing at Heidelberg University and Heidelberg Graduate School MathComp. Moreover, I would like to thank for the support of following grants and projects LC06052 (Jindřich Nečas Center for Mathematical Modeling) financed by MŠMT, GAČR grant no. 201/09/0917, grant SVV-2010-261316, GAUK grants no. 306-10/252509 and 306-10/251404.

I hereby declare that I have written the thesis by myself, using only cited sources.

Ich erkläre an Eides statt, dass ich die vorliegende Arbeit selbstständig verfasst, andere als die angegebenen Quellen/Hilfsmittel nicht benutzt, und die den Quellen wörtlich und inhaltlich entnommenen Stellen als solche kenntlich gemacht habe.

Prohlašuji, že jsem tuto disertační práci vypracovala samostatně a výhradně s použitím citovaných pramenů, literatury a dalších odborných zdrojů.

Beru na vědomí, že se na moji práci vztahují práva a povinnosti vyplývající ze zákona č. 121/2000 Sb., autorského zákona v platném znění, zejména skutečnost, že Univerzita Karlova v Praze má právo na uzavření licenční smlouvy o užití této práce jako školního díla podle § 60 odst. 1 autorského zákona.

V Praze dne

Petra Pustějovská

Název práce: Biochemické a mechanické procesy v synoviálních tekutinách – modelování, analýza, počítačové simulace

Autor: Petra Pustějovská (`petra.pustejovska@karlin.mff.cuni.cz`)

Školící pracoviště:
    Matematický ústav UK, Univerzita Karlova v Praze
    Institut für Angewandte Mathematik, Universität Heidelberg

Vedoucí disertační práce:
    prof. RNDr. Josef Málek CSc., DSc. (`malek@karlin.mff.cuni.cz`)
    Matematický ústav UK, Univerzita Karlova v Praze,
    Prof. Dr. Dr. h.c. mult. Willi Jäger (`jaeger@iwr.uni-heidelberg.de`)
    Institut für Angewandte Mathematik, Universität Heidelberg

Abstrakt: Synoviální tekutina je polymerní roztok, který se obecně chová jako viskoelastická tekutina, a to především díky obsaženým makromolekulám hyaluronanu. V této práci se zabýváme biologickými a biochemickými vlastnostmi synoviálních tekutin, dále jejich komplexní reologií a jejich interakcí se synoviálními membránami během filtrace. Z matematického hlediska modelujeme synoviální tekutiny jako vazké nestlačitelné tekutiny, pro něž jsme vyvinuli nový zobecněný model mocninného typu, jehož exponent závisí na koncentraci výše zmíněného hyaluronanu. Takový popis je adekvátní, pokud synoviální tekutina nepodléhá vysokým zátěžovým testům. Dále se zabýváme popisem lineárních viskoelastických odezev synoviálních tekutin z dostupných experimentálních dat, opět hledáme příslušné parametry modelů jako funkce koncentrace. Pro popis proudění používáme zobecněné Navierovy–Stokesovy rovnice svázané s podmínkou nestlačitelnosti a rovnice pro konvekci–difúzi koncentrace hyaluronanu. V části práce zabývající se matematickou analýzou formulujeme stacionární úlohu a dokážeme existenci odpovídajícího slabého řešení. Důkaz existence je založen na metodě monotónních operátorů, kde klíčovou roli hraje důkaz Hölderovské spojitosti koncentrace. V numerické části teze se zabýváme výběrem a implementací vhodných stabilizačních metod pro numerické řešení problému s dominantní konvekcí, jak je charakteristické pro synoviální tekutiny. Numericky pak řešíme pro různé modely zobecněné vazkosti a různé stabilizační metody systém řídících rovnic v obdélníkové oblasti, jakožto testovací domény, která naznačuje případné rozšíření modelu pro realistickou geometrii. Jako poslední se zabýváme problémem filtrace. Zde formulujeme podmínky na hranici membrány pro proudění a tok koncentrace, které formálně popisují částečnou polopropustnost membrány, hromadění koncentrace před membránou (v případě jednosměrného toku) a vliv osmotického tlaku.

Klíčová slova: Synoviální tekutina, zobecněná viskozita, lineární viskoelasticita, Navierovy–Stokesovy rovnice, zobecněné Sobolevovy prostory, $C^{0,\alpha}$–regularita, stabilizované metody konečných prvků, transport přes membránu.

Titel: Biochemische und Mechanische Prozesse von synovialen Fluiden – Modellierung, mathematische Analysis und Computersimulationen

Autor: Petra Pustějovská (`petra.pustejovska@karlin.mff.cuni.cz`)

Department:
Matematický ústav UK, Univerzita Karlova v Praze
Institut für Angewandte Mathematik, Universität Heidelberg

Betreuer:
prof. RNDr. Josef Málek CSc., DSc. (`malek@karlin.mff.cuni.cz`)
Matematický ústav UK, Univerzita Karlova v Praze,
Prof. Dr. Dr. h.c. mult. Willi Jäger (`jaeger@iwr.uni-heidelberg.de`)
Institut für Angewandte Mathematik, Universität Heidelberg

Kurzfassung: Ein synoviales Fluid ist eine polymerische Flüssigkeit, die sich im Allgemeinen wie eine viskoelastische Flüssigkeit verhält. Dieses Verhalten ist auf die Wirkung enthaltender Polysaccharide, sogenannte Hyaluronen, zurückzuführen. In dieser Arbeit werden biologische und biochemische Eigenschaften von synovialen Flüssigkeiten untersucht, sowie deren komplexe Rheologie und die Interaktion mit synovialen Membranen bei Filterprozessen. Vom mathematischen Standpunkt aus modellieren wir das synoviale Fluid als ein viskoses, inkompressibles Fluid, für welches wir ein neues Potenzgesetz–Modell entwickeln, wobei der Exponent im Potenzgesetz von der Konzentration der Hyaluronen abhängt. Ein solches Modell ist dazu geeignet, um ein synoviales Fluid zu beschreiben, solange es zu keinen plötzlichen Impulsen kommt. Des Weiteren beschreiben wir geeignete lineare viskoelastische Modelle, welche das viskoelastische Verhalten der synovialen Fluide bei kleinen Deformationen als eine Funktion der Konzentration beschreiben. In weiterer Folge werden die zugehörigen Modellgleichungen betrachtet, und zwar die Inkompressibilitätsbedingung, das Momentengleichgewicht – die verallgemeinerten Navier–Stokes Gleichungen und die Konvektionsdiffusionsgleichung für die Konzentration des Hyaluron. Das Kapitel zur mathematischen Analysis konzentriert sich im Wesentlichen auf die Formulierung des stationären Problems im schwachen Sinne und den Beweis der Existenz einer zugehörigen schwachen Lösung für den Fall einer verallgemeinerten Viskosität mit einer vom Potenzgesetzexponenten abhängenden Konzentration. Dazu verwenden wir die Methode der monotonen Operatoren, wobei der Beweis der Hölder–Stetigkeit der Konzentration den Hauptteil darstellt. Im Kapitel zur Numerik werden verschiedene stabilisierte Finite Elemente Methoden für Probleme mit dominierender Konvektion betrachtet, welche typisch für synoviale Fluide sind. Numerische Beispiele werden für rechteckige Gebiete präsentiert, um eine Einsicht in das Verhalten des Fluids zu bekommen und um es zukünftig in realistischeren Gebieten lösen zu können. Des Weiteren werden die Lösungen der verschiedenen Viskositätsmodelle für die einzelnen stabilisierten Finite Elemente Methoden miteinander verglichen. Im letzten Kapitel wird ein mathematisches Modell für die Strömung und den Transport einer verdünnten Lösung betrachtet, welches anschließend auf das synoviale Fluid übertragen wird. Dabei sind die Gebiete durch eine semipermeable Membran getrennt. Wir formulieren Transmissionsbedingungen für die Strömung und die Konzentration der Lösung auf der Membran. Dabei kommt es zu einem teilweisen Rückgang der Konzentration, welcher auf die Eigenschaften der Membran zurückzuführen ist. Die Ablagerung der Lösung an der Membran und der Einfluss der Konzentration der Lösung auf die Strömung ist als osmotischer Effekt bekannt.

Schlüsselwörter: Synoviale Flüssigkeiten, verallgemeinerte Viskosität, lineare Viskoelastizität, Navier–Stokes Gleichungen, verallgemeinerte Sobolev Räume, $C^{0,\alpha}$–Regularität, Stabilisierte Finite Elemente Methoden, Membrantransport.

Title: Biochemical and mechanical processes in synovial fluid –
modeling, mathematical analysis and computational simulations

Author: Petra Pustějovská (`petra.pustejovska@karlin.mff.cuni.cz`)

Department:
    Matematický ústav UK, Univerzita Karlova v Praze
    Institut für Angewandte Mathematik, Universität Heidelberg

Supervisors:
    prof. RNDr. Josef Málek CSc., DSc. (`malek@karlin.mff.cuni.cz`)
    Matematický ústav UK, Univerzita Karlova v Praze,
    Prof. Dr. Dr. h.c. mult. Willi Jäger (`jaeger@iwr.uni-heidelberg.de`)
    Institut für Angewandte Mathematik, Universität Heidelberg

Abstract: Synovial fluid is a polymeric liquid which generally behaves as a viscoelastic fluid due to the presence of polysaccharide molecules called hyaluronan. In this thesis, we study the biological and biochemical properties of synovial fluid, its complex rheology and interaction with synovial membrane during filtration process. From the mathematical point of view, we model the synovial fluid as a viscous incompressible fluid for which we develop a novel generalized power–law fluid model wherein the power–law exponent depends on the concentration of the hyaluronan. Such a model is adequate to describe the flows of synovial fluid as long as it is not subjected to instantaneous stimuli. Moreover, we try to find a suitable linear viscoelastic model which can describe the viscoelastic responses of synovial fluid during small deformation experiments, as, again, a function of concentration. Then, we consider the governing equations, namely the constraint of incompressibility, the balance of linear momentum – generalized Navier–Stokes equations and the convection–diffusion equation for the concentration of hyaluronan. The part of mathematical analysis is focused on the formulation of the stationary problem in the weak sense and the proof of the existence of the corresponding weak solution, for the case of a generalized viscous problem with concentration dependent power–law exponent. For that, we use the method of monotone operators, where the essential role plays the proof of Hölder continuity of the concentration. In the numerical part of the thesis, we consider different numerical stabilization methods which ensure better numerical solvability of the system with dominant convection, as is typical for synovial fluid flow. By their implementation into already existing code, we numerically solve for the flow of the synovial fluid in a rectangular cavity, in order to gain some insight into the response of such a fluid so that we can solve in the future the flows in more realistic geometries. We also compare the solutions obtained with different models of generalized viscosities and different stabilization techniques. As last, we propose a mathematical model for flow and transport processes of diluted solutions, and afterwards of synovial fluid, in domains separated by a leaky semipermeable membrane. We formulate transmission conditions for the flow and the solute concentration across the membrane which take into account the property of the membrane to partly reject the solute, the accumulation of rejected solute at the membrane, and the influence of the solute concentration on the volume flow, known as the osmotic effect.

Keywords: Synovial fluid, generalized viscosity, linear viscoelasticity, Navier–Stokes equations, generalized Sobolev space, $C^{0,\alpha}$–regularity, stabilized finite element methods, membrane transport.

Contents

Chapter 1

Introduction

1.1. Structure of the thesis

This thesis is concepted as an extended research on synovial fluids[1] from the point of view of the mathematical modeling. The mathematical modeling of biological materials always has to be supported by deep physical, biological and chemical investigations to be able to create reasonable models. Thus, we include to this work the introductory chapters concerning the synovial joints and their single parts, on which basis we establish new models for description of rheology of synovial fluid. Of course, by determination of new models, valid under some specific restrictions, the work does not end, rather it continues with the following mathematical analysis of the particular system of equations and the computational simulations involving suitable numerical methods and their adaptations.

In order to keep a clear structure of the whole thesis, we introduce each field of the research connected with the synovial fluid in a separate chapter. The reader then can always choose to read the work as a whole or pick topics of his or her interest. We refer between chapters to clarify particular assumptions and derivations made before, complement the research by several figures for better visual understanding of the problem, emphasize the main goal at the beginning of the actual chapter or section, and attempt to summarize the known previous results and developments.

As a whole, this thesis is divided into three main parts, sometimes slightly overlapping each other:

$\boxed{\text{MODELING PART}}$

Chapter 2.	Biology of joints
Chapter 3.	Description of response of viscous and viscoelastic material in connection with synovial fluid
Chapter 4.	Rheology of synovial fluid
Chapter 5.	Modeling of viscous responses
Chapter 6.	Modeling of viscoelastic responses
Chapter 10.	Synovial membranes modeling

$\boxed{\text{ANALYTICAL PART}}$

Chapter 7.	Problem formulation: governing equations and mathematical analysis

$\boxed{\text{NUMERICAL PART}}$

Chapter 8.	Numerical methods
Chapter 9.	Computational simulations
Chapter 10.	Synovial membranes modeling

---

[1]Synovial fluid is a biological fluid present in the cavities of mammalian movable joints.

1.2. Why is the mathematical modeling of synovial fluid important?

Mathematical studies of mechanical and rheological behavior of systems close or directly connected with human physiology play an important role in several areas of bio–engineering and medicine. One of the best examples is the mathematical modeling and consecutive computational simulations which can predict important features of particular organs, tissues or whole systems, otherwise difficult or even impossible to determine *in vivo*. Of course, one needs to have by hand reasonable mathematical models, suitable (experimental) data, fast reliable numerical methods, software and hardware, and experts who are able to interact with the models and interpret the results. For example, the modeling of cardiovascular systems, especially of the vessel parts and their interaction with blood, modeling of the heart muscle or evolution of the aneurysms, or modeling in the field of neurology, becomes a standard part of modern medical investigations. For these reasons, the fundamental research on biological systems plays a crucial role for the future medical treatments or bio–engineering development.

In our case, we are focused on the understanding of the physiology and mechanisms concerning human movable joints, more precisely, the mathematical description of the synovial fluid rheology. To this date, there have not been fully understood the conditions and origins of some pathological diseases, the mechanics of human joint lubrication or shock load absorbing, for which the synovial fluid[2] is an essential medium. These features could be, nevertheless, a great enhancement in the engineering of designing the life–long functional joint prostheses or in the disease treatment.

1.3. State of the art and main aims of the thesis

Mathematical modeling. To our knowledge, there are several models describing the synovial fluid, see for example Rudraiah et al. (1991), Lai et al. (1978), Morris et al. (1981). Nevertheless, they are great simplifications of the otherwise complex rheology of synovial fluid, usually based on the simple experiments adapted for the linear theories, both viscoelastic and viscous. In this we see the main obstacle in development of reliable models capturing the most important non–Newtonian features of synovial fluid. To be more specific, the synovial fluid has been modeled as either viscous shear–thinning fluid or linear viscoelastic fluid–like material. The importance of the concentration of the molecules of hyaluronan, which determines its non–linear character, was often undermined or completely neglected. **The aim**: Our aim is to study such rheological behavior of synovial fluid, based on the existing experimental literature, and create novel viscous and viscoelastic models, describing the influence of concentration. Mainly, we focus on the description of viscous responses of synovial fluid, as a fluid thinning the shear. Moreover, we intend to study the filtration process of the synovial fluid through the synovial membrane and, on that basis, to create a reasonable, nevertheless phenomenological, model for the synovial membrane transport.

Mathematical analysis. The existence theory of incompressible Navier–Stokes equations with the viscosity of power–law type has been studied for more than 40 years, see for example Ladyzhenskaya (1967), Málek et al. (1993), Frehse et al. (2000), Diening et al. (2010b). On the other hand, the study of non–trivial coupling of the Navier–Stokes equations with another governing equation, for example for temperature or electric field, through the power–law index has been introduced in the recent decade. For instance in Růžička (2004), the variable index is considered as a function of the electric field, in simplification of the space variable, or in Antontsev and Rodrigues (2006), the variable index is temperature dependent. The latter system is the closest to ours, nevertheless the proof is not constructive, based on the use of the fixed point theory. Moreover, the diffusion of the temperature is considered to be linear, and thus the standard Laplacian theory can be used to obtain necessary Hölder continuity of the temperature and consequently of the variable power–law index. To the best of our knowledge, the theory is not known for the case of the non–linear diffusion.

The aim: Since we model the flow of synovial fluid by the incompressible Navier–Stokes equations coupled with the convection–diffusion equation for the concentration, and, the

---

[2]Here, of course, other parts of synovial joints, like cartilage and tendons, are essential and their mathematical modeling as well as the understanding of their mutual interaction is necessary.

viscosity of synovial fluid by a power–law type model with the shear–thinning exponent dependent of the concentration, the mathematical approach introduced by Růžička (2004) needs to be adopted for our case as well. The aim is then to prove the existence of the weak solution for the stationary problem with Dirichlet boundary conditions for both the velocity and the concentration in the framework of the generalized Sobolev spaces.

Numerical methods. In the case of dominated convection of the concentration, as is the case of hyaluronan in synovial fluid, the numerical method needs to be adapted by an introduction of suitable numerical stabilization. To this date, there are several stabilized finite element methods, nevertheless, their application needs to be considered with respect to several aspects. Since the objective of our study is a physical variable, the positiveness of the scheme plays a crucial role. On the other hand, one needs to consider the convergence rate and, particularly, the requirements for implementation and following numerical computations. For these reasons, the streamline upwind Petrov–Galerkin method (Johnson (1982), Hughes and Franca (1989)), continuous interior penalty method (Douglas and Dupont (1976), Turek and Ouazzi (2007)) and Galerkin least squares method (Jiang (1998), Bochev and Gunzburger (2009)) seems suitable for our case.

The aim: We intend to implement different stabilizations for an already existing code for finite element method and study their characters in connection with the problem of the flow of the synovial fluid. Then, we intend to compute and compare the numerical solutions for different viscosity models and different stabilized finite elements. As last, we aim to simulate the transport of the synovial fluid through the synovial membrane.

1.4. Summary of main results

Here, we would like to, very shortly, summarize the main results of this thesis. We have decided to organize the results following the concept of the thesis, it means as the chapters go.

The Chapters 2 and 3 are meant as introductory chapters. The Chapter 2 characterizes the synovial joint system and its functions, the latter, Chapter 3, introduces the basic concept of the generalized viscosity and viscoelasticity from the point of view of continuum mechanics.

Chapter 4. Rheology of synovial fluid

Here, we summarize the various rheological descriptions and available experimental data of previous studies, and try to understand the nature of responses of synovial fluid under different test conditions, for both normal and pathological synovial fluid.

Chapter 5. Modeling of viscous responses

In this chapter, we establish a novel generalized power–law fluid model for viscosity of synovial fluid, wherein the power–law exponent depends on the concentration, characterizing the concentration dependence of the shear–thinning phenomenon of the synovial fluid. By the fitting procedure on the experimental data, we obtain the values of all free parameters for such model.

Chapter 6. Modeling of viscoelastic responses

We try to use the theory of linear viscoelasticity on the known characteristic of synovial fluid corresponding to small amplitude oscillatory tests. We generalize the Maxwell and Oldroyd–B models in the sense that we consider their material parameters as concentration dependent. Again, we use the fitting procedure for finding the suitable values of all free parameters. As it seems, even for small deformations, the synovial fluid behaves in a more complex, non–linear way. Nevertheless, we are able to obtain qualitatively satisfactory results for the concentrations in the physiological range.

Chapter 7. Problem formulation: governing equations and mathematical analysis

We determine the equations of flow for synovial fluid as a generalized viscous fluid with concentration, as coupled system of the generalized Navier–Stokes equations and convection–diffusion equation with a non–linear diffusivity. We formulate the corresponding stationary problem for the model with the variable power–law exponent and prove the existence of the weak solution by using the theory of monotone operators in the framework of generalized Sobolev spaces. The concept of the generalized Lebesgue and Sobolev function spaces with a variable exponent needs to be involved since the spaces where we look for the weak solution

are "dependent" on the solution itself, and thus, we a priori do not know them. The principal step in the proof is then the proof of Hölder continuity of the concentration, which ensures Hölder continuity of the variable exponent, a crucial assumption for the density of smooth functions in the generalized Sobolev spaces, generalizations of embedding theorems and Korn's inequality. To the best of our knowledge, this is the first result concerning such a system.

Chapter 8. Numerical methods

This chapter is focused on the formulation of the problem in the framework of finite element method, which we use for the computation of numerical solutions. Since the Péclet number corresponding to the synovial fluid is of the order of $10^{-7} - 10^{-6}$, we are challenged with the convection dominated flow problem. Thus, for avoiding spurious oscillations in the numerical solution, we introduce and implement three different numerical stabilization techniques, namely the streamline upwind Petrov–Galerkin method, the continuous interior penalty method and the Galerkin least squares method, which we compare for two different testing problems.

Chapter 9. Computational simulations

Here, we focus on the computational simulations of the synovial fluid flow in two dimensions. We compare different stabilization methods and the differences between models for generalized viscosity as introduced in Chapter 5. Moreover, we run the simulations for two different geometries to demonstrate the influence of the ratio of length and width of the domain on the solution.

Chapter 10. Synovial membranes modeling

In this chapter, we propose a phenomenological model for the flow and transport process of diluted solutions, and later of synovial fluid, in domains separated by a leaky semipermeable membrane. We formulate transmission conditions for the flow and the solute concentration across the membrane which take into account the property of the membrane to partly reject the solute, the accumulation of rejected solute at the membrane, and the influence of the solute concentration on the volume flow, known as the osmotic effect. The model is solved numerically for the situation of a domain in two dimensions, consisting of two subdomains separated by a rigid fixed interface representing the membrane. The numerical results for different values of the material parameters and different computational settings are compared.

Despite the variety of the work, we were not able to cover all of the topics concerning synovial fluid modeling. To them belong "hot topics" of recent years, such as

- fluid–structure interaction of membrane and synovial fluid, or the whole joint system,
- computer simulations in real geometry,
- modeling of non–linear viscoelastic responses,
- mathematical modeling of pathological synovial fluids,
- mathematical analysis of the full evolutionary system,
- mathematical analysis and development of reliable numerical methods for the viscoelastic models.

These, nevertheless, can be considered as possible topics for the future work.

Chapter 2

Biology of joints

2.1. Joints

Biological joints are formed between two or more bones of endoskeleton and are designed to allow coordinated movement and stability of otherwise rigid skeleton. Considering that adult human body has 206 bones, the total number of joints in human body is about hundreds. Many of them are in some sense inconsistent with our basic notion of the body joint, since they are indistinct, fully or dominantly rigid. It concerns for example the skull sutures which are important in the infant growth, the joints of pelvic girdle which bear the weight of the upper body and still allow sufficient expansion during the late pregnancy period and childbirth, or slightly movable joints between vertebrae protecting the spinal cord. The whole group of biological joints is thus very complex having wide functional, anatomical, structural or biomechanical variety. For our needs, it is important to understand the functional and structural classifications which actually largely overlap.

Structural classification determines the connecting material between the adjacent bones while functional classification specifies the degree of the movement of the joint. The three main classes are summarized in the Table 2.1.

Synarthroses are all those joints in which the surfaces of bones are in almost direct contact, fastened together by intervening connective tissue, mostly by fibrous material. This type of junction does not allow relative movement of the adjacent bones, it only meets the needs of growth over years. One of the examples of synarthrosis are the skull sutures, providing firm connection between skull bones but still allowing the skull growth during skeletal maturation.

The second major type of bone junctions are the *amphiarthroses*. The contiguous bony surfaces of amphiarthrosis are either connected by broad flattened disks of fibrocartilage or are united by an interosseous ligament. As the name suggest, these junctions are both, protective and slightly flexible. The flexibility occurs by bending under load, on the other hand the extreme stability is required as a safety wall against external impacts and fractures.

Classification		Class characteristics (degree of movement and filling material)
Functional	Structural	
Synarthrosis	Fibrous	No mobility Fibrous filling
Ampiartrosis	Cartilaginous	Slight mobility Cartilaginous filling
Diarthrosis	Synovial	Variety of movement Synovial fluid, cartilage

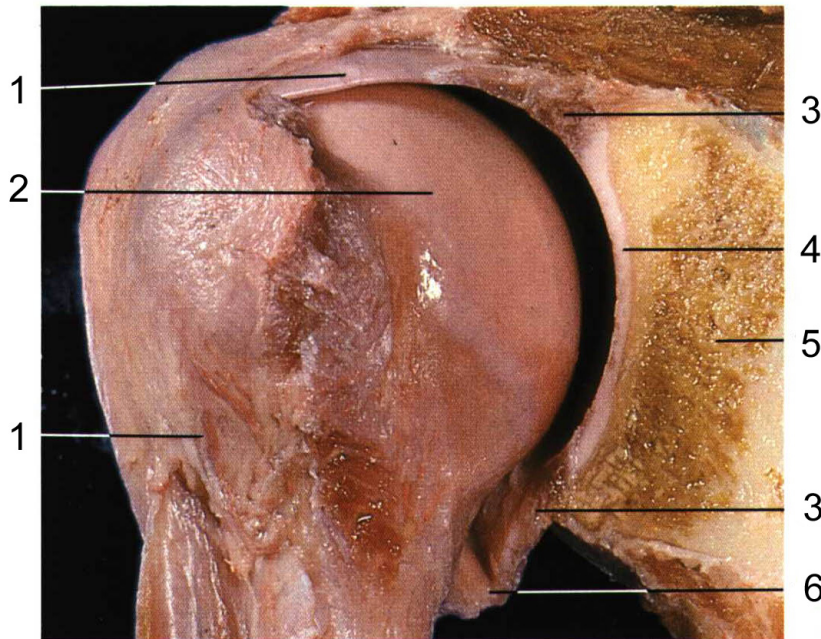TABLE 2.1. Basic classification of joints

FIGURE 2.1. Real structure of human shoulder joint: 1. Tendon of long head of biceps brachii muscle; 2. Head of humerus (arm bone); 3. Glenoid labrum (ligament attached to glenoid); 4. Articular cartilage of glenoid fossa (articular surface of shoulder blade); 5. Scapula (shoulder blade); 6. Articular capsule. From Rohen et al. (1998).

The typical examples of amphiarthroses are junctions of vertebrae, joints between ribs and sternum or pubic symphysis.

The last class of joints, and for our needs the most important, is the class of *diarthroses*. All diarthotic joints are synovial joints and are the most common form of articulation between adjacent bones. They are highly movable junctions accommodating unique physical demands of particular body part. However, diarthoses share the common design of relatively congruent opposing cartilaginous surfaces enclosed within a synovial capsule filled with lubricating synovial fluid. Characteristic examples are the knee, hip, elbow, shoulder, etc. Detailed description of synovial joints shall be presented in the next section.

2.2. Synovial joint

In general, the structure of the bones connection in synovial joint can be complicated like in e.g. knee joint where more than two bones are connected via complicated system of intraarticular ligaments and other fibrocartilaginous disks (e.g. meniscus). For this reason we shall focus on the characteristic description of synovial joints in simpler constituted joint of shoulder, as presented in the Fig. 2.1.

As mentioned before, the synovial joint is designed to ensure mobility along with stability of the connected system. Mostly it serves to drive the bone head into adjacent socket as in the case of shoulder joint, schematically visualized in Fig. 2.2. The common feature of all synovial joints is the enclosed articular capsule containing synovial fluid (6) which lubricates articulating plates of cartilages (7) that slide against each other. The closure of the capsule is provided by the synovial membrane (5) which generates the synovial fluid and keeps it inside of the capsule during the articulation. The stability is supported mechanically by the shape of the junction and supportive ligaments, tendons and muscles, and biochemically which shall be described in the section of biochemical introduction, Chapter 4.

From rheological point of view, synovial joint is an effective lubricating configuration, highly reducing the musculoskeletal friction. The effectiveness of this type of lubrication has not been even approached by any man–designed machine. The principal answer to
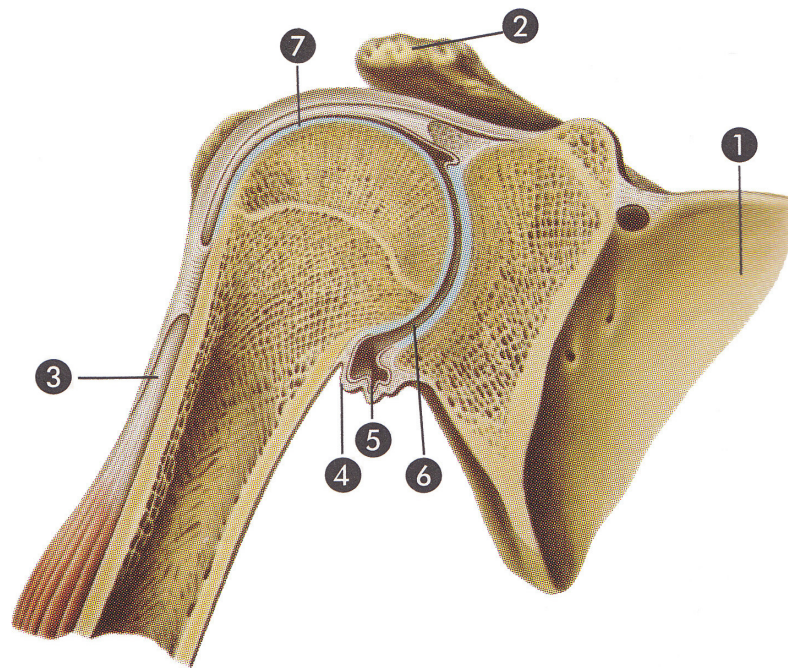
FIGURE 2.2. Schematic structure of shoulder joint: 1. scapula (shoulder blade); 2. Acromion (feature on the scapula articulating with clavicle (collar bone)); 3. Tendon of biceps bracii muscle (two head muscle of the arm); 4. Articular capsule; 5. Synovial membrane; 6. Joint cavity containing synovial fluid; 7. Articular cartilage. From Rigutti (2000).

the friction problem does not lie in the separated parts of the synovial joints but in their coexistence in the open biological system. Nevertheless, for deeper understanding of synovial joint as the whole we need to understand the morphology and biological properties of its individual components, which shall be described in the next sub–sections 2.2.1–2.2.4.

2.2.1. Articular cartilage. Adjacent bones in synovial joint are covered by hyaline (from Greek hyalos, *glass*) cartilage. Its thickness varies from joint to joint, in human body it is thickest in the knee joint $(2 - 4\,\mathrm{mm})$. Hyaline cartilage is a highly specialized tissue with porous structure, containing no nerves, lymphatics or blood vessels. In spite of the fact that the hyaline cartilage comprises of approximately 75% of water it is not a soft tissue. Its resilient and firm properties come from the macromolecular content. Approximately 15% of wet weight of cartilage consists of collagen fibers stabilizing the network of proteoglycan aggregates, which are structured macromolecules of glycosaminoglycan polymers, mainly chondroitin sulfate and keratin sulfate, branched away from central protein cores that themselves branch off from even larger glycosaminoglycan – hyaluronic acid, see Fig. 2.3. Large amount of negatively charged sulfate SO_4^- and carboxyl COO^- groups in the molecules of proteoglycans causes that the neighbor branches repel each other but they are attractive for the water molecules which is important for hydratation of the cartilage and thus principal in its lubrication properties. On the other hand, the glycosaminoglycans are covalently restrained within the collagen framework which resists the movement of interstitial water from cartilage and thus it allows the tissue to bear mechanical loading without permanent distortion. The lowest concentration of proteoglycans (and chondrocytes) is in the thin superficial zone where the concentration of collagen is highest. This slick fibrilar layer. see Fig.2.4, has ability to resist shear stresses and thus it plays an important role in lubricating properties of cartilage.

To the middle of the last century, it was considered that the articular cartilage is devoid of all metabolic pathways due to its lack in blood/lymphatic supplies and nerves, and blockade of non–permeable calcified cartilage from the side of subchondral bone. This view was
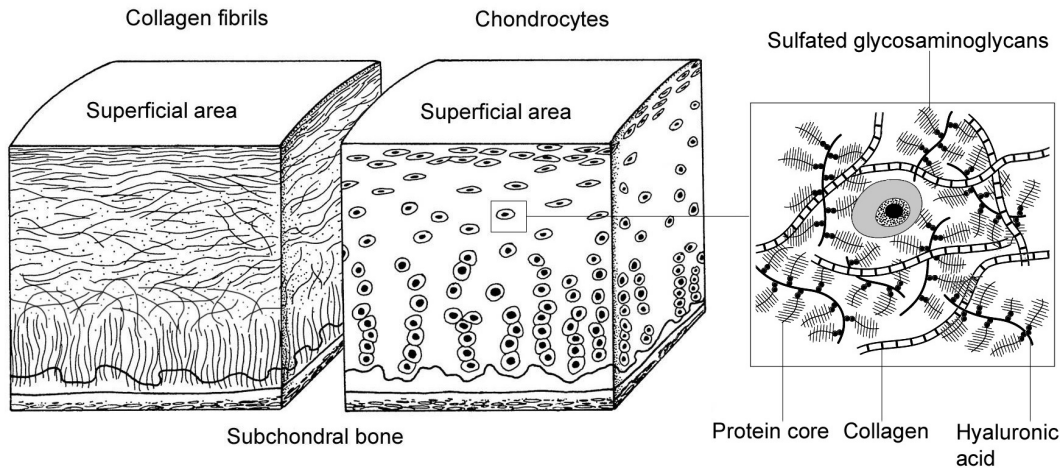
FIGURE 2.3. Schematic cross–section through the articular cartilage. For lucidity the cell and fibrous fractions are shown separately. Picture on the left demonstrates the directional orientation of collagen fibers which are perpendicular to the articular surface in the deep zone and becomes tangentially oriented close to the superficial area. Picture in the middle shows the distribution of cartilage cells, chondrocytes. Curved line represents tidemark – boundary between calcified and non–calcified cartilage. Picture on the right hand side demonstrates the macromolecular composition of extracellular matrix with formation of proteoglycans having the structure of bottle–brush.
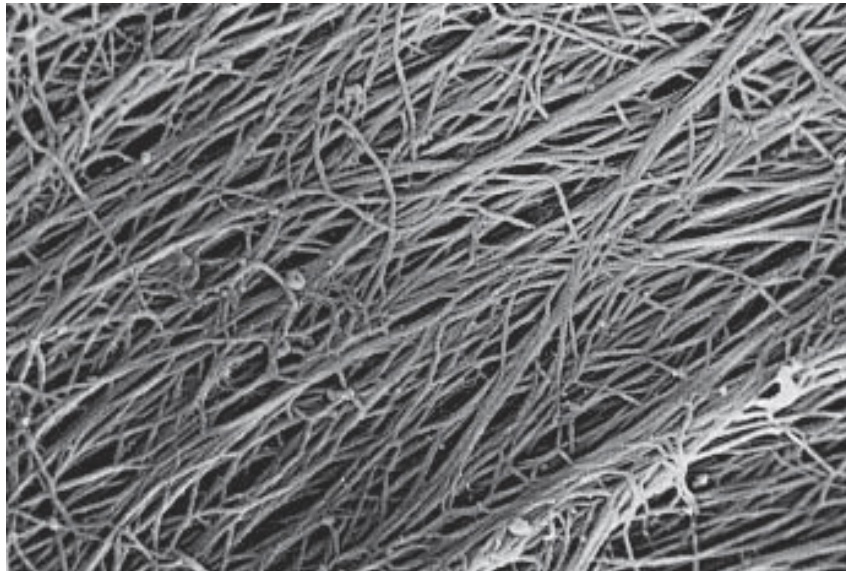
FIGURE 2.4. Scanning electron microscopy of the articulating surface of hyaline cartilage in synovial joint; magnification: ×8000. The collagen fibers are oriented in one main direction and cross over each other in acute angles. Cell elements and ground substance are not visible. From Kühnel (2003).

changed in connection with use of modern technologies like radioactive tracer method or scanning microscopy which proved the biological activity of articular cartilage. The delivery of nutrients and removal of metabolic wastes from chondrocytes is governed by fluid exchange between cartilage and lubricating synovial fluid during oscillatory movement of synovial
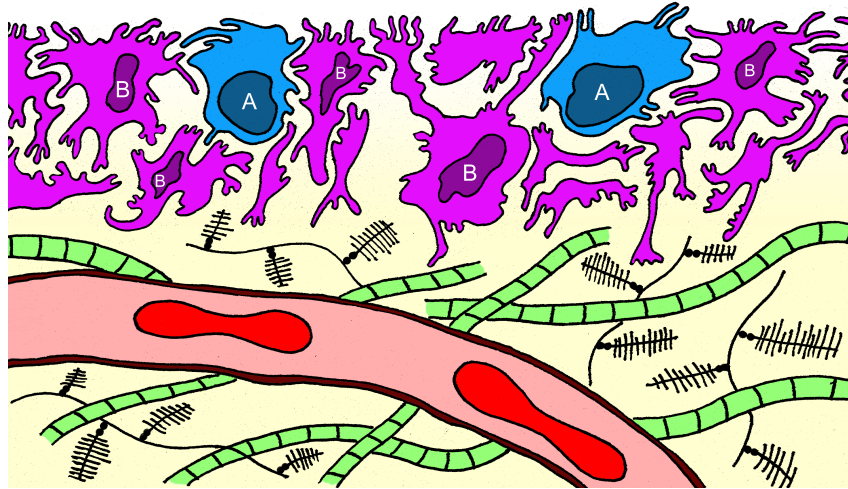
FIGURE 2.5. Schematic drawing of the cross–section of synovial membrane. In the inimal part of the membrane, two types of synoviocytes are present – type A cells (blue) are located at the superficial layer on the synovial intima, type B cells (violet) are present at various depths of synovial intima, in the yellow subintimal part, there is a blood capillary embedded in the extracellular mixture of macromolecule aggregates of glycoproteins (bottle–brush structure) and collagen fibrils (green strings). The upper white part represents the joint cavity occupied by the synovial fluid.

joints. The synovial fluid is itself exposed to molecular/cellular exchange with blood vessels and lymphatics in synovium. The negative consequence of this type of supplementation can be found in immobilized joints where the cartilage slowly degenerates due to unduly slow nutrient transport.

2.2.2. Synovial membrane. Synovium (or synovial membrane) plays an important role in the metabolism of synovial fluid (and consequently in metabolism of articular cartilage). Anatomically, it is characterized as a tissue enclosing the synovial cavity around the surfaces of articular cartilage. Synovium is connected to the articular cartilage on its peripheral rim and from the external side it is underlined by fibrous layer of the subsynovium. The Area of synovial membrane is surprisingly large (for example in human knee joint it makes approx. $280\,cm^2$) what ensures that synovium is not mechanically limiting the movement of the synovial joint when cartilages slide against each other. On the other hand, the potential pinch between cartilaginous surfaces would be destructive and thus the synovium folds and expanses like the folding of an accordion.

Synovial tissue, which is up to $25\,\mu$m thick, comprises of two histologically different parts, see Fig. 2.5. The thinner superficial layer, called intima, features a unique discontinuous cellular lining, rarely more than three cells thick. The intimal cells (synoviocytes) are not linearly organized into layers like in epidermis, instead, they are irregularly emplaced through this thin superficial part. Recent microscopical studies revealed that synoviocytes are connected via loose cell junctions and their extracellular distribution creates pores of effective size of approximately $50\,$nm. Histologically, synoviocytes are of two types – macrophagic cells (type A cells) which are imunoreactive and can phagocytose waste and cell debris, and dominant fibroplast–like cells (type B cells) which are characteristic for their rich rough endoplasmic reticulum indicating intensive protein activities. The real scans of synovial intima are presented in Fig. 2.6 and 2.7.

The thicker outer layer of synovium, called subintima, is cell–free loose connective tissue. Based on the composition of the subintimal tissue, the synovial membranes are usually classified as areolar, adipose and fibrous. In the complicated system of synovial joint like in
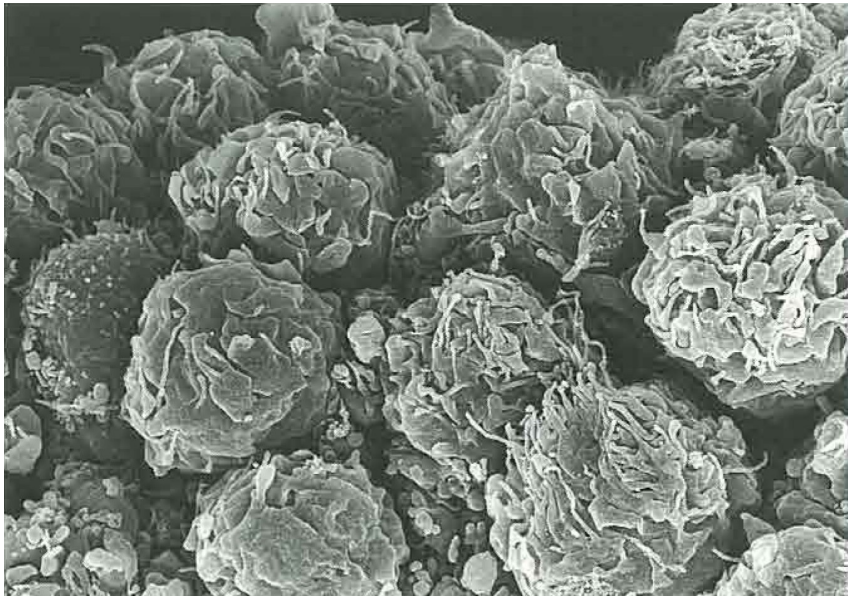
FIGURE 2.6. Scanning electron microscopic visualization of aggregation of synoviocytes on the superficial area of synovial membrane; Magnification: ×3400. From Iwanaga et al. (2000).
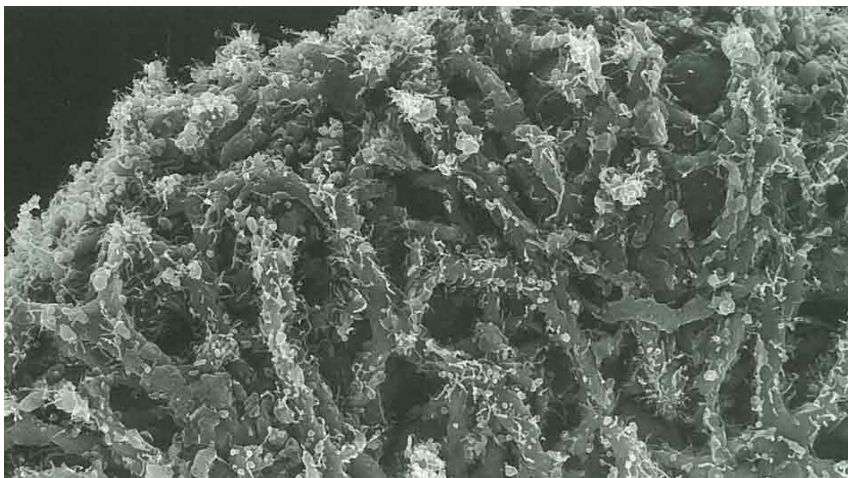
FIGURE 2.7. Scanning electron microscopic visualization of superficial area of synovial membrane; The foldings and microvili of the membrane are clearly visible; Magnification: ×2300. From Iwanaga et al. (2000).

the knee joint, all three types of synovium are present. The most important type of synovium is areolar which usually occurs in areas where synovium undergo the most extensive excursions and where the production and drainage of synovial fluid is dominant. It is composed of relatively thick cellular intima (3 cells depth), and its subintimal extracellular matrix, as the name suggests, is rich in blood capillaries and lymphatics supported by extensive meshwork of collagen fibrils with proteoglycan macromolecules. For adipose (fatty) type of synovial membrane is typical cellular layer composed of single flattened lining cells underlined by a layer of adipose cells and it usually lines articular fat pads. The fibrous type of synovial
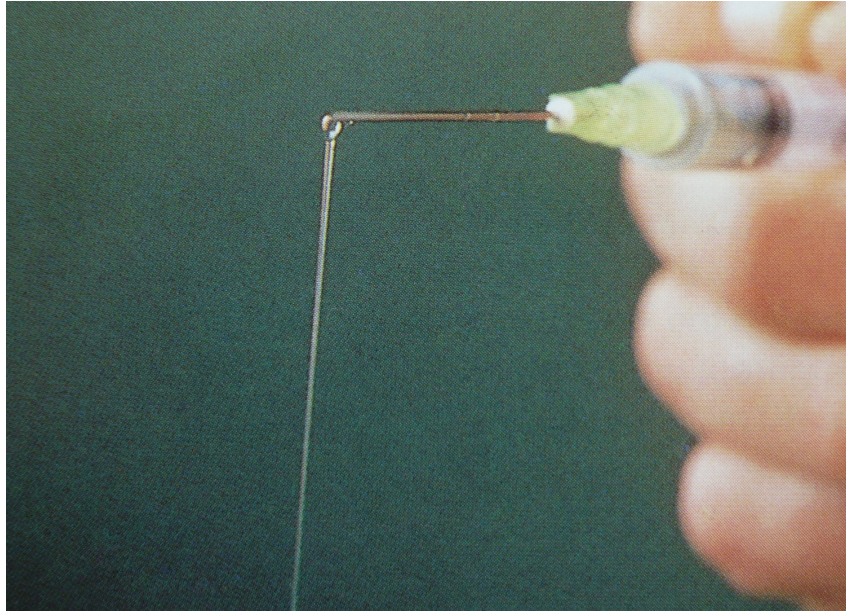
FIGURE 2.8. Consistency and visual appearance of synovial fluid. From Rijswijk (1992).

membrane is usually found over tendons and ligaments and it is characteristic in dense collagenous tissue of subintima[1].

From physiological point of view, synovial membrane is essential organ controlling homeostasis of synovial joint cavity. Its principal function is to maintain the synovial fluid inside the joint cavity (even during high oscillatory loading), but also, the fibroplast–like intimal cells are place of origin of the main chemical constituent of synovial fluid – the hyaluronan (hyaluronic acid). The third important function of synovial membrane is its property of a biological sieve which allows nutrients to enter the synovial cavity and consequently the avascular cartilage but protects the fluid–filled cavity from invasion of possible aggressors from close blood stream.

2.2.3. Synovial fluid. Since the study of synovial fluid is the main topic of this thesis, we shall employ ourselves in deeper research on the biological, chemical and mechanical properties of synovial fluid. This characteristics change with the health condition of the involved synovial joint, however, in this section, we shall focus only on the characterization of the normal[2] synovial fluid. The study of pathological cases shall be then elaborated in later section.

Synovial fluid is foremost contained in the cavity of synovial joint but in small amount it is found in the articular cartilages and synovium, as well. The amount of synovial fluid in synovial joint is very small to its internal surface area. In the human knee, for example, the total volume of synovial fluid varies from 0.5 to 3 ml, occupying internal surface of approximately 420 cm^2. Normal synovial fluid is transparent, colorless, noticeably thick with consistency like egg–white (hence the name, from Latin ovum, *egg*). With its chemical constitution, synovial fluid is primarily an ultrafiltrate of blood plasma, with almost the same electrolyte concentration but small concentration of blood proteins, see Tab. 2.2. The blood plasma is ultrafiltrated from the blood capillaries in synovium and at the intimal layer of synovium it is enriched by two types of locally synthesized molecules, hyaluronan (in higher quantities) and lubricin (in smaller amount). Both of them are actively synthesized and

---

[1]Some authors regard the subintimal layer as a part of subsynovium and thus they consider the synovial membrane to be only the cellular layer. In this thesis, we consider the subintima to be a part of synovial membrane.

[2]By normal synovial fluid we mean the synovial fluid with rheological responses and biochemical composition as that of a healthy young individual.

Molecule of plasma	SF/plasma ratio
Na+	0.93
Cl-	0.01
Urea	0.96
Albumin	$0.37 - 0.45$
Transferrin	0.24
Immunoglobulin G	0.21
$\alpha 2-$macroglobulin	$0.03 - 0.19$
Total protein fraction	0.28
Hyaluronan	70000

TABLE 2.2. Ratio between concentration of particular plasma molecules in synovial fluid (SF) and blood plasma. From Wright and Radin (1993).

secreted by the synoviocytes (lining cells) of type B. Total cell count in normal synovial fluid does not exceed 200 per mm^3. Most of the nucleated cells are from group of white blood cells while erythrocytes are absent.

Biological function. As it has been already mentioned before, synovial fluid has three vital biological functions. First, it supplies the cells of avascular cartilage with nutrients and removes their metabolic waste, second, it lubricates the articular cartilage surfaces during joint movement, and third, it stabilizes the joint capsule during joint movement or intensive shock loading due to its exceptional viscoelastic behavior. While the nutrition of the joint is predominantly biological issue, the lubrication and joint stabilization are primarily based on bio–mechanical principles requiring the understanding of rheological responses of important chemicals which are contained in synovial fluid. The main mechanical aspects of responses of synovial fluid are in detail elaborated in Chapter 4, specifically focused on the rheology of synovial fluid.

Joint nutrition. Despite very low cellular fraction of cartilage, which is about 5%, the total cellular mass of cartilage highly exceeds the cellular mass of the synovium. Thus, under normal conditions, cartilage consumes approximately 70% of glucose supply which comes from subintimal capillaries of synovial membrane. This nutrient microcirculation in synovial cavity is crucial in maintenance of the effective rheological properties of the cartilage, and thus in prevention of cartilage from wearing and consequently from joint diseases. The nutrient microcirculation in synovial cavity is closely related to synovial fluid exchange and its chemical composition.

2.2.4. Ligaments, tendons, muscles. Last piece ensuring the synovial joint stability are the strong supportive tissues like the ligaments and tendons. While ligaments are elastic connections between adjacent bones in joints (they reversibly stretch up to 10%), the tendons serve as an inextensible connection tissue between bone and muscle. In both cases, they are composed of arrays of collagen fibers. The composition of such bone junctions is designed to permit allowed flexion and extension of the joint but prevent any other inappropriate motion or hyperextension. On the other hand, joint muscles predominantly serve as a contractive tissue for voluntary skeletal movement and in maintaining the posture.

2.3. Joint diseases

To this date, it is known over 100 pathological disorders of synovial joints. They do not share single cause or common pathway, and moreover, still some of them are not fully understand. This diversity, nevertheless, has one common feature: the pain beyond imagination of a healthy person. Each form of arthritis tends to target certain group of joints, and thus it must be related to a joint function or its articular structure. The most common forms of joint diseases are osteoarthritis, rheumatoid arthritis, gout and septic arthritis.

The joint diseases have noninflammatory stage during which the cell count in the synovial fluid is not greater than $2,000$ cells per mm^3. The exceeding of this limit is already considered
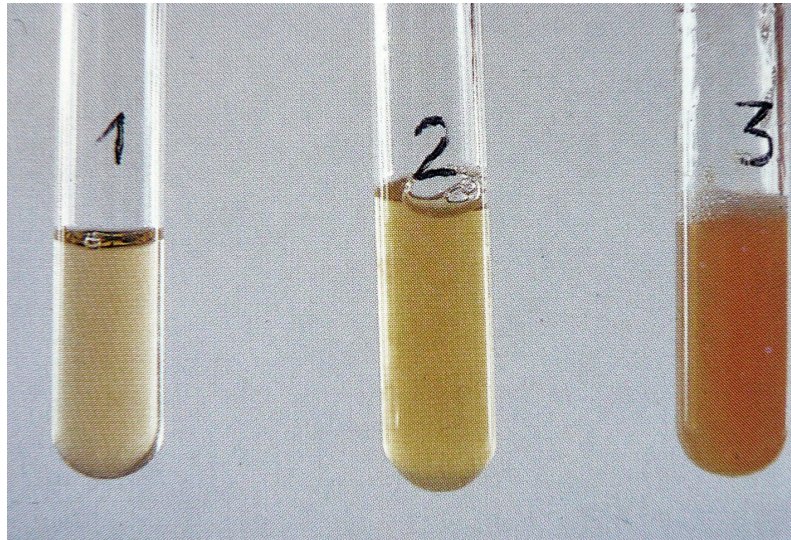
FIGURE 2.9. Visual appearance of different pathological synovial fluids. 1. synovial fluid from osteoarthritic joint, cell count 300 cells/mm^3, does not exhibit almost any changes in visual appearance; 2. slightly inflammatory synovial fluid, less than $6,000$ cells/mm^3; 3. extremely inflammatory synovial fluid, rheumatoid arthritis $100,000$ cells/mm^3 and septic arthritis $150,000$ cells/mm^3. From: Rijswijk (1992).

as an inflammatory process. Correlation of the pathological synovial fluid is demonstrated in Fig. 2.9.

Osteoarthritis. This degenerative joint disease is caused by mechanical wearing and degeneration of the hyaline cartilage in synovial joint which lack the ability of self–regeneration. Mainly, it is characterized by remodeling of the joint due to replacement of worn cartilage by tougher tissue, which results the bony growths in the joint cavity. The common symptoms of osteoarthritis are chronic pain caused by the dragging of the bony growths, joint stiffness as the movement becomes painful, and joint effusion (volume of synovial fluid can be increased up to 10–times).

Osteoarthritis can be caused by aging, or by repeated trauma, surgery, joint injury, as well as by obesity or hormonal disorders. As emerge from the osteoarthritis character, it affects predominantly large weight–bearing joint, such as knees and hips or spine.

Unfortunately, osteoarthritis can not be fully healed. Nevertheless, first stages can be treated by lifestyle modification (weight–loss, exercises) or joint injection resulting short–term pain relief. On the other hand, popular and expensive nutritional supplements are by scientific community believed to have only placebo effect. Advanced stage of osteoarthritis can be treated only by the joint replacement.

Rheumatoid arthritis. Rheumatoid arthritis is autoimmune disorder which forces the immune system to mistakenly attack the healthy organ. The initial immune attack is aimed against the synovium which results in retarded production of synovial fluid and consequently in the inflammatory expansion to the joint cavity and neighboring tissues. Primary symptoms of rheumatoid arthritis are chronic pain, morning stiffness, joint swelling. Nevertheless, the patient may not suffer from any of them for a long time from the beginning of the illness or the symptoms can come and go.

The cause of such autoimmune disorders remains unknown to this day. For long time, the infectious agents such as viruses, bacteria or fungi have been suspected, nevertheless, none of them has been claimed as the prime cause. Yet, stress, allergies, family history, smoking and environmental factors are significantly correlated with inception of rheumatoid arthritis.

In contrast to osteoarthritis, rheumatoid arthritis affects small joints in a symmetric fashion, such as the finger joints of both hands, wrists or the small joints of feet. There is no known cure for rheumatoid arthritis, but some treatment tools can soften the symptoms and relief pain. Common treatments consist in the joint injections and usage of anti–inflammatory agents and analgetics.

Gout. In the case of big toe, gout is known as podagra. It is a disorder of purine metabolism which final metabolite, uric acid, crystallizes and precipitate in synovial joints and surrounding tissues. Elevated uric acid level then initiates the local immune inflammatory reaction. Gout is characteristic for red, tender and swollen joint with pain occurring during the night.

Gout is caused by significantly increased level of uric acid in the blood from many reasons such as alcohol consumption, obesity, insulin resistance or chemotherapy. First stage of treatment is focused on the acute inflammatory attack, and after, the medicament reducing the uric acid level in the blood are prescribed.

Septic arthritis. Septic arthritis is an inflammatory reaction in the joint caused by presence of infectious agent, usually bacteria. They are introduced to joint through the synovial membrane (from blood stream or acute trauma of adjacent tissue) and after they all over the joint. Septic arthritis is an medical emergency requiring immediate treatment otherwise the permanent joint damage occurs within few days. Septic arthritis is treated with intravenous antibiotics and joint washouts.

Description of response of viscous and viscoelastic material in connection with synovial fluid

Before we discuss in more detail the rheological properties of synovial fluid, we shall provide here a brief phenomenological background of the nature of viscous/viscoelastic behavior and describe how such mechanical properties can be experimentally measured especially in connection with synovial fluid. It is assumed that the reader is familiar with the fundamentals of the classical theory of continuum, and thus, we shall not recall the basic definitions of fluid/solid mechanics. For rigorous definitions and derivations of mentioned terms and relations we refer the reader to books of introduction to mechanics of continuum, for example by Truesdell and Rajagopal (2000), book with applications to biomechanics by Fung (1993), or specifically mechanics of viscoelasticity of polymers by Ferry (1980). Through the whole chapter we shall focus mainly on the description of the fluid–like materials, nevertheless the comparison with solid–like bodies shall be commented.

It is well documented that for modeling of non–Newtonian[1] fluids the classical theory of continuum mechanics is not always sufficient. Instead, new approaches were derived to model the non–linear effects of real materials, for instance the description of body deformation by the means of natural configuration, which is very promising. Nevertheless, in the case of synovial fluid we do not have the sufficient experimental data which we need for description of non–linear responses, and thus, we can not model the responses of synovial fluid with the new, more rigorous, descriptions. For these reasons, we shall describe the deformation relations by the means of classical continuum mechanics.

In what follows, for simplification, we consider the incompressible material to be exposed to one–dimensional simple shear, as illustrated in Fig. 3.1. We denote the shear stress by τ , shear strain by γ and shear rate by $\dot{\gamma}$. In the tensor notation, the strain $\boldsymbol{\varepsilon}$ and stress $\boldsymbol{T} = -p\boldsymbol{I} + \boldsymbol{S}$ are expressed as

$$(3.1) \qquad \boldsymbol{\varepsilon} = \frac{1}{2} \begin{pmatrix} 0 & \gamma & 0 \\ \gamma & 0 & 0 \\ 0 & 0 & 0 \end{pmatrix}, \quad \boldsymbol{T} = \begin{pmatrix} -p & 0 & 0 \\ 0 & -p & 0 \\ 0 & 0 & -p \end{pmatrix} + \begin{pmatrix} S_{11} & \tau & S_{13} \\ \tau & S_{22} & S_{23} \\ S_{31} & S_{32} & S_{33} \end{pmatrix}.$$

3.1. Ideal versus real material

The classical theories of hydrodynamics and elasticity deal with the mechanical properties of ideal materials such as linear viscous fluid and linear elastic solid, respectively. In the case of a linear viscous fluid, or as often called a Newtonian fluid, its deformation is described by the Newton's law which states that the stress is always directly proportional to the strain rate but is independent of strain itself. This material does not adopt fixed state of deformation if

---

[1]Non–Newtonian fluid is such that can not be described by one constant material parameter, the viscosity. We would like to emphasize, that viscoelastic fluid is a subclass of the non–Newtonian fluid.
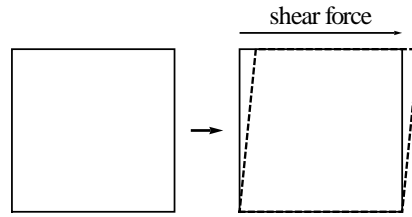
FIGURE 3.1. Simple shear deformation.
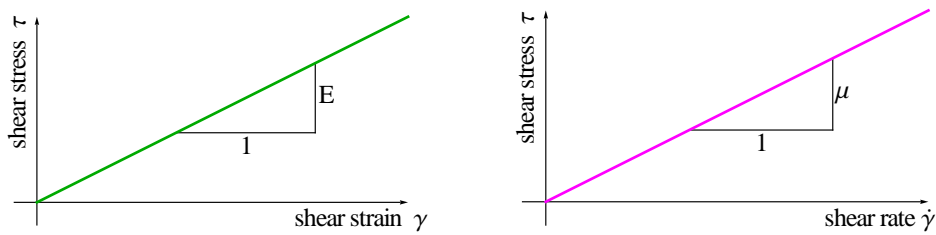
FIGURE 3.2. Shear stress–strain plot for a linear elastic solid and shear stress–shear rate plot for a linear viscous fluid. Here, μ and E represent the material parameters of linear viscous fluid – viscosity, and linear elastic solid – Young's modulus, respectively.

exposed to constant stress, and thus, it itself never recovers form deformation. On the other hand, the response of a linear elastic solid obeys the Hooke's law (therefore the name Hokean solid) postulating linear relationship between stress and strain, see Fig. 3.2. In contrast to linear viscous fluid, the elastic solid recovers completely from the deformation after the removal of applied load. The schematic illustration of mechanical responses of ideal materials during simple shear is shown in Fig. 3.3.

Even though these categories are idealizations, and for some materials they are good approximations for infinitesimal deformation, the real material is known to behave in a more complex way, combining liquid–like and solid–like characteristics. This behavior is (unsurprisingly) called viscoelastic. Such material does not store or dissipate all of the energy input, and it exhibits various, sometimes truly spectacular, non–linear properties, as described for instance in Rajagopal (1993) for the case of fluids.

The mechanical response of an ideal elastic material is characterized by linear shear stress–strain relation and thus the ideal elastic material is specified by a single number, the slope of its deformation line, which is considered to be a material property. This is analogous to the Newtonian fluid, which is characterized by one material parameter, the viscosity, defined as a slope of shear stress–shear rate graph. The situation of viscoelastic material is significantly different. The mechanical response varies and thus the material characterizations can not be single numbers but the entire response curves.

In general, we distinguish between two standard types of experiments for determining the material properties of viscoelastic materials: *transient* and *dynamic* experiments. In the case of transient experiments, commonly, the material is subjected to a simple shear, while in the case of dynamic tests the material is exposed to sinusoidal shear oscillations. While the oscillatory test are typical for description of linear viscoelasticity, the transient experiments are suitable for description of non–Newtonian characteristic of a material response. In the next sections, let us go through the particular specifics of both types of experiments.

3.2. Transient experiments

Typical features of non–Newtonian behavior during transient experiments are stress–relaxation and creep, as depicted in Fig. 3.4 and 3.5. In the case of stress–relaxation, the material subjected to a continuous shear strain deformation exhibit non–immediate response
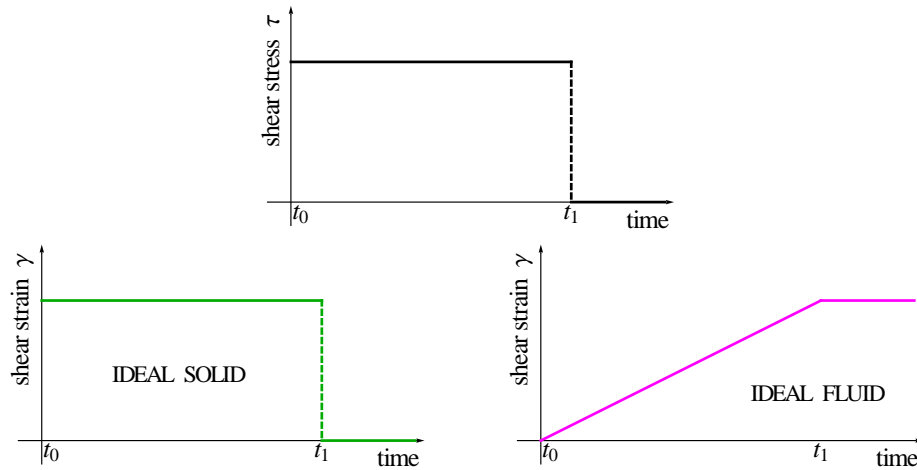
FIGURE 3.3. Mechanical response of ideal materials to step stress test. Top: Step stress test, at time t_0 the shear stress is instantly increased to a certain level and then held constant to time t_1. Bottom: The instantaneous response of linear elastic solid (green) and linear viscous fluid (pink).
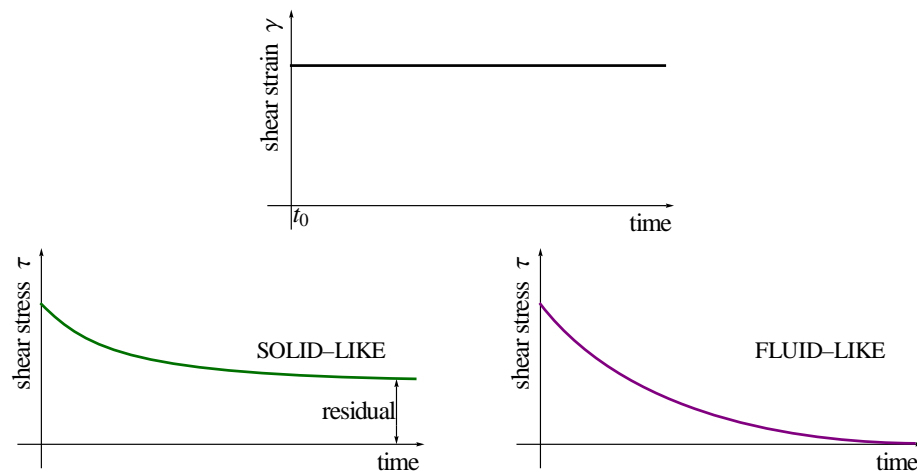
FIGURE 3.4. Stress relaxation. Top: Continuous strain history. Bottom: response of viscoelastic solid (left) and viscoelastic fluid (right) to a strain test. After some time, the fluid–like material does not require any additional stress to maintain in the new shape, while solid–like materials do. The decrease of stress at constant strain is called stress–relaxation.

in shear stress, in other words, it relaxes the stress. On the other hand, for the material exhibiting the creep phenomena the stress recovery after the immediate strain removal is relaxed. Generally, the material recovers only part of the strain (in the case of viscoelastic fluid) or approaches the zero strain state asymptotically (in the case of viscoelastic solid). Nevertheless, there are many other non–Newtonian behaviors which are observed by transient experiments, among them the normal stress differences (for simple shear deformation the normal stresses are different), yield stress (the deformation occurs after some critical value of shear stress is reached) or shear tinning/thickening (see below). One can find more on non–Newtonian fluids for example in Truesdell and Noll (1965). For now, let us focus for a while on one specific slight departure from Newtonian characteristic, called shear–thinning, since this is well documented for synovial fluid.
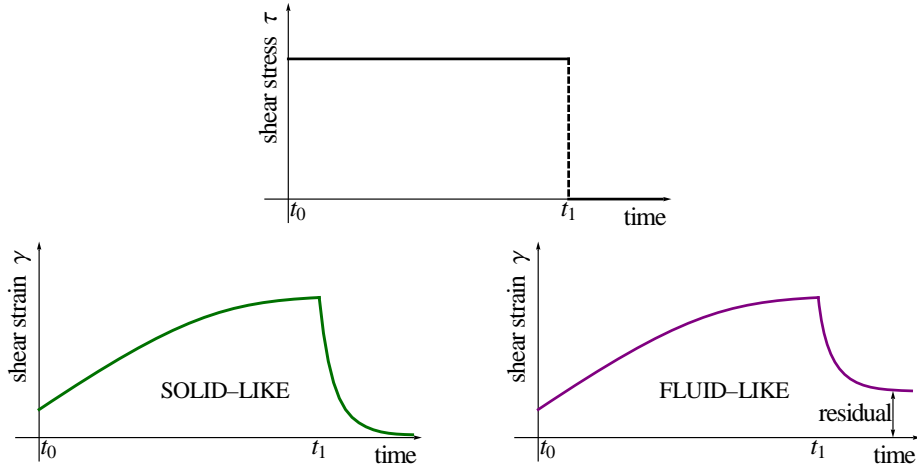
FIGURE 3.5. Mechanical response of viscoelastic material to step stress test – creep. Top: Step stress load. Bottom: Response to step stress of viscoelastic solid (left) and viscoelastic fluid (right). For solid–like materials all the strain is recovered and thus it asymptotically approaches zero, while for fluid–like materials, only part of the strain is recovered, hence the asymptotic approach to a constant value. This continued straining is called creep. Compare with ideal materials in Fig. 3.3.
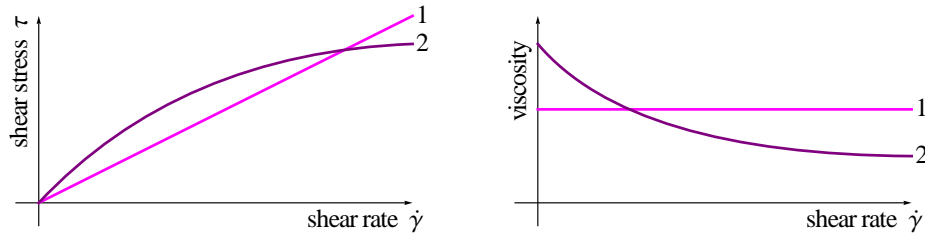
FIGURE 3.6. Shear–thinning (left) and generalized viscosity (right) in comparison with Newtonian fluid (curve 1).

Shear–thinning. As it has been defined above, the viscosity is a material parameter of Newtonian fluid, a proportion between shear stress and shear rate during simple shear, see curve 1 in Fig. 3.6. However, in some fluids (especially in polymeric solutions) distinguished departure from this linear relationship is observed (see curve 2 in Fig. 3.6). This non–linearity then evokes as if viscosity is a function of shear rate. Following this phenomenological approach we define the so–called generalized viscosity μ_g, through

$$(3.2) \qquad \mu_g\left(\dot{\gamma}\right) = \frac{\tau}{\dot{\gamma}}.$$

Even though such fluid is not Newtonian, one can still describe it in this framework, and thus, sometimes such fluid is called generalized Newtonian. One should notice that the viscosity is monotonic decreasing function of shear rate, as the fluid thins the shear rate. For most shear–thinning fluids it has been observed experimentally that the generalized viscosity tends to some limit value for very high shear rates.

3.3. Small amplitude sinusoidal oscillations

Now, let us discuss the oscillatory experiment in greater detail since the experimental data of viscoelastic response of synovial fluid we obtained are of this kind.

In what follows, we assume that the material is an incompressible fluid, which rheological behavior is expected to be describable by the model of *linear* viscoelastic fluid. This is a
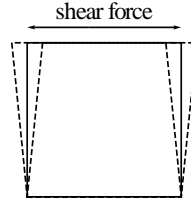
FIGURE 3.7. Harmonically oscillatory simple shear.
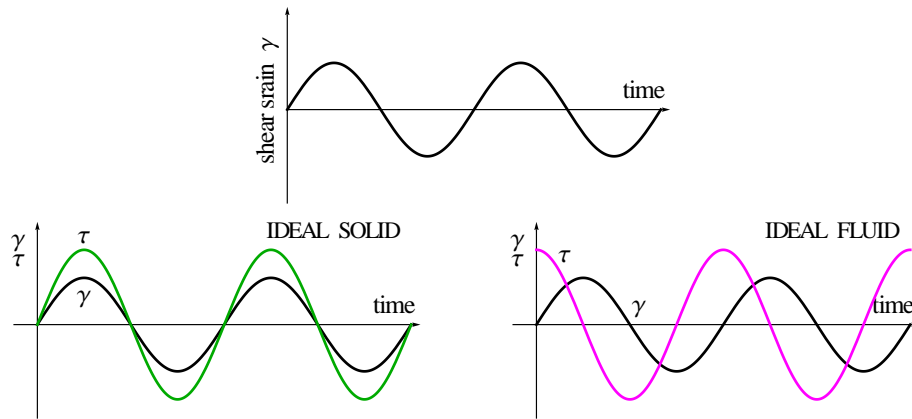
FIGURE 3.8. Mechanical response of ideal material to harmonically changing deformation. Top: The sinusoidal strain. Bottom: The response of linear elastic solid (green) with zero phase shift between shear strain and shear stress and linear viscous fluid (pink) with exactly $\pi/2$ phase shift between shear strain and stress.
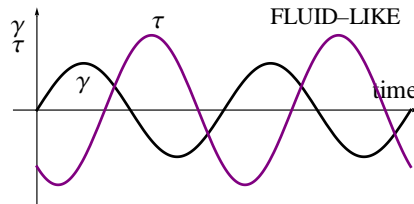
FIGURE 3.9. Mechanical response of linear viscoelastic material to harmonically changing deformation. The phase shift between strain and stress in the case of linear viscoelastic material is general. Compare with ideal materials in Fig. 3.8.

good approximation for most of the viscoelastic materials in such type of experiment, e. g. small amplitudes and small frequencies deformation. For now, since it will be advantageous for the derivation and understanding of some physical quantities used commonly in the engineering/experimentalist community, let us start from the constitutive equation describing the strain stress relation by an integral formula (see Lai et al. (1978), Ferry (1980) or Rajagopal and Srinivasa (2000) for more details)

$$(3.3) \qquad \boldsymbol{T} = -p\boldsymbol{I} + \boldsymbol{S}, \qquad \boldsymbol{S}(t) = 2\int_{-\infty}^{t} \boldsymbol{\mathcal{G}}(t - t')\boldsymbol{D}(t')\mathrm{d}t',$$

where $\boldsymbol{T}$ is the stress tensor, p is the pressure, $\boldsymbol{I}$ is the identity tensor and $\boldsymbol{S}$ is known as the extra stress tensor expressed in terms of history of all relative deformations. Here, $\boldsymbol{D}$ is

the symmetric part of velocity gradient, $\boldsymbol{D} = \frac{1}{2}\left(\nabla \boldsymbol{v} + \nabla \boldsymbol{v}^{\mathrm{T}}\right)$, and $\boldsymbol{\mathcal{G}}(t)$ is tensor of 4th order called (tensorial) relaxation function.

Consider one–dimensional deformation of oscillating simple shear, with small amplitude sinusoidal shear strain

$$(3.4) \qquad \varepsilon(t) = \frac{1}{2}\begin{pmatrix} 0 & \gamma(t) & 0 \\ \gamma(t) & 0 & 0 \\ 0 & 0 & 0 \end{pmatrix}, \qquad \gamma(t) = \gamma_0 \sin(\omega t),$$

with frequency ω in rad/sec ($\omega = 2\pi\nu$, ν in Hz) and strain amplitude γ_0 small enough, assuring that the material response is in the linear range, as illustrated in Fig. 3.7. Then the symmetric part of velocity gradient and shear rate are

$$(3.5) \qquad \boldsymbol{D}(t) = \frac{1}{2}\begin{pmatrix} 0 & \dot{\gamma}(t) & 0 \\ \dot{\gamma}(t) & 0 & 0 \\ 0 & 0 & 0 \end{pmatrix}, \qquad \dot{\gamma}(t) = \omega\gamma_0 \cos(\omega t),$$

and thus the extra shear stress reduces to

$$(3.6) \qquad S_{12} = \tau(t) = \int_{-\infty}^{t} \mathcal{G}(t - t')\dot{\gamma}(t')\mathrm{d}t',$$

where $\mathcal{G}(t)$ is called the relaxation modulus, considered as the material function. In order to use this integral constitutive equation, the material function $\mathcal{G}(t)$ has to be determined by an experiment. One should notice, that other components of stress tensor do not have to be automatically zero, even though the strain tensor takes the form of (3.4).

Substituting equation (3.5) into (3.6) and denoting $t - t'$ by s, we have

$$\tau(t) = \int_{0}^{\infty} \mathcal{G}(s)\omega\gamma_0 \cos[\omega(t - s)]\mathrm{d}s =$$

$$(3.7) \qquad = \gamma_0\left[\omega\int_{0}^{\infty}\mathcal{G}(s)\sin(\omega s)\mathrm{d}s\right]\sin(\omega t) + \gamma_0\left[\omega\int_{0}^{\infty}\mathcal{G}(s)\cos(\omega s)\mathrm{d}s\right]\cos(\omega t).$$

In the case of viscoelastic fluid, the integrals make sence since $\mathcal{G}(s) \to 0$ as $s \to \infty$. As one can see, the shear stress τ is periodic as well as the strain γ, constructed by superposition of two terms which are in the phase (as linear elastic solid response, see Fig. 3.8) and out of phase by $\pi/2$ (as linear viscous fluid response) with strain. Thus, the relative phase shift between shear strain and shear stress of linear viscoelastic fluid is of a degree depending on the relative magnitudes of the coefficients in brackets in (3.7), which are frequency dependent but free of dependency of elapsed time. Thus the constitutive equation can be rewritten in terms of

$$(3.8) \qquad \tau(t) = \gamma_0\left\{G'(\omega)\sin(\omega t) + G''(\omega)\cos(\omega t)\right\},$$

where

$$(3.9) \qquad G'(\omega) = \omega\int_{0}^{\infty}\mathcal{G}(s)\sin(\omega s)\mathrm{d}s,$$

$$(3.10) \qquad G''(\omega) = \omega\int_{0}^{\infty}\mathcal{G}(s)\cos(\omega s)\mathrm{d}s.$$

The frequency functions G' and G'' are called the shear storage (or elastic) modulus and shear loss (or viscous) modulus, respectively. In fact, modulus G' is a measure of energy which is stored and subsequently released per cycle of deformation and thus it reflects the elastic nature of the material. On the other hand, G'' is a measure of energy which is dissipated as heat per deformation cycle and therefore it is connected with the events having the viscous nature.

Another possibility how to describe the material properties of linear viscoelastic fluid exposed to small amplitude oscillations is to formulate the shear stress with the phase difference angle δ and stress amplitude τ_0

$$(3.11) \qquad \tau(t) = \tau_0 \sin(\omega t + \delta(\omega)) = \tau_0 \cos(\delta(\omega))\sin(\omega t) + \tau_0 \sin(\delta(\omega))\cos(\omega)t,$$

in relationship to G' and G''

$$(3.12) \qquad G'(\omega) = \frac{\tau_0}{\gamma_0} \cos\delta(\omega), \qquad G''(\omega) = \frac{\tau_0}{\gamma_0} \sin\delta(\omega), \qquad \frac{G''(\omega)}{G'(\omega)} = \tan\delta(\omega).$$

For each periodic measurement at a given frequency, one gets two independent quantities describing the material response in regime of sinusoidal oscillatory deformation, either G' and G'' or δ and τ_0/γ_0.

Since the complex shear modulus G^* is quite commonly used in the literature concerning experimental measurements, let us briefly outline its derivation. Consider the stress and strain in complex notation

$$(3.13) \qquad \gamma^* = \gamma_0 e^{i\omega t}, \qquad \tau^* = \tau_0 e^{i(\omega t + \delta)},$$

and the complex shear modulus defined as

$$(3.14) \qquad G^* := \frac{\tau^*}{\gamma^*}.$$

Then, its real and imaginary parts are the G' and G''

$$(3.15) \qquad G^* = \frac{\tau^*}{\gamma^*} = \frac{\tau_0}{\gamma_0} e^{i\delta} = \frac{\tau_0}{\gamma_0}(\cos\delta + i\,\sin\delta) = G' + iG''.$$

The approach of complex quantities has advantage, as it represent the elastic and viscous responses simultaneously and moreover, it allows the introduction of complex viscosity defined in a natural way $\mu^* := \tau^*/\dot{\gamma}^*$. Nevertheless, in the chapter concerning fitting the synovial fluid responses as of viscoelastic material, we use the approach of G', G'' involved in the shear stress through (3.8).

Remark. For complicated materials, as most biological fluids and solids, the models of linear viscoelasticity are strongly limited, usually applicable to certain very small range of deformations. The theory of **non–linear viscoelasticity** proposes a bigger class of models, but this direction of material modeling is quite new, not deeply adapted by experimentalists. That is the reason, why the experiments are often carried on in the traditional way, suitable for description of linear viscoelasticity. Even in our case, the available experimental data concerning viscoelastic properties of synovial fluid are characterized by G' and G'' only, and thus, we have no other possibility than to restrict ourselves to the linear viscoelastic modeling.

Chapter 4

Rheology of synovial fluid

Rheological properties of synovial fluid have never been studied as frequently as for example of blood. The main reasons are that the synovial fluid is not essential to life as for example the blood or biological fluids of the brain, and, that the extraction of normal synovial fluid from human joints is a difficult and painful process. Hence, the samples of human synovial fluid for experimental needs are often substituted by these from animal synovial joints, like of rabbits, oxes or horses, or the examination is accomplished on biological fluids chemically analogous to synovial fluid, for example on the solutions from umbilical cord or rooster comb. On the other hand, the rheological properties of pathological synovial fluid are well documented. In this thesis, we study properties of normal synovial fluid, nevertheless, we shall, in some cases, comment alternations arising from possible pathological deviations.

First intensive scientific investigations of composition and properties of synovial fluid date back to the late thirties of the last century (Meyer et al. (1939), Ropes et al. (1940), Davies (1946)), which were shortly followed by deeper study of the special rheological properties of synovial fluid which were attributed to the main chemical constituent of synovial fluid, hyaluronan, (Ogston and Stanier (1953), Sunblad (1953)). This pioneering work draw attention especially after the introduction of joint disorder treatments by hyaluronan injections what entirely accelerated the interest in study of hyaluronan functions in aqueous solutions and its relation to viscoelastic properties of synovial fluid. For this reason, it is necessary to understand the physico–chemical properties of hyaluronan molecules in liquid solutions, on which we can build phenomenologically justified mathematical model describing synovial fluid mechanical responses.
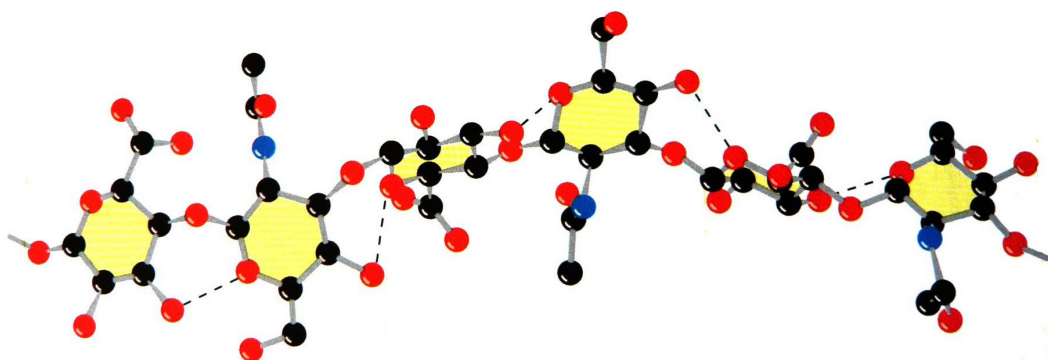
FIGURE 4.1. Schematic structure of hyaluronan molecule. The polyanion forms an extended left–handed helix with three disaccharide units per one turn. From Voet and Voet (2004).

Name	Number of anionic (sulfated) groups per disaccharide unit	Molecular mass M_r[Da]	Occurrence
Hyaluronan	1 (0)	$4 - 7 \times 10^6$	synovial fluid, skin, vitreous humour
Chondroitin–4–(6–)sulfate	2 (1)	$1 - 5 \times 10^4$	major component of cartilage
Dermatan sulfate	2 (1)	$1 - 5 \times 10^4$	mostly in skin, but also in blood vessels walls
Keratan sulfate	1 (1)	$5 - 15 \times 10^3$	component of cornea, cartilage, bone
Heparin	4 (3)	$5 - 20 \times 10^3$	blood clot inhibitor, not part of connective tissues

TABLE 4.1. Comparison of typical glycosaminoglycans, focused on the chain length and anionicity. From Voet and Voet (2004).
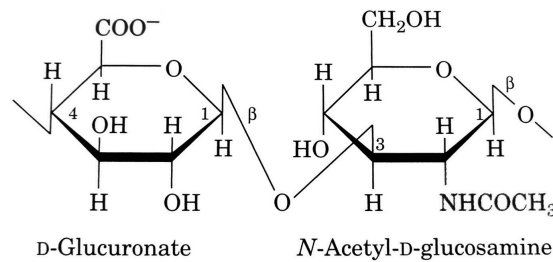
FIGURE 4.2. Disaccharide unit of hyaluronan molecule.

4.1. Hyaluronan

Hyaluronan (also called hyaluronic acid) is a long–chained polysaccharide typically found in the soft connective tissues of vertebrates, especially in the synovial fluid, cartilage, vitreous humor of the eye, umbilical cord or skin. Notable amount is found in the internal organs, very little in the blood serum. Summary of typical concentrations of hyaluronan in different human body organs is shown in Tab.4.1. Hyaluronan structurally belongs to the group of glycosaminoglycans, the unbranched polysaccharides of alternating uronic acid and hexosamine residues, often associated with tissue collagen fibrils. Nevertheless, hyaluronan is quite distinct from other glycosaminoglycans. It is does not bond to proteins or polypeptides to form proteoglycans (common aggregates found in cartilage, see section 2.2.1), it is not sulfated and its molecular weight in normal synovial fluid, for example, reaches millions, which is $10^2 - 10^3$ times higher than for any other glycosaminoclycan molecules, see for comparisons Tab. 4.1.

Molecule of hyaluronan is unbranched, composed of disaccharide units consisting of D–glucuronic acid and N–acetyl–D–glucosamine linked by alternating $\beta(1 \rightarrow 3)$ and $\beta(1 \rightarrow 4)$ bond (see Fig.4.2). Unlike other glycosaminoglycans, its chain is composed of up to 25000 repeating disaccharides units which makes the hyaluronan of an extraordinarily high molecular

Organ or fluid	Concentration [μg/g]
Umbilical cord	4100
Synovial fluid	$1400 - 3600$
Dermis	200
Vitreous body	$140 - 338$
Brain	$35 - 115$
Urine	$0.1 - 0.3$
Plasma serum	$0.01 - 0.1$

TABLE 4.2. Normal concentrations of hyaluronan in various organs of human body. From Fraser et al. (1997).
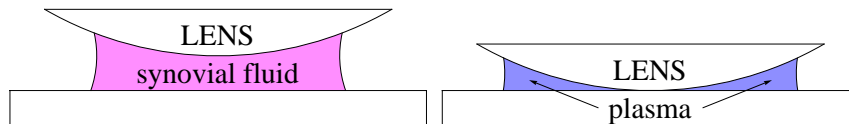
FIGURE 4.3. Demonstation of elastic–like properties of synovial fluid documented by Ogston and Stanier (1950). The elasticity of the solution was related to the height of the gap between the lower plate and the lens, measured by the resulting Newton rings when the lens was illuminated.

weight, of $4 - 7 \times 10^6$ Da. If straightened, the molecule would be several micrometers long, approximately $2-$times longer than disk diameter of typical human erythrocyte. Closer biochemical description can be found for example in Voet and Voet (2004).

In the aqueous solution, the polymer takes up the helical configuration which is stabilized by hydrogen bonds parallel with the chain axis, see Fig.4.1. The anionic carboxyl and carboxamide groups of glucuronic acid residues and hydroxyl group of N–acetyl–D–glucosamine sugar residues are facing outward the chain core. This configuration and the strong anionicity of abundant hydrophilic groups allow the chain to adopt overall expanded coil structure, which can be regarded as a heavily hydrated sphere of radius of about 200 nm, containing up to 1000 times more water than the organic material of the molecule itself, see for example Laurent and Fraser (1992). Domains of hydrated hyaluronate molecules are so vast that they overlap already at very low concentration $\sim 0.1\%$, Sabaratnam et al. (2006). At higher concentrations the chains create uniform three–dimensional network continuously spanned through the whole solution. This network is stiffened by specific transient non–covalent and relatively weak chain–chain interactions, nevertheless it does not require other participant to hold it together, Scott et al. (1991). These crosslinks are of low density and together with highly flexible chains of hyaluronan molecules, the mesh can undergo large deformations, whilst the covalently linked polymers are free of flow properties undergoing only reversible deformations.

4.2. Viscoelastic properties of hyaluronan solution

Physiological hyaluronate solutions at neutral pH, like in synovial fluid, feature an extraordinary viscoelastic characteristic. The existence of an elastic–like property of synovial fluid was early documented by Ogston and Stanier (1950), who noticed the behavior of the synovial fluid in comparison with human blood plasma in a simple experiment of examining the Newton rings, as briefly depicted in Fig. 4.3. Later viscoelastic measurements were done by, for example, Gibbs et al. (1968) and Morris et al. (1980), or by Thurston and Greiling (1978) who investigated the loss of viscoelastic behavior of pathological synovial

fluid, or recently by Kobayashi et al. (1994) investigating the influence of molecular weight of hyaluronan on the viscoelasticity of synovial fluid or Rwei et al. (2008) who measured viscoelastic effect under different physical or chemical conditions. Typical and widely used experimental test measuring viscoelastic responses of synovial fluid is the (small amplitude) oscillatory measurement for wide range of frequencies, as shown in Fig. 4.4. The response is presented in terms of G' and G'', where G' is associated with elastic phenomena and thus called storage modulus, while G'' is associated with viscous dissipation of energy, and it is, therefore, called the loss modulus, for definition see Chapter 3, section 3.3. At low frequencies of oscillation, loss modulus G'' is evidently greater than the store modulus G', in other words viscous responses are dominant to elastic responses, which is the consequence of the fact that at lower frequencies of oscillations the molecular network is transient, or in other words, the period of oscillations is long relative to the lifetime of hyaluronan chain–to–chain interactions and thus the rearrangement of the molecules occurs. Hence the characteristic viscous flow. On the other hand, at higher frequencies elastic responses are predominant which is the consequence of the storing energy in elastic short–time network deformation. The magnitude of the moduli (both G' and G'') is increasing with the concentration which is correlated with the "density" of hyaluronan mesh in the solution. The characteristic crossover of G' and G'' is strongly influenced by the pH, enzymatic activity, protein or cell concentration, and by the concentration and length/molecular weight of hyaluronan molecules as well, see Fig. 4.7, or articles by Gibbs et al. (1968) and Thurston and Greiling (1978).

At first sight, the relation between concentration and the magnitude of response is simple. Nevertheless, one must be careful with the understanding of term of concentration related to hyaluronate solutions. For example for pathological inflammatory synovial fluids, the concentration of hyaluronan can be relatively high but the length of molecules is short due to intensive enzymatic hydrolytic reactions, which causes that the molecules cannot form such quasi–continuous network through the solution, and thus, the elastic–like responses diminish. For this reason, if we talk about concentration of hyaluronan, we always have in mind only that part of concentration which refers to high molecular hyaluronan. Deeper investigation of influence of molecular mass of hyaluronan on the rheological behavior of the solution can be found for example in Bothner and Wik (1987) or Kobayashi et al. (1994).

While elastic part in synovial fluid response is important for joint stabilization during the joint loading and high oscillatory shearing (like during running), the viscous part of the response is crucial for joint lubrication at lower rates of the movement. Even though, it is quite tempting to distinguish the elastic responses from viscous ones, it is not possible to separate them, and thus one has to keep in mind that terms "viscous–like" and "elastic–like" are meant in the sense of predominance.

4.3. Bulk flow properties of hyaluronan solution

During unloaded non–oscillating simple shear flows synovial fluid exhibit characteristic viscous behavior. Typical experimental setting for viscosity measurement is then the flow in the Couette viscosimeter, see example of the experimental result in Fig. 4.5. As one can see, synovial fluid viscosity is not constant as in the case of Newtonian fluid but it exhibits strong shear–thinning, peculiar to polymeric solutions. The difference is, that in the case of hyaluronan solution, this phenomena is observed already at very low concentration due to the extraordinary molecule length. The apparent viscosity of hyaluronan solution is increasing with decreasing rate of shear while at higher rates of movement the viscosity drops. This entails that the joint is "dynamically" stabilized and well lubricated during slower motions but at higher rates of movement the drag of the bones faced against each other in synovial joint is significantly reduced. Here, again, the concentration of hyaluronan in synovial fluid significantly influences the behavior of the mechanical response, as expressed in Fig. 4.5. It is observed that for concentration of hyaluronan close to 1mg/ml, by which the hyaluronan chains are more or less separated (as described above), the apparent viscosity becomes almost Newtonian and the shear–thinning vanishes.

The shear thinning of synovial fluid is the well–known phenomena but also other non–Newtonian effects at transient flow were described in relation to synovial fluid. Davies and Palfrey (1968) and King (1966) reported the normal stress differences, see Fig. 4.6, one of
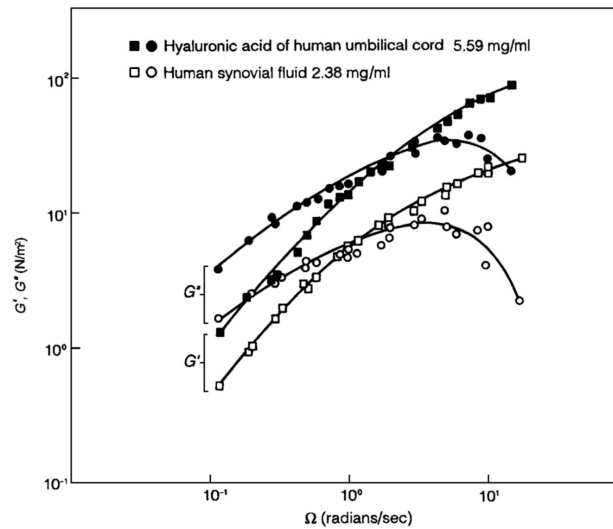
FIGURE 4.4. Small deformation experiment of hyaluronan solution. Dynamic storage moduli G' and dynamic loss moduli G'' plotted against frequency of oscillation in logarithmic scale. Experiment was done in Weissenberg Rheogoniometer. From Balazs and Gibbs (1970).
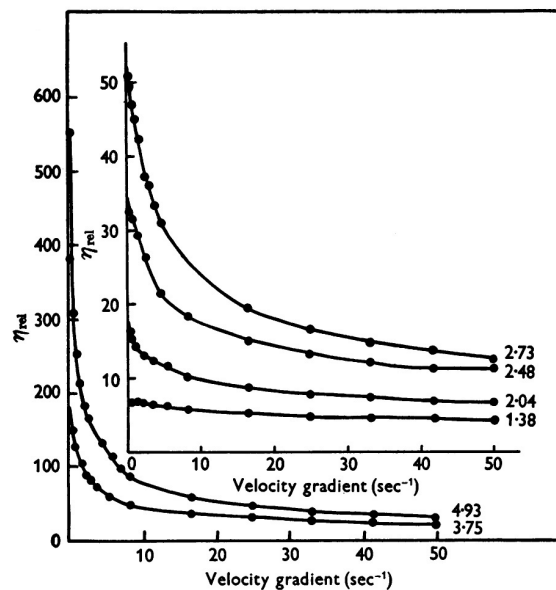
FIGURE 4.5. Shear–thinning experiment on synovial fluid over a wide range of physiological concentration of hyaluronan. Relative viscosity η_{rel} against velocity gradient. Viscosity was measured in the Couette viscosimeter. From Ogston and Stanier (1953).

the physical consequence of non-zero normal stress differences is the effect "die swell", well visible in Fig. 2.8 of Chapter 2. The stress relaxation from modeling point of view was studied for example by Mow and Lai (1979).

4.4. Rheology of pathological synovial fluid

It is well documented that physico–chemical properties of synovial fluid extremely changes with introduced joint disease, as the viscoelastic responses of synovial fluid are strongly
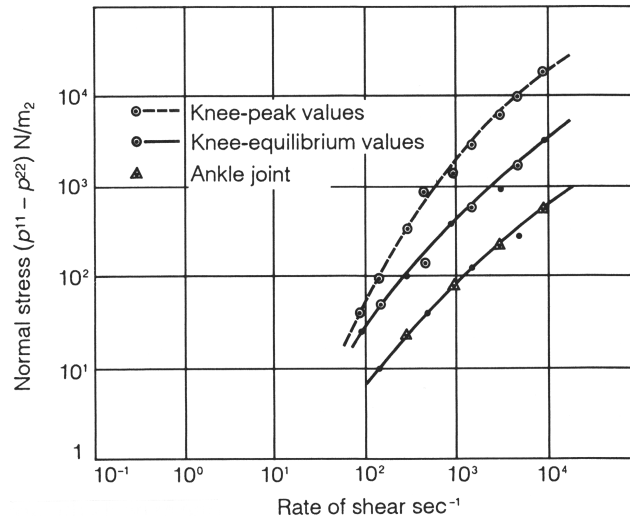
FIGURE 4.6. Normal stress differences as functions of shear rate. Two samples of bullock's synovial fluid (from ankle and knee) were tested in the Weissenberg rheogoniometer. The plot shows the peak values developed within few seconds after beginning of the experiment. Then the normal stress differences fell and reached the equilibrium values (after aprox. 50 seconds). In the case of the ankle joint, the differences between peak and equilibrium values were not significant and thus the peak values are not plotted. From King (1966).

limited, see Balazs (1968), Thurston and Greiling (1978), Gomez and Thurston (1993), or Fig. 4.7. Higher synovial membrane permeability and decreased high–molecular weight hyaluronan concentration in synovial fluid and synovial membrane cause that the protein, cells and inflammation mediators can relatively easily penetrate into the joint cavity and set in the immune enzymatic reactions which hydrolyze hyaluronan chains into small molecular fragments. Low molecular weight hyaluronan then can not form an extended network through the solution, moreover, it can penetrate the synovial membrane and consequently leave the joint cavity. This results in the repression of cartilage nutrition and reduced lubrication. The molecular network in the synovial fluid then clearly reflects its rheological properties and *vice versa*.

In the case of inflammatory diseases, the synovial fluid is characterized as a Newtonian fluid with relatively small viscosity due to lowered polymer size of hyaluronan and very high level of inflammation mediators. On the other hand, synovial fluid affected by noninflammatory degenerative joint disease (like osteoarthritis) has relatively normal composition and still it reflects differences in the elastic stress–strain behavior, see Tab.4.3. This means, most probably, that other factors independent of polymer size can influence the rheology, such as type of protein in the fluid and thus type of protein–hyaluronan interactions, variable ionic strength or presence of abnormal solutes, see Gomez and Thurston (1993).
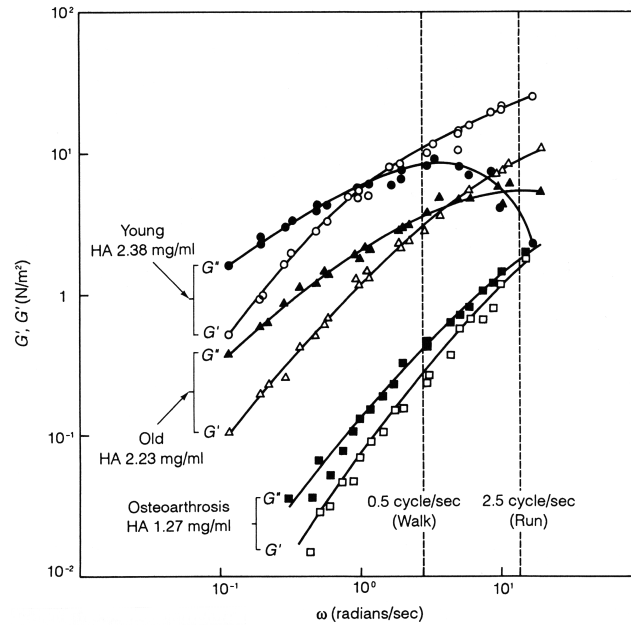
FIGURE 4.7. Dynamic storage and loss moduli of three human synovial fluid samples of different hyaluronan (here marked as HA) concentration plotted against frequency. Dashed vertical lines indicate the frequencies corresponding to the movement of the human knee joint during walking and running regime. Data from Balazs (1968) reproduced by Fung (1993).

Sample	Protein concentration [mg/ml]	Cell count per mm^3	η_v[P]	η_E[P]
noninflammatory cases				
Osteoarthritis	27	20	1.07	1.39
Traumatic arthritis	34	20	0.61	0.50
inflammatory cases				
Rheumatoid arthritis	–	25600	0.07	0.02
Rheumatic fever	48	5400	0.15	0.09

TABLE 4.3. Mean values of selected rheological properties of different pathological synovial fluid samples, obtained from shear rate dependencies of shear stress at frequency of oscillation of 2 Hz. Viscous η_v and elastic η_E parts of complex coefficient of viscosity are related to viscous and elastic part of complex modulus G^* by: $\eta_v = G''/\omega$ and $\eta_E = G'/\omega$. For comparison, experimental dynamic moduli of normal synovial fluid are approx. $\eta_E \doteq \eta_v = 4.5$ (from Balazs (1968)). Data in table from Thurston and Greiling (1978).

Chapter 5

Modeling of viscous responses

In this chapter, we shall create a new phenomenological model for the generalized viscosity of normal[1] synovial fluid which captures the well documented shear–thinning effect. The rheological model of generalized viscosity shall be also, besides the shear rate, dependent of concentration of hyaluronic acid which plays an important role in mechanical responses of synovial fluid.[2] These rheological properties of synovial fluid were closely described in Chapter 4.

5.1. Constitutive equation

Even though synovial fluid is a complex biological material, a mixture of ultrafiltrated blood plasma and hyaluronan molecules, under normal conditions, it can be approximated as an isotropic incompressible homogeneous single constituent fluid. This homogenization can be done since the physiological mass concentration of the hyaluronan is very low (usually less than 1%) and other high–molecular chemicals in normal synovial fluid are not present (like high–molecular proteins or aggressors of inflammation). In general, one would have to use a mixture theory approach and deal with the material properties of both constituents – solute and solvent, we, however, for the reasons mentioned above, assume the effect of hyaluronan molecules on the properties of plasma (solvent) only as the influence of its concentration on the fluid material parameter – the generalized viscosity μ. For simplification, we shall further call the generalized viscosity only as viscosity.

Since the response of the fluid depends on the nature of the flow, the model for synovial fluid must depend on the "dynamics" of the flow. Higher shear rates imply higher alignment of the chains and thus a decrease in the viscosity. On the other hand, the influence of concentration works contrariwise because higher concentration of hyaluronan implies higher enlacement of the chains, which increases the viscosity. In previous studies, the viscous behavior of synovial fluid has been mathematically modeled by a shear–thinning fluid with constant concentration (Rudraiah et al. (1991); Lai et al. (1978)) or the effects of concentration and the shear rate on the viscosity were separated (Morris et al. (1980, 1981)). This is contrary to the results of the experiments (see Fig. 4.5) which show that the concentration influences the shear rate response itself. Briefly speaking, the concentration determines how much the fluid thins the shear. Hence, the restriction of constant concentration is not appropriate for modeling the synovial fluid behavior under physiological conditions since, in real joints, the concentration of hyaluronan varies. For example, it has been shown (see Coleman et al. (1999)) that hyaluronan creates some kind of a boundary layer near the synovium with concentration five times higher than in the central parts of the synovial joint cavity (this is the consequence of the varying hyaluronan production in the synovium combined with the flow conditions). Thus, we assume that the viscosity μ of the synovial

---

[1]By normal synovial fluid we mean the synovial fluid with rheological responses and biochemical composition as that of a healthy young individual.

[2]Partial results of this chapter were already published in Hron et al. (2010)

fluid is a function of concentration and shear rate and propose the constitutive equation for synovial fluid when it flows:

$$(5.1) \qquad \boldsymbol{T} = -p\boldsymbol{I} + 2\mu(c, |\boldsymbol{D}|^2),$$

where $\boldsymbol{T}$ is the stress tensor, $\boldsymbol{D}$ is the symmetric part of velocity gradient, $\boldsymbol{I}$ is the identity tensor, p is the hydrodynamic pressure and c is the concentration.

5.2. Model for viscosity

Due to the shear–thinning effect of synovial fluid, we consider only models for the viscosity μ that belong to the power–law class. We compare the model introduced in the literature (for instance Lai et al. (1978); Laurent et al. (1995)), where the varying concentration plays the role only as a "scaling factor" of the shear rate response

$$(\text{Model 1}) \qquad \mu = \mu_0 e^{\alpha c} \left(1 + \gamma |\boldsymbol{D}|^2\right)^n,$$

with our new model that takes into account the concentration influence on the shear–thinning effect itself, specifically the shear–thinning index of the considered power–law model

$$(\text{Model 2}) \qquad \mu = \mu_0 \left(\beta + \gamma |\boldsymbol{D}|^2\right)^{n(c)}.$$

In both models, the parameters α, β, γ and n are unknown and they have to be determined by comparison with experiment. Since the synovial fluid with zero concentration of hyaluronan is basically blood plasma, the parameter μ_0 should represent the plasma viscosity. Here, as one can see, the Model 1 exhibit wrong characteristic for this limiting case. When the concentration tends to zero, the fluid should stop to feature any non–Newtonian effects any more and the viscosity should become constant with the value of the plasma. In contrast to the Model 2, the Model 1 captures the shear–thinning effects always.

Because the natural values of concentration of hyaluronan in synovial fluid occurs normally between $0 \, \text{mg/ml}$ and $15 \, \text{mg/ml}$ and for concentrations higher than $20 \, \text{mg/ml}$ the solution starts to turn into a gel (for which our approach is inappropriate), we make the parametrization of the concentration in the following fashion: $c = c_{\text{real}}/c_{\text{lim}}$, where $c_{\text{lim}} = 20 \, \text{mg/ml}$ and c is the parametrized concentration of hyaluronan with values between 0 and 1. For now, let us just intuitively accept, that the symmetric part of velocity gradient is free of unit as well. The closer description of non–dimensionalization of the system is introduced in the Chapter 7.

For Model 2 we need to specify also the dependence of the shear–thinning index on the concentration c. To find such a suitable form for function $n(c)$, it has to satisfy the natural conditions for the shear–thinning index, which are:

- the values of $n(c)$ have to remain in the range between $(-0.5, 0)$ to ensure the shear–thinning characteristic,
- the dependence on the concentration has to be monotonic,
- $n(0) = 0$, as the synovial fluid becomes Newtonian for zero concentration.

Moreover, it is desirable to consider the function of shear–thinning index as simple as possible, with a small number of free parameters.

We decided to use the exponential behavior with one free parameter

$$(\text{Model 2a}) \qquad n(c) = \frac{1}{2} \left(e^{-\alpha c} - 1\right),$$

and a simple rational function with two free parameters

$$(\text{Model 2b}) \qquad n(c) = \omega \left(\frac{1}{\alpha c^2 + 1} - 1\right),$$

which both satisfy the mentioned conditions, and, mainly, the fitting procedures, which are the topic of the next section, lead to better results than for any other "simple" function with only one or two free parameters.

5.3. Identification of the model parameters – fitting procedure

Each of the models introduced above contains some unknown parameters. For Model 1 and Model 2a they are three, α, γ, n and α, β, γ, respectively, and in Model 2b we have four unknown parameters α, β, γ, ω. We find the values of these parameters by a fitting technique applied on the experimental data from Ogston and Stanier (1953). Specifically, we use the least square method which can be described as follows.

The viscosity is measured as a function of two variables (concentration and shear rate), thus, the experimental data have to be considered as a set of

$$(5.2) \qquad \{(\boldsymbol{x}_1, \mu_1), ..., (\boldsymbol{x}_i, \mu_i), ..., (\boldsymbol{x}_n, \mu_n)\},$$

where $\boldsymbol{x}_i \in \mathbb{R}^2$ are specific two–dimensional input data representing the given combination of values of concentration and shear rate, for which we have the observed output data $\mu_i \in \mathbb{R}^1$ – the values of viscosity. Coefficient n responses to the number of single measurements. This approach ensures that the output data are fitted together at once for all the concentrations.

Let us denote the unknown model parameters by a vector $\boldsymbol{a} \in \mathbb{R}^m$, where m is the number of the model parameters (in the case of Model 2a, for example, $m = 3$ and $\boldsymbol{a} = (\alpha, \beta, \gamma)$) and the considered model of viscosity by $\tilde{\mu} : \mathbb{R}^m \times \mathbb{R}^2 \to \mathbb{R}^1$, as a function of variables $\boldsymbol{x}$ and parameters $\boldsymbol{a}$. Moreover, we shall call the departure of the mathematical model for viscosity from the measured data as a vector $\boldsymbol{F} : \mathbb{R}^m \to \mathbb{R}^n$, where

$$(5.3) \qquad F_i(\boldsymbol{a}) = \tilde{\mu}(\boldsymbol{a}, \boldsymbol{x}_i) - \mu_i, \qquad i = 1, ..., n.$$

Then, the residual function for the least squares method is defined as

$$(5.4) \qquad r(\boldsymbol{a}) = |\boldsymbol{F}(\boldsymbol{a})|^2 = \sum_{i=1}^{n} \left(\tilde{\mu}(\boldsymbol{a}, \boldsymbol{x}_i) - \mu_i \right)^2,$$

and the least squares method can be formulated as procedure of finding the minimum of residual function over all parameters within suitable range $\mathcal{M}$

$$(5.5) \qquad \min_{\boldsymbol{a} \in \mathcal{M}} r(\boldsymbol{a}).$$

This can be found by solving the system of equations

$$(5.6) \qquad \frac{\partial r(\boldsymbol{a})}{\partial a_j} = 0, \qquad j = 1, ..., m,$$

(the decrease of the residual function is controlled during the algorithm processing which ensures that the sought critical point is minimum) equivalent to

$$(5.7) \qquad \sum_{i=1}^{n} 2 F_i(\boldsymbol{a}) \frac{\partial F_i(\boldsymbol{a})}{\partial a_j} = \sum_{i=1}^{n} 2 \left(\tilde{\mu}(\boldsymbol{a}, \boldsymbol{x}_i) - \mu_i \right) \frac{\partial \tilde{\mu}(\boldsymbol{a}, \boldsymbol{x}_i)}{\partial a_j} = 0, \quad j = 1, ..., m.$$

If we denote the Jacobian matrix of the vector $\boldsymbol{F}(\boldsymbol{a})$ by $\boldsymbol{J} = \frac{\partial \boldsymbol{F}(\boldsymbol{a})}{\partial \boldsymbol{a}}$, the system of equations (5.7) can be schematically rewritten in the form

$$(5.8) \qquad \boldsymbol{J}^{\mathrm{T}}(\boldsymbol{a})\boldsymbol{F}(\boldsymbol{a}) = 0.$$

Whether one substitutes the partial derivatives by the explicit formula or whether one computes it numerically by, for instance, the method of finite differences, the fitting procedure reduces to solving the system of non–linear algebraic equations (5.8) (as the model is non–linear function of its parameters).

In our case, the system of (5.8) can be numerically solved by iterative methods, such as the Newton method, which require an initial guess of the solution. One full Newton iteration consists of finding the solution update $\boldsymbol{\delta_a}$ by solving the linearized system of the form

$$(5.9) \qquad \left(\boldsymbol{J}^{\mathrm{T}}\boldsymbol{J} + \sum_i F_i \boldsymbol{H}_i \right) \boldsymbol{\delta_a} = -\boldsymbol{J}^{\mathrm{T}}\boldsymbol{F},$$

where $\boldsymbol{H}$ is a vector of matrices, with $\boldsymbol{H}_i$ standing for the Hessian matrix of the function F_i, in other words the matrices of second derivatives of $\boldsymbol{F}$. Another possibility to iterate is to use the quasi–Newton method. In that case the Jacobian matrix is only approximated, by neglecting higher order derivatives.

Model 1 $e^{\alpha c}(1 + \gamma |\boldsymbol{D}|^2)^n$		Model 2a $(\beta + \gamma |\boldsymbol{D}|^2)^{\frac{1}{2}(e^{-\alpha c}-1)}$		Model 2b $(\beta + \gamma |\boldsymbol{D}|^2)^{\omega\left(\frac{1}{\alpha c^2 + 1} - 1\right)}$	
α	21.3	α	3.3	α	31.0
γ	13.9	β	7.1×10^{-9}	β	1.1×10^{-8}
n	-0.28	γ	5.8×10^{-8}	γ	1.5×10^{-7}
—		—		ω	0.44

TABLE 5.1. Fitted values of the unknown parameters for all three models; $\mu_0 = 0.01 \, \mathrm{Pa \cdot s}$, other parameters are non–dimensional.

Model 1 $e^{\alpha c}(1 + \gamma |\boldsymbol{D}|^2)^n$	Model 2a $(\beta + \gamma |\boldsymbol{D}|^2)^{\frac{1}{2}(e^{-\alpha c}-1)}$	Model 2b $(\beta + \gamma |\boldsymbol{D}|^2)^{\omega\left(\frac{1}{\alpha c^2 + 1} - 1\right)}$
6922	3370	599

TABLE 5.2. Errors $r(\boldsymbol{a}^*)$.

Since our models are non–linear, multiple local minima can occur, and thus the initial values determine to which local minimum the algorithm converges. How to find suitable initial values is a difficult task and should be guided by the physical insight to the model.

Once the best possible fit is obtained, let us denote the corresponding values of parameters by $\boldsymbol{a}^*$, one is interested in the error of the fit with respect to the data. This quantity is exactly the residual $r(\boldsymbol{a}^*)$ and based on its value we decide which of the considered models fits the data best.

For our problem we used Matlab, particularly the built–in function `lsqcurvefit`. This algorithm is based on minimization procedure as described above with the use of quasi–Newton method combined with trust–region–reflective method to deal with the assumed parameter constrains. For details, see for example Coleman and Li (1996).

5.4. Fitted results and their discussion

We present the final fits in Fig. 5.1 and the values of models' parameters in Tab. 5.1. From the fitting procedure, we also present the total errors $r(\boldsymbol{a}^*)$, see Tab. 5.2, and closer diagnostic of the fit departure $|F_i(\boldsymbol{a}^\star)|$ in each experimental measurement point i, in Fig. 5.3.

Diagnostic of the errors presented in Tab. 5.2 indicates that the best fit of the experimental data is the Model 2b. This is evident even from the comparison of the plots 5.1 (a) – (c) and from Fig. 5.3 where distances between data and fits are plotted (here, the differences are not squared). As we can see, error of Model 2a is accumulated at the very small shear rates while the rest of the fit is comparable with the fit of Model 2b.

For illustration of the models characteristics, we include Fig. 5.2 – 5.5. Fig. 5.2 shows the shear–thinning indexes as functions of the concentration. As we can see, $n(c)$ of Model 2b has smaller derivative at zero than Model 2a and thus it can fit the data for small concentrations more accurately, see Fig. 5.1 for comparison. On the other hand, the characteristic of shear–thinning indexes of the model of class 2 when the concentration tends towards unity, i. e. when the fluid behaves close to gel, the power–law indexes tend to values close to -0.5, which is the parametric value that determines the limit of shear thinning. It is worthy to mention that the shear–thinning indexes of models of class 2 rapidly change their values in the range of concentrations $(0 - 0.75)$, where $c = 0.75$ represents the concentration limit

(a) $\mu_0\, e^{\alpha c}(1+\gamma\,|\boldsymbol{D}|^2)^n$

(b) $\mu_0\,(\beta+\gamma\,|\boldsymbol{D}|^2)^{\frac{1}{2}\left(e^{-\alpha c}-1\right)}$

(c) $\mu_0\,(\beta+\gamma\,|\boldsymbol{D}|^2)^{\left(\omega\,(1/(\alpha c^2+1)-1)\right)}$
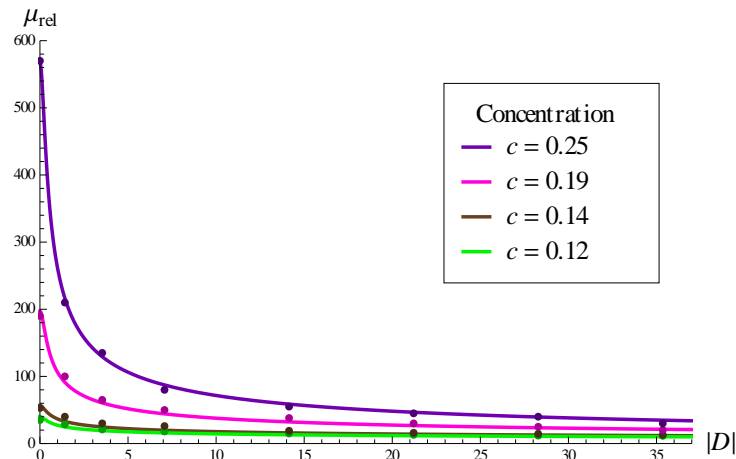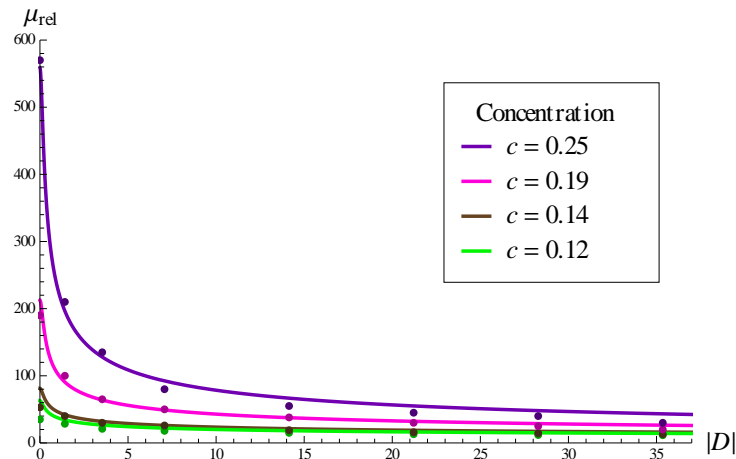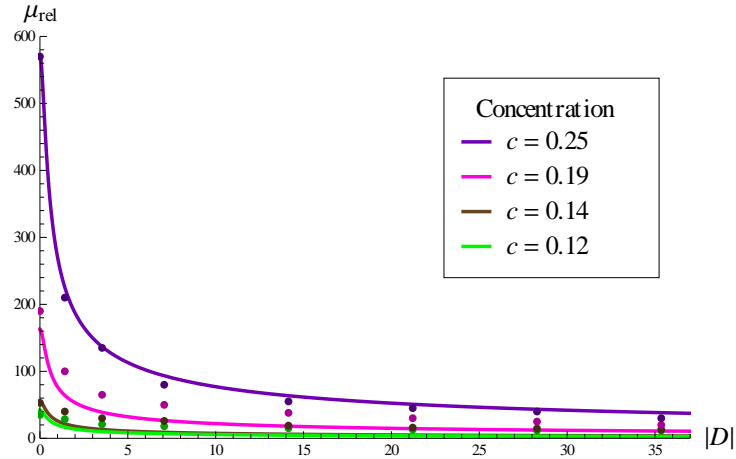
FIGURE 5.1. Relative viscosity against shear rate for different physiological concentrations. Graphs of the relative viscosity of all the models show the fitted curves and the experimental data (points) which were taken for the fitting procedure. Here we use the notation from Ogston and Stanier (1953) for $\mu_{\text{rel}} = \mu/\mu_{\text{ref}}$, where μ_{ref} refers to the viscosity of the glycerol solution.
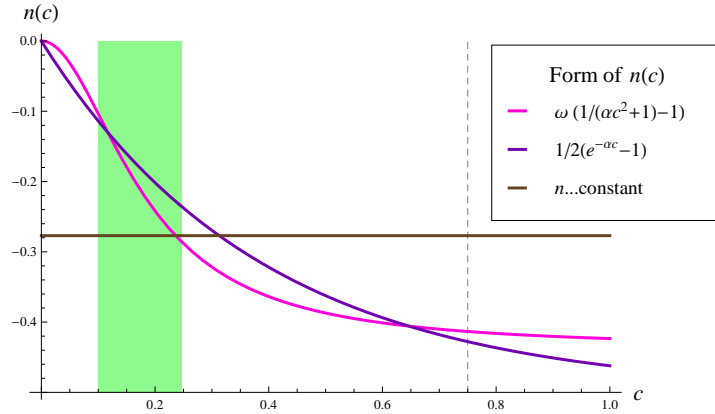
FIGURE 5.2. Shear–thinning index of all models. The green highlighted area represents the concentration range of the experimental data, the mean concentrations in synovial fluid under normal physiological conditions. Dashed line at $c = 0.75$ represents the concentration limit which is observed *in vivo* close to the synovial membrane.

(a) Model 1   (b) Model 2a   (c) Model 2b
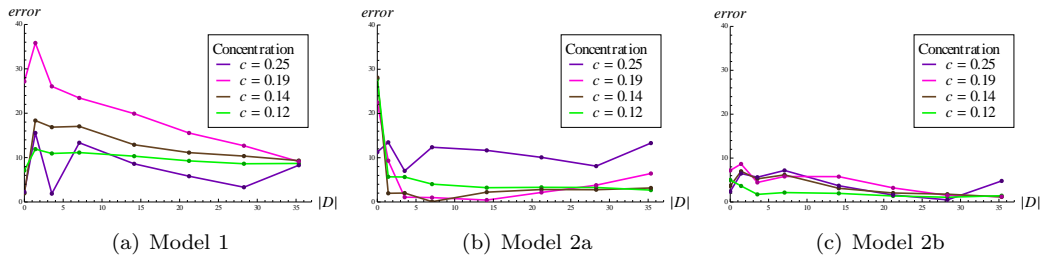
FIGURE 5.3. Departures of considered models from experimental data: $|F_i(\boldsymbol{a}^\star)|$ $(i = 1, .., n)$, displayed as function of shear rate for different concentrations.

which is observed *in vivo* close to the synovial membrane. This, in fact, advocates that the usage of models of class 2 is reasonable.

In Fig. 5.4, there are portrayed series of plots of relative viscosity for higher concentrations than that of the studied experiment, specifically $c \in (0.1 - 0.6)$. From these graphs, it is easy to observe that the models of class 2 predict more realistic values of viscosity even for higher concentrations, while the viscosity prescribed by Model 1 excessively grows with concentration. This behavior of the viscosity as a function of concentration is demonstrated in Fig. 5.5.

Still, from all mentioned above, the Model 1 can fit the data reasonably well for some specific applications in the range of the concentrations in which it was fitted, this means in the range of $0.14 - 0.25$. Moreover, even though the models of class 2 extrapolate the viscosity values for higher concentrations accurately, their reasoning can be validated only by experiments for extended range of concentrations.

Zoom

Logarithmic scale

(a) $\mu_0\, e^{\alpha c}(1+\gamma\,|\boldsymbol{D}|^2)^n$

(b) $\mu_0\, e^{\alpha c}(1+\gamma\,|\boldsymbol{D}|^2)^n$

(c) $\mu_0\,(\beta+\gamma\,|\boldsymbol{D}|^2)^{\frac{1}{2}\left(e^{-\alpha c}-1\right)}$

(d) $\mu_0\,(\beta+\gamma\,|\boldsymbol{D}|^2)^{\frac{1}{2}\left(e^{-\alpha c}-1\right)}$

(e) $\mu_0\,(\beta+\gamma\,|\boldsymbol{D}|^2)^{\left(\omega\,(1/(\alpha c^2+1)-1)\right)}$

(f) $\mu_0\,(\beta+\gamma\,|\boldsymbol{D}|^2)^{\left(\omega\,(1/(\alpha c^2+1)-1)\right)}$
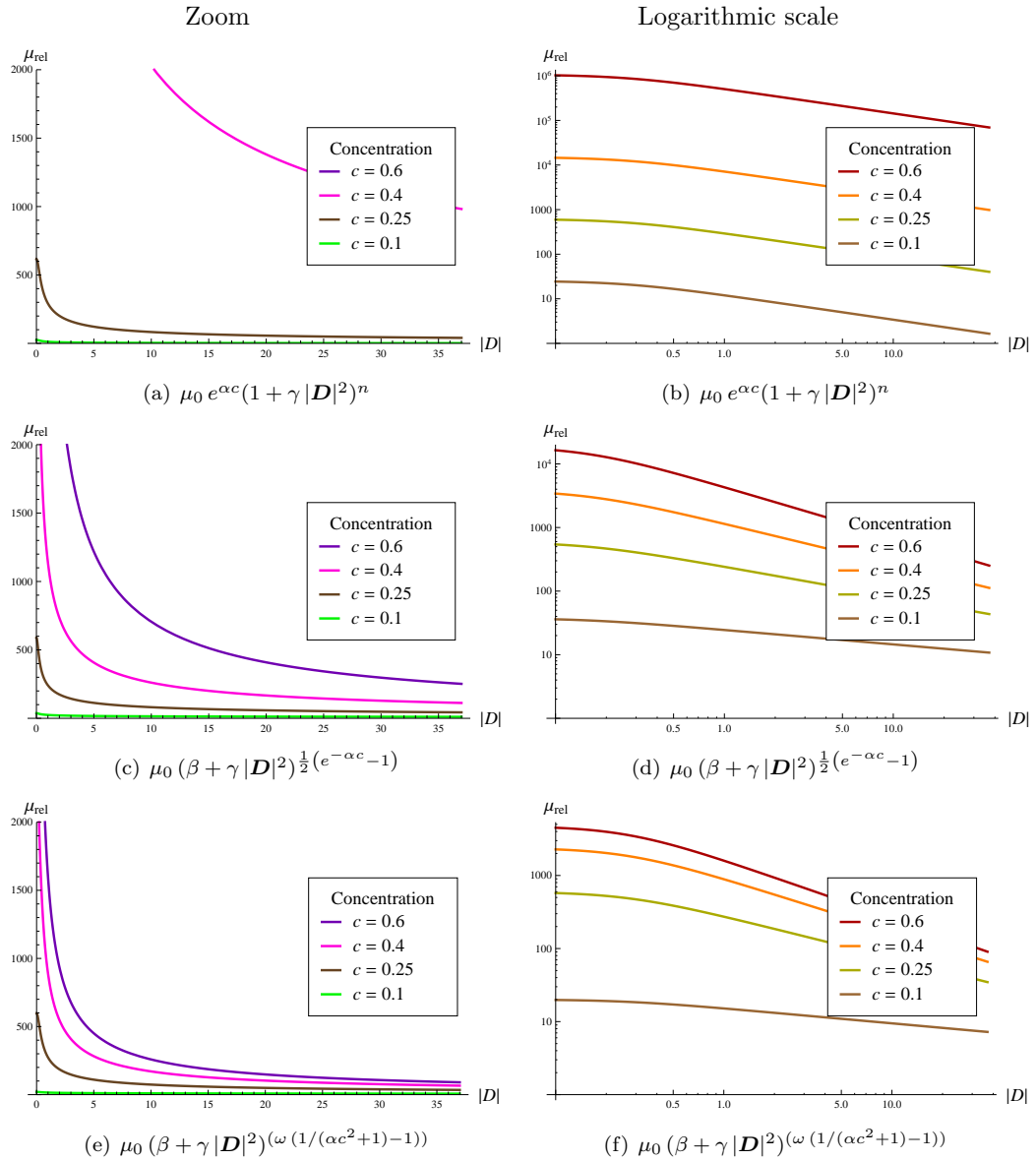
FIGURE 5.4. Relative viscosity against shear rate for higher concentrations, plots (a), (c), (e) in zoom, and the same graphs in the logarithmic scale, plots (b), (d), (f). Here we use notation from Ogston and Stanier (1953) for $\mu_{\mathrm{rel}} = \mu/\mu_{\mathrm{ref}}$.

Zoom   Logarithmic scale

(a) $\mu_0\, e^{\alpha c}(1 + \gamma\, |\boldsymbol{D}|^2)^n$

(b) $\mu_0\, e^{\alpha c}(1 + \gamma\, |\boldsymbol{D}|^2)^n$

(c) $\mu_0\, (\beta + \gamma\, |\boldsymbol{D}|^2)^{\frac{1}{2}\left(e^{-\alpha c} - 1\right)}$

(d) $\mu_0\, (\beta + \gamma\, |\boldsymbol{D}|^2)^{\frac{1}{2}\left(e^{-\alpha c} - 1\right)}$

(e) $\mu_0\, (\beta + \gamma\, |\boldsymbol{D}|^2)^{\left(\omega\, (1/(\alpha c^2 + 1) - 1)\right)}$

(f) $\mu_0\, (\beta + \gamma\, |\boldsymbol{D}|^2)^{\left(\omega\, (1/(\alpha c^2 + 1) - 1)\right)}$

FIGURE 5.5. Relative viscosity as a function of concentration for different shear rates. Graphs (a), (c), (e) are plotted in zoom for concentration up to 0.3 (limit of value of concentration from the experiment), graphs (b), (d), (f) are plotted in logarithmic scale for the whole range of concentration $(0, 1)$. Here we use notation from Ogston and Stanier (1953) for $\mu_{\text{rel}} = \mu/\mu_{\text{ref}}$.

Chapter 6

Modeling of viscoelastic responses

In this chapter, we focus on the mathematical description of viscoelastic responses of the synovial fluid. The first section disserts upon the relevancy of the experimental data in connection with synovial fluid, how they are measured and how little they are saying about the viscoelasticity of the material. Then we introduce the Maxwell and Oldroyd–B models, in both frameworks, as parallels to the mechanical analogues as in the standard forms of characteristic times. Then, we fit the models to the available linear data, trying to find suitable material parameters of the fluid as functions of the concentration.

6.1. Experimental data

The basics of classical theory of linear viscoelasticity were first laid in 1867 by Maxwell (1867), where he discussed one–dimensional mathematical model for gas exhibiting viscous and elastic behavior. Few years later, in 1874, Boltzmann formulated in his famous paper ,Boltzmann (1874), the basic hypothesis of the linear viscoelastic theory (again in one–dimensional case), which, in fact, had not changed till beginning of 50' of the last century, when the seminal work Oldroyd (1950) was published. Oldroyd there developed a fully three–dimensional systematic framework to obtain frame invariant constitutive relations describing rheological behavior of viscoelastic fluids. The use of the objective (frame invariant) convected derivative then led to introduction of more general non–linear three–dimensional models, developed by generalization of one–dimensional models. Nevertheless with non–linearity coming from the geometrical description. The consideration of a material non–linearity in viscoelastic models was elaborated much later, by Rajagopal and Srinivasa (2000). They introduced a new thermodynamically consistent methodology developing new constitutive relations for rate type fluids, by the means of evolution of natural configuration. More recently, another thermodynamically consistent framework based on the Gibbs potential formulation was proposed by the same authors in Rajagopal and Srinivasa (2011).

Regarding the experimental settings, at least concerning the viscoelastic experiments on synovial fluids, the examination of non–linear relationships during viscoelastic behavior is not standard. At the beginning, the experimentalists had no other choice th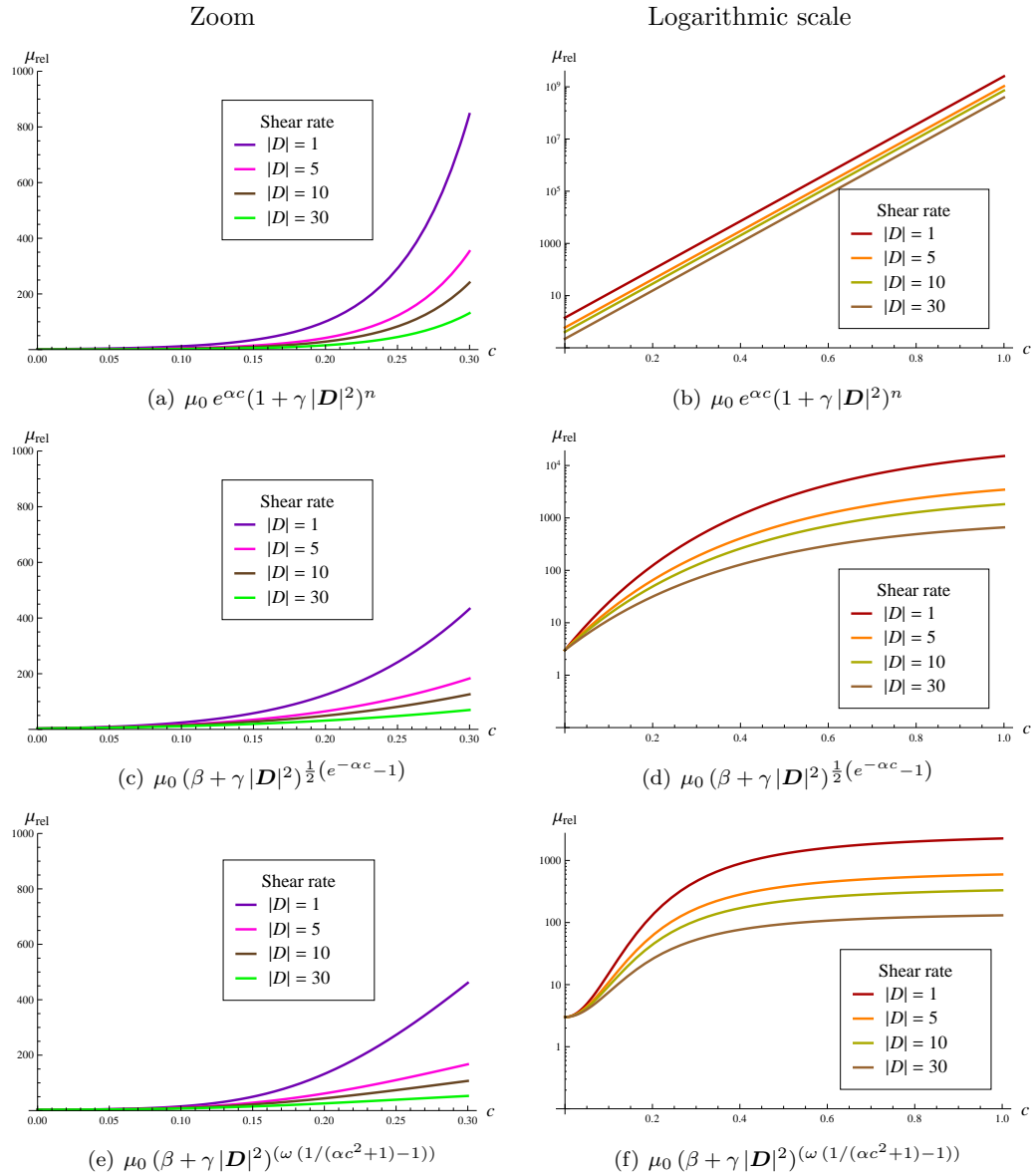an to adapt the experiments to the limited theory of viscoelasticity since other models were not known. The reformulation of the one–dimensional version of linear viscoelasticity in the terms of new material functions, as creep, stress relaxation function or frequency–dependent complex modulus, then became very useful, since these functions are more or less directly measurable. Nevertheless, the experiments were simplistic, since the deformation (strain) had to be small enough, to presume the response of the material in a "linear" regime of responses. On principle, such data reduction is not correct if dealing with non–linear viscoelastic material, as in the case of synovial fluid. Let us be more specific and describe the limitation of standard *small amplitude oscillatory test* which is, to our knowledge, the most popular way of studying the viscoelasticity of synovial fluid.

6.1.1. Experiment of oscillatory flow. In what follows, we use the notation introduced in Chapter 3, which is consistent with notation used by Balazs (1968), from where

(a) Physiological range of concentration   (b) Physiological limits of concentration
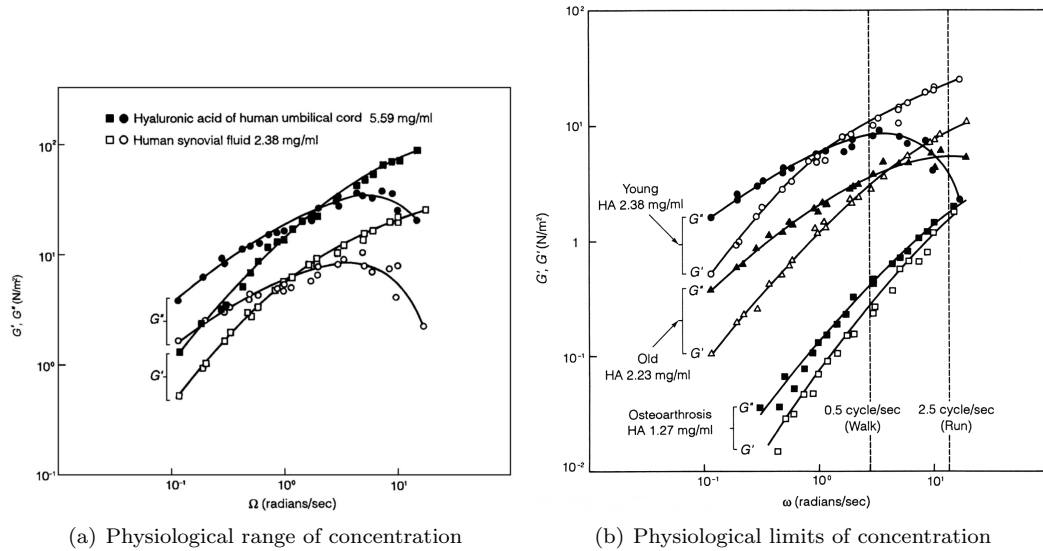
FIGURE 6.1. Small deformation experiment of hyaluronan solution. Dynamic storage modulus G' and dynamic loss modulus G'' plotted against frequency of oscillation in logarithmic scale. Experiment was performed in the Weissenberg rheogoniometer. Data from Balazs (1968), reproduced by Fung (1993).
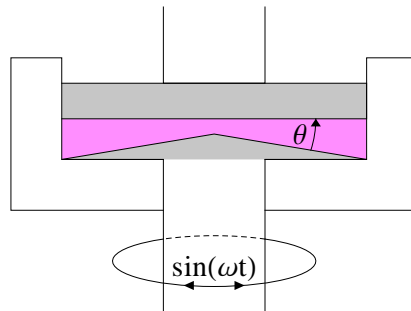
FIGURE 6.2. Simplified visualization of rheogoniometer. The main parts of rheogoniometer are the (upper) plate and shallow cone, in the picture represented by gray color. The sample of fluid (represented by pink color) is placed in the space between these two parts. In this case, the cone is mechanically driven with a given oscillatory rotation and on the plate the torque is measured with a sensing device (not pictured).

the experimental data are obtained, see Fig. 6.1. The experiment itself was performed in Weissenberg rheogoniometer. Sketch of such apparatus is depicted in Fig. 6.2.

The experimental determination of small amplitude oscillatory test is a complex ratio of force to displacement $(\tau^\star/\gamma^\star)$, strictly speaking, complex ratio of torque to angular displacement. In the framework of real–valued periodic variables, the complex ratio is equivalent to information of ratio of maximal magnitudes of force to displacement and their mutual phase shift. The assumption, that the stress/strain can be related to force/displacement ratios and that they are periodic of the same frequency is presupposed by assumption that the fluid is a linear viscoelastic fluid, or at least, it behaves as linear viscoelastic fluid in the regime of "infinitesimal" deformations, thus when the amplitude and frequency of oscillations are very small. Second presumption made here is, that the gap of the rheogoniometer is small, which is equivalent to the saying that the the sample thickness is sufficiently small compared

with the wavelength of the shear variation propagated through the fluid. In other words, the shear rate on the upper plate is approximated by a constant mean value which can be questionable in the experiment on a non–linear viscoelastic fluid.

Considering all the assumptions laid above as good approximations, the shear stress/ strain (τ/γ) relation is proportional to torque/angular displacement (T/α) relation

$$(6.1) \qquad \frac{\tau}{\gamma} = b\frac{T}{\alpha}, \qquad b = \frac{1}{2\pi}\frac{3\theta}{R^3},$$

where θ is the angle of rheogoniometer cone to the plate, see Fig. 6.2, and R is the radius of the cone. Then, one can describe the response of the material by two frequency–dependent functions, $G'(\omega)$ and $G''(\omega)$, the dynamic storage modulus and dynamic loss modulus, respectively, see Fig. 6.1. Both functions are in fact the decomposition of the complex dynamic modulus $G^\star = \tau^\star/\gamma^\star$, and thus, see equation (3.15), they can be related to the measured torque and angular displacement through

$$(6.2) \qquad G' = b\frac{T_0}{\alpha_0}\cos(\delta), \qquad G'' = b\frac{T_0}{\alpha_0}\sin(\delta),$$

where T_0 and α_0 are the amplitudes (peaks) of oscillatory torque and angular displacement, respectively, and δ is the phase shift between them.

6.2. Linear viscoelastic model for synovial fluid

Fitting fully[1] non–linear viscoelastic model to the experimental data we have at hand would be at this point useless with respect to their linear character. Thus, in this section we lay stress on the famous Oldroyd–B model in comparison to the model of Maxwell[2].

Let us recall the basic formulas we shall need and derive the explicit functions for dynamic moduli G' and G''. The (one–dimensional) deformation during oscillatory test is given by sinusoidal shear strain γ with frequency of oscillations ω

$$(6.3) \qquad \gamma = \gamma_0\sin(\omega t) \quad \longrightarrow \quad \dot\gamma = \gamma_0\omega\cos(\omega t),$$

where $\dot\gamma$ is the shear rate, and thus, in matrix notation, the symmetric part of velocity gradient is

$$(6.4) \qquad \boldsymbol{D} = \frac{1}{2}\begin{pmatrix} 0 & \gamma_0\omega\cos(\omega t) & 0 \\ \gamma_0\omega\cos(\omega t) & 0 & 0 \\ 0 & 0 & 0 \end{pmatrix}.$$

The Cauchy stress tensor, having the form of

$$(6.5) \qquad \boldsymbol{T} = -p\boldsymbol{I} + \boldsymbol{S}, \qquad \boldsymbol{S} = \begin{pmatrix} S_{11} & \tau & S_{13} \\ \tau & S_{22} & S_{23} \\ S_{13} & S_{23} & S_{33} \end{pmatrix},$$

where τ is the shear stress, is then given by the constitutive relation of particular viscoelastic model. Since the shear stress τ is decomposable into the sines and cosines, see derivation of equation (3.8),

$$(6.6) \qquad \tau = \gamma_0\{G'(\omega)\cos(\omega t) + G''(\omega)\sin(\omega t)\},$$

we can identify the functions $G'(\omega)$ and $G''(\omega)$ in the constitutive relation.

Algorithm of obtaining the explicit formula for $G'(\omega)$ and $G''(\omega)$ can be summarized:

1. take the rate type constitutive relation $\boldsymbol{S} \leftrightarrow \boldsymbol{D}$,
2. solve the system of differential equations[3] for S_{11}, τ, S_{22}, S_{23}, S_{31}, S_{33} with respect to time, for boundary value problem (we deal with periodic functions),

---

[1]Even though the three–dimensional Maxwell or Oldroyd–B models are non–linear, they are generalizations of linear one–dimensional models (one–dimensional Maxwell and Jeffrey model), and thus, their non–linearity comes only from the geometrical description. For simplicity, we shall call these models linear (for completeness, some authors use the term "quasilinear"). By fully non–linear viscoelastic models we mean such, that involve a material non–linearity.

[2]From now on, if not explicitly specified, we assume the three–dimensional generalizations of the models.

[3]In the case of Maxwell and Oldroyd–B models, the system is not fully coupled.

3. assume steady state oscillations (in the solution, the exponential $e^{-\text{const.}t}$ vanishes for $t \to \infty$),

4. decompose the solution of τ into sine and cosine and their coefficients identify with $G'(\omega)$ and $G''(\omega)$.

Before we introduce the viscoelastic Maxwell and Oldroyd–B models, let us recall the Oldroyd upper convected derivative, denoted by symbol $\triangledown$, and having the definition of

$$(6.7) \qquad \overset{\triangledown}{\boldsymbol{A}} = \frac{\partial \boldsymbol{A}}{\partial t} + (\text{grad } \boldsymbol{A})\, \boldsymbol{v} - \boldsymbol{L}\boldsymbol{A} - \boldsymbol{A}\boldsymbol{L}^{\mathrm{T}},$$

or

$$(6.8) \qquad \overset{\triangledown}{\boldsymbol{A}} = \frac{\partial \boldsymbol{A}}{\partial t} + (\text{grad } \boldsymbol{A})\, \boldsymbol{v} - \boldsymbol{W}\boldsymbol{A} + \boldsymbol{A}\boldsymbol{W} + a\,(\boldsymbol{D}\boldsymbol{A} + \boldsymbol{A}\boldsymbol{D}), \quad a = -1.$$

Once again, $\boldsymbol{L}$ is gradient of velocity $\boldsymbol{v}$, while $\boldsymbol{D}$ and $\boldsymbol{W}$ are its symmetric and antisymmetric parts, respectively.

6.2.1. Maxwell model.
The constitutive equations for Maxwell fluid is given by

$$(6.9) \qquad \boldsymbol{S} + \lambda_1 \overset{\triangledown}{\boldsymbol{S}} = 2\eta_0 \boldsymbol{D},$$

involving two material constants, λ_1 and η_0. In the simple shearing flow, with the velocity components $v_1 = \dot{\gamma}y$ ($\dot{\gamma}$ being a constant), $v_2 = v_3 = 0$, one has

$$(6.10) \qquad S_{11} = 2\lambda_1\eta_0\dot{\gamma}^2, \quad \tau = S_{12} = \eta_0\dot{\gamma},$$

$$(6.11) \qquad S_{22} = S_{23} = S_{13} = S_{33} = 0,$$

so that parameter η_0 is called the steady shear viscosity, or sometimes zero–strain rate viscosity. Clearly, η_0 corresponds to apparent viscosity of the fluid. On the other hand, in a relaxation test, the relaxation function decays with e^{t/λ_1}, and thus, the parameter λ_1 is called the relaxation time.

For simple oscillatory flow (γ and $\dot{\gamma}$ are harmonic functions of time), the constitutive equation (6.9) can be expressed as

$$(6.12) \qquad \frac{\partial S_{11}}{\partial t} = \frac{-S_{11}}{\lambda_1} + 2S_{12}\dot{\gamma},$$

$$(6.13) \qquad \frac{\partial S_{12}}{\partial t} = \frac{-S_{12}}{\lambda_1} + S_{22}\dot{\gamma} + \frac{\eta_0\dot{\gamma}}{\lambda_1},$$

$$(6.14) \qquad \frac{\partial S_{13}}{\partial t} = \frac{-S_{13}}{\lambda_1} + S_{23}\dot{\gamma},$$

$$(6.15) \qquad \frac{\partial S_{22}}{\partial t} = \frac{-S_{22}}{\lambda_1}, \quad \frac{\partial S_{23}}{\partial t} = \frac{-S_{23}}{\lambda_1}, \quad \frac{\partial S_{33}}{\partial t} = \frac{-S_{33}}{\lambda_1}.$$

One can solve this system of differential equations (with periodic boundary conditions), and obtain explicit formulas for storage and loss moduli

$$(6.16) \qquad G' = \frac{\lambda_1\eta_0\omega^2}{1 + \lambda_1^2\omega^2}, \qquad G'' = \frac{\eta_0\omega}{1 + \lambda_1^2\omega^2}.$$

We recall, that relations (6.16) are expected to be valid for small amplitudes and frequencies of oscillations.

6.2.2. Oldroyd–B model.
In comparison to the Maxwell model, the Oldroyd–B model is three–parametric,

$$(6.17) \qquad \boldsymbol{S} + \lambda_1 \overset{\triangledown}{\boldsymbol{S}} = 2\eta_0 \left(\boldsymbol{D} + \lambda_2 \overset{\triangledown}{\boldsymbol{D}} \right).$$

In addition to λ_1 and η_0, having the same meaning as in the Maxwell model, the Oldroyd–B involves the material constant λ_2. It is known as the retardation time, since in a single step shear creep test, the creep function reaches the asymptotic value according to the creep factor $(1 - e^{-t/\lambda_2})$.

We can, analogously to Maxwell, express the constitutive relation (6.17) for the oscillatory flow, solve the system of differential equations and obtain explicit formulas for the dynamic moduli. Specifically, the equations take form of

$$(6.18) \qquad \frac{\partial S_{11}}{\partial t} = \frac{-S_{11}}{\lambda_1} + 2S_{12}\dot{\gamma} - \frac{2\lambda_2\eta_0\dot{\gamma}^2}{\lambda_1},$$

$$(6.19) \qquad \frac{\partial S_{12}}{\partial t} = \frac{-S_{12}}{\lambda_1} + S_{22}\dot{\gamma} + \frac{\eta_0}{\lambda_1}\left(\dot{\gamma} + \lambda_2\frac{\partial\dot{\gamma}}{\partial t}\right),$$

$$(6.20) \qquad \frac{\partial S_{13}}{\partial t} = \frac{-S_{13}}{\lambda_1} + S_{23}\dot{\gamma},$$

$$(6.21) \qquad \frac{\partial S_{22}}{\partial t} = \frac{-S_{22}}{\lambda_1}, \quad \frac{\partial S_{23}}{\partial t} = \frac{-S_{23}}{\lambda_1}, \quad \frac{\partial S_{33}}{\partial t} = \frac{-S_{33}}{\lambda_1},$$

and the dynamic moduli are

$$(6.22) \qquad G' = \frac{(\lambda_1 - \lambda_2)\eta_0\omega^2}{1 + \lambda_1^2\omega^2}, \qquad G'' = \frac{(1 + \lambda_1\lambda_2\omega^2)\eta_0\omega}{1 + \lambda_1^2\omega^2}.$$

Here again, the apparent viscosity can be identified with η_0 since the constitutive equation for simple shear (of constant shear rate) reduces to

$$(6.23) \qquad S_{11} = 2\eta_0(\lambda_1 - \lambda_2)\dot{\gamma}^2, \quad \tau = S_{12} = \eta_0\dot{\gamma},$$

$$(6.24) \qquad S_{22} = S_{23} = S_{13} = S_{33} = 0.$$

Moreover, the ratio of λ_1/λ_2 suggest the "measure" of non–Newtonian character of the fluid, as it becomes Newtonian for $\lambda_1/\lambda_2 \to 1$.

6.2.3. Mechanical analogues. As it has been mentioned before, Maxwell and Oldroyd–B models are generalizations of linear one–dimensional models to the three dimensions. For better understanding of the character of 3D models, let us briefly discuss the 1D models, which in fact, will be very useful in the next section of finding fits to the experimental data.

One possibility of deriving the 1D viscoelastic models is to use the spring–dashpot formalism. It is claimed that the theory of linear viscoelasticity can be derived from assumption that the matter, on some microscopic level, can be regarded as intricate network of linear viscous elements – linear dashpots and linear elastic elements – linear springs (from Coleman and Noll (1961)). Shortly, the one–dimensional stress/strain relation of linear viscoelastic material can be correlated with force/displacement of mechanical network of springs and dashpots.

Let us discuss the representation of 1–dimensional Maxwell and Oldroyd models by mechanical analogues.
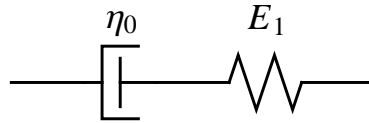
FIGURE 6.3. Spring–dashpot analogue for the Maxwell fluid. Parameters η_0 and E_1 are the dashpot and spring constants, respectively.

Maxwell. Even though Maxwell himself did not mention dashpot/spring in his famous work (Maxwell (1867)), his model is based on superposition of viscous and elastic forces, which refers to connection of one spring and one dashpot in series, see Fig. 6.3. If we balance the total force with the total displacement of such assemblage, we obtain the (one–dimensional) formula of the Maxwell fluid

$$(6.25) \qquad F + \frac{\eta_0}{E_1}\frac{\partial F}{\partial t} = \eta_0\frac{\partial e}{\partial t},$$

where F is the total force and e the total elongation. The way of generalization of the model to three dimensions is then obvious. The force/displacement functions are replaced by the tensors of the stress and the symmetric part of the velocity gradient, and partial derivative

by objective upper convected derivative. While the viscosity η_0 keeps its physical meaning, the relaxation time is

$$(6.26) \qquad\qquad \lambda_1 = \frac{\eta_0}{E_1}.$$

The calculation of dynamic moduli in terms of "viscosity" η_0 and "elasticity" E_1 is straightforward, nevertheless lengthy, so let us introduce here just the result

$$(6.27) \qquad\qquad G' = \frac{E_1 \eta_0^2 \omega^2}{E_1^2 + \eta_0^2 \omega^2}, \quad G'' = \frac{E_1^2 \eta_0 \omega}{E_1^2 + \eta_0^2 \omega^2}.$$
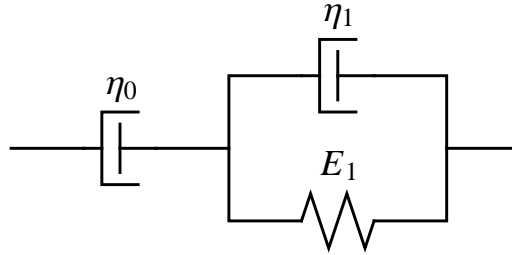
FIGURE 6.4. Spring–dashpot analogue for the Oldroyd fluid model. Parameters η_0, η_1 and E_1 are the dashpots and spring constants, respectively.

Oldroyd. Similar analogue can be constructed for the Oldroyd fluid. Since the model has to have three parameters and it should describe the fluid–like material, the composition of dashpots/spring is unique, as depicted in Fig. 6.4. Another combination of elements would lead either to a description of solid–like material or to a two–parametric model. The total force/displacement balance of such assemblage gives the relation

$$(6.28) \qquad\qquad F + \frac{\eta_0 + \eta_1}{E_1} \frac{\partial F}{\partial t} = \eta_0 \left(\frac{\partial e}{\partial t} + \frac{\eta_1}{E_1} \frac{\partial^2 e}{\partial t^2} \right),$$

which can be generalized to the three dimensions in the same way as in the Maxwell case. The parameters of analogue model and (3D) Oldroyd–B model are following

$$(6.29) \qquad\qquad \lambda_1 = \frac{\eta_0 + \eta_1}{E_1}, \quad \lambda_2 = \frac{\eta_1}{E_1}.$$

Again, η_0 is in both models identical, and represents the apparent viscosity in the simple shear. At last, let us express the G' and G'' in terms of η_0, η_1 and E_1

$$(6.30) \qquad G' = \frac{E_1 \eta_0^2 \omega^2}{E_1^2 + (\eta_0 + \eta_1)^2 \omega^2}, \quad G'' = \frac{\eta_0 \omega \left(E_1^2 + \eta_1 (\eta_0 + \eta_1) \omega^2 \right)}{E_1^2 + (\eta_0 + \eta_1)^2 \omega^2}.$$

6.3. Concentration dependence – finding fits to data

In this section, our goal is to find the best possible fit to available experimental data. We are considering only linear viscoelastic models due to the reasons mentioned before. Algorithm of the procedure ,the least squares method, is the same as in the Chapter 5, and thus, it shall not be described again.

The experimental data are expressed in terms of dynamic moduli as functions of frequencies of oscillations and concentrations. While the dependence on frequency is well studied, the concentration dependence has been, to our knowledge, avoided. Our approach of the inclusion of the concentration in the standard formulas of dynamic moduli is through the material parameters of the particular model.

Even though the measurements were done for four different concentrations, $c = 5.59$mg/ml, 2.38 mg/ml, 2.23 mg/ml and 1.28 mg/ml, the most relevant set of data are those for high concentrations, namely $c = 5.59$ mg/ml and 2.38 mg/ml. The other two sets of data can be influenced by other pathological factors which can change the viscoelasticity of synovial fluid in a different, for this data unknown, way, see Chapter 4. Nevertheless, the concentration

conc. [mg/ml]	$c[-]$
5.59 mg/ml	0.28
2.38 mg/ml	0.12
1.27 mg/ml	0.06

TABLE 6.1. Parametrization of concentration data. Exact scaling formula was introduced in section 5.2 of Chapter 5.

	c	E_1	η_0	η_1
Maxwell	0.06	3.76	0.21	0
	0.12	19.52	8.30	0
	0.28	67.46	17.78	0
Oldroyd–B	0.06	3.90	0.21	num0
	0.12	19.41	8.78	0.10
	0.28	67.54	17.38	num0

TABLE 6.2. Calculated values of particular model parameters.

dependence is obvious even in pathological cases, and as expected, the data for limit concentration ≈ 1 mg/ml correctly suggest rapid loss in both types of responses, viscous–like and elastic–like. The set of data for concentration 1.28 mg/ml shall be then considered as well but one should keep in mind its limitations.

Before the fits, let us recall the parametrization for particular concentrations, see Tab. 6.1, as was introduced in the previous chapter.

6.3.1. Separate fits for different concentrations. Unfortunately, we have almost no information about the characteristic dependence of material parameters of the Maxwell/Old–royd–B models on concentration. In the past, some authors performed mathematical fits of linear viscoelastic models to experimental data (see Mow and Lai (1979), for example), but the concentration influence was never considered. Hence, let us to fit the formulas of G' and G'' of both models, (6.30) and (6.27), to the data for separate concentrations but simultaneously for both moduli. Then, based on the results, we shall try to suggest a possible phenomenological dependence of the material parameters on the concentration.

There are three parameters in the Oldroyd–B model, which need to be specified. Namely, they are E_1, η_0 and η_1. In the case of the Maxwell fluid, we have two parameters, E_1 and η_0. Their values can be obtained by the method of least squares method in the same manner as described in Chapter 5. The resultant separate fits are shown in Fig. 6.5 and the values of calculated parameters in Tab. 6.2, for comparison, the results of both models are presented together.

As we can see, the fits for Maxwell and Oldroyd–B do not differ almost at all. This is caused by the smallness of the third parameter η_1 in Oldroyd–B model, fitted as numerical zero for two cases from three, which represent with respect to the Maxwell fluid the additional dashpot, see Tab. 6.2. This suggests, that in the range of linear viscoelasticity of synovial fluid the Maxwell model could be sufficient. Thus, in what follows, we shall assume the Maxwell model, only.

We demonstrate the change of particular parameters E_1 and η_0, in fact particular elements of the mechanical analogues, with concentration in Fig. 6.6. Since we have only

(a) Maxwell – linear scale   (b) Oldroyd–B – linear scale

0.28	0.12	0.06

(c) Maxwell – logarithmic scale   (d) Oldroyd–B – logarithmic scale

0.28	0.12	0.06
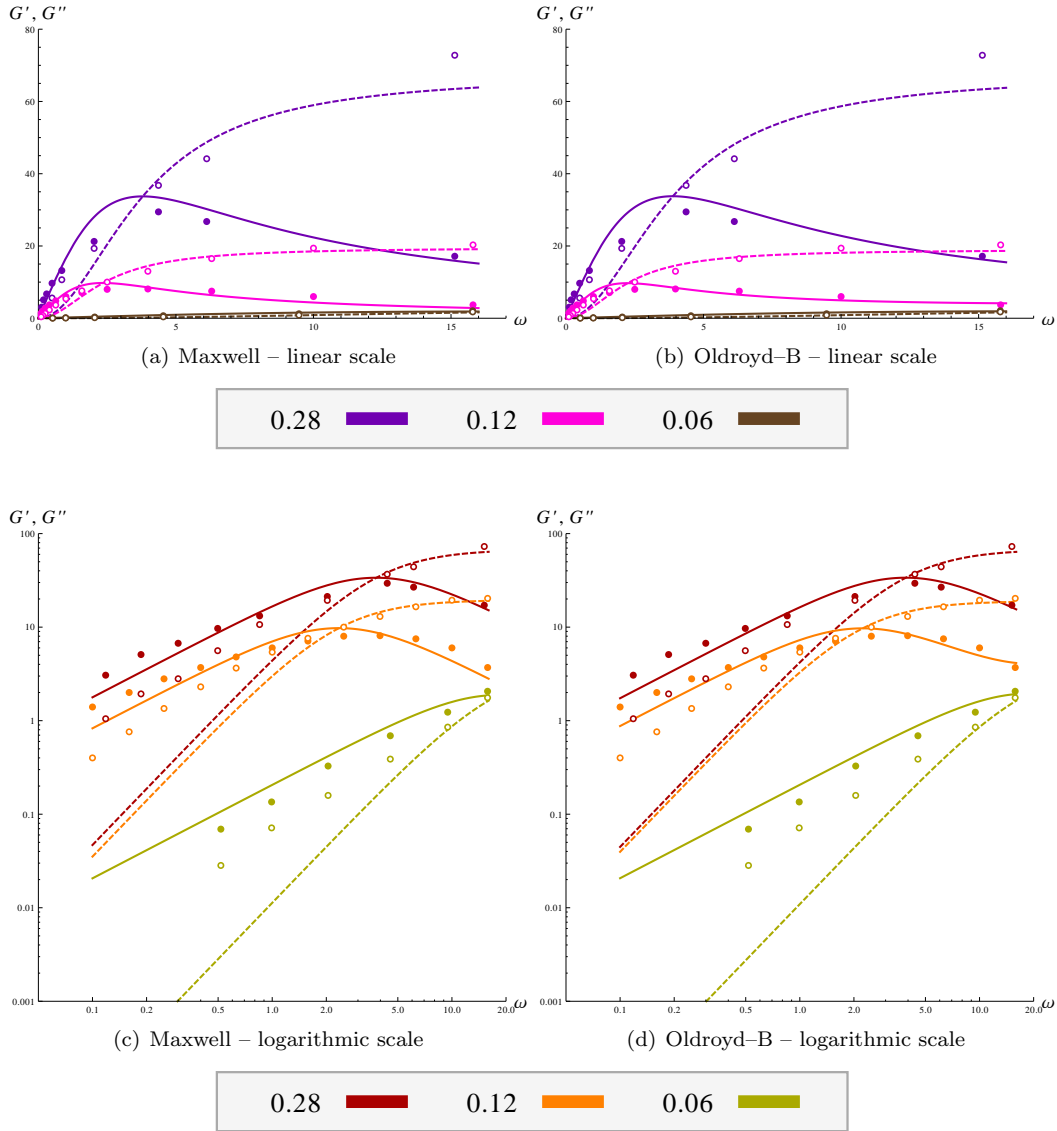
FIGURE 6.5. Fitted curves of dynamic moduli for three different concentrations. The fits are performed separately. Experimental data are represented by points, solid points are data of dynamic loss modulus G'', circles represent dynamic storage modulus G'. Solid lines are calculated curves of dynamic loss modulus and dashed lines are calculated curves of dynamic modulus.

data for three different concentrations, the comparison of the full three–dimensional models with their one–dimensional simplifications shall help us to choose suitable form of parameter–concentration relations. The linear growth of E_1 (as the only elastic element of the models) with c is obvious, and it basically reflects that the storage modulus G' is "only" scaled with the concentration, that it does not change the behavior of the function itself. Summarizing, we assume the following relations between model parameters and concentration

$$(6.31) \qquad\qquad E_1 = a_1 c + b_1,$$

$$(6.32) \qquad\qquad \eta_0 = b_2 e^{a_2 c}.$$

6.3.2. Simultaneous fits. Having the relations (6.31)–(6.32), we can fit the experimental data simultaneously for all concentrations. Instead of two material parameters, we have to find values of four constants a_1, b_1, a_2 and b_2. Perceive, the fits we have obtained before are the best possible fits.

(a) parameter E_1 (b) parameter η_0
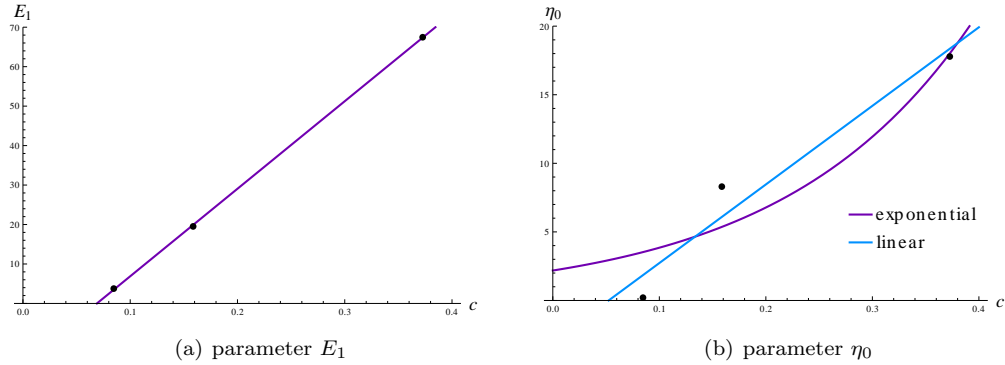
FIGURE 6.6. Model parameters growth tendencies with concentration for the Maxwell model. Points represent the computed values of particular parameters, violet curves are the functions we take as the approximative relationships, and for comparison, we include linear regressions – blue line.

Model/data	Error
2 sets of data	
Maxwell	335.794
3 sets of data	
Maxwell	351.324

TABLE 6.3. Errors $r(\boldsymbol{a}^*)$ of the best fits computed for the Maxwell model for two and three sets of experimental data corresponding to the concentrations of $\{0.12, 0.28\}$ and $\{0.06, 0.12, 0.28\}$, respectively.

During the computation we have challenged few difficulties. First of all, the models are quite sensitive to even slight change of the parameters. Second, the values of dynamic moduli for the small concentrations are in a different range than that of the high concentrations. This results in obviously wrong fits of dynamic moduli to the set of data for the smallest (and in fact very limiting) concentration. That was the reason, we run the computations twice, once for all data of all concentrations $\{0.06, 0.12, 0.28\}$ and once only for data of two highest concentrations $\{0.12, 0.28\}$, which represent concentration of hyaluronan in normal synovial fluid.

The resulting fitted curves are shown in Fig. 6.7, the errors of the fits are summarized in Tab. 6.3 and the explicit values of computed parameters are presented in Tab. 6.4.
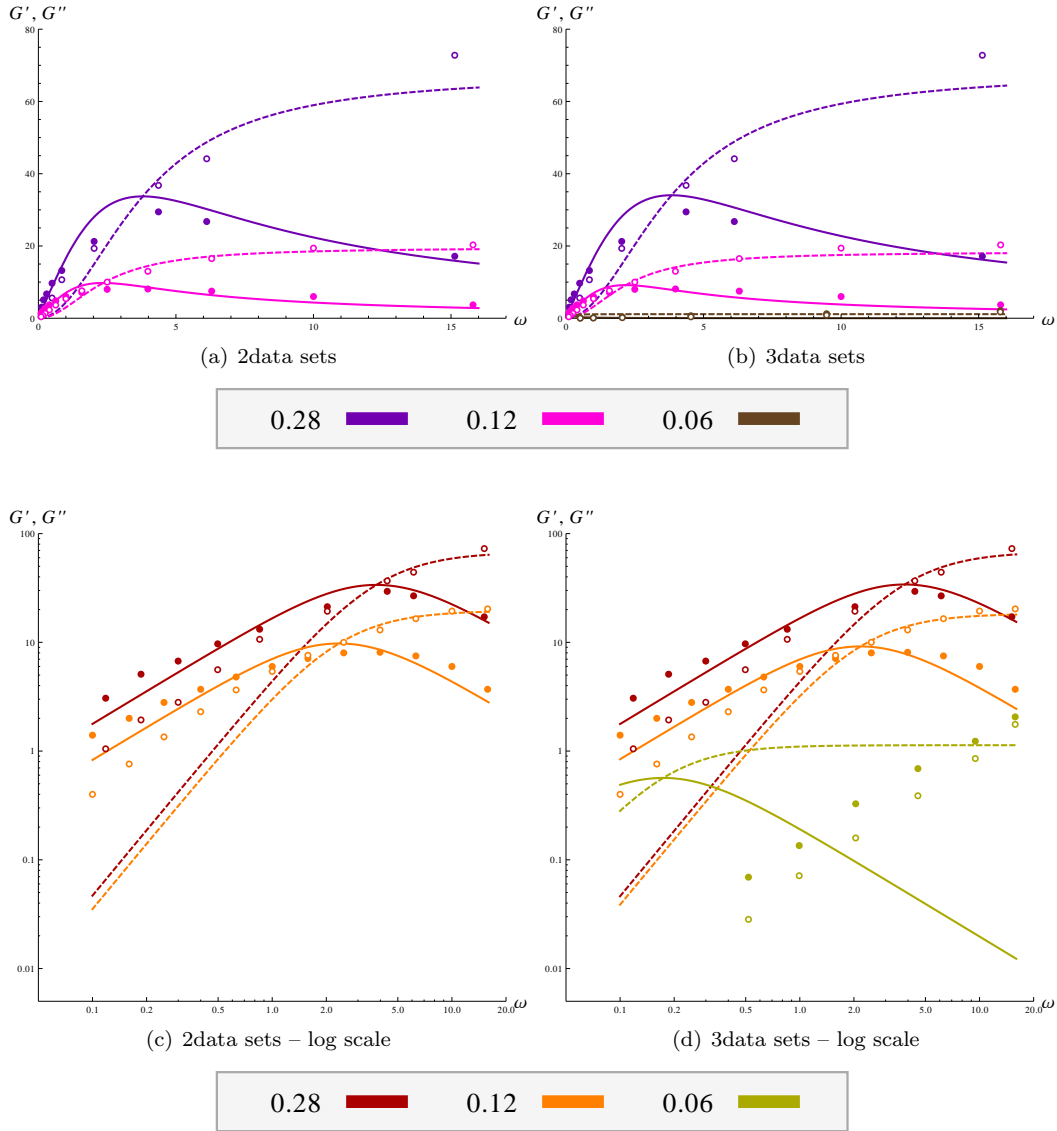
FIGURE 6.7. Resulting curves of fitted dynamic moduli to two (left) and three (right) sets of experimental data corresponding to the concentrations of $\{0.12, 0.28\}$ and $\{0.06, 0.12, 0.23\}$, respectively. Dynamic loss modulus – solid lines, dynamic storage modulus – dashed lines; solid points – dynamic loss modulus experimental data, circles – dynamic storage modulus experimental data.

Model/data	Parameters			
	a_1	b_1	a_2	b_2
2 sets of data				
Maxwell	14.93	-16.02	0.237	4.72
3 sets of data				
Maxwell	15.50	-18.55	0.232	4.85

TABLE 6.4. Values of parameters in material functions of Maxwell model, computed as best fits to two and three experimental data sets corresponding to the concentrations of $\{0.12, 0.28\}$ and $\{0.06, 0.12, 0.28\}$, respectively. The relationships of the parameters to the material functions are: $E_1 = a_1 c + b_1$, $\eta_0 = b_2 e^{a_2 c}$.

6.4. Generalization of the Maxwell model

In the Chapter 5, we have studied the viscous responses of synovial fluid as shear rate dependent. We have generalized the viscosity to a function of the shear rate and concentration. We can make similar generalization in the viscoelastic model as well. First of all, the material function η_0 corresponds to apparent viscosity of the fluid in simple (constant) shear, thus we can identify the generalized viscosity μ from Chapter 5 with η_0. Second, as one can see, the "elasticity" of the fluid keeps its character for all concentrations, thus we shall exclude its dependency on the dynamics of the flow. In this section, we shall consider again the Maxwell model only, since both models, Oldroyd–B and Maxwell, give similar results.

We recall the formulas of generalized viscosity, expressed by means of parameters already used in this chapter:

(Model 1)
$$\eta_0 = b_2 e^{a_2 c} \left(1 + \epsilon_1 |\boldsymbol{D}|^2\right)^n,$$

and

(Model 2b)
$$\eta_0 = b_2 \left(\epsilon_2 + \epsilon_1 |\boldsymbol{D}|^2\right)^{\left(1/(a_2 c^2 + 1) - 1\right)},$$

with a_2, b_2, ϵ_1, ϵ_2 and n being constant. The second material function, E_1, is the same as above, namely

(6.33)
$$E_1 = a_1 c + b_1.$$

It is obvious, that if we want to use even one of the material functions as frequency–dependent (or generally $|\boldsymbol{D}|^2$ dependent), we can not use the forms of G' and G'' (6.30) and (6.27), as they were derived for constant material parameters. This complicates the whole fitting procedure since we are not able to solve the system of differential equations (6.17) analytically anymore. The system has to be solved numerically[4]. The dynamic moduli G' and G'' are in relation to τ via

(6.34)
$$\tau = \gamma_0 \{G' \cos(\omega t) + G'' \sin(\omega t)\},$$

and thus, we have to expand the shear–component of the numerical solution (periodic as well) in Fourier series

(6.35)
$$\tau = \frac{a_0}{2} + \sum_{n=1}^{\infty} a_n \sin(n\omega t) + b_n \cos(n\omega t),$$

where the desired moduli are the second and third coefficients of the series, coefficients for $n = 1$. Other coefficients are supposed to be negligible. Explicitly, the dynamic moduli are

(6.36)
$$G' = a_1 = \frac{\omega}{\pi} \int_0^{\frac{2\pi}{\omega}} \tau \cos(\omega t) \mathrm{d}t,$$

(6.37)
$$G'' = b_1 = \frac{\omega}{\pi} \int_0^{\frac{2\pi}{\omega}} \tau \sin(\omega t) \mathrm{d}t.$$

This means, that after the numerical solving of the differential equations, another numerical procedure has to be called – the numerical integration.

Again, the fits were computed for experimental data sets of two and three concentrations. The results are presented in Fig. 6.8 and values of parameters and errors of particular fits summarized in Tab. 6.5.

6.5. Discussion

The lack of experimental data which demonstrate the non–linear viscoelastic behavior of synovial fluid forced us to consider linear viscoelastic models and their generalizations, only. Nevertheless, even for the experiment of small deformations, e. g. amplitudes and frequencies of oscillations are small enough, the models were able to fit the data only approximately. This suggest, that even for small deformations the fluid exhibit some non–linear characteristic.

---

[4]The numerical solution of the system is obtained by using buit–in Matlab function bvp4c, function for solving the boundary value problem of systems of ordinary differential equations.

(a) $\eta_0 = b_2 e^{a_2 c}$

(b) $\eta_0 = b_2 e^{a_2 c}$

(c) $\eta_0 =$ Model 1

(d) $\eta_0 =$ Model 1

(e) $\eta_0 =$ Model 2b
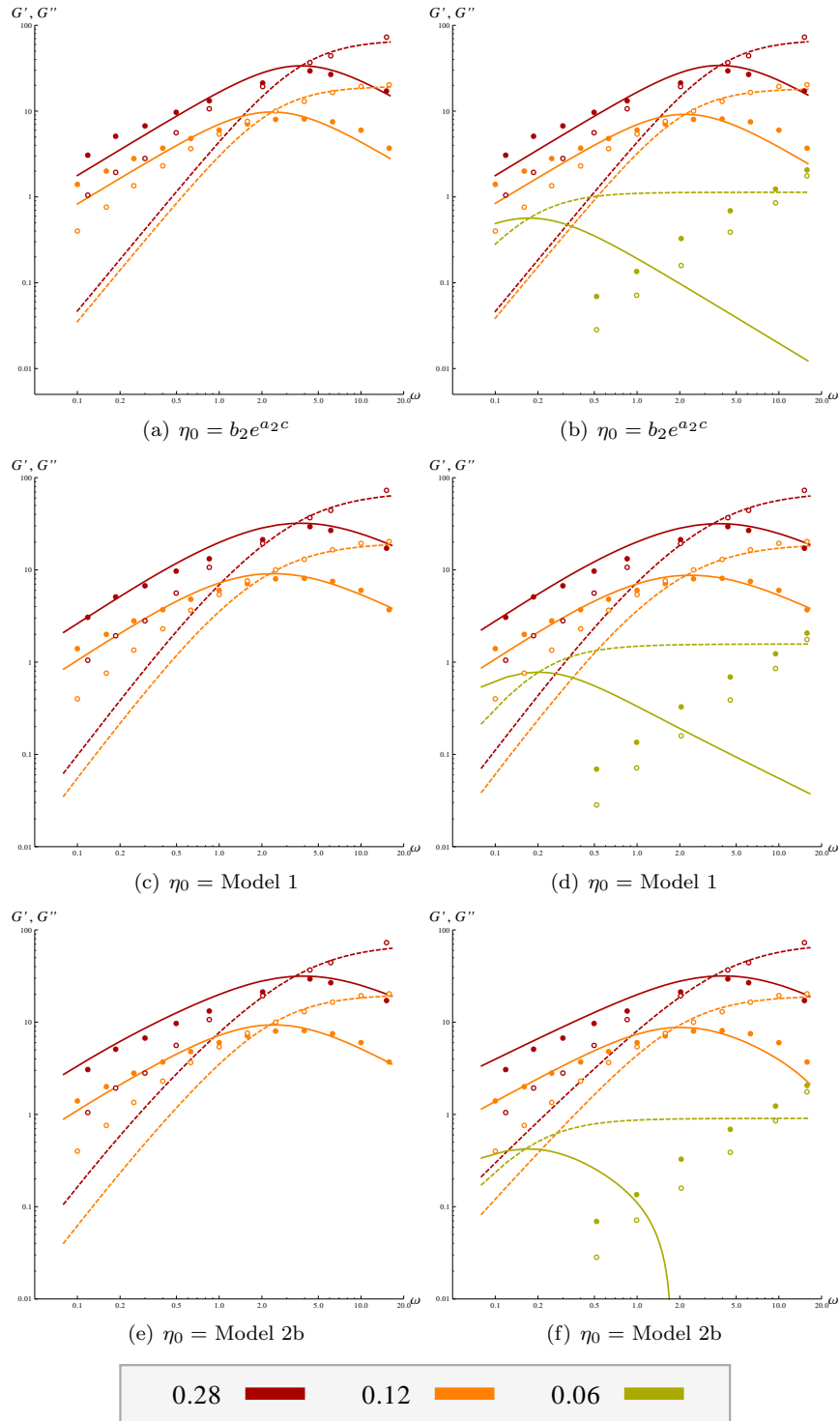
(f) $\eta_0 =$ Model 2b

| 0.28 | 0.12 | 0.06 |

FIGURE 6.8. Comparison of best fits of Maxwell model and its generalizations to experimental data. The variation between the models is in the form of η_0. Dynamic loss modulus – solid lines, dynamic storage modulus – dashed lines; solid points – dynamic loss modulus experimental data, circles – dynamic storage modulus experimental data.

Model/data	Error & Parameters
2 sets of data	
Maxwell	$\boldsymbol{r(a^*) = 287}$
$E_1 = a_1 c + b_1$	$a_1 = 314.0 \quad b_1 = -17.6$
$\eta_0 = b_2 e^{a_2 c} \left(1 + \epsilon_1 |\boldsymbol{D}|^2\right)^n$	$a_2 = 7.73 \quad b_2 = 5.3$
	$\epsilon_1 = 22.4 \quad n = -0.11$
Maxwell	$\boldsymbol{r(a^*) = 280}$
$E_1 = a_1 c + b_1$	$a_1 = 314.0 \quad b_1 = -17.4$
$\eta_0 = b_2 \left(\epsilon_2 + \epsilon_1 |\boldsymbol{D}|^2\right)^{\gamma\left(1/(a_2 c^2 + 1) - 1\right)}$	$a_2 = 72.0 \quad b_2 = 2.1$
	$\epsilon_1 = 2 \times 10^{-8} \quad \epsilon_2 = 1 \times 10^{-10}$
	$\gamma = 0.14$
3 sets of data	
Maxwell	$\boldsymbol{r(a^*) = 308}$
$E_1 = a_1 c + b_1$	$a_1 = 314.0 \quad b_1 = -17.6$
$\eta_0 = b_2 e^{a_2 c} \left(1 + \epsilon_1 |\boldsymbol{D}|^2\right)^n$	$a_2 = 8.0 \quad b_2 = 5.4$
	$\epsilon_1 = 28.7 \quad n = -0.12$
Maxwell	$\boldsymbol{r(a^*) = 285}$
$E_1 = a_1 c + b_1$	$a_1 = 326.0 \quad b_1 = -19.8$
$\eta_0 = b_2 \left(\epsilon_2 + \epsilon_1 |\boldsymbol{D}|^2\right)^{\gamma\left(1/(a_2 c^2 + 1) - 1\right)}$	$a_2 = 92.0 \quad b_2 = 2.1$
	$\epsilon_1 = 3 \times 10^{-8} \quad \epsilon_2 = 1 \times 10^{-13}$
	$\gamma = 0.14$

TABLE 6.5. Values of parameters in material functions of generalized Maxwell model, computed as best fits to two and three sets of experimental data corresponding to the concentrations of $\{0.12, 0.28\}$ and $\{0.06, 0.12, 0.28\}$, respectively.

The fits of the Maxwell model are almost identical to the fits done for the Oldroyd–B fluid. When separate concentration data fitted, both models were able to predict reasonably well the viscoelastic response for limiting concentration of 0.06 (which corresponds to $1.28\,\text{mg/ml}$). Nevertheless, the explicit inclusion of concentration variable to the rheological models led to wrong description of viscoelasticity for very small concentrations. We assume that this can be partially the effect of small values of G' and G'' in comparison to the values of dynamic moduli for higher concentrations.

Of course, one could adapt the least squares method by introduction of weights, which would increase the significance of small values. Here, we must admit, we were not successful with finding such weights. We have even generalized the models by introducing the extra parameter a in the convected Oldroyd derivative, see definition (6.8). Nevertheless, the numerical fits were almost independent of the value of a in the considered range $a \in [-1, 1]$.

Since we have no more information about the concentration/frequency dependencies, we can not point out other aspects influencing the dynamic moduli, and thus improve the considered phenomenological model.

Chapter 7

Problem formulation: governing equations and mathematical analysis

7.1. Governing equations

To this point, we have been focused on the description of the material only, by choosing the suitable model for synovial fluid which can fit the experimental data in some known range of deformations. Now, let us formulate the balance laws describing the flow of synovial fluid under some justified simplifications. Before writing down the explicit equations, let us conclude these simplifications we made in previous chapters

- synovial fluid can be approximated by homogeneous single constituent fluid – the continuous approach is applicable,
- synovial fluid is incompressible,
- hyaluronan influences synovial fluid mechanical responses through its concentration,
- concentration appears in the material parameters of the model for synovial fluid,
- pathological cases are not considered.

7.1.1. Balance laws. We describe the flow of synovial fluid in the terms of the velocity field $\boldsymbol{v}$ and the pressure field p which are governed by the *generalized Navier–Stokes equations* and the constrain of *incompressibility*. The concentration distribution, the scalar field c, which influences the flow only through the material parameter(s) in constitutive equation(s) is described by the *convection-diffusion equation*[1]. The system of the governing equations takes the form

$$(7.1) \qquad\qquad \operatorname{div} \boldsymbol{v} = 0,$$

$$(7.2) \qquad\qquad \varrho \frac{\partial \boldsymbol{v}}{\partial t} + \varrho[\operatorname{grad} \boldsymbol{v}]\boldsymbol{v} = -\operatorname{grad} p + \operatorname{div} \boldsymbol{S} + \varrho \boldsymbol{f},$$

$$(7.3) \qquad\qquad \frac{\partial c}{\partial t} + (\operatorname{grad} c) \cdot \boldsymbol{v} = \operatorname{div} \boldsymbol{q}_c,$$

where $\boldsymbol{f}$ represents the specific external body force field, ϱ is the density of synovial fluid and $\boldsymbol{S}$ is the extra stress tensor of the Cauchy stress tensor. Term $\boldsymbol{q}_c$ represents the diffusive flux of the concentration c which, analogously to extra stress tensor $\boldsymbol{S}$, has to be specified by the constitutive equation for the diffusivity of concentration. In our case, we assume that the diffusion is given by the Fick's law

$$(7.4) \qquad\qquad \boldsymbol{q}_c = D_c(c, |\boldsymbol{D}|^2) \operatorname{grad} c,$$

where D_c is the diffusivity, the characteristic of solute with respect to the solvent. In general it is a tensorial function. As it was experimentally documented by Rudraiah et al. (1991) or Gribbon et al. (1999), for instance, the diffusivity is dependent of concentration and shear rate. Nevertheless, the consideration of constant diffusivity is quite often used in many

---

[1]The use of mixture theory would lead to balancing both constituents - the hyaluronan as solute and ultrafiltrated blood plasma as solvent and to identification of their interaction terms.

applications as the variations and even the values of diffusivity itself are very small compared to dominant convection, see for example Coleman et al. (1999). The stress tensor $\boldsymbol{S}$ is given by one of the considered viscous/viscoelastic models derived in Chapter 5 or 6. In comparison with the viscous flow, the viscoelastic descriptions introduces one more (tensor) equation which needs to be solved together with (7.1)–(7.3), the equation for the extra stress tensor.

Further, since the concentration of hyaluronan is very low, we assume that the density ϱ is not influenced by the varying concentration c and hence it remains constant. Regarding the equation (7.3), one could even extend the convection–diffusion by the volumetric destruction term which would represent eventual enzymatic hydrolytic reactions, often present at the inflammatory stage of pathological diseases of the synovial fluid. The positive volumetric term representing creation of the molecules of hyaluronan is non–realistic since hyaluronan is produced only by the synovial membrane, in our setting represented by the boundary of considered flow domain. Thus, in our case under consideration of non–pathological synovial fluid, the volumetric production term is always zero.

7.1.2. Non–dimensionalization. For the consecutive numerical computations, it will be useful to recast the equations (7.1)–(7.3) in terms of dimensionless variables. For that, we need to specify the explicit constitutive equation for extra stress tensor $\boldsymbol{S}$ in (7.2). Assuming the fact, that our main aim of this chapter is to accomplish the new existence results for the viscous models only, let us proceed with the non–dimenzionalization for the viscous case and at the end we shall remark the basic differences for the case of viscoelasticity. For the case of viscous model the form of the extra stress tensor $\boldsymbol{S}$ (as derived in Chapter 5) is following

$$(7.5) \qquad \boldsymbol{S} = 2\mu\left(c, |\boldsymbol{D}|^2\right)\boldsymbol{D},$$

where $\boldsymbol{D} = 1/2\left(\operatorname{grad}\boldsymbol{v} + (\operatorname{grad}\boldsymbol{v})^{\mathrm{T}}\right)$ and the viscosity function is specified by either Model 1 or Model 2, see Chapter 5. We define the non–dimensional variables

$$X = \frac{x}{L^*}, \quad \boldsymbol{V} = \frac{\boldsymbol{v}}{V^*}, \quad C = \frac{c}{C^*},$$

$$(7.6) \qquad P = \frac{p}{P^*}, \quad F = \frac{f}{g}, \quad M = \frac{\mu}{M^*}, \quad D = \frac{D_c}{D_c^*},$$

where L^* and V^* are the characteristic length and velocity, respectively, and g is the acceleration due to gravity. Regarding the concentration, we use the parametrization which has been introduced in Chapter 5. For consistency, we choose

$$(7.7) \qquad P^* = \varrho(V^*)^2 \quad \text{and} \quad M^* = \mu_0,$$

where M^* is the characteristic viscosity, analogously to D_c^* being the characteristic diffusivity. Time has been naturally non–dimensionalized with respect to L^*/V^* and extra stress tensor $\boldsymbol{S}$ with respect to M^*L^*/V^*.

From now on, for simplicity of the notation, instead of capitals the small letters for the non–dimensional variables are used. The system of governing equations is then transformed onto

$$(7.8) \qquad \operatorname{div}\boldsymbol{v} = 0,$$

$$(7.9) \qquad \frac{\partial\boldsymbol{v}}{\partial t} + [\operatorname{grad}\boldsymbol{v}]\boldsymbol{v} = -\operatorname{grad}p + \frac{1}{\mathrm{Re}}2\operatorname{div}\left(\mu(c, |\boldsymbol{D}|^2)\right)\boldsymbol{D} + \boldsymbol{f},$$

$$(7.10) \qquad \frac{\partial c}{\partial t} + (\operatorname{grad}c)\cdot\boldsymbol{v} = \frac{1}{\mathrm{Pe}}\operatorname{div}\left(D_c(c, |\boldsymbol{D}|^2)\operatorname{grad}c\right),$$

using the notation for reduced Reynolds number $\mathrm{Re} = \varrho L^*V^*/\mu_0$ and Péclet number $\mathrm{Pe} = L^*V^*/D_c^*$.

In the case of viscoelastic fluid, one introduces in the Navier–Stokes equations (7.9) additionally to Reynolds number the Weissenberg number, $\mathrm{We} = \varrho\lambda_1 V^*/L^*$, see for example Wineman and Rajagopal (2000), describing the characteristic of flow as product of relaxation time and shear rate.

7.2. Mathematical analysis

The objective of this section is to obtain an existence result for the stationary problem corresponding to (7.1)–(7.3) in two and more dimensions. First, we summarize the previously obtained results of similar problems, including evolutionary ones. Then, we introduce suitable vector spaces for the weak solution and their properties. We formulate the main existence theorem and, as last, we prove it.

In contrast to formulation of (7.1)–(7.3) which is classical for continuum mechanics, here, we use a different notation in order to achieve the consistency with the community of mathematical analysists. First of all, we express, due to the constraint of incompressibility,

$$(7.11) \qquad [\text{grad}\,\boldsymbol{v}]\boldsymbol{v} = \text{div}(\boldsymbol{v}\otimes\boldsymbol{v}), \quad \text{grad}\,c\cdot\boldsymbol{v} = \text{div}(c\boldsymbol{v})$$

where the tensor product $\boldsymbol{a}\otimes\boldsymbol{b}$ is the second–order tensor with components $(\boldsymbol{a}\otimes\boldsymbol{b})_{ij} = a_i b_j$. Moreover, we use notation of $\boldsymbol{D}(a) = 1/2(\nabla a + \nabla a^{\mathrm{T}})$, and thus we express the symmetric part of velocity gradient, as before denoted by $\boldsymbol{D}$, by $\boldsymbol{D}(\boldsymbol{v})$. The stationary system then reads

$$(7.12) \qquad \text{div}\,\boldsymbol{v} = 0,$$

$$(7.13) \qquad \text{div}(\boldsymbol{v}\otimes\boldsymbol{v}) - \text{div}\,\boldsymbol{S}(c,\boldsymbol{D}(\boldsymbol{v})) = -\nabla p + \boldsymbol{f},$$

$$(7.14) \qquad \text{div}(c\boldsymbol{v}) - \text{div}\,\boldsymbol{q}_c(c,\nabla c,\boldsymbol{D}(\boldsymbol{v})) = 0.$$

where the extra stress tensor $\boldsymbol{S}$ and the concentration flux $\boldsymbol{q}_c{}^2$ are of the form

$$(7.15) \quad \boldsymbol{S}(c,\boldsymbol{D}(\boldsymbol{v})) = \frac{2}{\text{Re}}\mu(c,|\boldsymbol{D}(\boldsymbol{v})|^2)\boldsymbol{D}(\boldsymbol{v}), \qquad \boldsymbol{q}_c(c,\nabla c,\boldsymbol{D}(\boldsymbol{v})) = \frac{1}{\text{Pe}}\boldsymbol{K}(c,|\boldsymbol{D}(\boldsymbol{v})|)\nabla c.$$

Moreover, the power–law index, as used before, is expressed as $n(c) = \frac{p(c)-2}{2}$, and thus the generalized viscosity is given by

$$(7.16) \qquad \mu(c,|\boldsymbol{D}(\boldsymbol{v})|^2) = \left(\kappa_1 + \kappa_2\,|\boldsymbol{D}(\boldsymbol{v})|^2\right)^{\frac{p(c)-2}{2}}.$$

To $p(\cdot)$ we shall refer as to a variable exponent.

In what follows, we use letters C, $\overline{C}$, C_1, C_2, ..., for constants, especially the symbol C without index stands for a generic constant which may vary from line to line, but depends only on data.

7.2.1. Survey of previous results. The existence results for the problem (7.12)–(7.14) with a generalized viscosity of the form (7.16) is not known. Nevertheless, mathematical analysis of simpler systems, both stationary and evolutionary, with constant shear–thinning index or analogous systems with viscosity shear–rate and concentration/temperature or electrical field dependent is developed for several special cases of boundary and initial conditions. All the references we shall mention here are representing the results for the incompressible fluid for the case of 3D.

The mathematical analysis of evolutionary Navier–Stokes equations for incompressible fluid with non–constant viscosity, particularly shear–rate dependent, was first introduced by O. A. Ladyzhenskaya in late 60'. She obtained the existence results for the weak solution for power–law index $p \geqslant \frac{11}{5}$ by using the method of monotone operators together with compactness arguments, for both periodic and no–slip Dirichlet boundary conditions, see Ladyzhenskaya (1967) and Ladyzhenskaya (1969). The same arguments can be used for the stationary case for $p \geqslant \frac{11}{5}$. Later, the existence results were extended for the spatially periodic problem by Málek, Nečas and Růžička for $p \geqslant \frac{9}{5}$ by the means of the method of regularities to obtain fractional higher differentiability, Málek et al. (1993), and for the no–slip Dirichlet boundary conditions , for $p \geqslant 2$, by the same authors in Málek et al. (2001). Further extension, for slip boundary conditions, was introduced by Frehse, Málek and Steinhauer for $p > \frac{8}{5}$ by using the method of L^∞–approximations, Frehse et al. (2000), and shortly after the results were even more broaden for index $p > \frac{6}{5}$ by Diening et al. (2010b) who proved the existence of the weak solution by the means of the method of Lipschitz approximations. Concerning the easier steady problem with no–slip Dirichlet boundary condition, the method

---

[2]The general tensor form of diffusivity $D_c(c,\boldsymbol{D}(\boldsymbol{v}))$ is denoted here as a tensor function $\boldsymbol{K}(c,|\boldsymbol{D}(\boldsymbol{v})|)$.

of L^∞–approximations was already used by Frehse et al. (1997) and Růžička (1997) obtaining the existence results for $p \geqslant \frac{3}{2}$ and the method of Lipschitz approximations was used by Frehse et al. (2003) for extension of the result to $p > \frac{6}{5}$.

The coupled system of Navier–Stokes equations with the equation for convection–diffusion –reaction with generalized viscosity of the form $\mu(c, |\boldsymbol{D}(\boldsymbol{v})|^2) \sim \mu_1(c)\mu_2(|\boldsymbol{D}(\boldsymbol{v})|^2)^{\frac{p-2}{2}}$ was studied by Bulíček et al. (2009) where the authors proved the long time existence of weak solutions for $p > \frac{8}{5}$.

The models with non–constant power–law index, developed for electrorheological fluids, are studied for instance in Růžička (2000), Růžička (2004). For this kind of fluids the extra stress tensor is (non–trivially) dependent of electric field $\boldsymbol{E}$ and thus the Navier–Stokes equation has to be solved with the (quasi-static) Maxwell's equations. Nevertheless, the governing equations are essentially uncoupled thus the Maxwell's equations can be solved first. The solution of electric field can be then considered as a known function, resulting that the problem reduces to the problem of incompressible Navier–Stokes problem with extra stress tensor having the growth property of $|\boldsymbol{S}| \leqslant C(1 + |\boldsymbol{D}(\boldsymbol{v})|^2)^{\frac{p(x)-2}{2}}$, where $p(x) := p(|\boldsymbol{E}(x)|^2)$ is given variable function (under some assumption of Hölder continuity), satisfying $1 < p^- < p(x) < p^+ < \infty$. Using the theory of monotone operators, the author was able to prove the existence of a weak solution for lower bound $p^- \geqslant \frac{9}{5}$, and in the case of stationary problem the existence result was extended to $p^- \geqslant \frac{6}{5}$ by Diening et al. (2008), by the means of the method of Lipschitz approximations.

The closest system to ours, (7.8)–(7.10), is studied in Antontsev and Rodrigues (2006). The authors consider the stationary system of Navier–Stokes equations coupled with equation for thermal diffusion obtained as Oberbeck–Boussinesq approximation of Fourier equation for the temperature, under the consideration that the power–law index of the generalized viscosity is dependent of temperature θ. For Dirichlet boundary conditions, for both velocity and temperature, they prove the existence of the global weak solution for the case of $\frac{9}{5} \leqslant p_\star < p(\theta) < \infty$ for large and sufficiently smooth data. There, the important assumption simplifying the proof is the assumption of the constant diffusion tensor $\boldsymbol{D}_\theta$, which ensures the Hölder continuity of the temperature.

7.2.2. Introduction of functions spaces. Before we formulate the problem and introduce the theory for proving the existence of the weak solution, let us introduce relevant functions spaces. It is obvious, that for the problem of non–constant viscosity with variable exponent of the power–law, the functional setting of classical Lebesgue/Sobolev spaces is not sufficient but more general approach needs to be introduced, in this case the setting of generalized Lebesgue/Sobolev spaces with variable exponent p. The topic of generalized Lebesgue/Sobolev spaces has been studied by many authors, for instance by Orlicz (1931), Nakano (1950), Sharapudinov (1978), Kováčik and Rákosník (1991), Fan et al. (2001) and Diening et al. (2011).

In what follows, the terms measure and measurable will always mean (d–dimensional) Lebesgue measure and (d–dimensional)Lebesgue measurable, and, the symbol Ω shall stand for the domain of our interest, measurable open subset of $\mathbb{R}^d$, with $0 < \text{meas}(\Omega) < \infty$.

Concerning standard definition of classical real valued[3] Lebesgue space $L^p(\Omega)$ for $1 \leqslant p < \infty$, equipped by $||\cdot||_p$ norm

$$(7.17) \qquad L^p(\Omega) := \left\{ f : \Omega \to \mathbb{R} \text{ measurable} : \int_\Omega |f(x)|^p \, dx < \infty \right\},$$

$$(7.18) \qquad ||f||_p = ||f||_{p,\Omega} := \left(\int_\Omega |f(x)|^p \, dx \right)^{1/p},$$

---

[3]The extension to the vector valued spaces is natural, for instance in the case of $[L^p(\Omega)]^d$ each component of the vector valued function belongs to the $L^p(\Omega)$ space.

and additionally

(7.19)
$$L^\infty(\Omega) := \left\{ f : \Omega \to \mathbb{R} \text{ measurable} : \underset{x \in \Omega}{\text{ess sup}} |f(x)| < \infty \right\},$$

(7.20)
$$\|f\|_\infty = \|f\|_{\infty,\Omega} := \underset{x \in \Omega}{\text{ess sup}} |f(x)|,$$

the generalized Lebesgue space $L^{p(\cdot)}$ and its norm must be defined more carefully. Generally, the $L^{p(\cdot)}$ spaces belong to the class of more general Musielak–Orlicz spaces, see for example Musielak (1983), and thus $L^{p(\cdot)}$ spaces can be properly defined by the use of this framework. Nevertheless, for our needs, we shall only introduce the basic notation and definitions, without the use of framework of general modular spaces. For closer study of Musielak–Orlicz spaces we refer the reader to work of Musielak (1983) or compact and self–contained book Diening et al. (2011).

DEFINITION 7.1 (Variable exponent $p(\cdot)$). *We denote the set of all measurable functions $p : \Omega \to [1, \infty]$ by $\mathcal{P}(\Omega)$, and call the function $p \in \mathcal{P}(\Omega)$ a variable exponent. Moreover, we define $p^- := \text{ess inf}_{x \in \Omega}\, p(x)$ and $p^+ := \text{ess sup}_{x \in \Omega}\, p(x)$, and, $\Omega_\infty := \{x \in \Omega : p(x) = \infty\}$ and $\Omega_1 := \{x \in \Omega : p(x) = 1\}$. We call the variable exponent to be bounded if $p^+ < \infty$.*

At this point, let us even define for $p \in \mathcal{P}(\Omega)$ the dual variable exponent $p' \in \mathcal{P}(\Omega)$ by $\frac{1}{p(x)} + \frac{1}{p'(x)} = 1$, for which we formally denote $\frac{1}{\infty} := 0$.

Now, having a notion of a variable exponent, we can define the so–called semimodular $\rho_{L^{p(\cdot)}(\Omega)}$ which induces a norm and the topology of generalized Lebesgue spaces.

DEFINITION 7.2 (Semimodular $\varrho_{L^{p(\cdot)}(\Omega)}$). *Let $p \in \mathcal{P}(\Omega)$. For $x \in \Omega$ and $t \geqslant 0$ we set $\Phi_{p(\cdot)}(x, t) := \varphi_{p(x)}(t)$, where*

$$\varphi_p(t) := t^p \text{ for } 1 \leqslant p < \infty, \quad \text{and} \quad \varphi_\infty(t) := \begin{cases} 0 & t \in \langle 0, 1 \rangle, \\ \infty & t \in (1, \infty). \end{cases}$$

Then, we define the semimodular

$$\varrho_{L^{p(\cdot)}(\Omega)}(f) := \int_\Omega \Phi_{p(x)}(|f(x)|)\, dx.$$

DEFINITION 7.3 ($L^{p(\cdot)}$ space). *The variable exponent Lebesgue space $L^{p(\cdot)}$ for $p \in \mathcal{P}(\Omega)$ is then defined*

$$L^{p(\cdot)}(\Omega) := \left\{ f : \Omega \to \mathbb{R} \text{ measurable} : \varrho_{L^{p(\cdot)}(\Omega)}(\lambda f) < \infty \text{ for some } \lambda > 0 \right\},$$

and equipped with the norm

$$\|f\|_{L^{p(\cdot)}(\Omega)} = \|f\|_{L^{p(\cdot)}} := \inf\left\{ \lambda > 0 : \varrho_{L^{p(\cdot)}(\Omega)}\left(\frac{f}{\lambda}\right) \leqslant 1 \right\},$$

which corresponds to the Luxemburg norm in Orlicz spaces.

In the case that $p < \infty$ everywhere on Ω, we directly get

(7.21)
$$L^{p(\cdot)}(\Omega) = \left\{ f : \Omega \to \mathbb{R} \text{ measurable} : \int_\Omega |f(x)|^{p(x)}\, dx < \infty \right\},$$

and for the case when $p^+ = \infty$ ($\text{meas}(\Omega_\infty) > 0$), we have to redefine the semimodular and consequently the norm as introduced by Kováčik and Rákosník (1991)

(7.22)
$$\varrho(f) := \varrho_{L^{p(\cdot)}(\Omega \setminus \Omega_\infty)}(f) + \|f\|_{\infty, \Omega_\infty}.$$

For the introduction of Sobolev and generalized Sobolev spaces, we need the notion of the weak derivative.

DEFINITION 7.4 (Weak derivative). *Let $\alpha = (\alpha_1, \alpha_2, \ldots, \alpha_d) \in \mathbb{N}_0^d$ be a multi–index, $|\alpha| = \alpha_1 + \cdots + \alpha_d$. Let $u, g \in L_{loc}^1$. We call the function g a weak derivative of u with respect to x^α if*

$$\int_\Omega u \, D^\alpha \varphi \, dx = (-1)^{|\alpha|} \int_\Omega \varphi \, g \, dx \quad \forall \varphi \in C_0^\infty(\Omega),$$

where $D^\alpha := \frac{\partial^{\alpha_1 + \cdots + \alpha_d}}{\partial^{\alpha_1} x_1 \cdots \partial^{\alpha_d} x_d}$. We denote by ∇u the weak gradient $\left(\frac{\partial u}{\partial x_1}, \ldots, \frac{\partial u}{\partial x_d} \right)$.

Since the terms weak and strong derivatives are closely related we shall denote the weak derivative by the same symbol, thus $D^\alpha u = g$. Recalling the standard definition of classical Sobolev space $W^{k,p}(\Omega)$ for $k \in \mathbb{N}_0$

(7.23) $$W^{k,p}(\Omega) := \{ f \in L^p(\Omega) : \ D^\alpha f \in L^p(\Omega) \ \forall \alpha : |\alpha| \leqslant k \},$$

and its norm

(7.24) $$\|u\|_{k,p} = \|u\|_{k,p,\Omega} := \begin{cases} \left(\sum_{|\alpha| \leqslant k} \|D^\alpha u\|_p^p \right)^{1/p} & p \in \langle 1, \infty \rangle, \\ \max_{|\alpha| \leqslant k} \|D^\alpha u\|_\infty & p = \infty, \end{cases}$$

the generalization of Sobolev space in a sense of variable exponent is then obvious.

DEFINITION 7.5 ($W^{k,p(\cdot)}$ space). *Let $k \in \mathbb{N}$ and $p \in \mathcal{P}(\Omega)$. The function $u \in L^{p(\cdot)}(\Omega)$ belongs to Sobolev space $W^{k,p(\cdot)}$ if all the weak derivatives $D^\alpha u$ with $|\alpha| \leqslant k$ exist and belong to $L^{p(\cdot)}(\Omega)$, particularly*

$$W^{k,p(\cdot)}(\Omega) := \left\{ u \in L^{p(\cdot)}(\Omega) : \ D^\alpha u \in L^{p(\cdot)}(\Omega) \ \forall \alpha : |\alpha| \leqslant k \right\}.$$

The semimodular defined on $W^{k,p(\cdot)}$ by

$$\varrho_{W^{k,p(\cdot)}(\Omega)}(u) := \sum_{|\alpha| \leqslant k} \varrho_{L^{p(\cdot)}(\Omega)}(D^\alpha u)$$

then induces a norm by

$$\|u\|_{k,p(\cdot)} = \|u\|_{k,p(\cdot),\Omega} := \inf \left\{ \lambda > 0 : \ \varrho_{W^{k,p(\cdot)}(\Omega)} \left(\frac{u}{\lambda} \right) \leqslant 1 \right\}.$$

As in the case of classical L^p and $W^{k,p}$, the functions of generalized Lebesgue and Sobolev spaces are defined up to measure zero and thus we identify that functions which are equal almost everywhere. Here, let us mention one straightforward property of $L^{p(\cdot)}$ and $W^{k,p(\cdot)}$, namely, for constant exponent p on Ω, indeed the generalized spaces coincide with classical L^p and $W^{k,p}$, as well as the norms (thus the same notation).

Additionally, we denote by $C(\overline{\Omega})$ the space of all continuous functions equipped with the norm $\| \cdot \|_\infty$. Then, we denote by $C^k(\overline{\Omega})$, $k \in \mathbb{N}$, the set of all continuously differentiable functions up to the degree k, by $C^\infty(\overline{\Omega})$ the set of smooth functions – the functions arbitrarily many times continuously differentiable, and by $C_0^\infty(\Omega)$ the set of smooth functions with compact support. As last, we introduce the set of Hölder continuous functions

(7.25) $$C^{k,\alpha}(\Omega) := \left\{ f \in C^k(\overline{\Omega}) : \sup_{\substack{x,y \in \Omega \\ x \neq y}} \frac{|D^\beta x - D^\beta y|}{|x - y|^\alpha} < \infty \quad \forall \beta : |\beta| \leqslant k \right\},$$

for $\alpha \in (0, 1]$, $k \in \mathbb{N}_0$.

In comparison with classical L^p and $W^{k,p}$, the generalized $L^{p(\cdot)}$ and $W^{k,p(\cdot)}$ exhibit similar properties, like completeness, separability, reflexivity, etc. These we introduce without any proof in the following theorem, nevertheless, the reader can find the exact proofs in the following references Kováčik and Rákosník (1991), Fan et al. (2001) or Diening et al. (2011).

THEOREM 7.1 (Basic properties of generalized spaces). *The spaces $L^{p(\cdot)}(\Omega)$ and $W^{k,p(\cdot)}(\Omega)$ are Banach spaces for any exponent $p \in \mathcal{P}(\Omega)$, separable for $p \in \mathcal{P}(\Omega)$ with $p^+ < \infty$, and reflexive and uniformly convex for any $p \in \mathcal{P}(\Omega)$ with $1 < p^- \leqslant p^+ < \infty$.*
Moreover, $\left(L^{p(\cdot)}(\Omega)\right)' = L^{p'(\cdot)}(\Omega)$ holds for any $p \in \mathcal{P}(\Omega)$, and for $p \in \mathcal{P}(\Omega)$ with $p^+ < \infty$, the space $C_0^\infty(\Omega)$ is dense in $L^{p(\cdot)}(\Omega)$.
In addition, for any exponent $p \in \mathcal{P}(\Omega)$, the generalized Hölder inequality holds, i. e.
for any $f \in L^{p(\cdot)}(\Omega)$ and $g \in L^{q(\cdot)}(\Omega)$ and any $p, q, s \in \mathcal{P}(\Omega)$ such that

$$\frac{1}{s(x)} = \frac{1}{p(x)} + \frac{1}{q(x)},$$

the following holds

$$\varrho_{s(\cdot)}(fg) \leqslant \varrho_{p(\cdot)}(f) + \varrho_{q(\cdot)}(g),$$
$$||fg||_{s(\cdot)} \leqslant 2||f||_{p(\cdot)}||g||_{q(\cdot)}.$$

Particularly, for $s = 1$

$$\int_\Omega |fg| \, dx \leqslant \varrho_{p(\cdot)}(f) + \varrho_{p'(\cdot)}(g),$$
$$||fg||_1 \leqslant 2||f||_{p(\cdot)}||g||_{p'(\cdot)}.$$

While above mentioned spaces properties are rather functional analysis–type, more specific tools need to be involved for the study of partial differential equations, such as density of regular functions or Sobolev embeddings, which, however, require additional regularity of the exponent. While the smooth functions C_0^∞ are dense in $L^{p(\cdot)}$, $p^+ < \infty$, as proved by Kováčik and Rákosník (1991), the same is not true for the space of Sobolev functions $W^{k,p(\cdot)}$. Already Zhikov (1987) presented a counter–example to the density of smooth functions in $W^{1,p(\cdot)}$, for bounded but discontinuous exponent p. As Fan et al. (2006) showed, the discontinuity does not play the crucial role rather the "non–regularity" of the set of points of discontinuity, or, as demonstrated by Hästö (2005) and Diening et al. (2005) the non–sufficient regularity of crucial points as saddle points. To this date, the density of smooth functions or continuous functions is not resolved, nevertheless, sufficient but not necessary conditions which guarantee the density are known. Among others, it is the important log–Hölder continuity condition on exponent p, as studied by Edmunds and Rákosník (1992), Samko (2000) or Fan et al. (2006).

DEFINITION 7.6 (log–Hölder continuous exponent). *We say that a function $p : \Omega \to \mathbb{R}$ is locally log–Hölder continuous on Ω if there exists $C_1 > 0$ such that*

$$|p(x) - p(y)| \leqslant \frac{C_1}{\ln\left(e + \frac{1}{|x-y|}\right)} \quad \forall x, y \in \Omega.$$

Moreover, if the function p satisfies so–called log–Hölder decay

$$\exists p_\infty \in \mathbb{R}, \, C_2 > 0 : \quad |p(x) - p_\infty| \leqslant \frac{C_2}{\ln(e + |x|)} \quad \forall x \in \Omega,$$

we say that the function is globally log–Hölder continuous.
Then, we define a class of variable exponents such that

$$\mathcal{P}^{\log}(\Omega) := \{p \in \mathcal{P}(\Omega) : 1/p \text{ is globally log–Hölder continuous}\}.$$

REMARK. In some literature, instead of $\mathcal{P}^{\log}$ the acceptable class of exponents p is the set of $p \in \mathcal{P}$ with $p^+ < \infty$ satisfying

$$(7.26) \qquad |p(x) - p(y)| \leqslant \frac{C_1}{-\ln|x-y|} \quad \forall x, y \in \Omega : |x - y| \leqslant \frac{1}{2}.$$

In fact, both descriptions are equivalent, since the mapping $p \mapsto \frac{1}{p}$ is bilipschitz, see Diening (2004). Furthermore, the log–Hölder continuity condition is sometimes named as Dini–Lipschitz or weak Lipschitz.

At this point, we can state the basic theorem of density of smooth functions in generalized Sobolev spaces. The proof can be found in Diening et al. (2010b), Section 9.1.

THEOREM 7.2 (Density of smooth functions). *Let Ω be an open bounded set with Lipschitz boundary, $k \in \mathbb{N}$ and $p \in \mathcal{P}^{\log}(\Omega)$ be a bounded exponent. Then $C^{\infty}(\overline{\Omega})$ is dense in $W^{k,p(\cdot)}(\Omega)$.*

As we mentioned above, we can ask similar question of generalization about the embedding $W^{1,p} \hookrightarrow L^q$ for $q \leqslant p^*$, p^* being the Sobolev conjugate. Already Kováčik and Rákosník (1991) showed counter–example (with discontinuous exponent) that in general this generalization is not possible. This counter–example was even extended for continuous, but not uniformly continuous, exponent by Diening et al. (2005). Let us define the generalized Sobolev conjugate point–wisely

$$(7.27) \qquad p^*(x) := \begin{cases} \dfrac{np(x)}{n - p(x)} & p(x) < d, \\ \infty & p(x) \geqslant d. \end{cases}$$

For bounded Lipschitz domains Ω, Edmunds and Rákosník (2000) proved under assumption of $p(x)$ being Lipschitz with $\sup_{x \in \Omega} p(x) < d$[4] that $W^{1,p(\cdot)} \hookrightarrow L^{p^*(\cdot)}$, and later Edmunds and Rákosník (2002) extended this result for $p(x) \in W^{1,s}$ for some $s > d$, assuming $p^+ < d$. Later, Diening (2004) proved same optimal Sobolev embeddings for bounded Lipschitz domain and locally Hölder continuous $p(x)$ with $1 < p^- \leqslant p^+ < d$. Let us summarize the basic results on embedding, first, the type of embedding between variable and constant exponents Sobolev spaces, and after the generalization of one of the most widely used theorem in theory of partial differential equations.

THEOREM 7.3. *Let $p \in \mathcal{P}^{\log}(\Omega)$ and $|\Omega| < \infty$, then*

$$W^{k,p(\cdot)}(\Omega) \hookrightarrow W^{k,p^-}(\Omega).$$

The proof of Theorem 7.3 is based on the embedding $L^{p(\cdot)}(\Omega) \hookrightarrow L^{p^-}(\Omega)$ which was proven by Kováčik and Rákosník (1991).

THEOREM 7.4. *Let $p \in \mathcal{P}^{\log}(\Omega)$ satisfying $1 \leqslant p^- \leqslant p^+ < d$ and $q \in \mathcal{P}(\Omega)$ bounded such that $q(x) \leqslant p^*(x)$ for almost all $x \in \mathbb{R}^d$. Then for open bounded Ω with Lipschitz boundary*

$$W^{1,p(\cdot)}(\Omega) \hookrightarrow L^{q(\cdot)}(\Omega)$$

where the corresponding embedding constant depends only on the dimension n, $|\Omega|$, p^+ and constant of the log–Hölder continuity.

Moreover, if $q(x) < p^*(x)$ for almost all $x \in \mathbb{R}^d$, the embedding is compact.

The proof of Theorem 7.4 can be found in Diening (2004).

One can even ask more specific question from theory of fluid dynamics, the question of generalization of the Korn inequality. In other words, if we can, under some restriction, control the norm of the whole gradient $\nabla \boldsymbol{v}$ by the norm of its symmetric part $\boldsymbol{D}(\boldsymbol{v}) := \frac{1}{2}(\nabla \boldsymbol{v} + (\nabla \boldsymbol{v})^{\mathrm{T}})$ in the spaces with variable exponents.

---

[4]In fact, Edmunds and Rákosník (2000) proved the embedding even for $\sup_{x \in \Omega} p(x) = d$, nevertheless, the space $L^{p^*(x)}$ with $\sup p^*(x) = \infty$ has to be then replaced by a more general space of Orlicz–Musielak type.

THEOREM 7.5 (Korn's inequality). *Let $p \in \mathcal{P}^{\log}(\Omega)$ with $1 < p^- \leqslant p^+ < \infty$. Then there exists a constant $C \in (0, \infty)$ such that*

$$\|\nabla \boldsymbol{v}\|_{p(\cdot)} \leqslant C \|\boldsymbol{D}(\boldsymbol{v})\|_{p(\cdot)}$$

for all $\boldsymbol{v} \in [W_0^{1,p(\cdot)}]^d$.

The proof of Theorem 7.5 can be found in Diening et al. (2010a) or Diening et al. (2010b), Section 14.3.

Even though the condition $p \in \mathcal{P}^{\log}$ is very canonical, some techniques from the theory of spaces with constant exponents are not applicable, not even under assumption of higher regularity like for bounded $p \in C^{\infty}$. For instance, the spaces $L^{p(\cdot)}$ are not invariant with respect to translations, which results in difficulties with convolutions or continuity in the mean, for closer study see Kováčik and Rákosník (1991) or Fiorenza (2002). Particularly, for bounded non–constant $p \in \mathcal{P}(\Omega)$, $\|f \star g\|_{p(\cdot)} \leqslant C\|f\|_1 \|g\|_{p(\cdot)}$ is not valid.

7.2.3. Further notation. Additionally to the Lebesgue and Sobolev spaces and their generalizations, we introduce the function spaces relevant for the treatment of the problems of incompressible fluids. By $W_0^{1,r}(\Omega)$ and $W_{0,\mathrm{div}}^{1,r}(\Omega)$ we define the sets of

$$(7.28) \qquad W_0^{1,r}(\Omega) := \text{ closure of } C_0^{\infty}(\Omega) \text{ in } \|\cdot\|_{1,r} \text{ norm},$$

$$(7.29) \qquad W_{0,\mathrm{div}}^{1,r}(\Omega) := \{\boldsymbol{\phi} \in [W_0^{1,r}(\Omega)]^d : \mathrm{div}\,\boldsymbol{\phi} = 0\}.$$

Under the assumption of $\partial\Omega \in C^{0,1}$, there holds $W_0^{1,r}(\Omega) \equiv \{\phi \in W^{1,r}(\Omega) : \phi = 0 \text{ on } \partial\Omega\}$. Similarly we have

$$(7.30) \qquad W_0^{1,r(\cdot)}(\Omega) := \{\phi \in W^{1,r(\cdot)}(\Omega) : \phi = 0 \text{ on } \partial\Omega\},$$

$$(7.31) \qquad W_{0,\mathrm{div}}^{1,r(\cdot)}(\Omega) := \{\boldsymbol{\phi} \in [W_0^{1,r(\cdot)}(\Omega)]^d : \mathrm{div}\,\boldsymbol{\phi} = 0\}.$$

For the notation of the duality pairing between $f \in X$ and $g \in X^{\star}$ we use symbol $\langle f, g \rangle_{X, X^{\star}}$, or, if it is from the context obvious, we skip for simplicity the indexes and write $\langle f, g \rangle$.

7.2.4. Formulation of stationary problem. Let us assume stationary problem being defined on an open bounded set $\Omega \subset \mathbb{R}^d$, $d \geqslant 3$, with Lipschitz boundary $\partial\Omega$

$$\text{div}\,\boldsymbol{v} = 0, \tag{7.32}$$

$$\text{div}(\boldsymbol{v} \otimes \boldsymbol{v}) - \text{div}\,\boldsymbol{S}(c, \boldsymbol{D}(\boldsymbol{v})) = -\nabla p + \boldsymbol{f}, \tag{7.33}$$

$$\text{div}(\boldsymbol{v}c) - \text{div}\,\boldsymbol{q}_c(c, \nabla c, \boldsymbol{D}(\boldsymbol{v})) = 0. \tag{7.34}$$

with Dirichlet boundary conditions for both velocity and concentration

$$\boldsymbol{v}(x) = \boldsymbol{0}, \quad \text{and} \quad c(x) = c_d \quad \text{on } \partial\Omega. \tag{7.35}$$

Concerning the character of extra stress tensor $\boldsymbol{S}$ and concentration flux vector $\boldsymbol{q}_c$ of the suitable fluid model, explicitly

$$\boldsymbol{S}(c, \boldsymbol{D}(\boldsymbol{v})) = \mu_0 \left(\beta + \gamma\,|\boldsymbol{D}|^2\right)^{(\omega\,(1/(\alpha c^2+1)-1))} \boldsymbol{D}(\boldsymbol{v}), \tag{7.36}$$

$$\boldsymbol{q}_c(c, \nabla c, \boldsymbol{D}(\boldsymbol{v})) = \boldsymbol{K}(c, \boldsymbol{D}(\boldsymbol{v}))\nabla c, \tag{7.37}$$

we assume that $\boldsymbol{S} : \mathbb{R}_0^+ \times \mathbb{R}_{sym}^{d \times d} \to \mathbb{R}_{sym}^{d \times d}$ fulfills following growth, strict monotonicity and coercivity conditions for all $c \in \langle \min_{x \in \partial\Omega} c_d, \max_{x \in \partial\Omega} c_d \rangle$ and $\boldsymbol{D}, \boldsymbol{D}_1, \boldsymbol{D}_2 \in \mathbb{R}_{sym}^{d \times d}$

$$|\boldsymbol{S}(c, \boldsymbol{D})| \leqslant C_1(|\boldsymbol{D}|^{p(c)-1} + 1), \tag{7.38}$$

$$(\boldsymbol{S}(c, \boldsymbol{D}_1) - \boldsymbol{S}(c, \boldsymbol{D}_2)) \cdot (\boldsymbol{D}_1 - \boldsymbol{D}_2) > 0 \quad \boldsymbol{D}_1 \neq \boldsymbol{D}_2, \tag{7.39}$$

$$\boldsymbol{S}(c, \boldsymbol{D}) \cdot \boldsymbol{D} \geqslant C_2(|\boldsymbol{D}|^{p(c)} + |\boldsymbol{S}(c, \boldsymbol{D})|^{p'(c)} - 1), \tag{7.40}$$

where $p(\cdot)$ is Hölder continuous function such that $1 < p^- < p(\cdot) < p^+ < \infty$, and the concentration flux vector $\boldsymbol{q}_c$ satisfies the (7.37), where $\boldsymbol{K}(c, |\boldsymbol{D}(\boldsymbol{v})|) : \mathbb{R}_0^+ \times \mathbb{R}_0^+ \to \mathbb{R}^{d \times d}$ is continuous mapping with $K_{i,j} \in L^\infty(\Omega)$ such that the flux vector fulfills following conditions

$$|\boldsymbol{q}_c(c, \xi, \boldsymbol{D})| \leqslant K_1|\xi|, \tag{7.41}$$

$$\boldsymbol{q}_c(c, \xi, \boldsymbol{D}) \cdot \xi \geqslant K_2\,|\xi|^2. \tag{7.42}$$

Above, $C_1, C_2, K_1, K_2 \in (0, \infty)$ are constants and $\boldsymbol{A} \cdot \boldsymbol{B}$ is notation for the scalar product between two tensors. Moreover, we require that there exists a function

$$\tilde{c}_d \in C^{0,\beta} \cap W^{1,2}(\Omega), \ \beta > 0, \ \text{such that } tr(\tilde{c}_d) = c_d \text{ on } \partial\Omega. \tag{7.43}$$

Now, we are ready to formulate our existence theorem.

THEOREM 7.6. *Let $\Omega \subset \mathbb{R}^d$ be a bounded domain with Lipschitz boundary $\partial\Omega$ and let $p(\cdot)$ be a Hölder continuous variable exponent such that $p^- \leqslant p(\cdot) \leqslant p^+ < \infty$, where $p^- \geqslant \frac{3d}{d+2}$ and $p^- > \frac{d}{2}$. If $\boldsymbol{f} \in W^{-1,p^{-'}}(\Omega)$, $\boldsymbol{S}$ and $\boldsymbol{q}_c$ satisfy conditions (7.38)–(7.42) and there exists a function $\tilde{c}_d$ such that (7.43) holds and*

$$\exists \beta > 0: \ \forall x_0 \in \Omega \ \forall R > 0: \int\limits_{B_R(x_0) \cap \Omega} \frac{|\nabla \tilde{c}_d|^2}{R^{d-2+2\beta}} \leqslant C_3, \quad C_3 \in (0, \infty) \text{ is a constant,}$$

then there exists a weak solution $(\boldsymbol{v}, c)$ of the problem (7.32)–(7.34) satisfying the boundary conditions (7.35) such that

$$\boldsymbol{v} \in W_{0,\text{div}}^{1,1}(\Omega), \quad \boldsymbol{D}(\boldsymbol{v}) \in L^{p(c)}(\Omega),$$

$$(c - \tilde{c}_d) \in C^{0,\alpha}(\Omega) \cap W_0^{1,2},$$

for some $0 < \alpha \leqslant \beta$, α being function of Ω, K_1, K_2, and $(\boldsymbol{v}, c)$ fulfills the following weak formulation of the problem

$$-\int_\Omega \boldsymbol{v} \otimes \boldsymbol{v} \cdot \nabla \boldsymbol{\psi}\,dx + \int_\Omega \boldsymbol{S}(c, \boldsymbol{D}(\boldsymbol{v})) \cdot \boldsymbol{D}(\boldsymbol{\psi})\,dx = \langle \boldsymbol{f}, \boldsymbol{\psi} \rangle \qquad \forall \boldsymbol{\psi} \in W_{0,\text{div}}^{1,p(c)}(\Omega),$$

$$-\int_\Omega \boldsymbol{v}c \cdot \nabla \varphi\,dx + \int_\Omega \boldsymbol{q}_c(c, \nabla c, \boldsymbol{D}(\boldsymbol{v})) \cdot \nabla \varphi\,dx = 0 \qquad \forall \varphi \in W_0^{1,2}(\Omega).$$

To the best of our knowledge, this is the first result concerning the existence of the system (7.32)–(7.34), where the variable exponent is concentration dependent. Since the spaces where we look for the weak solution are "dependent" on the solution itself, we a priory do not know them, and thus, a more general concept of function spaces with variable exponent $p(\cdot)$, the so–called generalized Sobolev Spaces, needs to be involved. Nevertheless, certain restriction on $p(\cdot)$ is required, namely its Hölder continuity, a crucial assumption for the density of smooth functions in generalized Sobolev spaces, embedding theorems and Korn's inequality.

In the case, that the diffusivity matrix in the equation for the concentration is constant, or only concentration dependent, the use of standard theory for Laplace operator, see Ladyzhenskaya and Ural'tseva (1968), ensures the Hölder continuity of the concentration, and thus of the variable exponent. In contrast to Antontsev and Rodrigues (2006), where authors assumed the constant diffusivity matrix for similar equation of thermal diffusion, we assume the diffusivity to be non–constant, and thus, we a priori do not know if the concentration satisfies the Hölder continuity. Nevertheless, this we prove for certain, but not restrictive, assumptions by the introduction of Green test functions in the weak formulation for convection–diffusion equation. The proof of Hölder continuity of concentration is based on the results of de Giorgi (1957) and Nash (1958).

In such setting, we can use the theory of monotone operators to prove the desired existence. Nevertheless, this is restricted to the assumption of $p^- \geqslant \frac{3d}{d+2}$, in 3D setting $p^- \geqslant \frac{9}{5}$, which is required for the convective term $(\boldsymbol{v} \otimes \boldsymbol{v})$ being well defined for the test functions from $W^{1,p(c)}_{0,\mathrm{div}}$. Eventual relaxation of the lower bound of p would require to generalize the approach of Diening et al. (2008), the Lipschitz truncation method.

The second restriction on the minimal value of p in Theorem 7.6, explicitly $p^- > \frac{d}{2}$, comes from the requirement of c being Hölder continuous. The prove of the Hölder continuity is based on de Giorgi result for elliptic equation with measurable coefficients and the right hand side in some $W^{-1,q'}$ space with $q > d$. In our setting this means that we require $\mathrm{div}(c\boldsymbol{v}) \in W^{1,q'}$, which results, using boundedness of c, in $v \in L^q$ for $q > d$, and thus, using the embedding theorem, in the second restriction on p^-.

Proof. The proof presented here is constructive, based on the formulation of Galerkin approximations solving the approximate system. First, we formulate the suitable Galerkin approximations which existence is a direct consequence of the fixed point theorem in finite dimensional space. Then, after establishing the uniform estimates, we present the limit passage from the solutions of the approximative problems to the weak solution. As the last, we identify the limit of non–linear term introduced from $\mathrm{div}\,\boldsymbol{S}$. The proof of Hölder continuity of the concentration is then presented in the Appendix to the chapter.

(n, m)–approximate problem and uniform estimates. Let $\{\boldsymbol{w}_i\}^{\infty}_{i=1}$ be a basis of $W^{1,p^+}_{0,\mathrm{div}}(\Omega)$ such that $\int_{\Omega} \boldsymbol{w}_i \boldsymbol{w}_j \, dx = \delta_{ij}$ and $\{z_j\}^{\infty}_{j=1}$ be a basis of $W^{1,2}_0(\Omega)$, again $\int_{\Omega} z_i z_j \, dx = \delta_{ij}$. Then for positive, fixed $n, m \in \mathbb{N}$ we define the Galerkin approximations

$$(7.44) \qquad \boldsymbol{v}^{n,m} := \sum_{i=1}^{n} \alpha_i^{n,m} \boldsymbol{w}_i, \qquad\qquad c^{n,m} := \sum_{i=1}^{m} \beta_i^{n,m} z_i + \tilde{c}_d,$$

for which $\boldsymbol{\alpha}^{n,m}$ and $\boldsymbol{\beta}^{n,m}$ solve the approximate system

$$(7.45) \qquad -\int_{\Omega} (\boldsymbol{v}^{n,m} \otimes \boldsymbol{v}^{n,m}) \cdot \nabla \boldsymbol{w}_i \, dx + \int_{\Omega} \boldsymbol{S}(c^{n,m}, \boldsymbol{D}(\boldsymbol{v}^{n,m})) \cdot \boldsymbol{D}(\boldsymbol{w}_i) \, dx = \langle \boldsymbol{f}, \boldsymbol{w}_i \rangle$$

$$\forall i = 1, \ldots, n,$$

$$(7.46) \qquad -\int_{\Omega} \boldsymbol{v}^{n,m} c^{n,m} \cdot \nabla z_j \, dx + \int_{\Omega} \boldsymbol{q}_c(c^{n,m}, \nabla c^{n,m}, \boldsymbol{D}(\boldsymbol{v}^{n,m})) \cdot \nabla z_j \, dx = 0$$

$$\forall j = 1, \ldots, m.$$

The application of the fixed point theorem ,which is now standard since (7.45)–(7.46) is finite dimensional problem, will then ensure the existence of its solution $(\boldsymbol{v}^{n,m}, c^{n,m})$.

Now, we shall derive the uniform estimates that are independent of n, m in the corresponding function spaces. For simplicity, we shall use the notation of $\boldsymbol{S}^{n,m} := \boldsymbol{S}(c^{n,m}, \boldsymbol{D}(\boldsymbol{v}^{n,m}))$ and $\boldsymbol{q}_c^{n,m} := \boldsymbol{q}_c(c^{n,m}, \nabla c^{n,m}, \boldsymbol{D}(\boldsymbol{v}^{n,m}))$. Multiplying the i–th equation in (7.45) by $\alpha_i^{n,m}$ and taking the sum over $i = 1, ..., n$, we obtain

$$(7.47) \qquad -\int_\Omega (\boldsymbol{v}^{n,m} \otimes \boldsymbol{v}^{n,m}) \cdot \nabla \boldsymbol{v}^{n,m}\, dx + \int_\Omega \boldsymbol{S}^n \cdot \boldsymbol{D}(\boldsymbol{v}^{n,m})\, dx = \langle \boldsymbol{f}, \boldsymbol{v}^{n,m} \rangle,$$

where the convective term vanishes after integration by parts since $\operatorname{div} \boldsymbol{v}^{n,m} = 0$, and $\boldsymbol{v}^{n,m} = \boldsymbol{0}$ on boundary $\partial\Omega$. Thus, the equation (7.47) reduces to

$$(7.48) \qquad \int_\Omega \boldsymbol{S}^{n,m} \cdot \boldsymbol{D}(\boldsymbol{v}^{n,m})\, dx = \langle \boldsymbol{f}, \boldsymbol{v}^{n,m} \rangle,$$

and further, using the assumptions (7.40), (7.38) and standard duality estimates with Young's[5] and Korn's inequalities on the second term, we obtain that

$$(7.49) \qquad \int_\Omega |\boldsymbol{D}(\boldsymbol{v}^{n,m})|^{p(c^{n,m})}\, dx < C.$$

Next, multiplying the j–th equation in (7.46) by $\beta_j^{n,m}$ and taking the sum over $j = 1, ..., m$ we arrive at

$$(7.50) \qquad -\int_\Omega \boldsymbol{v}^{n,m} c^{n,m} \cdot \nabla(c^{n,m} - \tilde{c}_d)\, dx + \int_\Omega \boldsymbol{q}_c^{n,m} \cdot \nabla(c^{n,m} - \tilde{c}_d)\, dx = 0.$$

Again, the integration by parts of the first term and the assumptions of $\operatorname{div} \boldsymbol{v}^{n,m} = 0$, $\boldsymbol{v}^{n,m} = \boldsymbol{0}$ on $\partial\Omega$ reduce the equation (7.50) to

$$(7.51) \qquad \int_\Omega \boldsymbol{q}_c^{n,m} \cdot \nabla c^{n,m}\, dx = \int_\Omega \boldsymbol{q}_c^{n,m} \cdot \nabla \tilde{c}_d\, dx + \int_\Omega \tilde{c}_d \nabla c^{n,m} \cdot \boldsymbol{v}^{n,m}\, dx.$$

After the use of assumption (7.41), the first therm on right hand side is estimated by the use of the Hölder inequality with $\nabla \tilde{c}_d \in L^2(\Omega)$ and $\nabla c^{n,m} \in L^2(\Omega)$, followed by standard use of Young's inequality. The second term is estimated by the fact that $\tilde{c}_d$ is bounded and thus we can use the Hölder inequality with $\boldsymbol{v}^{n,m} \in L^2(\Omega)$ and $\nabla c^{n,m} \in L^2(\Omega)$ and consequently the Young inequality. All together with assumption (7.42), we arrives at

$$(7.52) \qquad \int_\Omega |\nabla c^{n,m}|^2\, dx < C \|\boldsymbol{v}^{n,m}\|_2^2 \leqslant C,$$

where we estimate the last term by the use of the Korn inequality on (7.49) together with the embedding $W^{1,p^-} \hookrightarrow L^2$ for $p^- \geqslant \frac{2d}{d+2}$.

Moreover, it is easy to show, as a direct consequence of assumption (7.38) and estimates (7.49), (7.52), that

$$(7.53) \qquad \int_\Omega \left(|\boldsymbol{S}^{n,m}|^{p^{+'}} + |\boldsymbol{q}_c^{n,m}|^2 \right) dx \leqslant C.$$

Limit $\boldsymbol{m \to \infty}$. Having the uniform estimate (7.49), the equivalence of norms in the finite dimensional spaces leads to the $|\boldsymbol{\alpha}^{n,m}| \leqslant C(n)$. Then, together with estimate (7.52), we can establish the following $m \to \infty$ convergence results for a suitable sub–sequences (for simplification not relabeled)

$$(7.54) \qquad \boldsymbol{\alpha}^{n,m} \to \boldsymbol{\alpha}^n \qquad \text{strongly in } \mathbb{R}^n,$$

$$(7.55) \qquad c^{n,m} \rightharpoonup c^n \qquad \text{weakly in } W^{1,2}(\Omega),$$

$$(7.56) \qquad \boldsymbol{S}^{n,m} \rightharpoonup \bar{\boldsymbol{S}}^n \qquad \text{weakly in } L^{p^{+'}}(\Omega),$$

$$(7.57) \qquad \boldsymbol{q}_c^{n,m} \rightharpoonup \bar{\boldsymbol{q}}_c^n \qquad \text{weakly in } L^2(\Omega),$$

and thus directly from (7.54) and the compact embedding $W^{1,2}(\Omega) \hookrightarrow\hookrightarrow L^2(\Omega)$ we obtain the convergences results

$$(7.58) \qquad \boldsymbol{v}^{n,m} \to \boldsymbol{v}^n \qquad \text{strongly in } W_{0,\mathrm{div}}^{1,p^+}(\Omega),$$

$$(7.59) \qquad c^{n,m} \to c^n \qquad \text{strongly in } L^2(\Omega).$$

---

[5]Lemma 7.12 in the subsection 7.3.2.

Moreover, since $\boldsymbol{S}$ and $\boldsymbol{q}_c$ are continuous with respect to their unknowns, (7.58)–(7.59) and growth condition on $\boldsymbol{S}$ and $\boldsymbol{q}_c$ imply that

$$(7.60) \qquad \bar{\boldsymbol{S}}^n = \boldsymbol{S}^n := \boldsymbol{S}(c^n, \boldsymbol{D}(\boldsymbol{v}^n))$$

$$(7.61) \qquad \bar{\boldsymbol{q}}_c^n = \boldsymbol{q}_c^n := \boldsymbol{q}_c(c^n, \nabla c^n, \boldsymbol{D}(\boldsymbol{v}^n))$$

Then, the convergence results allows to make the limit passage in the equation set (7.45)–(7.46) and obtain following system

$$(7.62) \qquad -\int_\Omega (\boldsymbol{v}^n \otimes \boldsymbol{v}^n) \cdot \nabla \boldsymbol{w}_i \, dx + \int_\Omega \boldsymbol{S}^n \cdot \boldsymbol{D}(\boldsymbol{w}_i) \, dx = \langle \boldsymbol{f}, \boldsymbol{w}_i \rangle \qquad \forall i = 1, \ldots, n,$$

$$(7.63) \qquad -\int_\Omega \boldsymbol{v}^n c^n \cdot \nabla \varphi \, dx + \int_\Omega \boldsymbol{q}_c^n \cdot \nabla \varphi \, dx = 0 \qquad \forall \varphi \in W_0^{1,2}(\Omega).$$

Minimum and maximum principle and further apriori estimates. Define $z_1^n := (c^n - \min_{x \in \partial\Omega} c_d)_-$ and $z_2^n := (c^n - \max_{x \in \partial\Omega} c_d)_+$, where $(a)_-$ and $(a)_+$ denote the negative and positive parts of a, respectively. It is clear, that functions $z_1^n, z_2^n \in W_0^{1,2}(\Omega)$ since $c^n = c_d$ on $\partial\Omega$, and thus, from (7.63), we get

$$(7.64) \qquad -\int_\Omega \boldsymbol{v}^n c^n \cdot \nabla z_1^n \, dx + \int_\Omega \boldsymbol{q}_c^n \cdot \nabla z_1^n \, dx = 0,$$

and

$$(7.65) \qquad -\int_\Omega \boldsymbol{v}^n c^n \cdot \nabla z_2^n \, dx + \int_\Omega \boldsymbol{q}_c^n \cdot \nabla z_2^n \, dx = 0.$$

Let us consider equation (7.64) at first. Using the fact that $\operatorname{div} \boldsymbol{v}^n = 0$ and that $\boldsymbol{v}^n = \boldsymbol{0}$ on $\partial\Omega$ on the first term, (7.37) and the property of negative part on the second term, we arrive at

$$(7.66) \qquad \int_{\Omega^-} \boldsymbol{v}^n \cdot \nabla c^n z_1^n \, dx + \int_{\Omega^-} K|\nabla c^n|^2 \, dx = 0,$$

where Ω^- is the part of the domain on which $z_1^n < 0$. Next, using that $\nabla c^n = \nabla z_1^n$ on Ω^- and again the extension of ∇c^n from Ω^- on the whole domain Ω by using the negative part, we obtain

$$(7.67) \qquad \int_\Omega \boldsymbol{v}^n \cdot \nabla z_1^n z_1^n \, dx + \int_\Omega K|\nabla z_1^n|^2 \, dx = 0.$$

Applying on the first term the chain rule and then the integration by parts, we find that the first term vanishes, and thus

$$(7.68) \qquad z_1^n = (c^n - \min_{x \in \partial\Omega} c_d)_- = \text{const.} \quad \text{a. e. in } \Omega.$$

Analogous treatment can be used on the equation (7.65) which consequently leads to $z_2^n = (c^n - \max_{x \in \partial\Omega} c_d)_+ = \text{const. a. e. in } \Omega$. Combining both results, we then obtain the boundedness of the concentration c^n

$$(7.69) \qquad \min_{x \in \partial\Omega} c_d \leqslant c^n \leqslant \max_{x \in \partial\Omega} c_d \quad \text{a. e. in } \Omega.$$

Similar to the previous subsection, we can establish further uniform estimates. Multiplying the i–th equation in (7.62) by α_i^n and taking the sum over $i = 1, \ldots, n$, we obtain after integration by parts together with condition (7.40), and using the same arguments on the term with force as above,

$$(7.70) \qquad \int_\Omega (|\boldsymbol{D}(\boldsymbol{v}^n)|^{p(c^n)} + |\boldsymbol{S}^n|^{p'(c^n)}) \, dx \leqslant C,$$

from which, by using the condition (7.38), we arrive at

$$(7.71) \qquad \int_\Omega |\boldsymbol{D}(\boldsymbol{v}^n)|^{p(c^n)} \, dx \leqslant C,$$

and thus

$$(7.72) \qquad \int_\Omega |\boldsymbol{D}(\boldsymbol{v}^n)|^{p^-} \, dx \leqslant C.$$

In equation (7.63) we can already use the approximation c^n as a test function and thus, similar as above, obtain

$$(7.73) \qquad \int_\Omega |\nabla c^n|^2 \leqslant C \, dx.$$

Additionally, it is easy to show from above estimates and (7.41) that

$$(7.74) \qquad \int_\Omega \left(|\boldsymbol{S}^n|^{p^{+\prime}} + |\boldsymbol{q}_c^n|^2 \right) dx \leqslant C \, dx.$$

As proven in the Appendix to the proof, section 7.3, Theorem 7.7, if $\boldsymbol{v}^n \in L_{0,\mathrm{div}}^{d+\delta}$ and $p^- > \frac{d}{2}$ then

$$(7.75) \qquad \|c^n\|_{0,\alpha} \leqslant C \qquad \text{for some } \alpha \leqslant \beta.$$

Limit $n \to \infty$. It follows from the estimates (7.69)–(7.74) that there are $\boldsymbol{v}$ and c to which converge some (again not relabeled) subsequences of approximations $\boldsymbol{v}^n$ and c^n as follows

$$(7.76) \qquad c^n \rightharpoonup c \qquad \text{weakly in } W^{1,2}(\Omega),$$

$$(7.77) \qquad c^n \overset{*}{\rightharpoonup} c \qquad *-\text{weakly in } L^\infty,$$

$$(7.78) \qquad c^n \to c \qquad \text{strongly in } C^{0,\alpha}(\Omega), \ 0 < \alpha \leqslant \beta$$

$$(7.79) \qquad \boldsymbol{v}^n \rightharpoonup \boldsymbol{v} \qquad \text{weakly in } W_{0,\mathrm{div}}^{1,p^-}(\Omega),$$

$$(7.80) \qquad \boldsymbol{S}^n \rightharpoonup \overline{\boldsymbol{S}} \qquad \text{weakly in } L^{p^{+\prime}}(\Omega),$$

$$(7.81) \qquad \boldsymbol{q}_c^n \rightharpoonup \overline{\boldsymbol{q}}_c \qquad \text{weakly in } L^2(\Omega),$$

and thus, from the compact embedding $W_{0,\mathrm{div}}^{1,p^-} \hookrightarrow\hookrightarrow L_{\mathrm{div}}^2$ and above convergences

$$(7.82) \qquad c^n \to c \qquad \text{strongly in } L^q(\Omega), \quad q < \infty$$

$$(7.83) \qquad \boldsymbol{v}^n \to \boldsymbol{v} \qquad \text{strongly in } L_{\mathrm{div}}^2(\Omega).$$

If we unify the limit $\overline{\boldsymbol{S}} = \boldsymbol{S}(c, \boldsymbol{D}(\boldsymbol{v}))$, this convergence results on the second level of the Galerkin approximations allow us to take the limit in the equation (7.62) and (7.63) and obtain

$$(7.84) \qquad -\int_\Omega (\boldsymbol{v} \otimes \boldsymbol{v}) \cdot \nabla \boldsymbol{\psi} \, dx + \int_\Omega \boldsymbol{S}(c, \boldsymbol{D}(v)) \cdot \boldsymbol{D}(\boldsymbol{\psi}) \, dx = \langle \boldsymbol{f}, \boldsymbol{\psi} \rangle \qquad \forall \boldsymbol{\psi} \in W_{0,\mathrm{div}}^{1,p^+}(\Omega),$$

$$(7.85) \qquad -\int_\Omega \boldsymbol{v} c \cdot \nabla \varphi \, dx + \int_\Omega \boldsymbol{q}_c(\nabla c) \cdot \nabla \varphi \, dx = 0 \qquad \forall \varphi \in W_0^{1,2}(\Omega).$$

Identification of the limit $\overline{\boldsymbol{S}}$ and $\overline{\boldsymbol{q}}_c$. Here, we shall show, using theory of monotone operators, that

$$(7.86) \qquad \overline{\boldsymbol{S}} = \boldsymbol{S}(c, \boldsymbol{D}(\boldsymbol{v})) \quad \text{a. e. in } \Omega.$$

Having the limit equation

$$(7.87) \qquad -\int_\Omega (\boldsymbol{v} \otimes \boldsymbol{v}) \cdot \nabla \boldsymbol{\psi} \, dx + \int_\Omega \overline{\boldsymbol{S}} \cdot \boldsymbol{D}(\boldsymbol{\psi}) \, dx = \langle \boldsymbol{f}, \boldsymbol{\psi} \rangle \qquad \forall \boldsymbol{\psi} \in W_{0,\mathrm{div}}^{1,p^+}(\Omega),$$

we need to show that $\overline{\boldsymbol{S}}$ and the convective term $(\boldsymbol{v} \otimes \boldsymbol{v})$ belong to the right dual spaces to obtain final weak formulation for the equation for velocity, and, to be able to use the Minthy method for the limit identification. First, we show that $\overline{\boldsymbol{S}} \in L^{p'(c)}(\Omega)$ and after that $(\boldsymbol{v} \otimes \boldsymbol{v}) \in L^{p'(c)}(\Omega)$.

Let us divide the domain Ω on parts where $|\overline{\boldsymbol{S}}| < 1$ and $|\overline{\boldsymbol{S}}| \geqslant 1$, and denote them in the same manner, then

$$(7.88) \qquad \int_\Omega |\overline{\boldsymbol{S}}|^{p'(c)} \, dx \leqslant \int_{|\overline{\boldsymbol{S}}|<1} |\overline{\boldsymbol{S}}|^{p'(c)} \, dx + \int_{|\overline{\boldsymbol{S}}|\geqslant 1} |\overline{\boldsymbol{S}}|^{p'(c)} \, dx.$$

It is obvious, that first term is bounded by a constant due to the boundedness of the variable exponent itself, $p(\cdot) \in \mathcal{P}(\Omega)$. Next, since

$$(7.89) \qquad c^n \to c \quad \text{in } C^{0,\alpha}(\Omega), \qquad \alpha > 0,$$

and due to the continuity of p, it is valid that

$$(7.90) \qquad \forall \varepsilon > 0 \; \exists N > 0 : \quad \forall n \geqslant N \; |p'(c^n) - p'(c)| \leqslant \frac{\varepsilon}{\Theta},$$

where $\Theta > 1$, large enough to satisfy $p'(c) - \frac{\Theta-1}{\Theta}\varepsilon > 1$. We can then deduce from estimate above that

$$(7.91) \qquad C \geqslant \int_\Omega |\boldsymbol{S}^n|^{p'(c^n)} \, dx \geqslant \int_{|\boldsymbol{S}^n| \geqslant 1} |\boldsymbol{S}^n|^{p'(c^n)} \, dx$$

$$\geqslant \int_{|\boldsymbol{S}^n| \geqslant 1} |\boldsymbol{S}^n|^{p'(c^n)-p'(c)+p'(c)-\varepsilon} \, dx \geqslant \int_{|\boldsymbol{S}^n| \geqslant 1} |\boldsymbol{S}^n|^{p'(c)-\frac{\Theta-1}{\Theta}\varepsilon} \, dx.$$

Then, after adding to the inequality the term $\int_{|\boldsymbol{S}^n|<1} |\boldsymbol{S}^n|^{p'(c)-\frac{\Theta-1}{\Theta}\epsilon} \, dx$, which is bounded by some constant $\bar{C}$, we obtain

$$(7.92) \qquad C + \bar{C} \geqslant \int_{|\boldsymbol{S}^n| \geqslant 1} |\boldsymbol{S}^n|^{p'(c^n)} \, dx + \bar{C} \geqslant \int_\Omega |\boldsymbol{S}^n|^{p'(c)-\frac{\Theta-1}{\Theta}\varepsilon} \, dx.$$

Using the weak lower semicontinuity, we see that

$$(7.93) \qquad \int_\Omega |\overline{\boldsymbol{S}}|^{p'(c)-\frac{\Theta-1}{\Theta}\varepsilon} \, dx \leqslant C,$$

and consequently, the Fatou lemma[6] with $\varepsilon \to 0$ will lead to

$$(7.94) \qquad \int_\Omega |\overline{\boldsymbol{S}}|^{p'(c)} \leqslant C.$$

Next, to have the convective term from admissible space $L^{p'(c)}(\Omega)$, we have to set up a constrain on the lower bound of the variable index p such that $W^{1,p(c)}(\Omega) \hookrightarrow L^{2p'(c)}(\Omega)$. This is exactly the constrain $p(c) \geqslant \frac{3d}{d+2}$, in the 3D setting $p(c) \geqslant \frac{9}{5}$ from Theorem 7.6. Having this, we obtain

$$(7.95) \qquad (\boldsymbol{v} \otimes \boldsymbol{v}) \in L^{p'(c)}(\Omega).$$

Now, since $p(\cdot)$ is Hölder continuous, smooth functions $C^\infty_{0,\mathrm{div}}$ are dense in $W^{1,p(c)}_{0,\mathrm{div}}$[7], we can rewrite the weak formulation of equation for velocity as

$$(7.96) \qquad -\int_\Omega (\boldsymbol{v} \otimes \boldsymbol{v}) \cdot \boldsymbol{D}(\boldsymbol{\psi}) \, dx + \int_\Omega \overline{\boldsymbol{S}} \cdot \boldsymbol{D}(\boldsymbol{\psi}) \, dx = \langle \boldsymbol{f}, \boldsymbol{\psi} \rangle \qquad \forall \boldsymbol{\psi} \in W^{1,p(c)}_{0,\mathrm{div}},$$

and consequently take the velocity $\boldsymbol{v}$ as a test function. Moreover, if we take $\boldsymbol{v}^n$ as a test function in (7.62), the convective terms vanish for both cases, and since

$$(7.97) \qquad \lim_{n\to\infty} \langle \boldsymbol{f}, \boldsymbol{v}^n \rangle = \langle \boldsymbol{f}, \boldsymbol{v} \rangle,$$

by comparison of the right hand sides we obtain

$$(7.98) \qquad \lim_{n\to\infty} \int_\Omega \boldsymbol{S}(c^n, \boldsymbol{D}(\boldsymbol{v}^n)) \cdot \boldsymbol{D}(\boldsymbol{v}^n) \, dx = \int_\Omega \overline{\boldsymbol{S}} \cdot \boldsymbol{D}(\boldsymbol{v}) \, dx.$$

Next, we use Minty method. Indeed, for all $\boldsymbol{\phi} \in C^\infty_{0,\mathrm{div}}(\Omega)$ it is valid that

$$(7.99) \qquad 0 \leqslant \int_\Omega (\boldsymbol{S}(c^n, \boldsymbol{D}(\boldsymbol{v}^n)) - \boldsymbol{S}(c^n, \boldsymbol{D}(\boldsymbol{\phi}))) \cdot (\boldsymbol{D}(\boldsymbol{v}^n) - \boldsymbol{D}(\boldsymbol{\phi}))) \, dx.$$

---

[6]Lemma 7.9 in the subsection 7.3.2.

[7]In fact, we know that smooth functions are dense in $W^{1,p(\cdot)}$, Theorem 7.2. To prove also the density of smooth solenoidal functions, it is enough to apply the Bogovskii lemma in spaces with variable exponents, which holds also for log–continuous exponents as is shown in Diening et al. (2011).

Using the strong convergence (7.82) and Lebesgue dominated convergence theorem 7.8, we obtain that

$$(7.100) \qquad \boldsymbol{S}(c^n, \boldsymbol{D}(\boldsymbol{\phi})) \to \boldsymbol{S}(c, \boldsymbol{D}(\boldsymbol{\phi})) \text{ strongly in } [L^q(\Omega)]^{d \times d}, \ q < \infty.$$

Now, we can take the limit $n \to \infty$ because of the (7.98), the growth condition (7.38) together with the weak convergence of $\boldsymbol{S}(c^n, \boldsymbol{D}(\boldsymbol{v}^n))$ and $\boldsymbol{D}(\boldsymbol{v}^n)$ in the admissible spaces. Thus, we obtain

$$(7.101) \qquad 0 \leqslant \int_\Omega (\overline{\boldsymbol{S}} - S(c, \boldsymbol{D}(\boldsymbol{\phi}))) \cdot (\boldsymbol{D}(\boldsymbol{v}) - \boldsymbol{D}(\boldsymbol{\phi})) \, dx \quad \forall \boldsymbol{\phi} \in W_{0,\mathrm{div}}^{1,p(c)}(\Omega),$$

which is already written for all $\boldsymbol{\phi} \in W_{0,\mathrm{div}}^{1,p(c)}(\Omega)$ since of the density of smooth functions. Then, the Minty trick with test functions $\boldsymbol{\phi} = \boldsymbol{v} \pm \lambda \boldsymbol{w}$, $\lambda > 0$, implies the desired identification $\overline{\boldsymbol{S}} = \boldsymbol{S}(c, \boldsymbol{D}(\boldsymbol{v}))$.

Finally, if $\boldsymbol{S}$ is strictly monotone, it follows from convergences results (7.80) and (7.82) that also $\boldsymbol{D}(\boldsymbol{v}^n) \to \boldsymbol{D}(\boldsymbol{v})$ strongly in $[L^1(\Omega)]^{d \times d}$. Hence, we can use the Lebesgue dominated convergence theorem[8] to identify the limit of $K(c^n, \boldsymbol{D}(\boldsymbol{v}^n))$ and obtain

$$(7.102) \qquad \overline{\boldsymbol{q}}_c = \boldsymbol{q}_c(\boldsymbol{D}(\boldsymbol{v}), \nabla c).$$

$\square$

7.3. Appendix to the proof

7.3.1. Hölder continuity of c^n. In what follows, we shall use notation for $B_r(x)$ denoting an open ball in $\mathbb{R}^d$ with the center at $x \in \Omega$ and fixed radius $r > 0$,

$$(7.103) \qquad B_r(x) \coloneqq \{y \in \mathbb{R}^d : |x - y| < r\}.$$

Moreover, we denote the average of a measurable function f over a set A by

$$(7.104) \qquad \langle f \rangle_A \coloneqq \frac{1}{|A|} \int_A f(x) \, dx,$$

where $|A|$ denotes the measure of the set.

THEOREM 7.7. *(Hölder continuity of concentration) Let $\Omega \subset \mathbb{R}^d$ be a bounded set with Lipschitz boundary and following conditions are satisfied*
for all $\boldsymbol{b} \in \mathbb{R}^d$ there exist constants $C_1, C_2 \in (0, \infty)$ such that

$$(7.105) \qquad K_{ij} \in L^\infty, \qquad |K_{ij}| \leqslant C_1, \qquad K_{ij} b_i b_j \geqslant C_2 |\boldsymbol{b}|^2,$$

$\tilde{c}_d \in W^{1,2}(\Omega)$ such that

$$(7.106) \quad \exists \beta > 0 : \ \forall x_0 \in \Omega \ \forall R > 0 : \int_{B_R(x_0) \cap \Omega} \frac{|\nabla \tilde{c}_d|^2}{R^{d-2+2\beta}} \leqslant C_3, \quad C_3 \in (0, \infty) \text{ is constant},$$

there exists $\delta > 0$ such that $\boldsymbol{v} \in L_{0,\mathrm{div}}^{d+\delta}(\Omega)$.
Then there exists exactly one $c \in W^{1,2}(\Omega)$ such that

$$(7.107) \quad \exists \beta \geqslant \alpha > 0 : \forall x_0 \in \Omega \ \forall R > 0 : \int_{B_R(x_0) \cap \Omega} \frac{|\nabla c|^2}{R^{d-2+2\alpha}} \leqslant C_4(\|\boldsymbol{v}\|_{d+\delta}, \Omega, \beta, C_1, C_2),$$

which fulfills the following weak formulation

$$(7.108) \qquad \int_\Omega (\boldsymbol{K} \nabla c) \cdot \nabla \varphi \, dx = \int_\Omega c \boldsymbol{v} \nabla \varphi \, dx \qquad \forall \varphi \in W_0^{1,2}(\Omega),$$

where α is a function of Ω, C_1, C_2, δ.

---

[8]Lemma 7.8 in the subsection 7.3.2.

The application of Morrey's lemma, see Theorem 7.11, then gives the requested Hölder continuity of c, more precisely $c \in C^{0,\alpha}(\Omega)$ where $0 < \alpha \leqslant \beta$, if $\tilde{c}_d \in C^{0,\beta}(\Omega)$. In the proof of the Theorem 7.7 we shall employ the Green function, thus, let us now recall the fundamental properties that will be used. Reader can find more details and exact proofs in Bensoussan and Frehse (2002), Chapter 1.3.

Let $Q \subset \mathbb{R}^d$ be a ball such that $\Omega \subset\subset Q$ and $x_0 \in \Omega$, then Green function G_{x_0} is the solution of

$$(7.109) \qquad \int_Q a\nabla\phi \cdot \nabla G_{x_0}\, dx = \phi(x_0) \qquad \forall \phi \in C_0^\infty(Q),$$

where $a(x)$ is a matrix $a : \mathbb{R}^d \to \mathbb{R}^{d \times d}$ such that there exist constants $M_1 > 0$ and $M_2 > 0$:

$$(7.110) \qquad M_1|\xi|^2 \geqslant a(x)\xi \cdot \xi \geqslant M_2|\xi|^2, \quad \forall \xi \in \mathbb{R}^d.$$

As can be found in Bensoussan and Frehse (2002), the Green function satisfies

$$(7.111) \qquad G_{x_0} \in W_0^{1,\mu}(Q) \text{ for } 1 \leqslant \mu < \frac{d}{d-1}, \qquad G_{x_0} \in L^\nu(Q) \text{ for } 1 \leqslant \nu < \frac{d}{d-2},$$

$$(7.112) \qquad C_1|x - x_0|^{2-d} \leqslant G_{x_0}(x) \leqslant C_2|x - x_0|^{2-d}, \ \forall x \in \overline{\Omega},$$

where C_1, C_2 depend only on M_1, M_2.

Since of the singularity at x_0, G_{x_0} does not belong to $W^{1,2}$ neither to L^∞. This is the reason we shall work with the approximations of the Green function $G_{x_0}^n \in W_0^{1,2}(Q) \cap L^\infty(Q)$ obtained as solution of

$$(7.113) \qquad \int_Q a\nabla\varphi \cdot \nabla G_{x_0}^n = \langle\varphi\rangle_{B_{1/n}(x_0) \cap Q} \qquad \forall \varphi \in W_0^{1,2}(Q).$$

For such approximations, we can then recognize that

$$(7.114) \qquad G_{x_0}^n \to G_{x_0} \qquad \text{strongly in } W^{1,2}(Q_{\varepsilon_1}) \ \forall \varepsilon_1 > 0,$$

$$(7.115) \qquad G_{x_0}^n \to G_{x_0} \qquad \text{strongly in } W^{1,\frac{d}{d-1}-\varepsilon_2}(Q) \ \forall \varepsilon_2 > 0,$$

where $Q_{\varepsilon_1} := Q \setminus B_{\varepsilon_1(x_0)}$.

Proof of Theorem 7.7. Again, let $Q \subset \mathbb{R}^d$ be a ball such that $\Omega \subset\subset Q$, and, let us fix $R_0 > 0$ such that $B_{4R_0}(x_0) \subset Q$ for all $x_0 \in \Omega$. In what follows, we shall always assume $R \in (0, R_0)$.

We define a smooth non–negative cut–off function $\tau_R \in C_0^\infty(Q)$ such that

$$(7.116) \qquad 0 \leqslant \tau_R \leqslant 1, \quad |\nabla\tau_R| \leqslant \frac{C}{R}, \quad \tau_R := \begin{cases} 1 & \text{in } B_R(x_0), \\ 0 & \text{in } \Omega \setminus B_{2R}(x_0), \end{cases}$$

and we shall call the corresponding annulus by $A_R(x_0) := B_{2R}(x_0) \setminus B_R(x_0)$.

As a suitable test function in the weak formulation (7.108) we choose

$$(7.117) \qquad \varphi(x) = \begin{cases} (c - c_R)\tau_R^2 G_{x_0}^n & \text{if } B_{2R}(x_0) \subset \Omega, \\ (c - \tilde{c}_d)\tau_R^2 G_{x_0}^n & \text{otherwise}, \end{cases}$$

which obviously belongs to $W_0^{1,2}(\Omega)$. Recalling (7.108)

$$(7.118) \qquad \underbrace{\int_\Omega \boldsymbol{K}\nabla c \cdot \nabla\varphi\, dx}_{LS} = \underbrace{\int_\Omega c\boldsymbol{v} \cdot \nabla\varphi\, dx}_{RS},$$

we shall first derive the uniform estimates for right hand side (RS), and after for left hand side (LS). Moreover, for now, we assume that $B_{2R}(x_0) \subset \Omega$.

After integration by parts, we obtain

$$(7.119) \qquad RS = -\int_\Omega \nabla c \cdot \boldsymbol{v}(c - c_R)\tau_R^2 G_{x_0}^n\, dx = -\frac{1}{2}\int_\Omega \nabla(c - c_R)^2 \cdot \boldsymbol{v}\tau_R^2 G_{x_0}^n\, dx$$

$$= \frac{1}{2}\int_\Omega (c - c_R)^2 \boldsymbol{v} \cdot (\tau_R\nabla\tau_R G_{x_0}^n + \tau_R^2\nabla G_{x_0}^n)\, dx,$$

and thus the limit $n \to \infty$, involving the properties of τ_R, $\boldsymbol{v} \in L_{0,\mathrm{div}}^{d+\delta}(\Omega)$ and the strong convergence of the Green function approximations, leads to

$$(7.120) \qquad \lim_{n \to \infty} RS = \frac{1}{2} \int_\Omega (c - c_R)^2 \boldsymbol{v} \cdot (\tau_R \nabla \tau_R G_{x_0} + \tau_R^2 \nabla G_{x_0}) \, dx$$

$$\leqslant C \|c\|_\infty \left(\int_{A_R(x_0)} |\boldsymbol{v}| \frac{G_{x_0}}{R} \, dx + \int_{B_{2R}(x_0)} |\boldsymbol{v}||\nabla G_{x_0}| \, dx \right)$$

$$\leqslant C \|c\|_\infty \left(R^{1-d} \int_{A_R(x_0)} |\boldsymbol{v}| \, dx + \int_{B_{2R}(x_0)} |\boldsymbol{v}||\nabla G_{x_0}| \, dx \right).$$

Now, since

$$(7.121) \qquad 1 - \frac{d}{d+\delta} > 0 \qquad \text{and} \qquad (d+\delta)' < \frac{d}{d-1},$$

we can use the Hölder inequality on both terms and obtain

$$(7.122) \qquad \lim_{n \to \infty} RS \leqslant C \|c\|_\infty \|\boldsymbol{v}\|_{d+\delta} \left(R^{1-d} |A_R(x_0)|^{1/(d+\delta)'} + \|\nabla G_{x_0}\|_{(d+\delta)'} \right)$$

$$\leqslant C \|c\|_\infty \|\boldsymbol{v}\|_{d+\delta} R^{1 - \frac{d}{d+\delta}} \leqslant C(\|c\|_\infty, \|\boldsymbol{v}\|_{d+\delta}) R^\gamma,$$

where $\gamma \ll 1$ depends on δ. From above we obtain a restriction on lower bound of variable index, $p^- > \frac{d}{2}$, since we require $W^{1,p^-} \hookrightarrow L^{d+\delta}$.

Now, let us focus on the left hand side of the equation (7.118). By simple calculations we have

$$(7.123) \qquad LS = \int_\Omega \boldsymbol{K} \, |\nabla c|^2 \, \tau_R^2 G_{x_0}^n \, dx + 2 \int_\Omega \boldsymbol{K} \nabla c (c - c_R) \tau_R \nabla \tau_R G_{x_0}^n \, dx$$

$$+ \int_\Omega \boldsymbol{K} \nabla c (c - c_R) \tau_R^2 \nabla G_{x_0}^n \, dx,$$

where the last term can be estimated by

$$(7.124) \qquad \int_\Omega \boldsymbol{K} \nabla c (c - c_R) \tau_R^2 \nabla G_{x_0}^n \, dx =$$

$$\underbrace{\frac{1}{2} \int_\Omega \boldsymbol{K} \nabla \left(|c - c_R|^2 \, \tau_R^2 \right) \nabla G_{x_0}^n \, dx}_{\geqslant 0} - \int_\Omega \boldsymbol{K} \, |c - c_R|^2 \, \tau_R \nabla \tau_R \nabla G_{x_0}^n \, dx$$

$$\geqslant - \int_{A_R(x_0)} \boldsymbol{K} \, |c - c_R|^2 \, \tau_R \nabla \tau_R \nabla G_{x_0}^n \, dx$$

$$\geqslant - \int_{A_R(x_0)} \boldsymbol{K} \, |c - c_R|^2 \, \tau_R (\nabla \tau_R)^2 G_{x_0}^n \, dx - \int_{A_R(x_0)} \boldsymbol{K} |c - c_R|^2 \tau_R \frac{\left| \nabla G_{x_0}^n \right|^2}{G_{x_0}^n} \, dx,$$

where we used the Young inequality and the the sign comes from the definition of the Green function (7.113) with a test function $\varphi = |c - c_R|^2 \tau_R^2$. Now, we can proceed with the limit $n \to \infty$ by using Fatou lemma since of the non–negativity of $G_{x_0}^n$

$$(7.125) \qquad \lim_{n \to \infty} LS \geqslant C \underbrace{\int_\Omega \frac{|\nabla c|^2 \tau_R^2}{|x - x_0|^{d-2}}}_{I_1} - C \underbrace{\int_{A_R(x_0)} \frac{|\nabla c||c - c_R|}{R^{d-1}} \, dx}_{I_2}$$

$$- C \underbrace{\int_{A_R(x_0)} \frac{|c - c_R|^2}{R^d} \, dx}_{I_3} - C \underbrace{\int_{A_R(x_0)} \frac{|c - c_R|^2 |\nabla G_{x_0}|^2}{G_{x_0}} \, dx}_{I_4}.$$

On the integral I_2 we can use the Hölder inequality with $\nabla c / R^{\frac{d-2}{2}} \in L^2$ and $|c - c_R|/R^{d/2} \in L^2$, Young's inequality and consequently the Poincaré inequality[9] and together with the

---

[9] Lemma 7.10 in the subsection 7.3.2.

integral I_3, estimated by the Poincaré inequality as well, we obtain the estimate

$$(7.126) \qquad -I_2 - I_3 \geqslant C \int_{A_R(x_0)} \frac{|\nabla c|^2}{R^{d-2}} \, dx.$$

The last integral I_4 has to be treated more carefully since it obtains ∇G_{x_0} for which we have no explicit estimate. Here, we have to use the definition of the Green function (7.109) with a suitably chosen test function which will give us the required term of I_4. Nevertheless, we have to extra treat the singularity of G_{x_0} at x_0. That we can manage by introducing a new cut–off function such as

$$(7.127) \qquad 0 \leqslant \eta_R \leqslant 1, \quad |\nabla \eta_R| \leqslant \frac{C}{R}, \quad \eta_R := \begin{cases} 1 & \text{in } A_R(x_0), \\ 0 & \text{in } B_{R/2}(x_0) \text{ and } Q \setminus B_{4R}(x_0). \end{cases}$$

Again, we define the annulus $A_R^\star(x_0) = B_{4R}(x_0) \setminus B_{R/2}(x_0)$.

Now, in the definition of G_{x_0}, equation (7.109), we take

$$(7.128) \qquad \phi = G_{x_0}^{-1/2} |c - c_R|^2 \eta_R^2,$$

which is suitably chosen since integral I_4 can be estimated by

$$(7.129) \quad I_4 \leqslant C \int_{A_R(x_0)} \frac{|c - c_R|^2 |\nabla G_{x_0}|^2}{G_{x_0}^{3/2}} G_{x_0}^{1/2} \, dx \leqslant C \int_{A_R(x_0)} \frac{|c - c_R|^2 |\nabla G_{x_0}|^2}{G_{x_0}^{3/2}} \frac{\eta_R^2}{R^{\frac{d-2}{2}}} \, dx,$$

and, recalling that $\phi(x_0) = 0$, we have from the definition of Green function

$$(7.130)$$
$$0 = \int_Q \boldsymbol{K} \nabla G_{x_0} \cdot \nabla (G_{x_0}^{-1/2} |c - c_R|^2 \eta_R^2) \, dx$$
$$= -\frac{1}{2} \int_Q \boldsymbol{K} \nabla G_{x_0} G_{x_0}^{-3/2} \cdot \nabla G_{x_0} |c - c_R|^2 \eta_R^2 \, dx + 2 \int_Q \boldsymbol{K} \nabla G_{x_0} \cdot G_{x_0}^{-1/2} \nabla \eta_R |c - c_R|^2 \eta_R \, dx$$
$$+ 2 \int_Q \boldsymbol{K} \nabla G_{x_0} \cdot G_{x_0}^{-1/2} (c - c_R) \nabla c \, \eta_R^2 \, dx.$$

Using the equality above and Young's inequality with ϵ sufficiently small, we can estimate

$$(7.131)$$
$$\int_Q \frac{|\nabla G_{x_0}|^2}{G_{x_0}^{3/2}} |c - c_R|^2 \eta_R^2 \, dx$$
$$\leqslant C \int_{A_R^\star(x_0)} \frac{|\nabla G_{x_0}|}{G_{x_0}^{1/2}} \left(\frac{|c - c_R|^2 \eta_R}{R} + |c - c_R| |\nabla c| \eta_R^2 \right) dx$$
$$\leqslant C \int_{A_R^\star(x_0)} \left(\frac{|\nabla G_{x_0}|^2 |c - c_R|^2 \eta_R^2}{G_{x_0}^{3/2}} \right)^{1/2} \left(\frac{G_{x_0}^{1/4} (c - c_R)}{R} + G_{x_0}^{1/4} |\nabla c| \eta_R \right) dx$$
$$\leqslant C \left(\frac{2}{\epsilon} \int_Q \frac{|\nabla G_{x_0}|^2 |c - c_R|^2 \eta_R^2}{G_{x_0}^{3/2}} \, dx + \int_{A_R^\star(x_0)} \frac{G_{x_0}^{1/2} |c - c_R|^2}{R^2} \, dx + \int_{A_R^\star(x_0)} G_{x_0}^{1/2} |\nabla c|^2 \eta_R^2 \, dx \right).$$

All together, the integral I_4 reads

$$(7.132) \quad I_4 \leqslant \int_{A_R^\star(x_0)} \frac{|\nabla G_{x_0}|^2 |c - c_R|^2}{R^{\frac{d-2}{2}} G_{x_0}^{3/2}} \, dx$$
$$\leqslant C \int_{A_R^\star(x_0)} \left(\frac{|c - c_R|^2}{R^2 |x - x_0|^{d-2}} + \frac{|\nabla c|^2}{|x - x_0|^{d-2}} \right) dx \leqslant C \int_{A_R^\star(x_0)} \frac{|\nabla c|^2}{|x - x_0|^{d-2}} \, dx$$

where we used the Poincaré inequality[10], on the last estimate.

---

[10] In fact, we wrote the Poincaré inequality, Lemma 7.10, for a ball, nevertheless, for the annulus, the lemma holds as well.

Now, we can reconstruct the estimate for the whole equation (7.118), for simplification we write $C = C(\|c\|_\infty, \|\boldsymbol{v}\|_{d+\delta})$,

$$(7.133) \qquad \int_{B_R(x_0)} \frac{|\nabla c|^2}{|x - x_0|^{d-2}}\, dx - C^\star \int_{A_R^\star(x_0)} \frac{|\nabla c|^2}{|x - x_0|^{d-2}}\, dx \leqslant LS = RH \leqslant CR^\gamma,$$

and thus
(7.134)

$$\int_{B_{R/2}(x_0)} \frac{|\nabla c|^2}{|x - x_0|^{d-2}}\, dx \leqslant \int_{B_R(x_0)} \frac{|\nabla c|^2}{|x - x_0|^{d-2}}\, dx \leqslant CR^\gamma + C^\star \int_{A_R^\star(x_0)} \frac{|\nabla c|^2}{|x - x_0|^{d-2}}\, dx.$$

In the case of $B_{2R}(x_0) \nsubseteq \Omega$, we test the equation (7.108) by $\varphi(x) = (c - \tilde{c}_d)\tau_R^2\, G_{x_0}^n$, where $c = \tilde{c}_d$ in $Q \setminus \Omega$, and by using the same arguments as above we obtain
(7.135)

$$\int_{B_{R/2}(x_0)} \frac{|\nabla c|^2}{|x - x_0|^{d-2}}\, dx \leqslant CR^\gamma + C^\star \int_{A_R^\star(x_0)} \frac{|\nabla c|^2}{|x - x_0|^{d-2}}\, dx + \int_{B_{4R}(x_0)} \frac{|\nabla \tilde{c}_d|^2}{|x - x_0|^{d-2}}\, dx.$$

Here, let us estimate the last term with $\tilde{c}_d$. Indeed, it is valid that

$$(7.136) \qquad \int_{B_{4R}(x_0)} \frac{|\nabla \tilde{c}_d|^2}{|x - x_0|^{d-2}}\, dx = \sum_{k=1}^\infty \int_{A_k} \frac{|\nabla \tilde{c}_d|^2}{|x - x_0|^{d-2}}\, dx,$$

where $A_k = A_{R_k}(x_0) := B_{R_{k-1}}(x_0) \setminus B_{R_k}(x_0)$, $R_k := \frac{4R}{2^k}$. Now, since the integral are expressed for the annuli, we can extimate

$$
\int_{B_{4R}(x_0)} \frac{|\nabla \tilde{c}_d|^2}{|x - x_0|^{d-2}}\, dx = \sum_{k=1}^\infty \int_{A_k} \frac{|\nabla \tilde{c}_d|^2}{|x - x_0|^{d-2}}\, dx \leqslant C \sum_{k=1}^\infty \int_{B_{2R_k}} \frac{|\nabla \tilde{c}_d|^2}{R_k^{d-2}}\, dx
$$

$$(7.137) \qquad \overset{(7.106)}{\leqslant} C \sum_{k=1}^\infty R_k^{2\beta} \leqslant R^{2\beta} C \sum_{k=1}^\infty \left(\frac{4}{2^k}\right)^{2\beta} \leqslant CR^{2\beta},$$

where we used the assumption (7.106) on $\tilde{c}_d$ of the Theorem 7.7.

Thus, all together, for all $R < R_0$ holds

$$(7.138) \qquad \int_{B_{R/2}(x_0)} \frac{|\nabla c|^2}{|x - x_0|^{d-2}}\, dx \leqslant CR^{\gamma + 2\beta} + C^\star \int_{A_R^\star(x_0)} \frac{|\nabla c|^2}{|x - x_0|^{d-2}}\, dx.$$

Since the second term on the right hand side is still derived for the annulus $A_R^\star(x_0)$, we need to fill the "hole" of $B_{R/2}(x_0)$ to obtain the final estimate. Adding the term

$$(7.139) \qquad C^\star \int_{B_{R/2}(x_0)} \frac{|\nabla c|^2}{|x - x_0|^{d-2}}\, dx$$

to both sides of the above inequality we get

$$(7.140) \qquad \int_{B_{R/2}(x_0)} \frac{|\nabla c|^2}{|x - x_0|^{d-2}}\, dx \leqslant CR^{\gamma + 2\beta} + \frac{C^\star}{1 + C^\star} \int_{B_{4R}(x_0)} \frac{|\nabla c|^2}{|x - x_0|^{d-2}}\, dx.$$

Dividing the above inequality by $(R/2)^{2\alpha}$ with some $2\alpha < \gamma + 2\beta$ yields
(7.141)

$$\int_{B_{R/2}(x_0)} \frac{1}{(R/2)^{2\alpha}} \frac{|\nabla c|^2}{|x - x_0|^{d-2}}\, dx \leqslant CR^{\gamma + 2\beta - 2\alpha} + \frac{8^{2\alpha} C^\star}{1 + C^\star} \int_{B_{4R}(x_0)} \frac{1}{(4R)^{2\alpha}} \frac{|\nabla c|^2}{|x - x_0|^{d-2}}\, dx$$

and by choosing 2α such that $\frac{8^{2\alpha} C^\star}{1 + C^\star} \leqslant 1$ we arrive at

$$(7.142) \qquad \int_{B_R(x_0)} \frac{1}{R^{2\alpha}} \frac{|\nabla c|^2}{|x - x_0|^{d-2}}\, dx \leqslant CR^{\gamma + 2\beta - 2\alpha} + \int_{B_{8R}(x_0)} \frac{1}{(8R)^{2\alpha}} \frac{|\nabla c|^2}{|x - x_0|^{d-2}}\, dx.$$

Let us denote $\vartheta := \gamma + 2\beta - 2\alpha$ and define

$$(7.143) \qquad r_k := \frac{R_0}{8^k}, \qquad\qquad a_k := \int_{B_{r_k}(x_0)} \frac{|\nabla c|^2}{r_k^{2\alpha}|x - x_0|^{d-2}}\, dx,$$

then from (7.142) we have

$$(7.144) \qquad a_{k+1} \leqslant C r_{k+1}^{\vartheta} + a_k \leqslant C R_0^{\vartheta} 8^{-k\vartheta} + a_k \leqslant C R_0^{\vartheta} \sum_{m=0}^{k} 8^{-m\vartheta} + a_0 \leqslant C R_0^{\vartheta} + a_0,$$

and thus

$$(7.145) \qquad \int_{B_{r_{k+1}}(x_0)} \frac{|\nabla c|^2}{r_{k+1}^{2\alpha} |x - x_0|^{d-2}} \, dx \leqslant C R_0^{\vartheta} + C \int_{B_{R_0}(x_0)} \frac{|\nabla c|^2}{R_0^{2\alpha} |x - x_0|^{d-2}} \, dx.$$

where $C = C(\|c\|_\infty, \|\boldsymbol{v}\|_{d+\delta}, R_0, \beta, \gamma)$

Let $R \in (0, R_0)$ be arbitrary, then we can find $k \in \mathbb{N}$ such that $r_{k+1} \leqslant R < r_k$. Consequently, we get

$$(7.146) \qquad \int_{B_R(x_0)} \frac{|\nabla c|^2}{R^{d-2+2\alpha}} \, dx \leqslant \int_{B_{r_k}(x_0)} \frac{|\nabla c|^2}{R^{d-2+2\alpha}} \leqslant \left(\frac{r_k}{R}\right)^{d-2+2\alpha} \int_{B_{r_k}(x_0)} \frac{|\nabla c|^2}{r_k^{d-2+2\alpha}}$$

$$\leqslant \left(\frac{r_k}{r_{k+1}}\right)^{d-2+2\alpha} a_k \leqslant 8^{k(d-2+2\alpha)} a_k \leqslant C,$$

where for the last inequaltiy we used (7.144). Thus, by using the Morrey's lemma[11] we obtain desired

$$(7.147) \qquad c \in C^{0,\alpha}(\Omega) \quad \text{for some } \alpha < \frac{\gamma}{2} + \beta.$$

$\square$

7.3.2. Auxiliary lemmas. Here, we list the mostly used lemmas for the theory of this chapter. We write the lemmas without proofs, nevertheless, we note the suitable references where they can be found.

LEMMA 7.8 (Lebesgue dominated convergence theorem, Lebesgue (1909)). *Let $\{f_k\}_{k\in\mathbb{N}} \subset L^1(\Omega)$ be a sequence converging a.e. to some f and $|f_k(x)| \leqslant g(x)$ for some $g \in L^1(\Omega)$. Then $f \in L^1(\Omega)$ and*

$$\lim_{k\to\infty} \int_A f_k(x) \, dx = \int_A f(x) \, dx$$

for any measurable $A \subset \Omega$.

LEMMA 7.9 (Fatou's lemma, Fatou (1906)). *Let $g \in L^1(\Omega)$ and $\{f_k\}_{k\in\mathbb{N}} \subset L^1(\Omega)$ be a sequence of non–negative functions such that $f_k \geqslant g$ a. e. for all $n \in \mathbb{N}$, then*

$$\int_\Omega \liminf_{n\to\infty} f_k \, dx \leqslant \liminf_{n\to\infty} \int_\Omega f_k \, dx.$$

LEMMA 7.10 (Poincaré inequality on a ball, Poincaré (1890)). *Let $f \in W^{1,2}(\Omega)$, and let ball $B_R \subset \Omega$, then*

$$\int_{B_R} |f - \langle f \rangle_{B_R}|^2 \, dx \leqslant C R^2 \int_{B_R} |\nabla f|^2 \, dx.$$

LEMMA 7.11 (Morrey's lemma, Morrey (1966), Theorem 3.5.2.). *Let $\Omega \subset \mathbb{R}^d$, $d > 1$, and $f \in W^{1,2}(\Omega)$. If there exist for each compact $K \subset \Omega$ constants $M, \alpha > 0$, $R \leqslant dist(K, \partial\Omega)$ such that*

$$\int_{B_r(a)} |\nabla f|^2 \, dx \leqslant M r^{d-2+2\alpha}$$

for all $a \in K$ and every $r \in (0, R)$, then $f \in C^{0,\alpha}(\Omega)$.

---

[11]Lemma 7.11 in the subsection 7.3.2.

LEMMA 7.12 (Algebraic Young's inequality). *Let a, b be non–negative real numbers, then*

$$\forall \varepsilon > 0: \quad ab \leqslant \varepsilon a^p + C_\varepsilon b^{p'}, \quad C_\varepsilon := \frac{\varepsilon^{1/p-1} \, p^{1/p'}}{p-1}.$$

Chapter 8

Numerical methods

The main aim of this work is the modeling of the flow of synovial fluid in the viscous regime, thus, we shall focus on description of numerical methods for the case of viscous fluids. At the end of this chapter we shall briefly comment the principal changes for the computations concerning the viscoelastic rheology.

First, we focus on the description of the numerical discretization of the system of equations we will use in the next chapters for computational simulations. Then, we describe the convection dominated problem typical for synovial fluid and introduce three different stabilization method for equation of concentration. These methods shall be then compared at once.

8.1. System of equations

Once again, let us recall the system of governing equations

$$\frac{\partial \boldsymbol{v}}{\partial t} + [\operatorname{grad} \boldsymbol{v}]\boldsymbol{v} = -\operatorname{grad} p + \frac{2}{\operatorname{Re}} \operatorname{div}\left(\mu(c, |\boldsymbol{D}|^2)\boldsymbol{D}\right), \tag{8.1}$$

$$\operatorname{div} \boldsymbol{v} = 0, \tag{8.2}$$

$$\frac{\partial c}{\partial t} + (\operatorname{grad} c) \cdot \boldsymbol{v} = \frac{1}{\operatorname{Pe}} \operatorname{div}\left(D_c(c, |\boldsymbol{D}|^2) \operatorname{grad} c\right), \tag{8.3}$$

where $\boldsymbol{v}, p, c$ is the velocity, pressure and concentration, respectively, μ, D_c is the non–constant generalized viscosity and diffusivity, and $\boldsymbol{D}$ denotes the symmetric part of the gradient of velocity. The domain where this system is considered, is bounded set in $\mathbb{R}^d$ ($d = 2, 3$) denoted by Ω with the Lipschitz boundary $\partial\Omega$. For description of the numerical methods we use in our computational simulations, we prescribe the Dirichlet and Neumann boundary conditions for velocity on parts of boundary Γ_{D}^v and Γ_{N}^v, respectively. It is assumed, that $\partial\Omega = \overline{\Gamma_{\mathrm{D}}^v \bigcup \Gamma_{\mathrm{N}}^v}$ and $\Gamma_{\mathrm{D}}^v \bigcap \Gamma_{\mathrm{N}}^v = \emptyset$. We can make such boundary decomposition for concentration as well, it means $\partial\Omega = \overline{\Gamma_{\mathrm{D}}^c \bigcup \Gamma_{\mathrm{N}}^c}$ and $\Gamma_{\mathrm{D}}^c \bigcap \Gamma_{\mathrm{N}}^c = \emptyset$, where the Dirichlet and Neumann boundary conditions for the concentration are prescribed. Explicitly, we consider

$$\begin{aligned}(\boldsymbol{v}(t,x) \cdot \boldsymbol{n})\boldsymbol{n} &= \boldsymbol{v}_1(t,x) \quad \text{on } \Gamma_{\mathrm{D}}^v, \qquad & c(t,x) &= c_D(t,x) \quad \text{on } \Gamma_{\mathrm{D}}^c, \\ \boldsymbol{v}_\tau(t,x) &= \boldsymbol{v}_2(t,x) \quad \text{on } \Gamma_{\mathrm{D}}^v,\end{aligned} \tag{8.4}$$

$$[\boldsymbol{T}(t,x)]\boldsymbol{n} = \boldsymbol{g}^v(t,x) \quad \text{on } \Gamma_N^v, \qquad \boldsymbol{q}_c(t,x) \cdot \boldsymbol{n} = g^c(t,x) \quad \text{on } \Gamma_N^c, \tag{8.5}$$

where $\boldsymbol{n}$ is the unit outward normal to the boundary and $\boldsymbol{v}_\tau = \boldsymbol{v} - (\boldsymbol{v} \cdot \boldsymbol{n})\boldsymbol{n}$. The Neumann boundary condition for velocity is prescribed by the condition for the whole Cauchy stress tensor $\boldsymbol{T} = -p\boldsymbol{I} + \frac{2}{\operatorname{Re}}\mu(c, |\boldsymbol{D}|^2)\boldsymbol{D}$, and in the case of concentration it is determined by the diffusive flux $\boldsymbol{q}_c = \frac{1}{\operatorname{Pe}}D_c(c, |\boldsymbol{D}|^2) \operatorname{grad} c$. These conditions are more physical since we determine on the boundary the physical force density and concentration flux, respectively. For now, we assume that $\operatorname{meas}(\Gamma_{\mathrm{N}}^v) \neq \emptyset$, otherwise we would have to additionally introduce extra pressure condition.

The time interval of interest is $I = \langle 0, T \rangle$, for which beginning time we have initial conditions $\boldsymbol{v}(0, x) = \boldsymbol{v}_0$ and $c(0, x) = c_0$ for all $x \in \Omega$. We emphasize, that the domain Ω and boundary parts Γ_{D}^v, Γ_{N}^v, Γ_{D}^c and Γ_{N}^c do not change with time.

In what follows, we describe the numerical method suitable for solving this system. First, we discretize the system in time by finite differences method, and then, after obtaining the stationary set of equations for each time step, we use the finite element method for discretizing the space.

8.2. Time discretization

For the time discretization of the system (8.1)–(8.3) we use θ–scheme, specifically the Crank–Nicholson scheme see e. g. Douglas Jr et al. (1970), Turek et al. (2006), which is described as follows. We divide the time interval I into n time steps $\langle t^k, t^{k+1} \rangle$, for $k = 0, ..., n-1$, where $t^0 = 0$ and $t^n = T$. The step length of interval $\langle t^k, t^{k+1} \rangle$ is then $\Delta t^k = t^{k+1} - t^k$. Approximating the time derivatives by the central differences–like quotient

$$(8.6) \qquad \frac{\partial f}{\partial t} \approx \frac{f(t^{k+1}) - f(t^k)}{\Delta t^k},$$

the θ–scheme applied on the system (8.1)–(8.3) leads to set of equations

$$(8.7) \qquad \boldsymbol{v}^{k+1} + \theta_1 \Delta t^k \left([\nabla \boldsymbol{v}^{k+1}] \boldsymbol{v}^{k+1} - \frac{2}{\mathrm{Re}} \operatorname{div} \left(\mu(c^{k+1}, |\boldsymbol{D}(\boldsymbol{v}^{k+1})|^2) \boldsymbol{D}(\boldsymbol{v}^{k+1})) \right) \right)$$
$$+ \Delta t^k \nabla p^{k+1}$$
$$= \boldsymbol{v}^k - \theta_2 \Delta t^k \left([\nabla \boldsymbol{v}^k] \boldsymbol{v}^k - \frac{2}{\mathrm{Re}} \operatorname{div} \left(\mu(c^k, |\boldsymbol{D}(\boldsymbol{v}^k)|^2) \boldsymbol{D}(\boldsymbol{v}^k)) \right) \right),$$

$$(8.8) \qquad \operatorname{div} \boldsymbol{v}^{k+1} = 0,$$

$$(8.9) \qquad c^{k+1} + \theta_1 \Delta t^k \left(\nabla c^{k+1} \cdot \boldsymbol{v}^{k+1} - \frac{1}{\mathrm{Pe}} \operatorname{div}(D_c(c^{k+1}, |\boldsymbol{D}(\boldsymbol{v}^{k+1})|^2) \nabla c^{k+1}) \right)$$
$$= c^k - \theta_2 \Delta t^k \left(\nabla c^k \cdot \boldsymbol{v}^k - \frac{1}{\mathrm{Pe}} \operatorname{div}(D_c(c^k, |\boldsymbol{D}(\boldsymbol{v}^k)|^2) \nabla c^k) \right),$$

expressed at each discrete time t^k, $k = 0, ..., n-1$. Here, notation of z^k represents $z(t^k)$ and $\theta_1 + \theta_2 = 1$. By choosing the values of θ_1 and θ_2, not necessarily the same for the equation of velocity and concentration, we are determining what scheme is used. For $\theta_1 = \theta_2 = 1/2$ we obtain Crank–Nicholson, while the backward and forward (implicit and explicit) Euler schemes are obtained for $\theta_1 = 1$, $\theta_2 = 0$ and $\theta_1 = 0$, $\theta_2 = 1$, respectively. Even though the Crank–Nicholson scheme is conditionally stable, we use it in our computations since it is a second–order method. For the incompressibility constraint and the pressure we use the implicit treatment which gives better stability properties and is consistent with the full space–time finite element method discretization.

At this point, the set of equations (8.7)–(8.9) can be considered as a set of stationary partial differential equations at a given time t^k.

8.3. Discretization in space

In order to use the finite element method on equations (8.7)–(8.9), we have to formulate them in a weak form by the means of test functions from appropriate spaces. The finite element method is based on the discretization of these spaces to finite dimensional spaces, and thus, the transformation of the partial differential equations to the set of algebraic equations, see e. g. Johnson (1987), Eriksson et al. (1996) or Feistauer et al. (2003).

Let us define the function spaces $\boldsymbol{V}$, P and C as

$$(8.10) \qquad \boldsymbol{V} = \{ \boldsymbol{v} \in [W^{1,2}(\Omega)]^d;\ \boldsymbol{v}|_{\Gamma_{\mathrm{D}}^v} = \boldsymbol{0} \},$$

$$(8.11) \qquad P = L^2(\Omega),$$

$$(8.12) \qquad C = \{ c \in W^{1,2}(\Omega);\ c|_{\Gamma_{\mathrm{D}}^c} = 0 \}.$$

Moreover, before the introduction of the weak formulation, we have to treat the non–homogeneous boundary conditions for velocity and concentration. We assume that there exist functions $\boldsymbol{v}^\star \in [W^{1,2}(\Omega)]^d$ and $c^\star \in W^{1,2}(\Omega)$ such that they satisfy in sense of traces the Dirichlet boundary conditions (8.4) on Γ_D^v, Γ_D^c, respectively.

Then, independently on the choice of particular $\boldsymbol{v}^\star$ and $c^\star$, the weak formulation for each time step $k = 0, \ldots, n-1$ with $t^n = T$, reads: find $(\boldsymbol{v}^{k+1} - \boldsymbol{v}^\star, p^{k+1}, c^{k+1} - c^\star) \in \boldsymbol{V} \times P \times C$ such that

$$(8.13) \quad (\boldsymbol{v}^{k+1}, \boldsymbol{\varphi})_\Omega + \theta_1 \Delta t^k \left([\nabla \boldsymbol{v}^{k+1}] \boldsymbol{v}^{k+1}, \boldsymbol{\varphi} \right)_\Omega$$

$$+ \theta_1 \Delta t^k \frac{2}{\mathrm{Re}} \left(\mu \left(c^{k+1}, |\boldsymbol{D}(\boldsymbol{v}^{k+1})|^2 \right) \boldsymbol{D}(\boldsymbol{v}^{k+1}), \nabla \boldsymbol{\varphi} \right)_\Omega$$

$$- \Delta t^k (p^{k+1}, \mathrm{div}\, \boldsymbol{\varphi})_\Omega - \theta_1 \Delta t^k \left(\boldsymbol{g}^v(t^{k+1}), \boldsymbol{\varphi} \right)_{\Gamma_N^v}$$

$$= (\boldsymbol{v}^k, \boldsymbol{\varphi})_\Omega - \theta_2 \Delta t^k \left([\nabla \boldsymbol{v}^k] \boldsymbol{v}^k, \boldsymbol{\varphi} \right)_\Omega - \theta_2 \Delta t^k \frac{2}{\mathrm{Re}} \left(\mu(c^k, |\boldsymbol{D}(\boldsymbol{v}^k)|^2) \boldsymbol{D}(\boldsymbol{v}^k), \nabla \boldsymbol{\varphi} \right)_\Omega$$

$$+ \theta_2 \Delta t^k \left(\boldsymbol{g}^v(t^k), \boldsymbol{\varphi} \right)_{\Gamma_N^v}$$

$$\forall \boldsymbol{\varphi} \in \boldsymbol{V},$$

$$(8.14) \quad (\mathrm{div}\, \boldsymbol{v}^{k+1}, \zeta)_\Omega = 0$$

$$\forall \zeta \in P,$$

$$(8.15) \quad (c^{k+1}, \psi)_\Omega + \theta_1 \Delta t^k \left(\nabla c^{k+1} \cdot \boldsymbol{v}^{k+1}, \psi \right)_\Omega$$

$$+ \theta_1 \Delta t^k \frac{1}{\mathrm{Pe}} \left(D_c(c^{k+1}, |\boldsymbol{D}(\boldsymbol{v}^{k+1})|^2) \nabla c^{k+1}, \nabla \psi \right)_\Omega - \theta_2 \Delta t^k \left(g^c(t^{k+1}), \psi \right)_{\Gamma_N^c}$$

$$= (c^k, \psi)_\Omega - \theta_2 \Delta t^k \left(\nabla c^k \cdot \boldsymbol{v}^k, \psi \right)_\Omega - \theta_2 \Delta t^k \frac{1}{\mathrm{Pe}} \left(D_c(c^k, |\boldsymbol{D}(\boldsymbol{v}^k)|^2) \nabla c^k, \nabla \psi \right)_\Omega$$

$$+ \theta_2 \Delta t^k \left(g^c(t^k), \psi \right)_{\Gamma_N^c}$$

$$\forall \psi \in C,$$

where $\boldsymbol{v}^0$ and c^0 are the corresponding initial conditions. Moreover, we assume the fluxes to be functions $\boldsymbol{g}^v \in [L^2(\Gamma_N^v)]^d$, $g^c \in L^2(\Gamma_N^c)$. As standard, we denote the scalar product in $L^2(\Omega)$ by $\int_\Omega fg = (f, g)_\Omega$.

The last piece we need for discretization of the function spaces $\boldsymbol{V}$, P and C, are the domain and boundary approximation and their following discretization. Let us cover the domain Ω by the set of quadrilaterals denoted by $\mathcal{T}_h$, suitably approximating the boundary $\partial\Omega$ by polygonal boundary $\partial\Omega_h$. The approximating domain Ω_h is then defined by the boundary $\partial\Omega_h$. Since the appropriate approximation of the domain is just technical but very lengthy, we, for simplicity, assume that the Ω has polygonal boundary itself, $\Omega_h \equiv \Omega$, and thus, no approximation of the boundary is needed. The elements of $\mathcal{T}_h$ are denoted by K and additionally we define parameter h by

$$(8.16) \qquad\qquad h := \max_{K \in \mathcal{T}_h} h_K,$$

where h_K is, in a suitable sense, a size-measure of the element K, the longest size of all elements edges, for example. We require that the mesh fulfills standard regularity conditions, in more detail in Ciarlet (1978), which are the local shape regularity and exclusion of hanging nodes. The first one guaranties that with $h \to 0$ the mesh elements shrink uniformly, precisely $h_K/d_K < C$ for all $K \in \mathcal{T}_h$, where d_K is the diameter of the largest ball inscribed into K and C being a constant. The second requirement guaranties that any two elements are either disjoint or have common whole edge or vertex.

Now, we can define the finite element spaces $\boldsymbol{V}_h$, P_h and C_h. Since we are dealing with incompressible fluid, the combination of velocity and pressure finite element spaces has to satisfy the Babuška–Brezzi stability condition (Babuška (1973) or Brezzi and Fortin (1991)) which guaranties the solvability of the coupled discrete system. Our choice (from many) is the Q_2, P_1^{disc} pair, the biquadratic and discontinuous linear polynomial spaces, chosen from computational and simplicity reasons. Moreover, they are known to be stable since, beyond

others, the incompressibility constrain is satisfied locally in the weak sense, it means as an "average" on each element of the mesh, see Elman et al. (2005). The definition of the finite element spaces is then as follows

(8.17) $$\boldsymbol{V}_h = \{\boldsymbol{v} \in [C(\Omega)]^d;\ \boldsymbol{v}|_K \in [Q_2(K)]^d \quad \forall K \in \mathcal{T}_h\},$$

(8.18) $$P_h = \{p \in L^2(\Omega);\ p|_K \in P_1^{\mathrm{disc}}(K) \quad \forall K \in \mathcal{T}_h\},$$

(8.19) $$C_h = \{c \in C(\Omega);\ c|_K \in Q_2(K) \quad \forall K \in \mathcal{T}_h\},$$

and for the treatment of Dirichlet boundary conditions we also define

(8.20) $$\boldsymbol{V}_{0h} = \{\boldsymbol{v} \in \boldsymbol{V}_h;\ \boldsymbol{v}|_{\Gamma_D^v} = \boldsymbol{0}\},$$

(8.21) $$C_{0h} = \{c \in C_h;\ c|_{\Gamma_D^c} = 0\},$$

where $Q_2(K)$ and $Q_1(K)$ denote the space of biquadratic, bilinear functions on the quadrilateral element K, respectively, and $P_1^{\mathrm{disc}}(K)$ denotes the space of linear functions on K, without the requirement of continuity between adjacent elements. All finite element spaces are conforming, since $\boldsymbol{V}_h \subset [W^{1,2}(\Omega)]^d$, $P_h \subset L^2(\Omega)$ and $C_h \subset W^{1,2}(\Omega)$.

The approximations of $\boldsymbol{v}^{k+1}$, p^{k+1} and c^{k+1} are $\boldsymbol{v}_h^{k+1}$, p_h^{k+1} and c_h^{k+1}, such that $\boldsymbol{v}_h^{k+1} - \boldsymbol{v}_h^\star \in \boldsymbol{V}_h$, $p_h^{k+1} \in P_h$ and $c_h^{k+1} - c_h^\star \in C_h$, where $\boldsymbol{v}_h^\star \in \boldsymbol{V}_h$ and $\boldsymbol{v}_h^\star|_{\Gamma_D^v} = \boldsymbol{v}_1 + \boldsymbol{v}_2$ and analogously $c_h^\star \in C_h$ and $c_h^\star|_{\Gamma_D^c} = c_D$, satisfying the discrete form of the equations (8.13)–(8.15)

(8.22) $$\begin{aligned}
(\boldsymbol{v}_h^{k+1}, \boldsymbol{\varphi})_\Omega &+ \theta_1 \Delta t^k \left([\nabla \boldsymbol{v}_h^{k+1}] \boldsymbol{v}_h^{k+1}, \boldsymbol{\varphi}\right)_\Omega \\
&+ \theta_1 \Delta t^k \frac{2}{\mathrm{Re}} \left(\mu\left(c_h^{k+1}, |\boldsymbol{D}(\boldsymbol{v}_h^{k+1})|^2\right) \boldsymbol{D}(\boldsymbol{v}_h^{k+1}), \nabla \boldsymbol{\varphi}\right)_\Omega \\
&- \Delta t^k (p_h^{k+1}, \mathrm{div}\,\boldsymbol{\varphi})_\Omega - \theta_1 \Delta t^k \left(\boldsymbol{g}^v(t^{k+1}), \boldsymbol{\varphi}\right)_{\Gamma_N^v} \\
&= (\boldsymbol{v}_h^k, \boldsymbol{\varphi})_\Omega - \theta_2 \Delta t^k \left([\nabla \boldsymbol{v}_h^k] \boldsymbol{v}_h^k, \boldsymbol{\varphi}\right)_\Omega \\
&- \theta_2 \Delta t^k \frac{2}{\mathrm{Re}} \left(\mu(c_h^k, |\boldsymbol{D}(\boldsymbol{v}_h^k)|^2) \boldsymbol{D}(\boldsymbol{v}_h^k), \nabla \boldsymbol{\varphi}\right)_\Omega + \theta_2 \Delta t^k \left(\boldsymbol{g}^v(t^k), \boldsymbol{\varphi}\right)_{\Gamma_N^v} \\
&\hspace{9cm} \forall \boldsymbol{\varphi} \in \boldsymbol{V}_{0h},
\end{aligned}$$

(8.23) $$(\mathrm{div}\,\boldsymbol{v}_h^{k+1}, \zeta)_\Omega = 0$$
$$\forall \zeta \in P_h,$$

(8.24) $$\begin{aligned}
(c_h^{k+1}, \psi)_\Omega &+ \theta_1 \Delta t^k \left(\nabla c_h^{k+1} \cdot \boldsymbol{v}_h^{k+1}, \psi\right)_\Omega \\
&+ \theta_1 \Delta t^k \frac{1}{\mathrm{Pe}} (D_c(c_h^{k+1}, |\boldsymbol{D}(\boldsymbol{v}_h^{k+1})|^2) \nabla c_h^{k+1}, \nabla \psi)_\Omega - \theta_1 \Delta t^k \left(g^c(t^k), \psi\right)_{\Gamma_N^c} \\
&= (c_h^k, \psi)_\Omega - \theta_2 \Delta t^k \left(\nabla c_h^k \cdot \boldsymbol{v}_h^k, \psi\right)_\Omega - \theta_2 \Delta t^k \frac{1}{\mathrm{Pe}} (D_c(c_h^k, |\boldsymbol{D}(\boldsymbol{v}_h^k)|^2) \nabla c_h^k, \nabla \psi)_\Omega \\
&+ \theta_2 \Delta t^k \left(g^c(t^k), \psi\right)_{\Gamma_N^c} \\
&\hspace{9cm} \forall \psi \in C_{0h},
\end{aligned}$$

for each time step $k = 1, \ldots, n-1$ with $t^n = T$.

Since the functions spaces $\boldsymbol{V}_h(\boldsymbol{V}_{0h})$, P_h and $C_h(C_{0h})$ have finite dimensions, it is equivalent to satisfy the equations (8.22)–(8.24) only for the bases functions of these spaces. Then, we obtain a finite system of non–linear algebraic equations, written in matrix form as

(8.25) $$\begin{aligned}
\left(\mathbf{M}_v + \theta_1 \Delta t^k \mathbf{A}_v(\mathbf{v}^{k+1}, \mathbf{c}^{k+1})\right) \mathbf{v}^{k+1} - \Delta t^k \mathbf{B}^T \mathbf{p}^{k+1} &= \boldsymbol{f}(\mathbf{v}^k, \mathbf{c}^k), \\
\mathbf{B}\mathbf{v}^{k+1} &= 0, \\
\left(\mathbf{M}_c + \theta_1 \Delta t^k \mathbf{A}_c(\mathbf{v}^{k+1})\right) \mathbf{c}^{k+1} &= \boldsymbol{g}(\mathbf{v}^k, \mathbf{c}^k)
\end{aligned}$$

where $\mathbf{v}^{k+1}$ represents the vector of coefficients obtained by expanding $\boldsymbol{v}_h^{k+1}$ in bases of $\boldsymbol{V}_h$, analogously for $\mathbf{p}^{k+1}$ and $\mathbf{c}^{k+1}$. Next, $\mathbf{M}_v$ and $\mathbf{M}_c$ represent the corresponding mass matrices, $\mathbf{B}$ is the discrete divergence operator, $\mathbf{A}_v(\mathbf{v}, \mathbf{c})$ and $\mathbf{A}_c(\mathbf{v})$ are the operators representing the convection and dissipation/diffusion parts of the corresponding equations and $\boldsymbol{f}$ and $\boldsymbol{g}$ are the non–linear vector functions of vectors from the previous time level. All together, we have $(\dim \boldsymbol{V}_h + \dim P_h + \dim C_h)$ equations, where $(\dim \boldsymbol{V}_h + \dim P_h + \dim C_h) - (\dim \boldsymbol{V}_{0h} + $

$\dim P_h + \dim C_{0h}$) is the number of equations representing the Dirichlet boundary conditions. The system of (8.25) we need to solve for each time step, with initial conditions represented by $\mathbf{v}^0$ and $\mathbf{c}^0$.

If the exact solution is regular enough, the finite element method as we described above is of convergence of order $p+1$, p being the polynomial degree of the approximation functions, as $h \to 0$

8.4. Computational algorithm

Let us discuss the algorithm of solution of the algebraic problem (8.25) for one time step. It will be useful to write the algebraic system of equations (8.25) in a more compact way as

$$(8.26) \qquad\qquad \boldsymbol{\mathcal{F}}(\bar{\mathbf{x}}) = 0,$$

where $\bar{\mathbf{x}} = (\mathbf{v}^{k+1}, \mathbf{p}^{k+1}, \mathbf{c}^{k+1})$ is the sought vector at the time step $k+1$, and $\boldsymbol{\mathcal{F}}$ is the non-linear operator representing the discrete system of equations (8.25). In our case, $\boldsymbol{\mathcal{F}}$ is differentiable and have invertible first derivative $\frac{\partial \boldsymbol{\mathcal{F}}}{\partial \mathbf{x}}$ since the Babuška–Brezzi condition is satisfied and all the non–linear terms are continuous in $\mathbf{x}$.

We solve the system (8.26) by using the iterative quasi–Newton method, see for example Kelley (1995), Kelley (2003). For the $n+1$ iteration step it can be formulated as

$$(8.27) \qquad\qquad \mathbf{x}^{n+1} = \mathbf{x}^n - \omega^n \left[\frac{\partial \boldsymbol{\mathcal{F}}}{\partial \mathbf{x}}(\mathbf{x}^n) \right]^{-1} \boldsymbol{\mathcal{F}}(\mathbf{x}^n),$$

where the parameter $\omega^n \in (0, 1\rangle$ is the damping factor improving the convergence of the Newton method. If the initial guess $\mathbf{x}^{n=0}$ is sufficiently close to the solution $\bar{\mathbf{x}}$, the Newton method gives a quadratic convergence, but on the other hand, a poor initial estimate can contribute to its non–convergence. The parameter ω^n is then implemented to ensure the global convergence by adaptively changing the length of the correction vector $\left[\frac{\partial \boldsymbol{\mathcal{F}}}{\partial \mathbf{x}}(\mathbf{x}^n) \right]^{-1} \boldsymbol{\mathcal{F}}(\mathbf{x}^n)$ being sought by standard line search algorithm, for detail see Deuflhard (2004). Of course, this is at the cost of decrease in order of convergence.

The block structure of the Jacobian matrix $\frac{\partial \boldsymbol{\mathcal{F}}}{\partial \mathbf{x}}$ is

$$(8.28) \qquad\qquad \frac{\partial \boldsymbol{\mathcal{F}}}{\partial \mathbf{x}}(\mathbf{x}) = \begin{pmatrix} \boxtimes & \boxtimes & \boxtimes \\ \boxtimes & 0 & 0 \\ \boxtimes & 0 & \boxtimes \end{pmatrix},$$

where each of its blocks $\boxtimes$ is sparse. This is due to the standard bases selection of the particular finite element spaces. Since we need to compute the derivative $\frac{\partial \boldsymbol{\mathcal{F}}}{\partial \mathbf{x}}$ at each iteration step, it is convenient to approximate the matrix by finite differences from the residual vector $\boldsymbol{\mathcal{F}}(\mathbf{x})$ which is possible because of the matrix sparsity. We write the approximation for $[\frac{\partial \boldsymbol{\mathcal{F}}}{\partial \mathbf{x}}]_{ij}$ which is linearization of i-th equation in j-th unknown

$$(8.29) \qquad\qquad \left[\frac{\partial \boldsymbol{\mathcal{F}}}{\partial \mathbf{x}} \right]_{ij}(\mathbf{x}) \approx \frac{[\boldsymbol{\mathcal{F}}]_i(\mathbf{x} + \varepsilon^n \mathbf{e}_j) - [\boldsymbol{\mathcal{F}}]_i(\mathbf{x} - \varepsilon^n \mathbf{e}_j)}{2\varepsilon^n},$$

where $\mathbf{e}_j$ are the unit bases vectors in $\mathbb{R}^m$, with m being the dimension of the vector $\mathbf{x}$, explicitly $m = \dim(\boldsymbol{V}_h \times P_h \times C_h)$, and coefficients ε^n are adaptively taken according to the change in the solution in the previous step.

One iteration of the used method can be summarized in the following steps:

1. Let $\mathbf{x}^n$ be some initial guess.
2. Set the residuum vector $\mathbf{r}^n = \boldsymbol{\mathcal{F}}(\mathbf{x}^n)$ and the Jacobian matrix $\mathbf{A} = \frac{\partial \boldsymbol{\mathcal{F}}}{\partial \mathbf{x}}(\mathbf{x}^n)$.
3. Solve $\mathbf{A}\boldsymbol{\delta} = \mathbf{r}^n$ for the correction $\boldsymbol{\delta}$.
4. Find optimal step length ω^n.
5. Update the solution $\mathbf{x}^{n+1} = \mathbf{x}^n - \omega^n \boldsymbol{\delta}$.

At the step #3 in the quasi–Newton method, the linear problem has to be solved. This can done by either the direct solver or iterative solver with preconditioning. In our case, with two–dimensional problem, we use sparse direct solver UMFPACK, see for example Davis (2004).

8.5. Convection–dominated problem

The straightforward numerical discretization described above works well for moderate values of Reynolds and Péclet numbers. In the case of synovial fluid, the Reynolds number is small due to small velocities and relatively high viscosity. On the other hand, the diffusivity of hyaluronan in synovial fluid is extremely small, as described in Chapter 4, and thus very high Péclet numbers are typical for the considered convection–diffusion equation. Due to these reasons, the discretization of equation for velocity behaves as expected, while the algebraic system corresponding to concentration does not meet desired matrix properties and thus the numerical solution exhibits non–physical effects.

Numerical solution of parabolic equation of convection–diffusion with small diffusivity shows spurious oscillations (usually originated at sharp layers) causing that the concentration becomes locally negative and the sharp layers of the approximate solution are delocalized. This completely numeric feature, worsening with the growing domination of convection, arises from the form of the matrix $\mathbf{A}_c(\mathbf{v})$ associated with the convection and diffusion terms. This phenomena is well known, see for example Johnson (1982) .

Let us demonstrate the structure of convection–diffusion matrix $\mathbf{A}_c(\mathbf{v})$ of convection–dominated problem in one–dimensional case of steady state convection-diffusion equation

$$(8.30) \qquad vc' - \frac{1}{\text{Pe}}c'' = 0,$$

with the given constant velocity v and diffusivity $D_c(c, |\mathbf{D}|^2)$ being constant D, and, for instance, zero boundary conditions on both ends of the considered one–dimensional domain. After discretization of the weak form of (8.30) by piecewise bilinear Q_1 functions on quadrilateral mesh with element size h, one gets the algebraic system

$$(8.31) \qquad \mathbf{A}_c(v)\mathbf{c} = 0,$$

with

$$\mathbf{A}_c(v) =$$

$$\frac{v}{2h}\begin{pmatrix} 1 & 0 & 0 & \dots & & \\ -1 & 0 & +1 & 0 & \dots & \\ 0 & -1 & 0 & +1 & 0 & \dots \\ & & & \ddots & & \end{pmatrix} + \frac{D}{h^2}\begin{pmatrix} 1 & 0 & 0 & \dots & & \\ -1 & 2 & -1 & 0 & \dots & \\ 0 & -1 & 2 & -1 & 0 & \dots \\ & & & \ddots & & \end{pmatrix}.$$

Here, the first row of the matrix $\mathbf{A}_c(v)$ corresponds to the boundary condition. From this scheme, it is clear that for $|v|h > 2D$ the matrix is not diagonally dominant (the absolute value of diagonal matrix entry is smaller than the sum of absolute values of non–diagonal entries), and thus, by most iterative methods the convergence of (8.31) is not guaranteed. This relation corresponds to the well known condition laid on Péclet number $\text{Pe} = L^* V^* / D_c^* \approx v/D$ claiming, that it has to be small enough to avoid non–physical phenomena in the solution. There is another thing one should notice, the refinement of the mesh and the choice of the approximation functions of higher order can positively influence the properties of $\mathbf{A}_c(\mathbf{v})$ as well, hence the solvability of (8.31).

For illustration of the plausible numerical oscillations, we present simple two–dimensional computations of the evolutionary non–coupled system

$$(8.32) \qquad \frac{\partial \mathbf{v}}{\partial t} + [\nabla \mathbf{v}]\mathbf{v} = -\nabla p + 2\frac{1}{\text{Re}}\,\text{div}\,\mathbf{D},$$

$$(8.33) \qquad \text{div}\,\mathbf{v} = 0,$$

$$(8.34) \qquad \frac{\partial c}{\partial t} + \nabla c \cdot \mathbf{v} = +\frac{1}{\text{Pe}}\Delta c,$$

assuming viscosity and diffusivity to be constants. The set of equations is considered on $I \times \Omega$, $I = \langle 0, 100 \rangle$ and $\Omega = \langle -1, 1 \rangle \times \langle -1, 1 \rangle$ square. We prescribe the boundary conditions
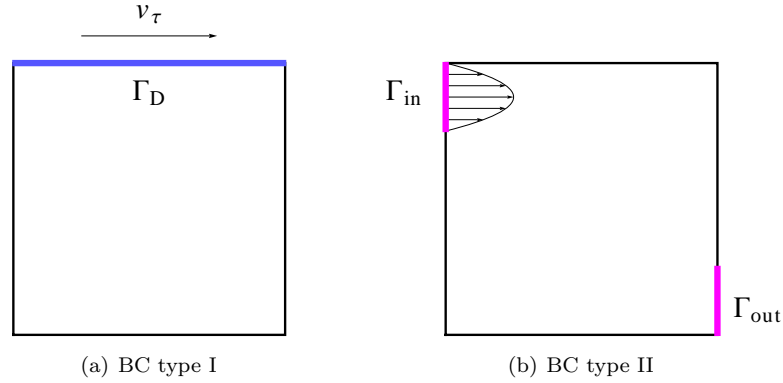
FIGURE 8.1. Boundary conditions; (a) driven cavity type of boundary conditions – on upper plate is prescribed tangential velocity and constant concentration, the rest of the boundary is the wall; (b) inflow/outflow test – on Γ_{in} is prescribed the velocity inlet and Dirichlet condition for concentration, on Γ_{out} is velocity and concentration outlet, the rest of the boundary is the wall. Under wall we understand type of boundary where the no–slip for the velocity and zero normal flux for concentration are prescribed.

of two types, as depicted in Fig. 8.1

$$(8.35) \quad \text{BC I} \begin{cases} \boldsymbol{v} \cdot \boldsymbol{n} = 0 & \text{on } \Gamma_{\text{D}} \\ \boldsymbol{v}_\tau = (x-1)(x+1)\boldsymbol{\tau} \\ c = 0.5 \\ \boldsymbol{v} = \boldsymbol{0} & \text{on } \Gamma \setminus \Gamma_{\text{D}} \\ \boldsymbol{q}_c \cdot \boldsymbol{n} = 0. \end{cases} \quad \text{BC II} \begin{cases} \boldsymbol{v} \cdot \boldsymbol{n} = -v_{in} & \text{on } \Gamma_{\text{in}} \\ \boldsymbol{v}_\tau = \boldsymbol{0} \\ c = 0.5 \\ [\boldsymbol{T}]\boldsymbol{n} = \boldsymbol{0} & \text{on } \Gamma_{\text{out}} \\ \boldsymbol{q}_c \cdot \boldsymbol{n} = 0 \\ \boldsymbol{v} = \boldsymbol{0} & \text{on } \Gamma \setminus \Gamma_{\text{D}} \\ \boldsymbol{q}_c \cdot \boldsymbol{n} = 0 \end{cases}$$

Using the standard Galerkin finite element method we get following computational results, see Fig. 8.2 and Fig. 8.4, for both mentioned boundary conditions. Simulations were computed for three different diffusivities and refinements of the mesh. The fashion of the solutions is visible at first sight. With higher diffusivity the Galerkin method produces oscillations even for very fine mesh and the values of concentration drops below zero or are higher than the concentration value on boundary Γ_D/Γ_{in} for all cases. The overshoot and undershoot of concentration is represented by pink/violet color. The situation worsen even more for function approximations of lower order, compare in Fig. 8.3 and Fig. 8.5. Standardly, as in the case of results presented in Fig. 8.2 and Fig. 8.4, we use the Q_2 approximations – piecewise biquadratic polynomials.

It is obvious, that for problems of dominated convection, like in the case of synovial fluid with physical diffusivity of hyaluronan in order of $10^{-7}\text{cm}^2/\text{s}$, one has to stabilize the whole system by suitable tools which should eliminate the spurious oscillations but should not significantly change the character of resulting solution. A number of stabilization methods for finite element method has been developed to overcome these typical numerical problems. Today, the most frequently used stabilization methods are the stream–line diffusion method introduced by Hughes and Brooks in 1979, also called streamline upwind Petrov–Galerkin (SUPG), and the Galerkin least squares (GLS) method. We shall, besides these two, introduce another alternative, the continuous interior penalty (CIP) method.

8.6. Streamline upwind Petrov–Galerkin method

The SUPG method (Johnson (1982), Hughes and Franca (1989), Fries and Matthies (2006)) is motivated by the finite difference method applied on parabolic equation and

(a) Pe $= 10^4$, $h = h_0$ (b) Pe $= 10^5$, $h = h_0$ (c) Pe $= 10^6$, $h = h_0$

(d) Pe $= 10^4$, $h = \frac{h_0}{2}$ (e) Pe $= 10^5$, $h = \frac{h_0}{2}$ (f) Pe $= 10^6$, $h = \frac{h_0}{2}$

(g) Pe $= 10^4$, $h = \frac{h_0}{4}$ (h) Pe $= 10^5$, $h = \frac{h_0}{4}$ (i) Pe $= 10^6$, $h = \frac{h_0}{4}$
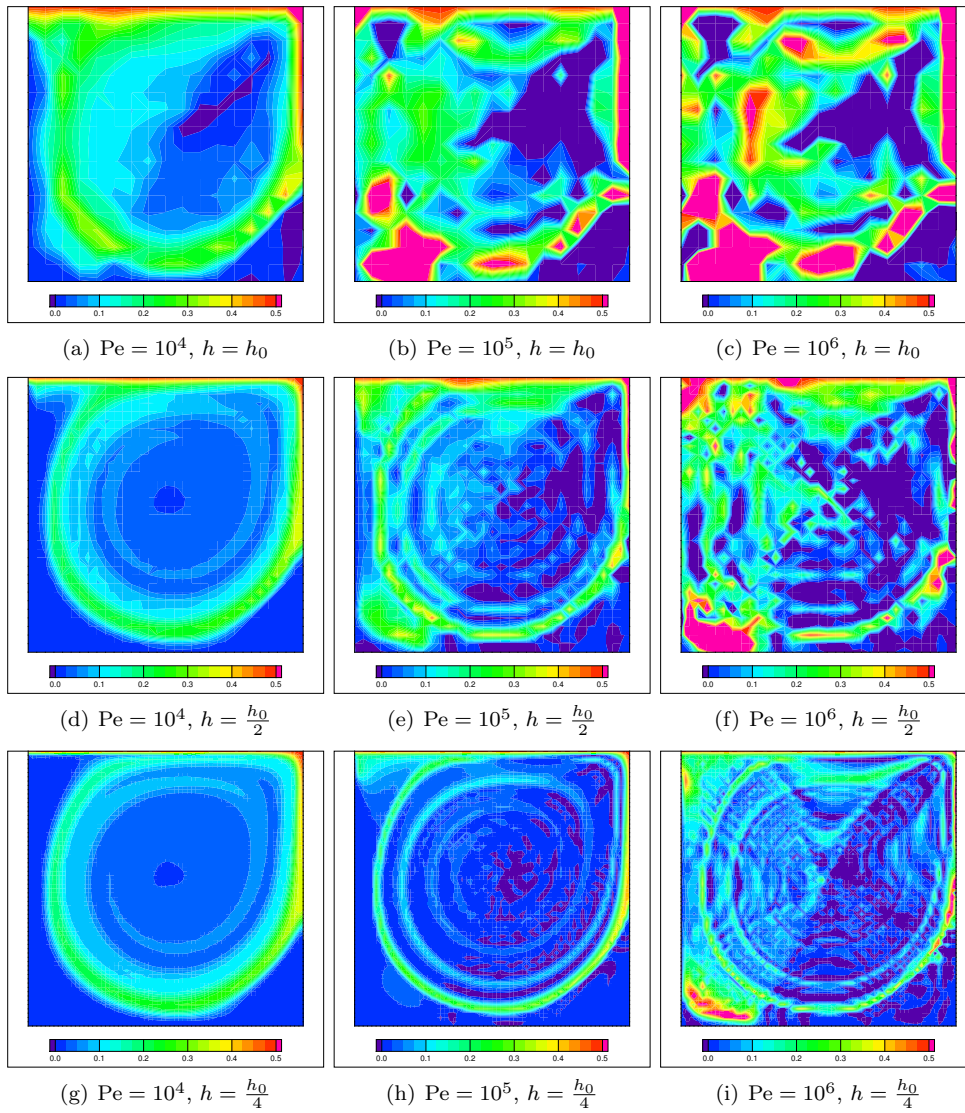
FIGURE 8.2. Computational results of concentration distribution for boundary conditions of type BC I – without stabilization; plotted at time $t = 50$.

(a) Q_1 (b) Q_2
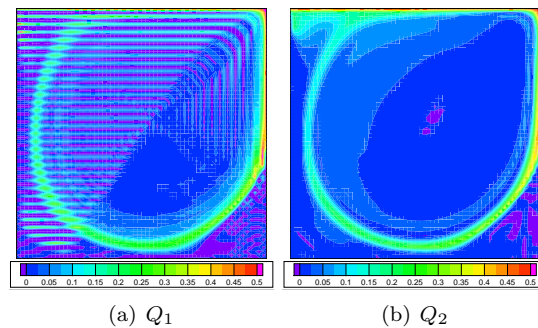
FIGURE 8.3. Comparison of results obtained by Q_1 and Q_2 approximations, Pe $= 10^5$, $h = \frac{h_0}{4}$ at $t = 50$.

(a) Pe $= 10^4$, $h = h_0$ (b) Pe $= 10^5$, $h = h_0$ (c) Pe $= 10^6$, $h = h_0$

(d) Pe $= 10^4$, $h = \frac{h_0}{2}$ (e) Pe $= 10^5$, $h = \frac{h_0}{2}$ (f) Pe $= 10^6$, $h = \frac{h_0}{2}$

(g) Pe $= 10^4$, $h = \frac{h_0}{4}$ (h) Pe $= 10^5$, $h = \frac{h_0}{4}$ (i) Pe $= 10^6$, $h = \frac{h_0}{4}$
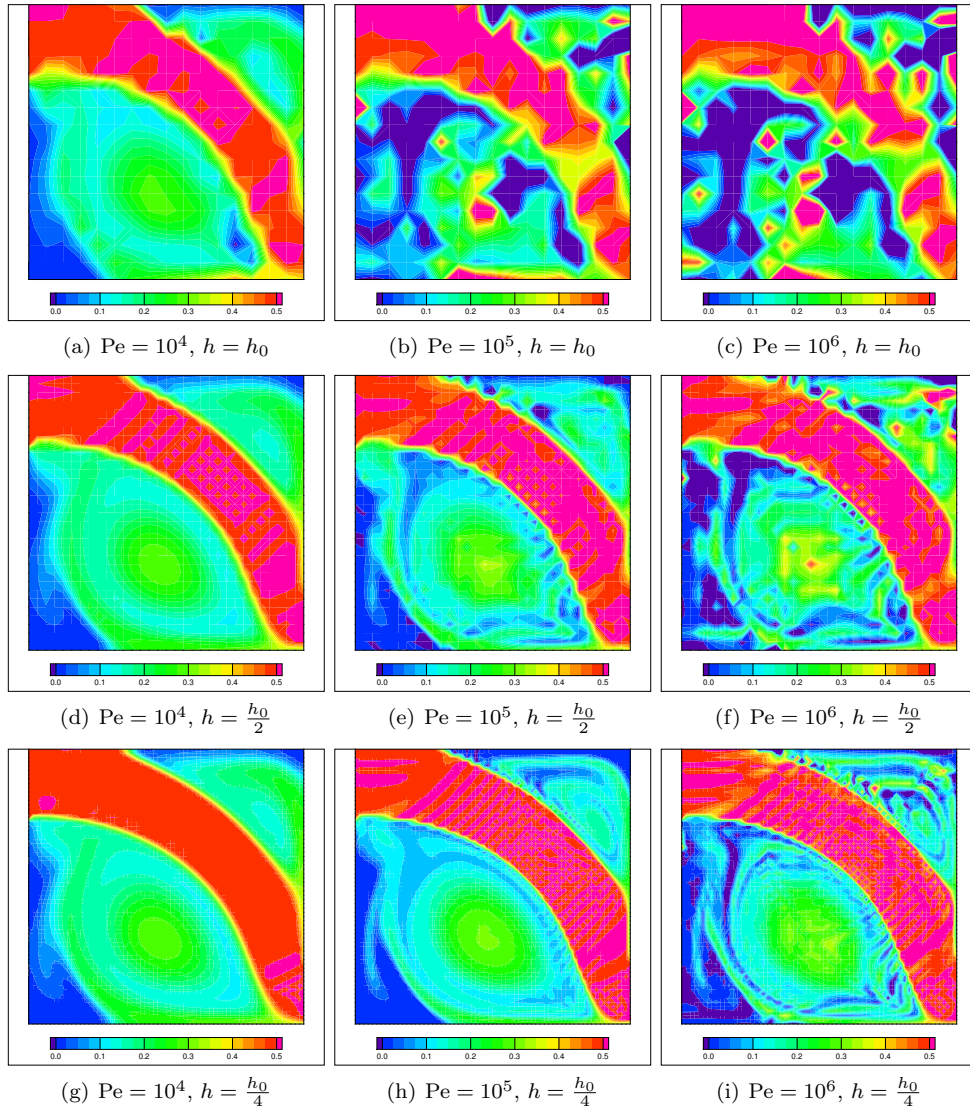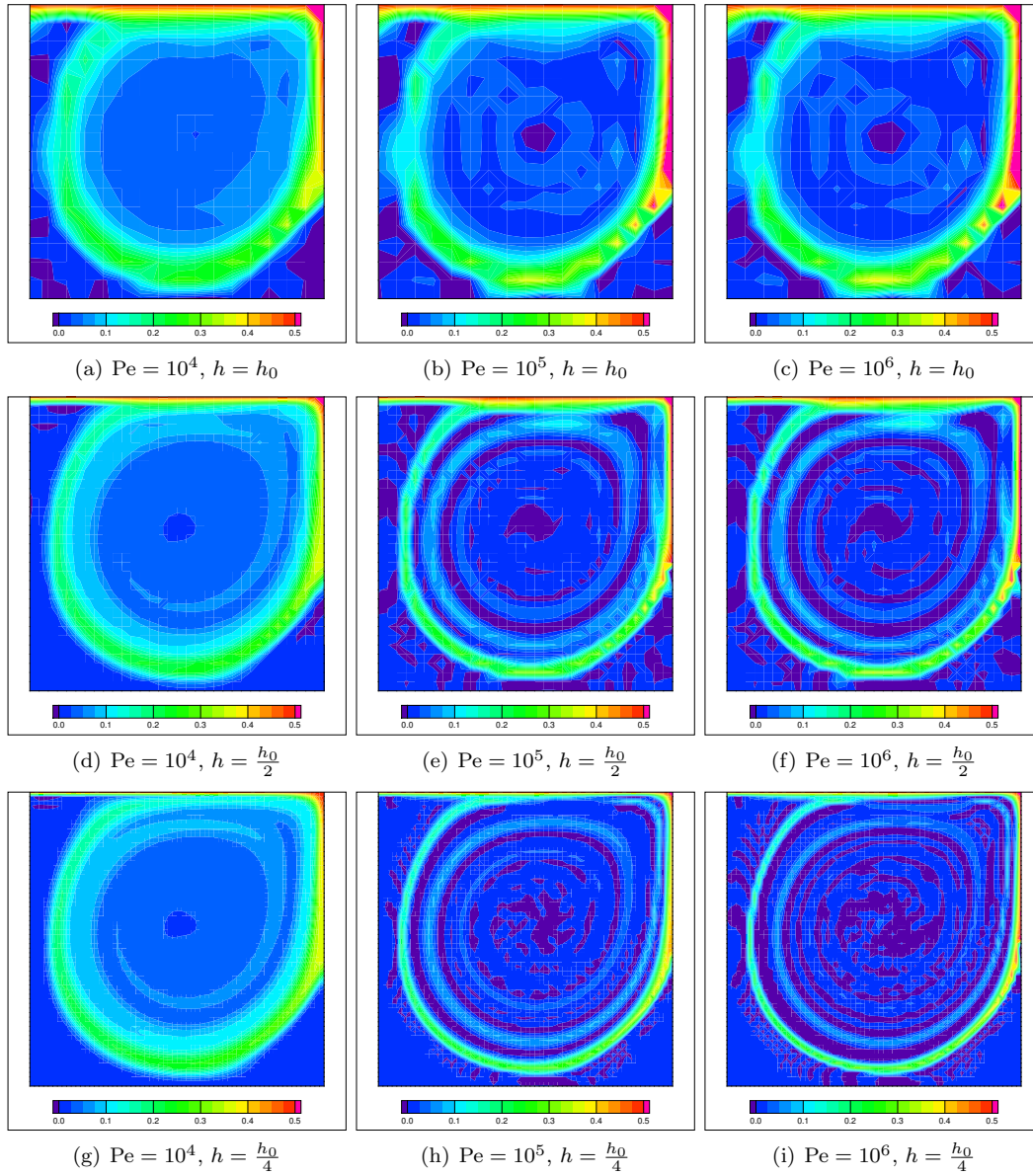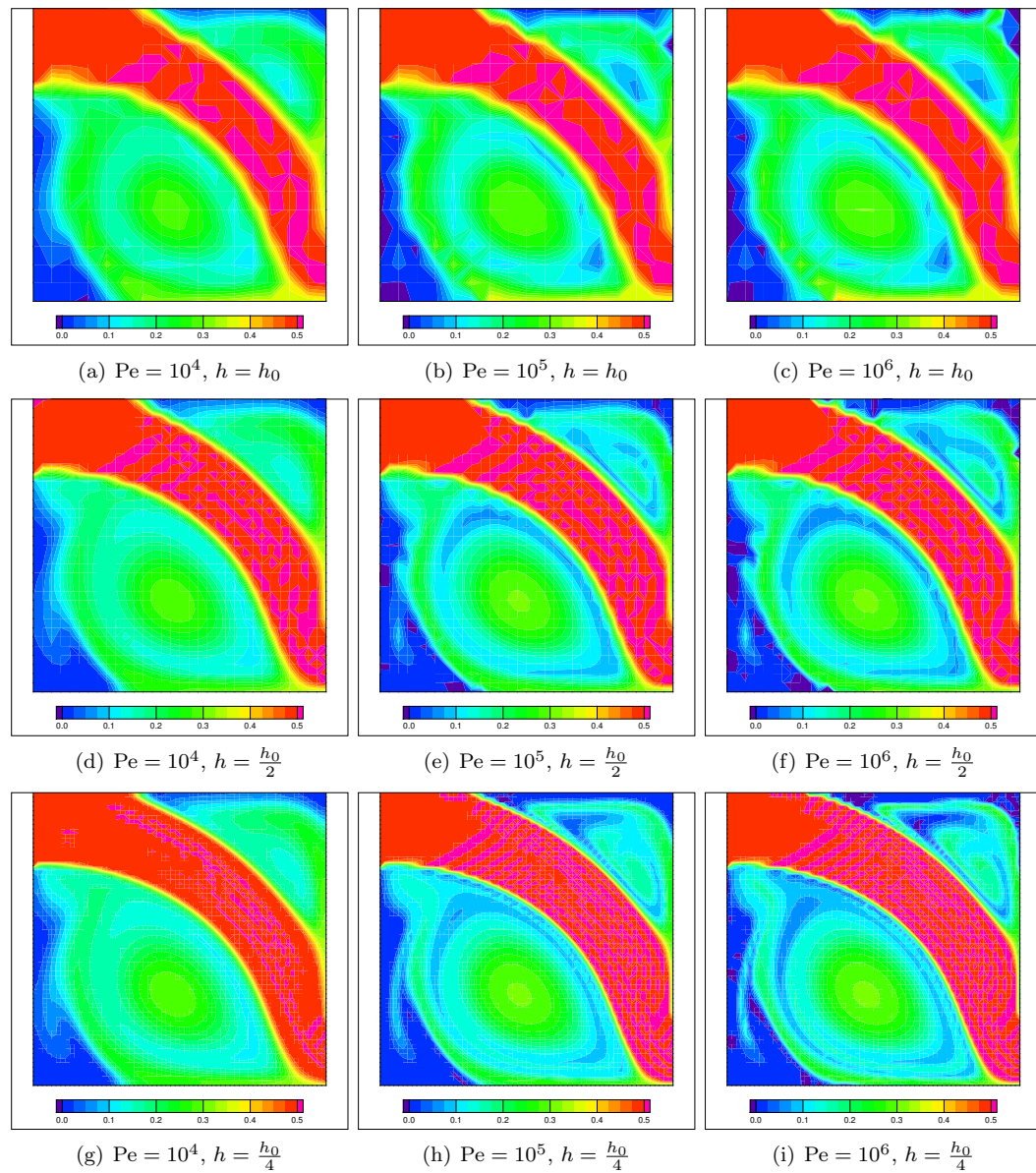
FIGURE 8.4. Computational results of concentration distribution for boundary conditions of type BC II – without stabilization; plotted at time $t = 50$.

(a) Q_1 (b) Q_2
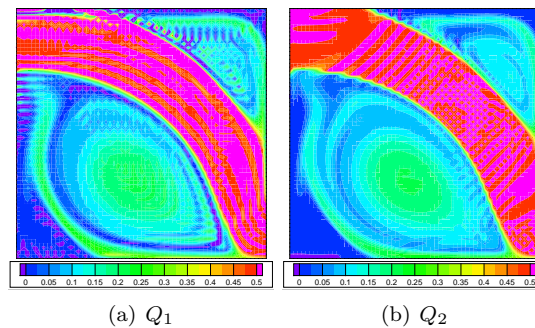
FIGURE 8.5. Comparison of results obtained by Q_1 and Q_2 approximations, Pe $= 10^5$, $h = \frac{h_0}{4}$ at $t = 50$.

stabilized by the means of additionally introduced artificial diffusion. In that case, the very small physical diffusivity D_c is increased by suitably chosen τ with the property of $\tau = O(h)$. Even though that the oscillations of the resulting numerical solution are eliminated the added diffusion is introduced in all directions which causes the blurring of sharp layers and non–physical increase of the concentration in some regions. Finite difference method was therefore adapted for application of artificial diffusion only in the streamline direction, which can be interpreted as "what is just about to inflow to the point, influences the solution at this point more than what has just passed away". Mathematically, the introduction of artificial diffusion can be formulated as a modification of the test function of the convective term. On this basis is developed the SUPG stabilization method for finite element method, but for consistency, the modified test function is applied to all terms of the weak form. In that case, the exact solution of the problem satisfies the weak form.

Since the discretization of the equation for the velocity and incompressibility constraint are unaltered, let us discuss the changes in the discretization of the equation for the concentration, only. Again, we consider the boundary conditions (8.4) and (8.5), and for simplicity, the diffusivity D_c to be constant. Then, after the discretization in time[1], one obtains

$$(8.36) \quad c^{k+1} + \theta_1 \Delta t^k \left(\nabla c^{k+1} \cdot \boldsymbol{v}^{k+1} - \frac{1}{\mathrm{Pe}} \Delta c^{k+1} \right)$$
$$= c^k - \theta_2 \Delta t^k \left(\nabla c^k \cdot \boldsymbol{v}^k - \frac{1}{\mathrm{Pe}} \Delta c^k \right)$$

at a given time step $k + 1$. Then, the streamline upwind Petrov–Galerkin method ads to the (still standard) space discretization with standard treatment of the boundary conditions

$$(8.37) \quad (c_h^{k+1}, \psi)_\Omega + \theta_1 \Delta t^k \left(\nabla c_h^{k+1} \cdot \boldsymbol{v}_h^{k+1}, \psi \right)_\Omega$$
$$+ \theta_1 \Delta t^k \frac{1}{\mathrm{Pe}} (\nabla c_h^{k+1}, \nabla \psi)_\Omega - \theta_1 \Delta t^k \left(g^c(t^{k+1}), \psi \right)_{\Gamma_N^c}$$
$$= (c_h^k, \psi)_\Omega - \theta_2 \Delta t^k \left(\nabla c_h^k \cdot \boldsymbol{v}_h^k, \psi \right)_\Omega$$
$$- \theta_2 \Delta t^k \frac{1}{\mathrm{Pe}} (\nabla c_h^k, \nabla \psi)_\Omega + \theta_2 \Delta t^k \left(g^c(t^k), \psi \right)_{\Gamma_N^c}$$
$$\forall \psi \in C_{0h},$$

an additional term "acting" in the streamline direction, treated element–wise,

$$(8.38) \quad \sum_{K \in \mathcal{T}_h} \tau_K \left(R_{h,K}^{k+1}, \nabla \psi \cdot \boldsymbol{v}_h^{k+1} \right)_K.$$

Here, $\{\tau_K\}_{K \in \mathcal{T}_h}$ is a set of stabilization parameters, constants on each element $K \in \mathcal{T}_h$ and $R_{h,K}^{k+1}$ is the residual of equation (8.36) expressed for approximations c_h^{k+1} and c_h^k on each element K[2]. Explicitly it is on each $K \in \mathcal{T}_h$

$$(8.39) \quad R_{h,K}^{k+1} = c_h^{k+1} - c_h^k + \theta_1 \Delta t^k \left(\nabla c_h^{k+1} \cdot \boldsymbol{v}_h^{k+1} - \frac{1}{\mathrm{Pe}} \Delta c_h^{k+1} \right)$$
$$+ \theta_2 \Delta t^k \left(\nabla c_h^k \cdot \boldsymbol{v}_h^k - \frac{1}{\mathrm{Pe}} \Delta c_h^k \right).$$

---

[1]The formulation for the initial conditions is the same as in the straightforward discretization described above.

[2]On each element, the equation in strong form makes sense, since the approximations are the polynomial functions on K.

Then, the SUPG method reads

$$(8.40) \quad (c_h^{k+1}, \psi)_\Omega + \sum_{K \in \mathcal{T}_h} \tau_K \left(c_h^{k+1}, \nabla \psi \cdot \boldsymbol{v}_h^{k+1} \right)_K$$

$$+ \theta_1 \Delta t^k \left[(\nabla c_h^{k+1} \cdot \boldsymbol{v}_h^{k+1}, \psi)_\Omega + \frac{1}{\text{Pe}} (\nabla c_h^{k+1}, \nabla \psi)_\Omega \right] - \theta_1 \Delta t^k \left(g^c(t^{k+1}), \psi \right)_{\Gamma_N^c}$$

$$+ \theta_1 \Delta t^k \sum_{K \in \mathcal{T}_h} \tau_K \left((\nabla c_h^{k+1} \cdot \boldsymbol{v}_h^{k+1}, \nabla \psi \cdot \boldsymbol{v}_h^{k+1})_K - \frac{1}{\text{Pe}} (\Delta c_h^{k+1}, \nabla \psi \cdot \boldsymbol{v}_h^{k+1})_K \right)$$

$$= (c_h^k, \psi)_\Omega + \sum_{K \in \mathcal{T}_h} \tau_K \left(c_h^k, \nabla \psi \cdot \boldsymbol{v}_h^{k+1} \right)_K$$

$$- \theta_2 \Delta t^k \left[(\nabla c_h^k \cdot \boldsymbol{v}_h^k, \psi)_\Omega + \frac{1}{\text{Pe}} (\nabla c_h^k, \nabla \psi)_\Omega \right] + \theta_2 \Delta t^k \left(g^c(t^k), \psi \right)_{\Gamma_N^c}$$

$$- \theta_2 \Delta t^k \sum_{K \in \mathcal{T}_h} \tau_K \left((\nabla c_h^k \cdot \boldsymbol{v}_h^k, \nabla \psi \cdot \boldsymbol{v}_h^{k+1})_K - \frac{1}{\text{Pe}} (\Delta c_h^k, \nabla \psi \cdot \boldsymbol{v}_h^{k+1})_K \right)$$

$$\forall \psi \in C_{0h}.$$

Recalling that the residual for (in space) exact solution is zero, the whole

$$(8.41) \qquad\qquad \sum_{K \in \mathcal{T}_h} \tau_K \left(R_K^{k+1}, \nabla \psi \cdot \boldsymbol{v}_h^{k+1} \right)_K = 0,$$

and thus the SUPG is a consistent method.

One can notice, that, as it has been mentioned before, the form of (8.40) can be obtained if the test function ψ in (8.37) is taken as

$$(8.42) \qquad\qquad \psi \longrightarrow \psi + \tau_K \boldsymbol{v} \cdot \nabla \psi.$$

What remains is the computation of algorithmic parameter τ_K, which is in fact a crucial question in application of the stabilization method on the convection dominated problem. To this date, there is a notable amount of literature references concerning the τ_K estimation, first time discussed in detail in Brooks and Hughes (1982). For the one–dimensional case, the τ_K can be optimally computed which is usually, together with assumptions from the convergence analysis, the base for (non–unique) higher–dimensional extension, Franca and Valentin (2000), Codina (2000).

From many, we use the proposal of τ_K by Codina (2000)

$$(8.43) \qquad\qquad \tau_K \sim \left(\frac{c_1}{\text{Pe}\, h_K^2} + \frac{c_2 |\boldsymbol{v}|}{h_K} \right)^{-1},$$

where c_1 and c_2 are constants, coming from the error estimate. However, the constant from inverse inequality can not be, in general, explicitly computed, and thus, the choice of c_1 and c_2 is not obvious. Nevertheless, the values are usually used as in the one–dimensional case, explicitly $c_1 = 4$ and $c_2 = 2$, as has been derived for linear elements, see Codina (2000).

For $c^{k+1} \in W^{p+1,2}(\Omega)$ and suitable τ_K (in our case of form (8.43)), the spatial error estimate can be then obtained as

$$(8.44) \qquad\qquad ||c^{k+1} - c_h^{k+1}||_{SUPG} \leq C \left(\text{Pe}^{-1/2} + h^{1/2} \right) h^p |c^{k+1}|_{p+1},$$

where $|| \cdot ||_{SUPG}$ is a suitable norm, see Roos and Stynes (1996). In comparison with the classical Galerkin formulation, the error has "extra accuracy" of half of power of h in the streamline direction.

Again, we present the exemplary computations for the same boundary and geometry settings as computed for the non–stabilized scheme above, see Fig. 8.6–8.7, which shall be discussed together with the other types of stabilization methods at end of the chapter.

(a) Pe $= 10^4$, $h = h_0$ (b) Pe $= 10^5$, $h = h_0$ (c) Pe $= 10^6$, $h = h_0$

(d) Pe $= 10^4$, $h = \frac{h_0}{2}$ (e) Pe $= 10^5$, $h = \frac{h_0}{2}$ (f) Pe $= 10^6$, $h = \frac{h_0}{2}$

(g) Pe $= 10^4$, $h = \frac{h_0}{4}$ (h) Pe $= 10^5$, $h = \frac{h_0}{4}$ (i) Pe $= 10^6$, $h = \frac{h_0}{4}$

FIGURE 8.6. Computational results of concentration distribution for boundary conditions of type BC I – SUPG stabilization; plotted at time $t = 50$.

(a) Pe $= 10^4$, $h = h_0$

(b) Pe $= 10^5$, $h = h_0$

(c) Pe $= 10^6$, $h = h_0$

(d) Pe $= 10^4$, $h = \frac{h_0}{2}$

(e) Pe $= 10^5$, $h = \frac{h_0}{2}$

(f) Pe $= 10^6$, $h = \frac{h_0}{2}$

(g) Pe $= 10^4$, $h = \frac{h_0}{4}$

(h) Pe $= 10^5$, $h = \frac{h_0}{4}$

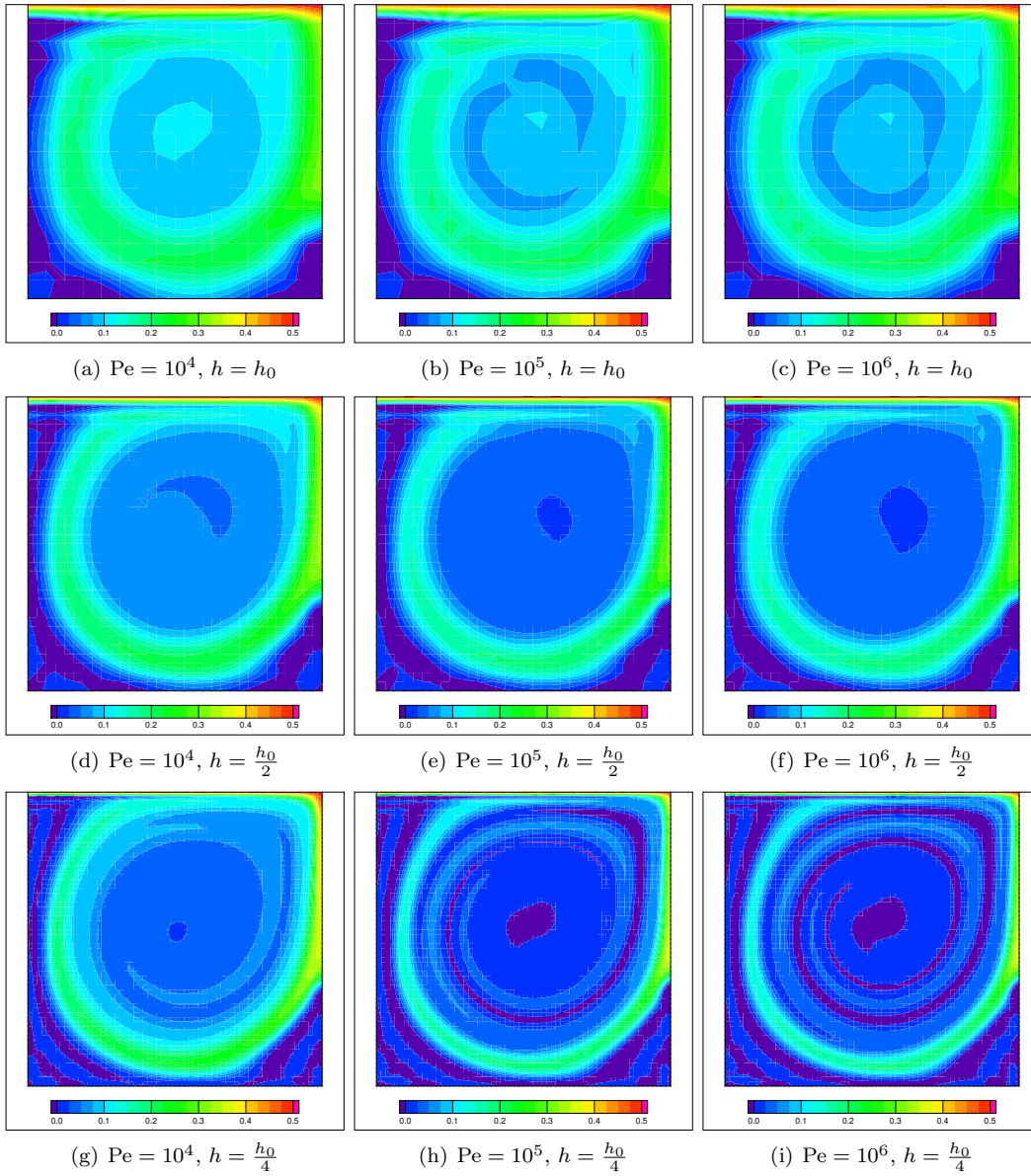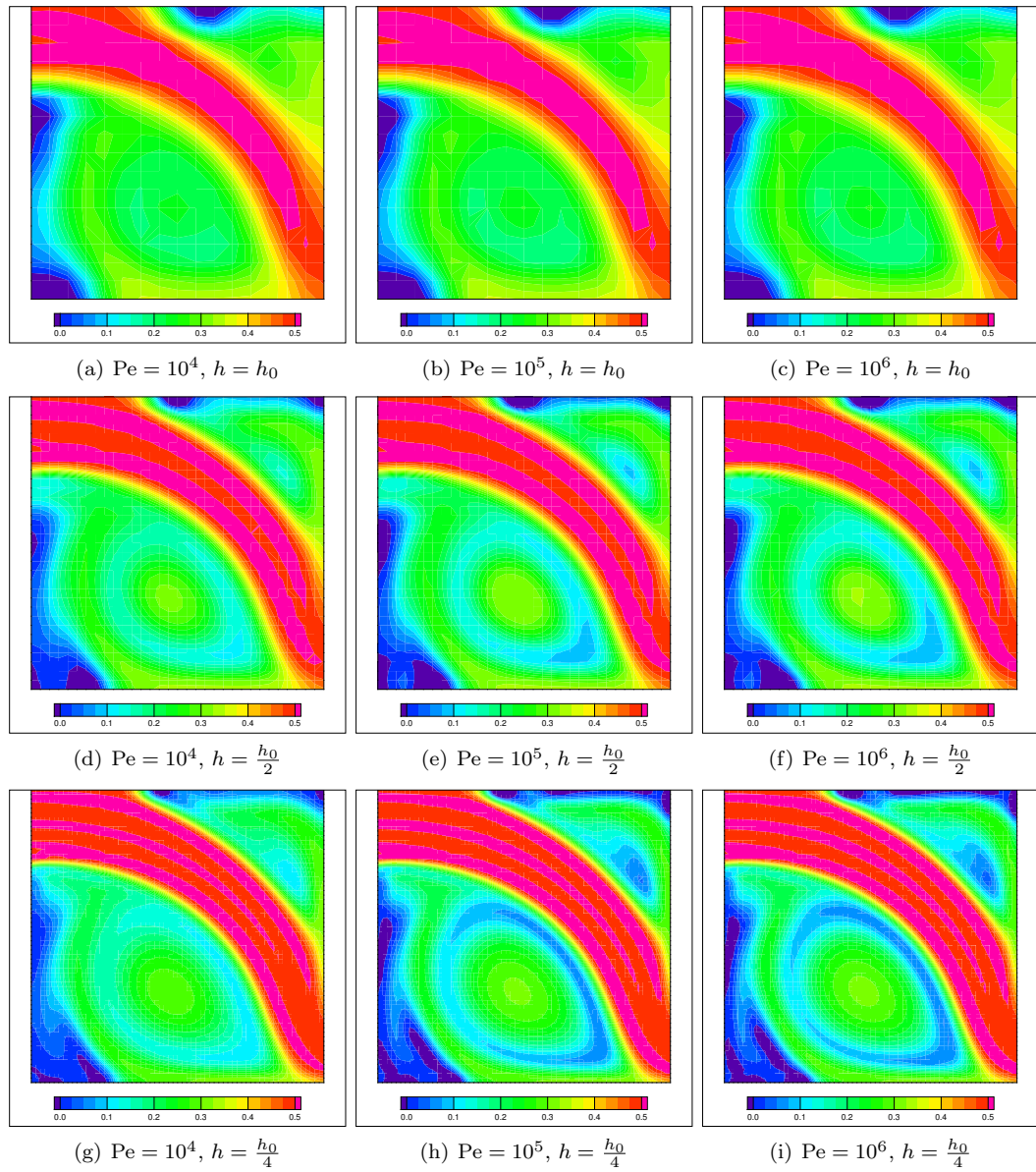(i) Pe $= 10^6$, $h = \frac{h_0}{4}$

FIGURE 8.7. Computational results of concentration distribution for boundary conditions of type BC II – SUPG stabilization; plotted at time $t = 50$.

8.7. Galerkin least squares method

While SUPG was motivated by the finite differences method and artificial diffusion, the Galerkin least squares method (Jiang (1998), Fiard et al. (1998), Bochev and Gunzburger (2009)) is based on formulation of the problem in the sense of minimizing the error functional in a suitable norm, usually the square of L^2–norm, resulting in symmetric positive definite matrix of the algebraic system.

Again, we shall describe the discretization of the equation for concentration, only, and directly start with the form after the time discretization

$$(8.45) \quad c^{k+1} + \theta_1 \Delta t^k \left(\nabla c^{k+1} \cdot \boldsymbol{v}^{k+1} - \frac{1}{\text{Pe}} \Delta c^{k+1} \right)$$
$$= c^k - \theta_2 \Delta t^k \left(\nabla c^k \cdot \boldsymbol{v}^k - \frac{1}{\text{Pe}} \Delta c^k \right).$$

If we set for each time level $k+1$

$$(8.46) \qquad \mathcal{L}_{k+1}(\boldsymbol{v}^{k+1}) c^{k+1} := c^{k+1} + \theta_1 \Delta t^k \left(\nabla c^{k+1} \cdot \boldsymbol{v}^{k+1} - \frac{1}{\text{Pe}} \Delta c^{k+1} \right),$$

$$(8.47) \qquad f_k(\boldsymbol{v}^k, c^k) := c^k - \theta_2 \Delta t^k \left(\nabla c^k \cdot \boldsymbol{v}^k - \frac{1}{\text{Pe}} \Delta c^k \right),$$

and after, for simplicity, drop the indexes (keeping in mind we operate on time level $k+1$),

$$(8.48) \qquad \mathcal{L}_{k+1}(\boldsymbol{v}^{k+1}) c^{k+1} = f_k(\boldsymbol{v}^k, c^k) \quad \longrightarrow \quad \mathcal{L}c = f,$$

one can formulate the problem (8.45) in the sense of GLS as: find the approximative solution $c_h \in C_h$ such that

$$(8.49) \qquad \| \mathcal{L}_h c_h - f_h \|_2^2 = \min_{\psi \in C_h} \| \mathcal{L}_h \psi - f_h \|_2^2,$$

where operator $\mathcal{L}_h = \mathcal{L}_{k+1}(\boldsymbol{v}_h^{k+1})$ and function $f_h = f_k(\boldsymbol{v}_h^k, c_h^k)$.

This can be reformulated as

$$(8.50) \qquad (\mathcal{L}_h c_h - f_h, \mathcal{L}_h \psi)_\Omega = 0 \quad \forall \psi \in C_h,$$

or in other words, we are looking for the stationary point for which the derivatives are zero in all directions. The equation (8.50) can be paralleled to standard Galerkin formulation if the test function ψ is replaced by $\mathcal{L}_h \psi$.

At this point, the matrix of the resulting algebraic system is symmetric positive definite. Nevertheless the operator $\mathcal{L}_h$ is of second order and thus (8.50) is equivalent to solving the *4th* order equation. Moreover, the formulation requires the direction $\psi \in W^{2,2}(\Omega)$, which is not true since $C_h \not\subset W^{2,2}(\Omega)$ in the case of the Lagrange finite elements. To resolve this complication, we can choose between two approaches. First, similar to SUPG, one can add to the weak formulation the stabilization term

$$(8.51) \qquad \sum_{K \in \mathcal{T}_h} \tau_K (R_K, \mathcal{L}_h \psi),$$

where $R_K = (\mathcal{L}_h c_h - f_h)|_K$ is the residuum on the element K and τ_K is the stabilization parameter. Or, one can reduce the order of the operator $\mathcal{L}$ by following reformulation of the equation (8.45), which is the approach we prefer since no additional information about the stabilization parameter is needed.

Let us formally rewrite the (8.45) by the help of additional variable $\boldsymbol{q}$

$$(8.52) \qquad \boldsymbol{q}^{k+1} = \nabla c^{k+1},$$

$$(8.53) \qquad c^{k+1} + \theta_1 \Delta t^k \left(\boldsymbol{q}^{k+1} \cdot \boldsymbol{v}^{k+1} - \frac{1}{\text{Pe}} \operatorname{div} \boldsymbol{q}^{k+1} \right),$$

$$(8.54) \qquad = c^k - \theta_2 \Delta t^k \left(\boldsymbol{q}^k \cdot \boldsymbol{v}^k - \frac{1}{\text{Pe}} \operatorname{div} \boldsymbol{q}^k \right).$$

Then, in the operator notation defined by

(8.55) $\qquad \boldsymbol{\mathcal{B}}(\boldsymbol{q}^{k+1}, c^{k+1}) := \boldsymbol{q}^{k+1} - \nabla c^{k+1}$

(8.56) $\qquad\qquad\qquad f_k := c^k - \theta_2 \Delta t^k (\boldsymbol{q}^k \cdot \boldsymbol{v}^k - \dfrac{1}{\mathrm{Pe}} \operatorname{div} \boldsymbol{q}^k)$

(8.57) $\qquad \mathcal{A}(\boldsymbol{q}^{k+1}, c^{k+1}) := c^{k+1} - \theta_1 \Delta t^k (\boldsymbol{q}^{k+1} \cdot \boldsymbol{v}^{k+1} - \dfrac{1}{\mathrm{Pe}} \operatorname{div} \boldsymbol{q}^{k+1}) - f_k$

one gets, again after dropping the indexes, the formally reformulated equation (8.45) in the form

(8.58) $\qquad\qquad\qquad\qquad\qquad \mathcal{A}(\boldsymbol{q}, c) = f,$

(8.59) $\qquad\qquad\qquad\qquad\qquad \boldsymbol{\mathcal{B}}(\boldsymbol{q}, c) = \boldsymbol{0},$

and, the GLS applied on this system together with boundary conditions represented by operator $\mathcal{C}$ reads

(8.60) $\qquad \|\mathcal{A}(\boldsymbol{q}_h, c_h) - f\|_2^2 + \|\boldsymbol{\mathcal{B}}(\boldsymbol{q}_h, c_h)\|_2^2 + \|\mathcal{C}(\boldsymbol{q}_h, c_h)\|_{2,\partial\Omega}^2$

$$= \min_{\substack{\boldsymbol{w} \in [C_h]^2 \\ \psi \in C_h}} \left(\|\mathcal{A}(\boldsymbol{w}, \psi) - f\|_2^2 + \|\boldsymbol{\mathcal{B}}(\boldsymbol{w}, \psi)\|_2^2 + \|\mathcal{C}(\boldsymbol{w}, \psi)\|_{2,\partial\Omega}^2 \right).$$

This minimum, as the stationary point of (8.60), is then found by solving the system of

(8.61) $\qquad 2\left(\mathcal{A} - f, \dfrac{\partial \mathcal{A}}{\partial \boldsymbol{q}_h}[\boldsymbol{w}] \right)_\Omega + 2\left(\boldsymbol{\mathcal{B}}, \dfrac{\partial \boldsymbol{\mathcal{B}}}{\partial \boldsymbol{q}_h}[\boldsymbol{w}] \right)_\Omega + 2\left(\mathcal{C}, \dfrac{\partial \mathcal{C}}{\partial \boldsymbol{q}_h}[\boldsymbol{w}] \right)_{\partial\Omega} = 0,$

(8.62) $\qquad 2\left(\mathcal{A} - f, \dfrac{\partial \mathcal{A}}{\partial c_h}[\psi] \right)_\Omega + 2\left(\boldsymbol{\mathcal{B}}, \dfrac{\partial \boldsymbol{\mathcal{B}}}{\partial c_h}[\psi] \right)_\Omega + 2\left(\mathcal{C}, \dfrac{\partial \mathcal{C}}{\partial c_h}[\psi] \right)_{\partial\Omega} = 0,$

for all directions $\boldsymbol{w} \in [C_h]^d$ and $\psi \in C_h$. By notation $\frac{\partial \mathcal{A}}{\partial c_h}[\psi]$ is understood the Gâteaux derivative $\frac{\mathrm{d}}{\mathrm{d}\varepsilon} \mathcal{A}(\boldsymbol{q}_h, c_h + \varepsilon\psi)|_{\varepsilon=0}$. The system of (8.61) and (8.62) is then the resulting system of non–linear algebraic equations $\boldsymbol{\mathcal{F}}(\bar{\mathbf{x}}) = 0$.

For the $c \in W^{p+1,2}(\Omega)$ and $\boldsymbol{q} \in [W^{p+1,2}(\Omega)]^d$ one can obtain the error estimate for GLS method

(8.63) $\qquad\qquad ||c - c_h||_{1,2} + ||\boldsymbol{q} - \boldsymbol{q}_h||_{1,2} \leq Ch^p \left(|c|_{p+1} + |\boldsymbol{q}|_{p+1} \right),$

see Cai et al. (1994), Cai et al. (1997) or Jiang (1998). The error estimate of GLS can be however improved for the case of GLS formulation by the means of stabilization term (8.51). Then, one can obtain similar estimate as (8.44), formulated for a GLS suitable norm, see for example Roos and Stynes (1996).

The exemplary computations for the case of the GLS stabilization are depicted in Fig. 8.8–8.9, which shall be discussed together with the other types of stabilization methods at end of the chapter.

(a) Pe $= 10^4$, $h = h_0$ (b) Pe $= 10^5$, $h = h_0$ (c) Pe $= 10^6$, $h = h_0$

(d) Pe $= 10^4$, $h = \frac{h_0}{2}$ (e) Pe $= 10^5$, $h = \frac{h_0}{2}$ (f) Pe $= 10^6$, $h = \frac{h_0}{2}$

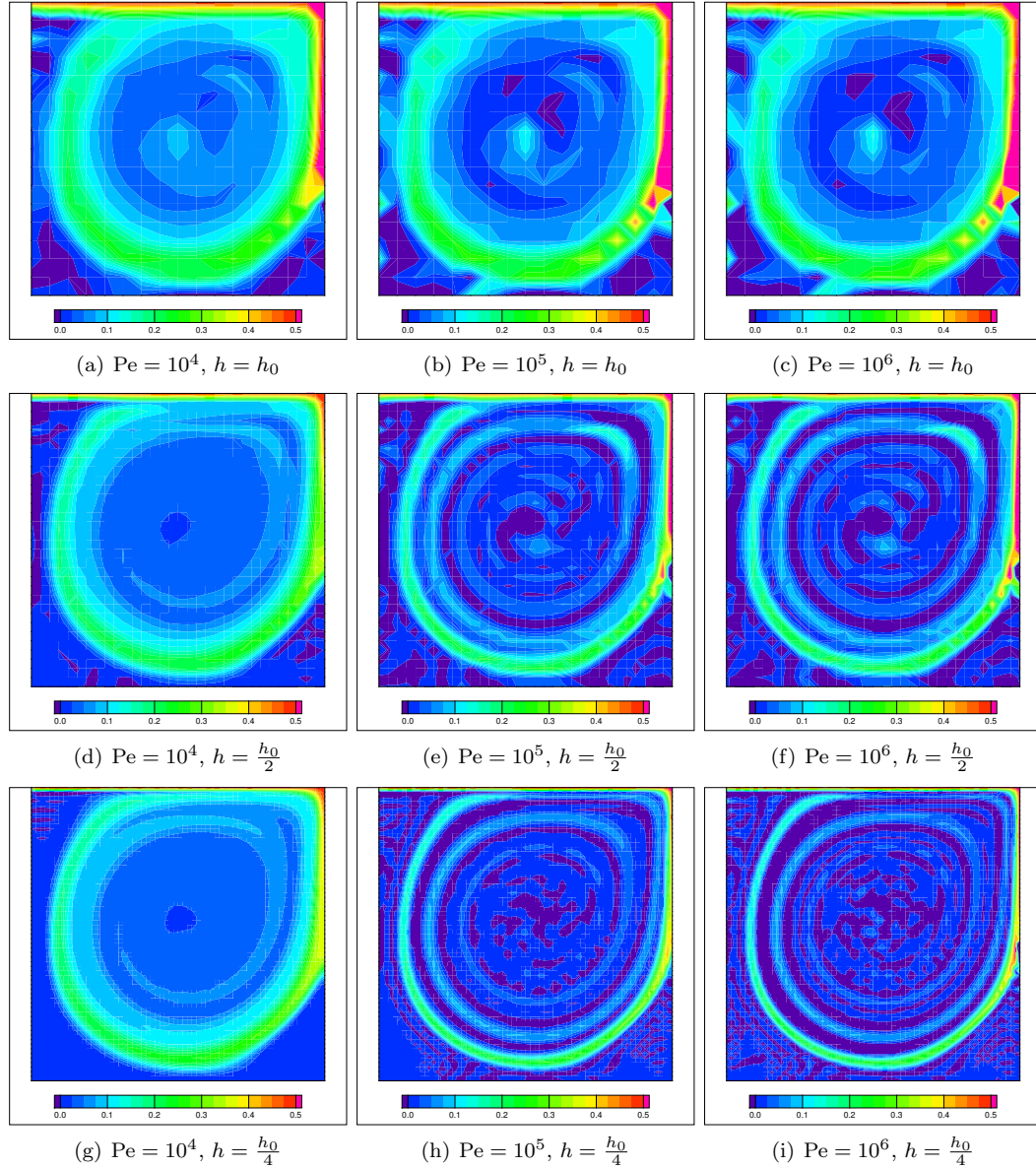(g) Pe $= 10^4$, $h = \frac{h_0}{4}$ (h) Pe $= 10^5$, $h = \frac{h_0}{4}$ (i) Pe $= 10^6$, $h = \frac{h_0}{4}$

FIGURE 8.8. Computational results of concentration distribution for boundary conditions of type BC I – GLS stabilization; plotted at time $t = 50$.
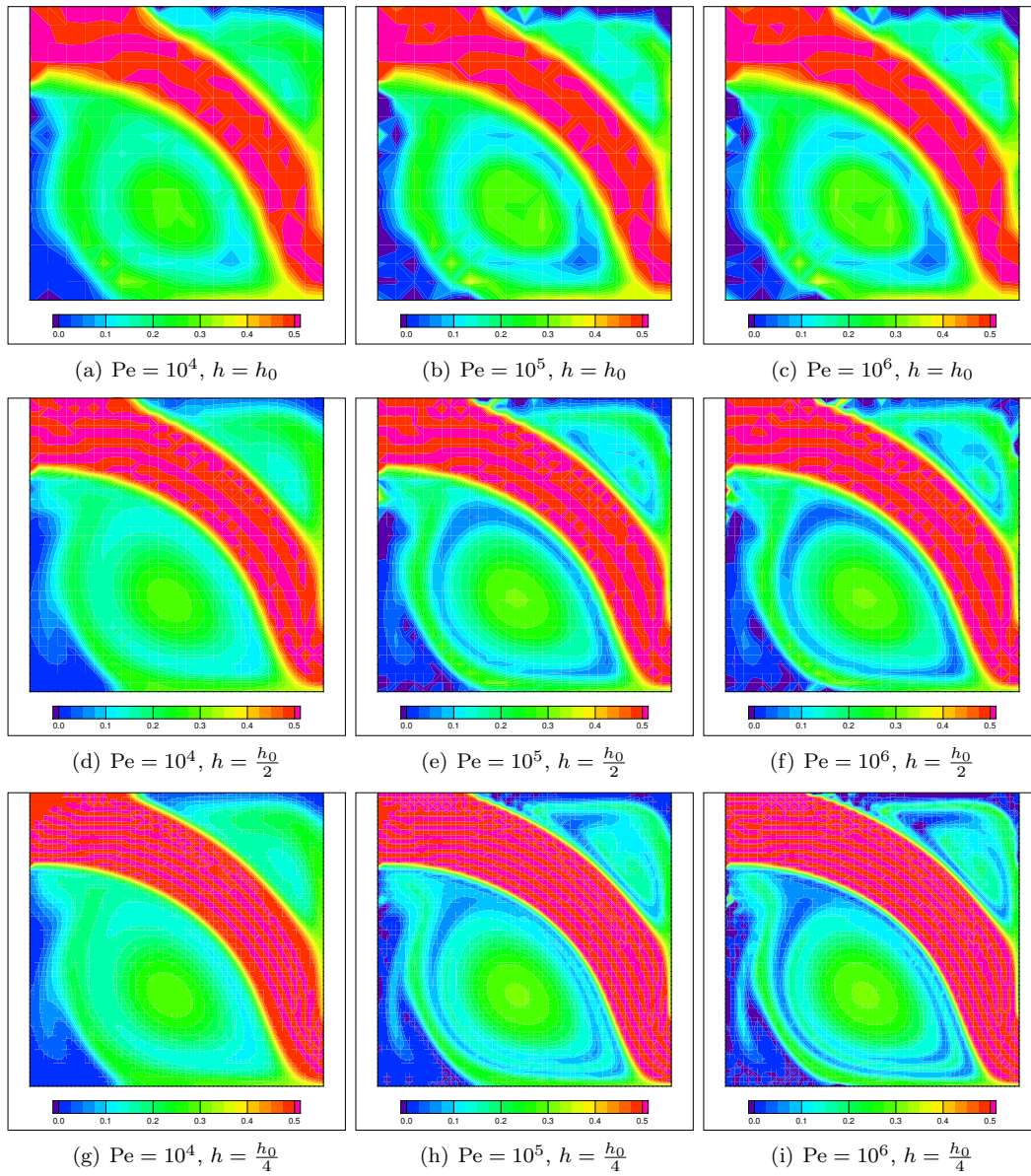
(a) Pe $= 10^4$, $h = h_0$

(b) Pe $= 10^5$, $h = h_0$

(c) Pe $= 10^6$, $h = h_0$

(d) Pe $= 10^4$, $h = \frac{h_0}{2}$

(e) Pe $= 10^5$, $h = \frac{h_0}{2}$

(f) Pe $= 10^6$, $h = \frac{h_0}{2}$

(g) Pe $= 10^4$, $h = \frac{h_0}{4}$

(h) Pe $= 10^5$, $h = \frac{h_0}{4}$

(i) Pe $= 10^6$, $h = \frac{h_0}{4}$

FIGURE 8.9. Computational results of concentration distribution for boundary conditions of type BC II – GLS stabilization; plotted at time $t = 50$.
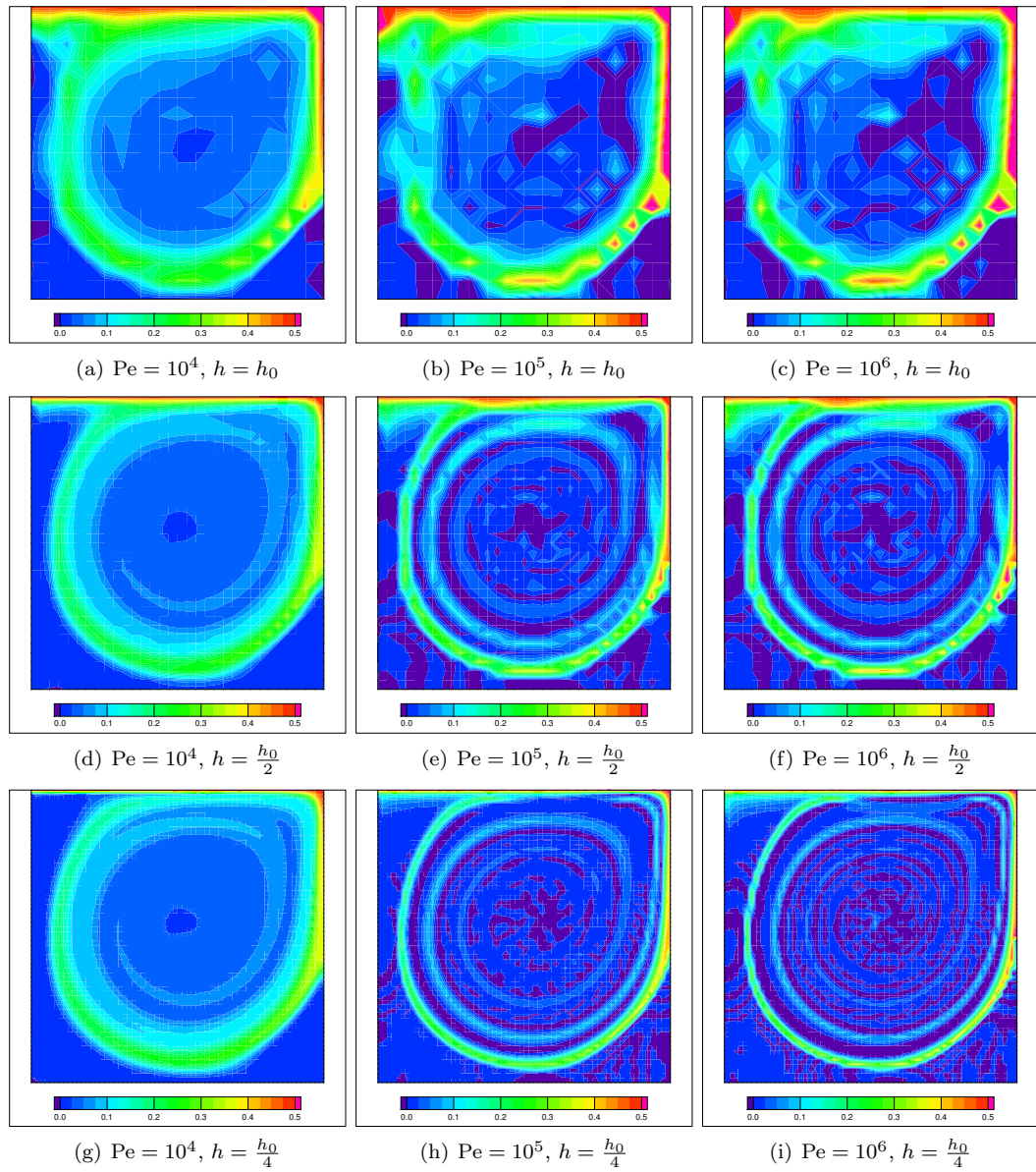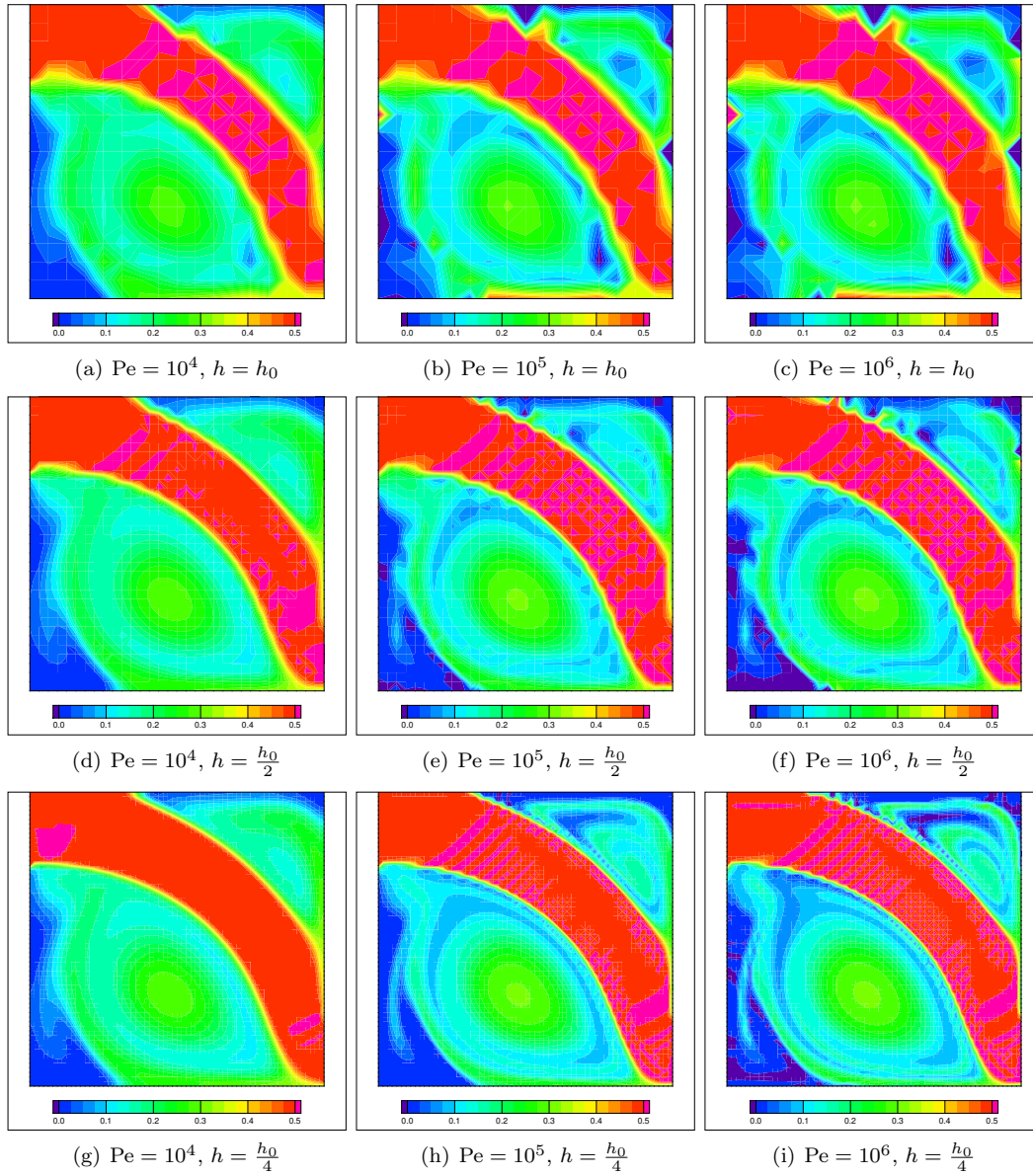
8.8. Continuous interior penalty method

The keystone of continuous interior penalty method (Douglas and Dupont (1976), Burman and Hansbo (2004), Burman and Ern (2007), Turek and Ouazzi (2007)) is the penalization of the gradient jumps of the discrete solution on the mesh interfaces, to evoke an apparent stiffness of rapidly changing fields in the space variables (like in the neighborhoods of sharp layers). In contrast to SUPG, the CIP method introduces only one symmetric stabilization term, generally independent of the diffusivity coefficient, which is important for error estimates int the case when diffusivity is non–constant. Then, the mass matrix of resulting algebraical system can be lumped. On the other hand, the CIP method results in more dense matrix of the algebraical system than SUPG or GLS, and from practical point of view, the extra information about the interior faces has to be recorded.

Before we formulate the stabilized problem, let us introduce new, nevertheless for CIP or discontinuous methods standard, notation. Let the interior face be called $F = K_1 \cap K_2$, where K_1 and K_2 are two distinct elements of $\mathcal{T}_h$, with the diameter h_F and unit outer normal $\boldsymbol{n}$. The set of all interior faces of the mesh is called $\mathcal{F}_h$. Then, on each interior face, we define the scalar–valued jump of gradient of scalar field a at the face F between elements K_1 and K_2 as

$$(8.64) \qquad [\nabla a \cdot \boldsymbol{n}]_F = \nabla a|_{K_1} \cdot \boldsymbol{n_1} + \nabla a|_{K_2} \cdot \boldsymbol{n_2},$$

where $\boldsymbol{n}_1$ and $\boldsymbol{n}_2$ are the outer normals with respect to elements K_1 and K_2.

The principle of CIP method is to add to the standard Galerkin discretization the term penalizing the gradient jumps. In the case of discretization scheme by continuous functions, the gradient jump is manifested in the normal direction only, and thus, the form of the penalization is expressed in notation of (8.64) as follows

$$(8.65) \qquad j_1(c_h, \psi) = \sum_{F \in \mathcal{F}_h} \int_F \gamma h_F^2 [\nabla c_h \cdot \boldsymbol{n}]_F [\nabla \psi \cdot \boldsymbol{n}]_F \, \mathrm{d}S$$

or in element notation

$$(8.66) \qquad j_1(c_h, \psi) = \sum_{K \in \mathcal{T}_h} \frac{1}{2} \int_{\partial K} \gamma h_{\partial K}^2 [\nabla c_h \cdot \boldsymbol{n}][\nabla \psi \cdot \boldsymbol{n}] \, \mathrm{d}S$$

where $[\cdot] = 0$ on $\partial K \cap \partial \Omega$, $h_{\partial K}^2 = h_{F_i}^2$, F_i being the edges of element K, and γ is a user–specified constant. Another possible variant is the weighting of the stabilization term by the normal flux through each edge, see for example Burman and Fernández (2009),

$$(8.67) \qquad j_2(c_h, \psi) = \sum_{K \in \mathcal{T}_h} \frac{1}{2} \int_{\partial K} \gamma h_{\partial K}^2 |\boldsymbol{v}_h \cdot \boldsymbol{n}| [\nabla c_h \cdot \boldsymbol{n}][\nabla \psi \cdot \boldsymbol{n}] \, \mathrm{d}S.$$

The CIP stabilization method then reads for each time step $k + 1$: find $c_h^{k+1} - c_h^\star \in C_h$ such that[3]

$$(8.68) \quad (c_h^{k+1}, \psi)_\Omega + \theta_1 \Delta t^k \left(\nabla c_h^{k+1} \cdot \boldsymbol{v}_h^{k+1}, \psi \right)_\Omega$$
$$+ \theta_1 \Delta t^k \frac{1}{\mathrm{Pe}} (\nabla c_h^{k+1}, \nabla \psi)_\Omega - \theta_1 \Delta t^k \left(g^c(t^{k+1}), \psi \right)_{\Gamma_N^c} + j(c_h, \psi)$$
$$= (c_h^k, \psi)_\Omega - \theta_2 \Delta t^k \left(\nabla c_h^k \cdot \boldsymbol{v}_h^k, \psi \right)_\Omega$$
$$- \theta_2 \Delta t^k \frac{1}{\mathrm{Pe}} (\nabla c_h^k, \nabla \psi)_\Omega + \theta_2 \Delta t^k \left(g^c(t^k), \psi \right)_{\Gamma_N^c}$$
$$\forall \psi \in C_{0h}.$$

Assuming the exact solution c belongs to $W^{2,2}(\Omega)$[4], the formulation (8.68) is consistent as

$$(8.69) \qquad j(c, \psi) = 0 \qquad \forall \psi \in C_{0h}.$$

---

[3]The treatment of Dirichlet boundary condition is the same as above, thus for the definition of $c_h^\star$ see section 8.3.

[4]In that case the trace of gradient is well defined.

Assuming the diffusivity is bounded from zero (the diffusive term does not vanish) and $c^{k+1} \in W^{p+1,2}(\Omega)$, then the a priori error estimate yields

$$(8.70) \qquad ||c^{k+1} - c_h^{k+1}||_2 \leq Ch^{p+1}|c^{k+1}|_{p+1},$$

see for example Douglas and Dupont (1976) or Burman and Hansbo (2004).

The exemplary computations are depicted in Fig. 8.10–8.13, regarding both variants of CIP. We call CIP1 the variant with stabilization term of (8.66) term, and CIP2 variant with the (8.67). The computational results shall be discussed, together with the other types of stabilization methods introduced before, in the next section.

(a) $Pe = 10^4$, $h = h_0$ (b) $Pe = 10^5$, $h = h_0$ (c) $Pe = 10^6$, $h = h_0$

(d) $Pe = 10^4$, $h = \frac{h_0}{2}$ (e) $Pe = 10^5$, $h = \frac{h_0}{2}$ (f) $Pe = 10^6$, $h = \frac{h_0}{2}$

(g) $Pe = 10^4$, $h = \frac{h_0}{4}$ (h) $Pe = 10^5$, $h = \frac{h_0}{4}$ (i) $Pe = 10^6$, $h = \frac{h_0}{4}$

FIGURE 8.10. Computational results of concentration distribution for boundary conditions of type BC I – CIP1 stabilization; plotted at time $t = 50$.

(a) Pe $= 10^4$, $h = h_0$

(b) Pe $= 10^5$, $h = h_0$

(c) Pe $= 10^6$, $h = h_0$

(d) Pe $= 10^4$, $h = \frac{h_0}{2}$

(e) Pe $= 10^5$, $h = \frac{h_0}{2}$

(f) Pe $= 10^6$, $h = \frac{h_0}{2}$

(g) Pe $= 10^4$, $h = \frac{h_0}{4}$

(h) Pe $= 10^5$, $h = \frac{h_0}{4}$

(i) Pe $= 10^6$, $h = \frac{h_0}{4}$

FIGURE 8.11. Computational results of concentration distribution for boundary conditions of type BC II – CIP1 stabilization; plotted at time $t = 50$.

(a) Pe $= 10^4$, $h = h_0$ (b) Pe $= 10^5$, $h = h_0$ (c) Pe $= 10^6$, $h = h_0$

(d) Pe $= 10^4$, $h = \frac{h_0}{2}$ (e) Pe $= 10^5$, $h = \frac{h_0}{2}$ (f) Pe $= 10^6$, $h = \frac{h_0}{2}$

(g) Pe $= 10^4$, $h = \frac{h_0}{4}$ (h) Pe $= 10^5$, $h = \frac{h_0}{4}$ (i) Pe $= 10^6$, $h = \frac{h_0}{4}$

FIGURE 8.12. Computational results of concentration distribution for boundary conditions of type BC I – CIP2 stabilization; plotted at time $t = 50$.

(a) Pe = 10^4, $h = h_0$ (b) Pe = 10^5, $h = h_0$ (c) Pe = 10^6, $h = h_0$

(d) Pe = 10^4, $h = \frac{h_0}{2}$ (e) Pe = 10^5, $h = \frac{h_0}{2}$ (f) Pe = 10^6, $h = \frac{h_0}{2}$

(g) Pe = 10^4, $h = \frac{h_0}{4}$ (h) Pe = 10^5, $h = \frac{h_0}{4}$ (i) Pe = 10^6, $h = \frac{h_0}{4}$

FIGURE 8.13. Computational results of concentration distribution for boundary conditions of type BC II – CIP2 stabilization; plotted at time $t = 50$.

8.9. Comparison of the stabilization methods

For comparison of all three stabilization methods, together with the scheme without stabilization, we present Tables 8.1 and 8.2, and the concentration profile cuts in Figures 8.15 and 8.16. For better comparison, all the computations were performed by the same direct solver, and, let us recall once again, we resolve the velocity field together with the concentration distribution at the same time. Nevertheless, the velocity is not influenced by the concentration distribution, since the equations are not fully coupled for this testing cases.

The Table 8.1 presents the maximal and minimal values of numerical solutions for both the computational settings, BC I and BCII. Since the analytical solution is satisfying the principle of maximum/minimum, the interior values of the solution should not cross over the boundary values of the concentration, explicitly, in our case, the values 0 and 0.5. We can see, none of the introduced stabilization conserves positiveness, and generally the driven cavity test sets higher demands on the numerical scheme. This is due the characteristic of the exact solution, having spiral character of sharp and thin layers. Even though the CIP1 stabilization gives much over/under–shooting critical values in comparison with SUPG and GLS, they are all concentrated near the boundary, which suggests that the implementation of boundary conditions is not appropriate, or/and the implementation of the CIP method close to the boundary is not properly "tuned". The comparison is held for the computational setting of $Pe = 10^6$ and the finest assumed mesh.

The comparison of number of degrees of freedom (only for concentration approximation by Q_2 polynomials) and relative computational cpu time[5] presents Table 8.2, concerning the driven cavity test, BC I, only. Since CIP stabilization introduces extra non–zero entries in the resulting approximation system, we present the sparsity of the matrix as well. As we can see, the number of degrees of freedom for basic, non–stabilized, numerical discretization for the mesh density $h = h_0/4$ is $16,641$, and only the SUPG and GLS methods increase it. In the case of GLS, that is caused by the additional gradient discretization (in fact we solve the equation of the fourth order, instead of second order) which is inevitable. On the other hand, the way we discretize the SUPG is not optimal. For the computation of residuum (8.39) we approximate the gradients as well, resulting in more robust approximation scheme. This can be avoided by, for example, the gradient recovery technique. For this reason we call streamline upwind Petrov–Galerkin by SUPG* in the Table 8.2, since, generally, the number of degrees of freedom does not need to be increased. Concerning the relative cpu time of each computation, the CIP method was fastest from all considered stabilization schemes, even though the density of resulting matrix is higher, see Table 8.2. This is due to the fact that the extra non–zero matrix entries represent simple linear symmetric additional coupling between the standard equations.

The concentration profiles on specific domain cuts (see green lines for each specific computational test domain in Fig. 8.14) are depicted in Figures 8.15 and 8.16. From Fig. 8.15 and Tab. 8.1 it is clear, that the CIP1 scheme and GLS are the most diffusive. This results that in the CIP1 case the concentration values on the specific cuts does not become negative but, on the other hand, the localized concentrations spiral layers are not well preserved, concerning driving cavity test. The sharp layers are conserved mostly by the GLS method. While while the SUPG and CIP2 methods are most oscillatory from all the considered stabilizations, for our computations they are least diffusive. Here, again, it is visible that the driven cavity is more computationally challenging than the inflow/outflow test. The comparison of oscillatory profiles is presented in Fig. 8.16. The base lines represent zero concentration. All the comparisons are made for computational setting of $Pe = 10^6$ and finest mesh $h = h_0/4$.

---

[5]Here, one should keep in mind that our aim is not to develop the high–performance computations, rather to compare the resulting numerical solutions.

Method	Driven cavity test		Inflow/outflow test	
	Absolute Min	Absolute Max	Absolute Min	Absolute Max
No stabilization	-0.404	0.737	-0.720	0.649
SUPG	-0.214	0.568	-0.061	0.557
GLS	-0.165	0.514	-0.219	0.523
CIP1	-0.726	0.624	-0.428	0.551
CIP2	-0.144	0.609	-0.264	0.576

TABLE 8.1. Comparison of considered stabilization methods concerning the overshoots and undershoots of numerical solution for both computational setting; SUPG – streamline upwind Petrov–Galerkin, GLS – Galerkin least squares, CIP1/2 – continuous interior penalty (both variants); the analytical bounds of concentration are 0 and 0.5. For both cases, $Pe = 10^6$ and $h = h_0/4$.

Method	DOF	#NZ	rel. cpu time
No stabilization	$16,641$	$263,169$	1.00
SUPG*	$25,091$	$263,169$	2.14
GLS	$25,091$	$263,169$	2.13
CIP1/2	$16,641$	$1.034,289$	1.68

TABLE 8.2. Comparison of considered stabilization methods for computational setting BC I, the driven cavity test, concerning the number of degrees of freedom (DOF) for Q_2 approximation of the concentration, the information of sparsity of the matrix of the resulting algebraic system represented by the number of its non–zero entries (#NZ), and relative cpu time of computation with respect to computational time of system without stabilization; SUPG* – streamline upwind Petrov–Galerkin, GLS – Galerkin least squares, CIP1/2 – continuous interior penalty (both variants). Comparison for computational setting $Pe = 10^6$ and $h = h_0/4$.

(a) BC I   (b) BC II
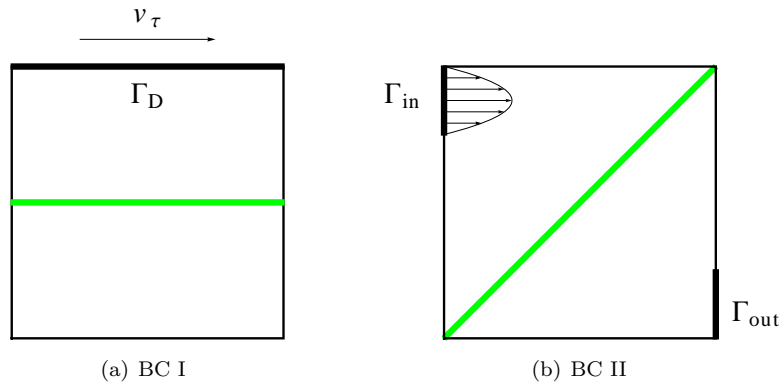
FIGURE 8.14. Domain cuts for driven cavity setting (BC I) at $y = 0$ and inflow/outflow setting (BC II) diagonal cut between points $[-1, -1]$ and $[1, 1]$.
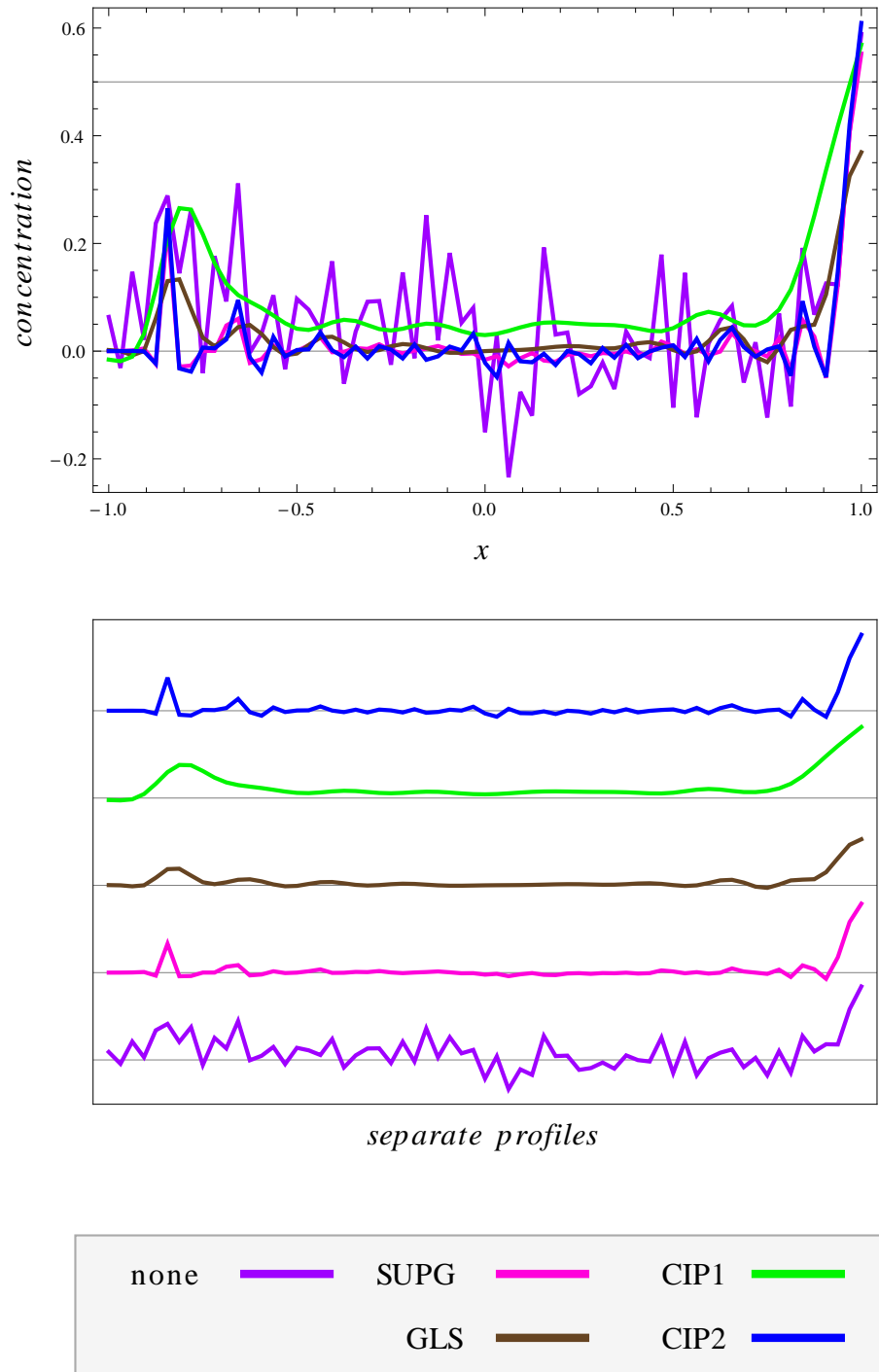
FIGURE 8.15. Concentration profiles of driven cavity test (BC I) for different stabilization methods, profiles on horizontal domain cut at $y = 0$ (see Fig. 8.14 (a)); gridlines represent the analytical bounds of concentration, top: $c_{min} = 0$ and $c_{max} = 0.5$, bottom: base line corresponds to $c = 0$.

FIGURE 8.16. Concentration profiles of inflow/outflow test (BC II) for different stabilization methods, profiles on diagonal domain cut between points $[-1, -1]$ and $[1, 1]$, parametrized from $-\sqrt{2}$ to $\sqrt{2}$, (see Fig. 8.14 (b)); gridlines represent the analytical bounds of concentration, top: $c_{\min} = 0$ and $c_{\max} = 0.5$, bottom: base line corresponds to $c = 0$.

8.10. Finite element method for viscoelastic flow

Generally, the numerical handling of the governing equations for viscoelastic flow is more difficult, since we need to consider additionally to the system of

$$(8.71) \qquad \frac{\partial \boldsymbol{v}}{\partial t} + [\operatorname{grad} \boldsymbol{v}]\boldsymbol{v} = -\operatorname{grad} p + \operatorname{div} \boldsymbol{S},$$

$$(8.72) \qquad \operatorname{div} \boldsymbol{v} = 0,$$

$$(8.73) \qquad \frac{\partial c}{\partial t} + (\operatorname{grad} c) \cdot \boldsymbol{v} = \frac{1}{\operatorname{Pe}} \operatorname{div}\left(D_c \operatorname{grad} c\right),$$

another tensor equation for the extra stress tensor $\boldsymbol{S}$. In the case of Maxwell($\lambda_2 = 0$)/Oldroyd–B fluid it takes the form of

$$(8.74) \qquad \boldsymbol{S} + \lambda_1 \overset{\triangledown}{\boldsymbol{S}} = 2\eta_0 \left(\boldsymbol{D} + \lambda_2 \overset{\triangledown}{\boldsymbol{D}} \right),$$

where λ_1, λ_2 and η_0 are material parameters of the viscoelastic fluid and $\triangledown$ denotes the upper convective derivative. Another three (in the case of $d = 2$) partial differential equations for S_{11}, S_{22} and $S_{12} = S_{21}$ thus need to be solved in coupling with (8.71)–(8.73), which can be handled by the finite element method algorithm as described above. Of course, we need to be careful with the value of characteristic number of viscoelasticity, the Weissenberg number $\mathrm{We} = \varrho \lambda_1 V^*/L^*$ which suggests, as Reynolds or Péclet number, the characteristic of the flow.

In our case, more challenging would be the fact that we consider (in the framework of the linear theory) the Maxwell model as a description of viscoelastic rheology of synovial fluid. It is well known that for $\lambda_2 \to 0$ the equation (8.74) turns to hyperbolic equation which is for the finite element method without suitable stabilization unsolvable. We can stabilize the Navier–Stokes equations similarly as in the case of convection–diffusion equation, or, we can stabilize the equations by the use the Oldroyd model instead of Maxwell with reasonably well chosen parameter λ_2. The latter seems applicable in our case, since Oldroyd–B, as fitted in Chapter 6, was giving similar characteristic as Maxwell model, considering the parameter λ_2 was fitted as $\lambda_2 \approx 10^{-2}$.

If we want to compute the flow of viscoelastic fluid described by Oldroyd–B model, we need to discretize the equation (8.74) as well. Nevertheless, it is more suitable to rewrite the equation for extra stress tensor in term of the conformation tensor $\boldsymbol{Z}$, defined through

$$(8.75) \qquad \boldsymbol{S} = 2k\boldsymbol{D} + m(\boldsymbol{Z} - \boldsymbol{I}),$$

with unknown constants k, m. Then, the convective derivative $\overset{\triangledown}{\boldsymbol{D}}$ in the additional tensor equation vanishes. Let us be more specific and consider that all the material parameters λ_1, λ_2 and η_0 are positive constants. Then the formal substitution of the extra stress tensor in terms of $\boldsymbol{Z}$ in (8.74) leads to ($\overset{\triangledown}{\boldsymbol{I}} = -2\boldsymbol{D}$)

$$(8.76) \qquad m\lambda_1 \overset{\triangledown}{\boldsymbol{Z}} = m(\boldsymbol{I} - \boldsymbol{Z}) + (2\eta_0 - 2m\lambda_1 - 2k)\boldsymbol{D} + (2\eta_0 \lambda_2 - 2k\lambda_1)\overset{\triangledown}{\boldsymbol{D}}.$$

By choosing the form of constants k and m as

$$(8.77) \qquad k = \frac{\eta_0 \lambda_2}{\lambda_1}, \quad m = \frac{\eta_0}{\lambda_1^2}(\lambda_1 - \lambda_2),$$

the terms with $\boldsymbol{D}$ and $\overset{\triangledown}{\boldsymbol{D}}$ in (8.76) vanish.

The system of equations then takes the form

$$(8.78) \qquad \frac{\partial \boldsymbol{v}}{\partial t} + [\operatorname{grad} \boldsymbol{v}]\boldsymbol{v} = -\operatorname{grad} p + 2\operatorname{div}(k\boldsymbol{D}) + \operatorname{div}(m(\boldsymbol{Z} - \boldsymbol{I})),$$

$$(8.79) \qquad \overset{\triangledown}{\boldsymbol{Z}} = \frac{1}{\lambda_1}(\boldsymbol{I} - \boldsymbol{Z}),$$

$$(8.80) \qquad \operatorname{div} \boldsymbol{v} = 0,$$

$$(8.81) \qquad \frac{\partial c}{\partial t} + (\operatorname{grad} c) \cdot \boldsymbol{v} = \frac{1}{\operatorname{Pe}} \operatorname{div}\left(D_c \operatorname{grad} c\right),$$

with k, m defined by (8.77). At this point, we can consider the material parameters λ_1, λ_2 and η_0 to be functions and formally introduce them in the equations.

Chapter 9

Computational simulations

9.1. Introduction to simulations of viscous models

We perform simulations for viscous model of synovial fluid as derived in Chapter 5, by the use of the material parameters setting from the fitting procedures. First, we consider driven cavity problem for domain setting as depicted in Fig. 9.1. For this case we study the influence of two different, having the least diffusive properties, stabilization techniques on the numerical solutions, explicitly the SUPG – streamline upwind Petrov–Galerkin method and the CIP2 – continuous interior penalty method with the weights, from now on called CIP. Later, we study the flow properties of fluid described by the proposed non–linear viscous models for synovial fluid. Next, we consider the domain setting illustrated in Fig. 9.18, where the domain aspect ratio is more realistic considering the synovial joint geometry. For this case we study the computational results for different viscous models for synovial fluid, as closely described in Chapter 5. In this chapter, one should keep in mind, that our aim is not to simulate the flow of synovial fluid in a real geometry, rather to study the properties of the flow itself in some kind of test geometry.

In all cases we assume the fully coupled system of governing equations, explicitly

$$\text{(9.1)} \qquad \frac{\partial \boldsymbol{v}}{\partial t} + [\text{grad}\,\boldsymbol{v}]\boldsymbol{v} = -\,\text{grad}\,p + \frac{2}{\text{Re}}\,\text{div}\left(\mu(c, |\boldsymbol{D}(v)|^2)\boldsymbol{D}(v)\right),$$

$$\text{(9.2)} \qquad \text{div}\,\boldsymbol{v} = 0,$$

$$\text{(9.3)} \qquad \frac{\partial c}{\partial t} + (\text{grad}\,c)\cdot\boldsymbol{v} = \frac{1}{\text{Pe}}\,\text{div}\left(D_c\,\text{grad}\,c\right),$$

with constant diffusivity and non–constant viscosity of suitable, later explicitly chosen form. The Péclet number referring to synovial fluid is of order 10^7.

In following sections, we shall assume the computational setting of driven cavity on a rectangular domain with the aspect ratio $10:1$ or $100:1$, see Fig. 9.1 and Fig. 9.18. We resolve the evolutionary problem with initial conditions of

$$\text{(9.4)} \qquad \boldsymbol{v}(0,x) = 0, \quad c(0,x) = 0.1.$$

The boundary conditions are set as follows: on the upper part Γ_1 of the domain Ω we prescribe the Dirichlet conditions, for both, the velocity and concentration, and, on the walls Γ_2 we assume the zero flux of concentration through the walls and no–slip boundary conditions for the velocity. Moreover, we consider the boundary conditions to be time–dependent, by
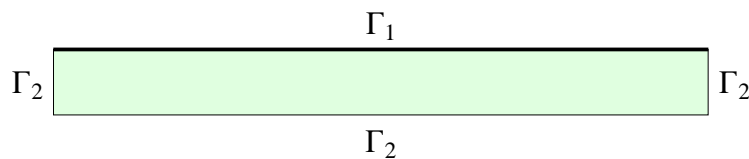
FIGURE 9.1. Domain Ω of tested problem with aspect ratio $10:1$.
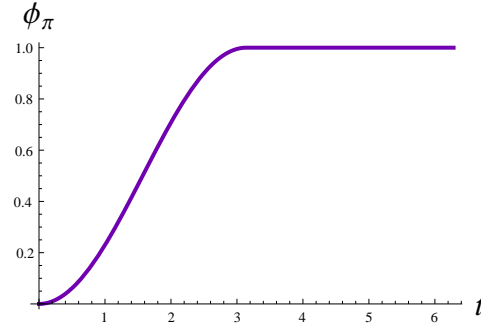
FIGURE 9.2. Time scale function $\phi_\pi(t)$

(a) concentration   (b) velocity
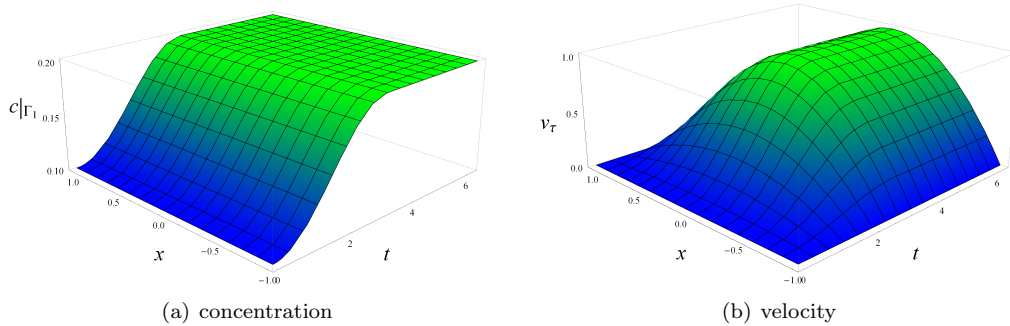
FIGURE 9.3. Time profiles of boundary functions for concentration and velocity on the Γ_1 wall.

which we aim to stabilize the passage from the initial state to the evolutionary state. For this reasons we assume the characteristic curve ϕ_π of a form

$$(9.5) \qquad \phi_\pi(t) = \begin{cases} \frac{1}{2}\left(1 + \cos(t - \pi)\right) & t \in \langle 0, \pi \rangle, \\ 1 & t > \pi, \end{cases}$$

with a graph plotted in Fig. 9.2.

All together, the boundary conditions read

$$(9.6) \qquad c(t, x) = c(0, x)(1 + \phi_\pi(t)),$$
$$v_\tau(t, x) = \bar{v}(x)\phi_\pi(t), \quad v_n|_{\Gamma_1} = 0, \qquad\qquad \forall x \in \Gamma_1,$$

$$(9.7) \qquad \frac{\partial c}{\partial \boldsymbol{n}}\big|_{\Gamma_2} = 0, \quad \boldsymbol{v}|_{\Gamma_2} = \boldsymbol{0} \qquad\qquad \forall x \in \Gamma_2,$$

where $\bar{v}(x) = -(1 + x)(1 - x)$, x parameterizing wall Γ_1, and v_n and v_τ being the normal and tangential components of velocity vector, in this domain setting consilient with the velocity vector components v_y and v_x, respectively. The time–evolution functions of boundary conditions on the moving wall Γ_1 are depicted in Fig. 9.3.

We discretize the domain Ω by a quadrilateral mesh, as shown in Fig. 9.4, quadratically refined in the vertical direction. By this we meet the higher computational requirements of the boundary condition settings.

9.2. Influence of stabilization – Model 2b

Here, let us present the numerical results we obtained by the approximate system described in Chapter 8. We assume for our computations the Model 2b only, since it predicts
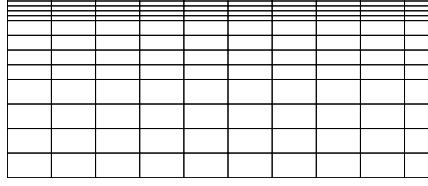
FIGURE 9.4. Cut of the computational mesh covering domain Ω (in vertical direction of full size). For computational reasons, the mesh is quadratically refined in the vertical direction.
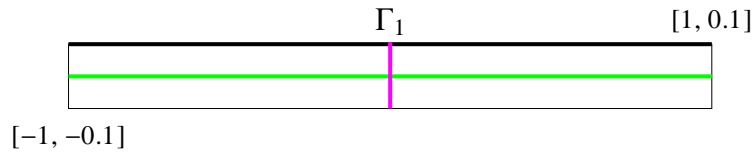
FIGURE 9.5. The geometrical positions of domain cuts; vertical cut (pink) is positioned between points $[0, -0.1]$ and $[0, 0.1]$, and horizontal cut (green) between points $[-1, 0]$ and $[1, 0]$.

the viscous properties of synovial fluid more accurately. We recall the formula for viscosity

$$(9.8) \qquad \mu = \mu_0 \left(\beta + \gamma |\boldsymbol{D}|^2 \right)^{n(c)},$$

where the shear–thinning index is of the form of

$$(9.9) \qquad n(c) = \omega \left(\frac{1}{\alpha c^2 + 1} - 1 \right).$$

From the stabilization techniques, we use the SUPG and CIP, which shall be compared. All figures are plotted for time $t = 100$. The structure of the presented results is following: we present the area distributions of concentration for different mesh refinements, for both, the SUPG and CIP stabilizations, see Fig. 9.6. For better comparison of the methods and meshes, we include the profile cuts of concentration on specific domain cuts as well, see Fig. 9.7 and 9.8. The domain cuts are visualized in Fig. 9.5. The last figure, Fig. 9.9, presents the relative differences between numerical solutions obtained by SUPG and CIP stabilizations, $|c_{\text{SUPG}} - c_{\text{CIP}}|/c_{\text{CIP}}$, for the mesh density of $h = h_0/2$.

As one can see, the trend of influence of the stabilization algorithms with the refinement of the meshes is obvious. The oscillations are becoming less distinguishable, and for the finest considered mesh they almost vanish. Moreover, on the finest mesh, both stabilizations yield almost identical numerical solutions. The differences between solutions are more visible on vertical rather than horizontal cut. This is well observable in the Fig. 9.9, where the relative differences between numerical solutions are plotted. The fashion of the numerical properties of the stabilizations and the mesh density is distinctive, the higher density of the mesh, the more similar the solutions of both stabilizations are.

(a) SUPG, $h = 2h_0$

(b) CIP, $h = 2h_0$

(c) SUPG, $h = h_0$

(d) CIP, $h = h_0$

(e) SUPG, $h = h_0/2$

(f) CIP, $h = h_0/2$
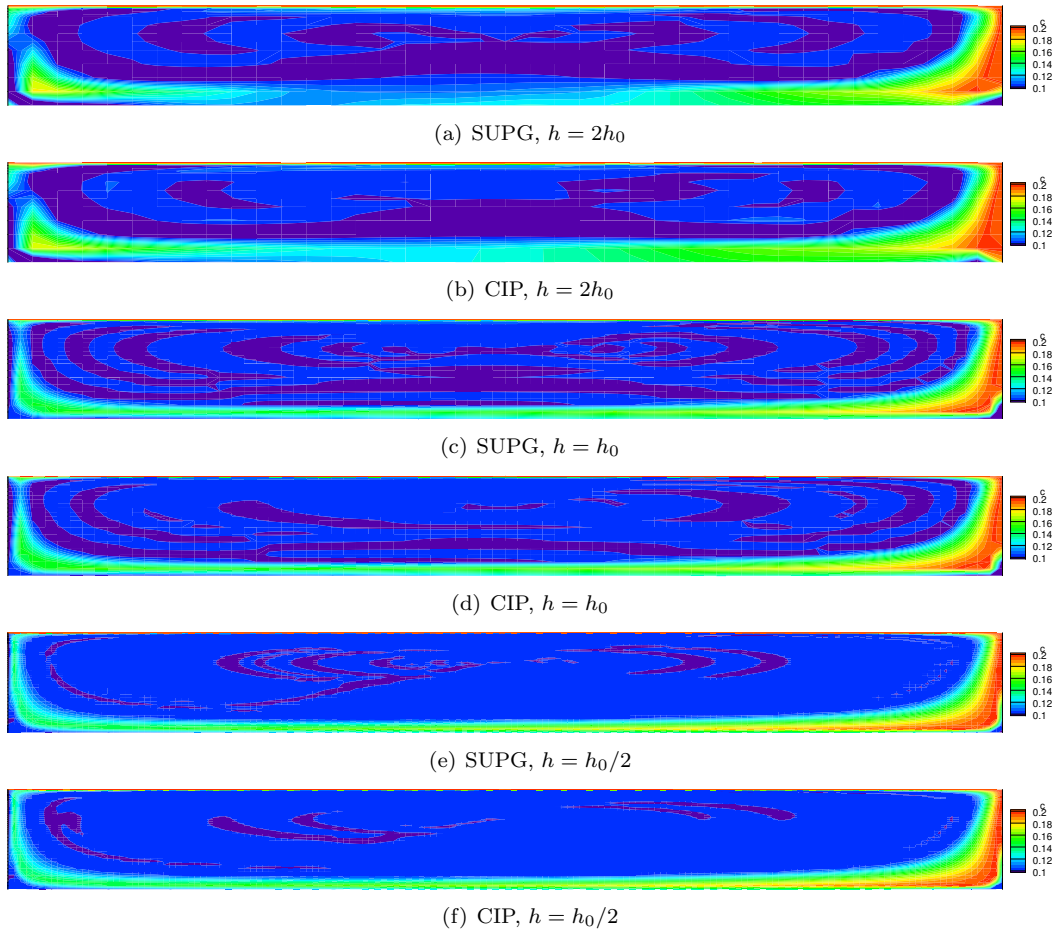
FIGURE 9.6. Distribution of concentration for different mesh densities, $h = 2h_0$, $h = h_0$ and $h = h_0/2$, and both SUPG and CIP stabilizations.
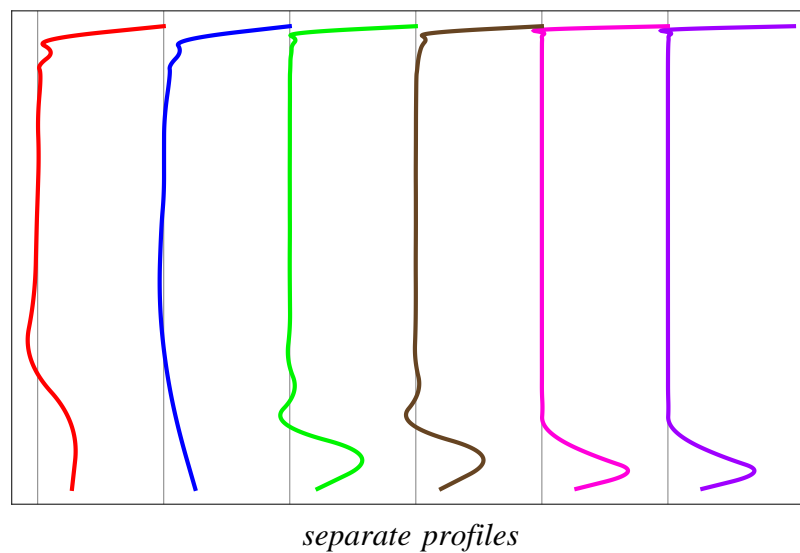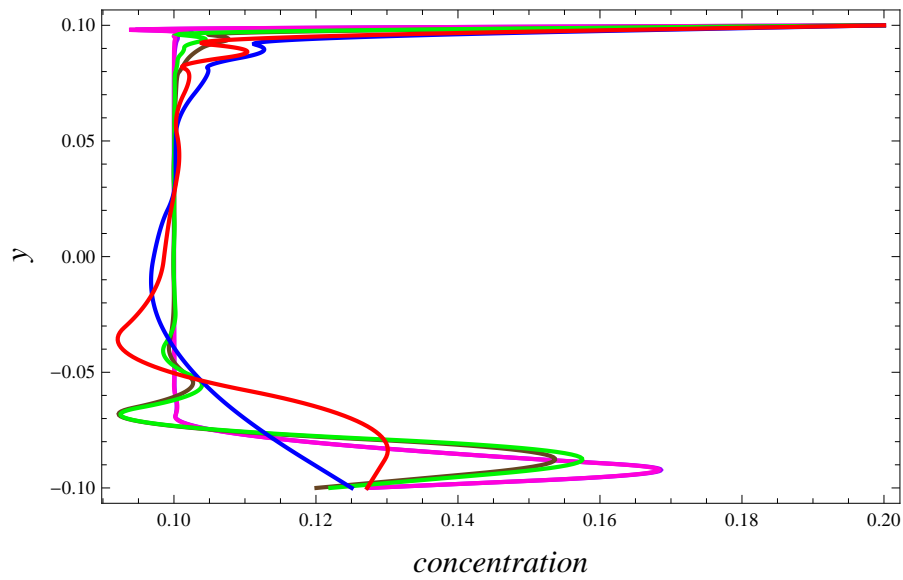
FIGURE 9.7. Concentration profiles on vertical cut of the domain, between points $[0, -0.1]$ and $[0, 0.1]$, for both stabilizations and three different mesh densities. The gridlines represent the concentration value of 0.1.

FIGURE 9.8. Concentration profiles on horizontal cut of the domain, between points $[-1, 0]$ and $[1, 0]$, for both stabilizations and three different mesh densities. The gridlines represent the concentration value of 0.1.
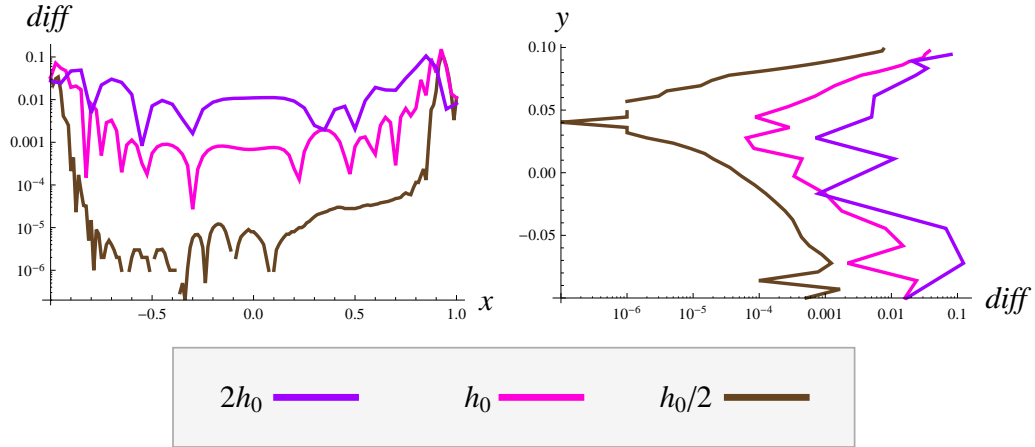
FIGURE 9.9. Relative differences between numerical solutions obtained by the use of SUPG and CIP stabilizations – $|c_{\text{SUPG}} - c_{\text{CIP}}|/c_{\text{CIP}}$.

9.3. Comparison of results for models with different viscosities

In this section, we present the results obtained by the SUPG method for the same geometry setting as above, but for different viscosity models for synovial fluid. We compare the Navier–Stokes fluid

(N–S)
$$\mu = 1,$$

with the viscosity models for synovial fluid from the Chapter 5

(Model 1)
$$\mu = e^{\alpha c}\left(1 + \gamma|\boldsymbol{D}|^2\right)^n,$$

(Model 2a)
$$\mu = \left(\beta + \gamma|\boldsymbol{D}|^2\right)^{\frac{1}{2}\left(e^{-\alpha c}-1\right)},$$

(Model 2b)
$$\mu = \left(\beta + \gamma|\boldsymbol{D}|^2\right)^{\omega\left(\frac{1}{\alpha c^2+1}-1\right)}.$$

We, again, present the area distributions and profiles on domain cuts, this time for all, concentration, velocity, viscosity and shear–thinning index, see Fig. 9.3–9.17. For better comparison, all the area distribution plots concerning the visualization of the same physical quantity are made with the same color scale. Regarding the concentration and viscosity profiles on domain cuts, the zooms at particular domain walls are included.

Concerning the concentration profiles in Fig. 9.3–9.11, only one dominant undershoot occurs, close to the boundary Γ_1, as closely visible in profiles on vertical domain cut. This is due to the boundary condition we impose on the wall. Figures 9.14–9.15 present the viscosity distributions. We can notice the differences of the models quite distinctively. This is due to the concentration and velocity/shear rate influence. In the profile on vertical domain cut, the first peak in viscosity is the result of different velocity profiles for particular models, more precisely, different maximas in the velocity cause different values of the shear rates, which are the cases where the viscosity models exhibit most differences. The second peak, the one closer to the lower wall, is a result of different concentration profiles. The next set of figures 9.12–9.13 represents the velocity distributions. While the first figure is picturing the area distribution of the velocity magnitude, the second figure of the set presents the profiles of particular velocity components on the vertical and horizontal domain cuts. In comparison of all models with the Navier–Stokes, the velocity profiles are more flattened and exhibiting smaller velocity maximas. Moreover, the slowest flow is obtained by the viscosity Model 1 which is due to the smallest value of shear–thinning index from all the models being compared, see sets of figures Fig. 9.16–9.17. Here, the variance of values of shear–thinning indexes is significant, where the smallest values refer to the Model 1.

(a) N–S

(b) Model 1

(c) Model 2a

(d) Model 2b
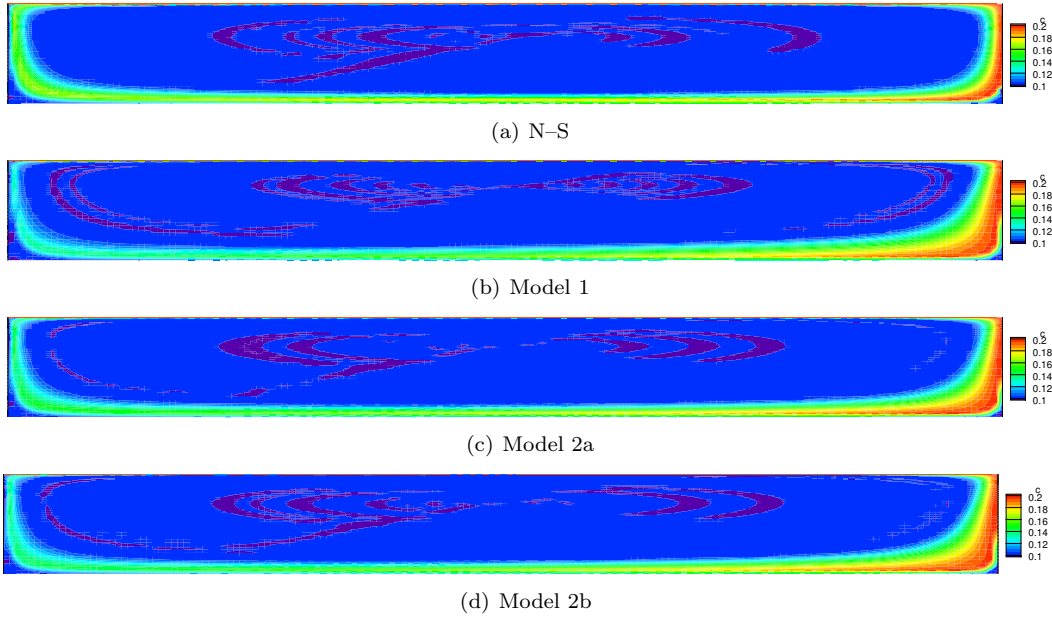
FIGURE 9.10. Concentration distribution for different viscosity models.
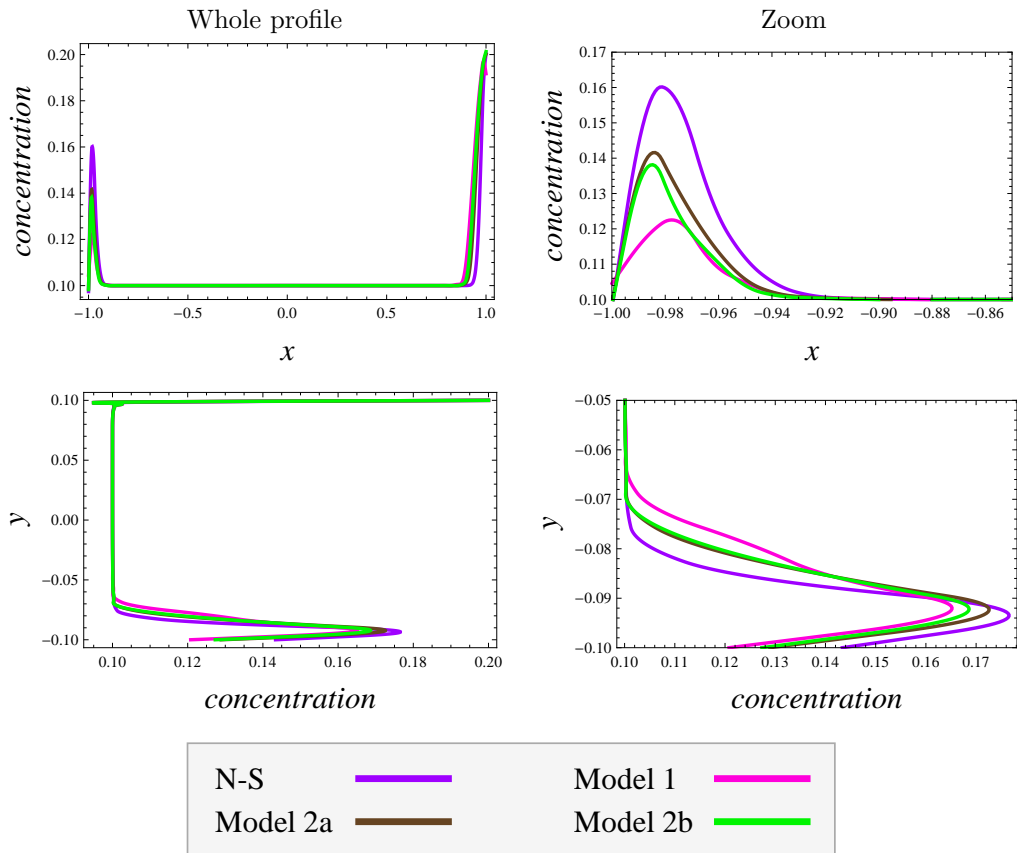
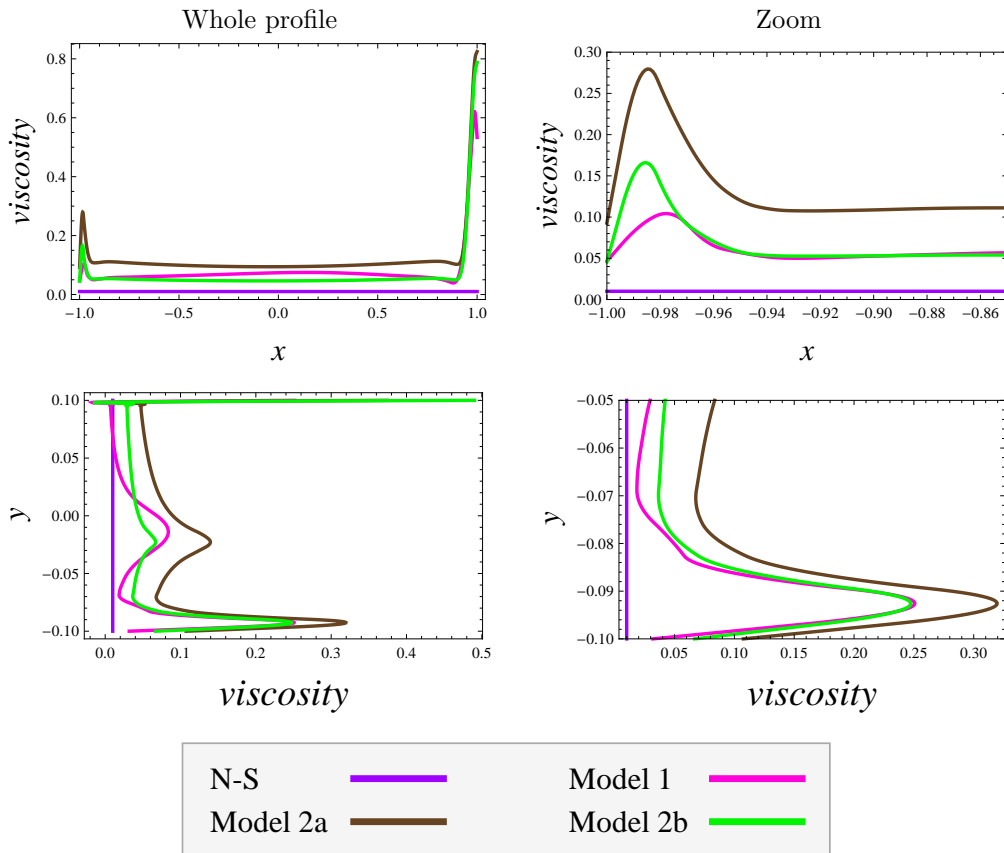

FIGURE 9.11. Concentration profiles on vertical and horizontal cuts of the computational domain. Top: Horizontal, bottom: vertical cuts, left: whole profile on the specific cut, right: zoom at the left/bottom edge.
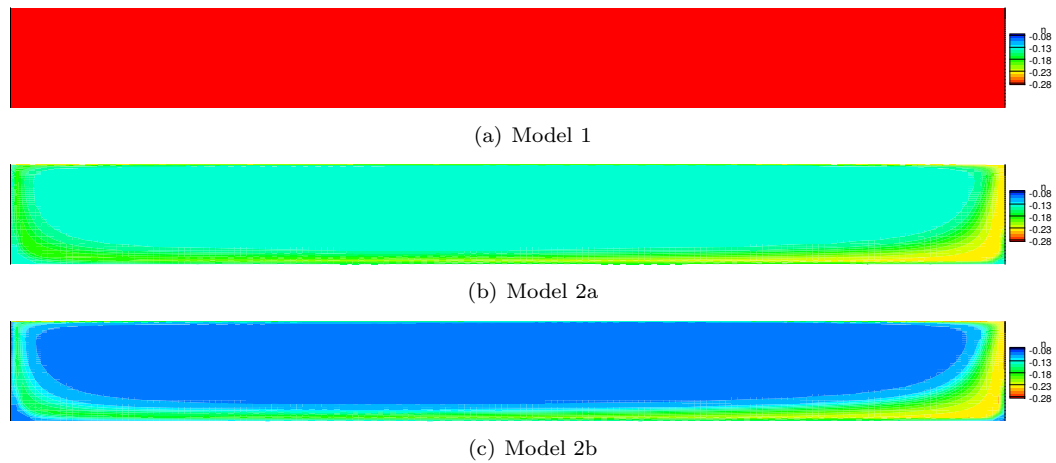
(a) N–S

(b) Model 1

(c) Model 2a

(d) Model 2b
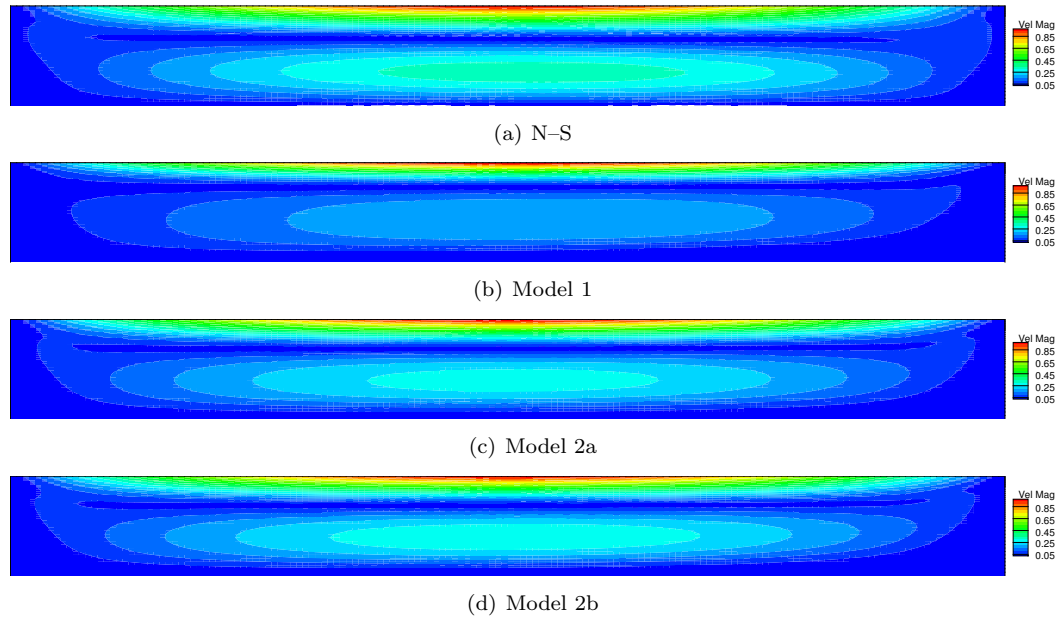
FIGURE 9.12. Magnitude of velocity for different viscosity models.
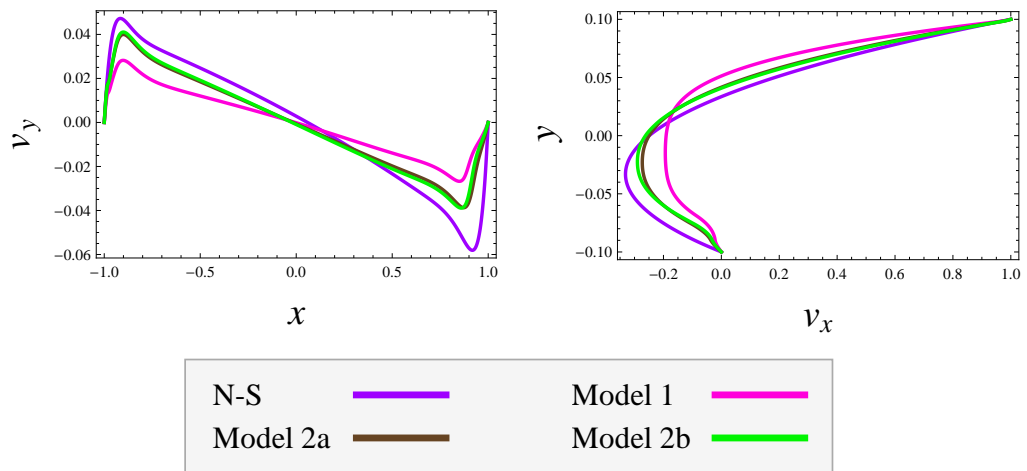
FIGURE 9.13. Velocity profiles on vertical and horizontal cuts of the computational domain. Left: v_y velocity profile on horizontal cut, right: profile of v_x component of velocity on vertical cut.

(a) N–S

(b) Model 1

(c) Model 2a

(d) Model 2b
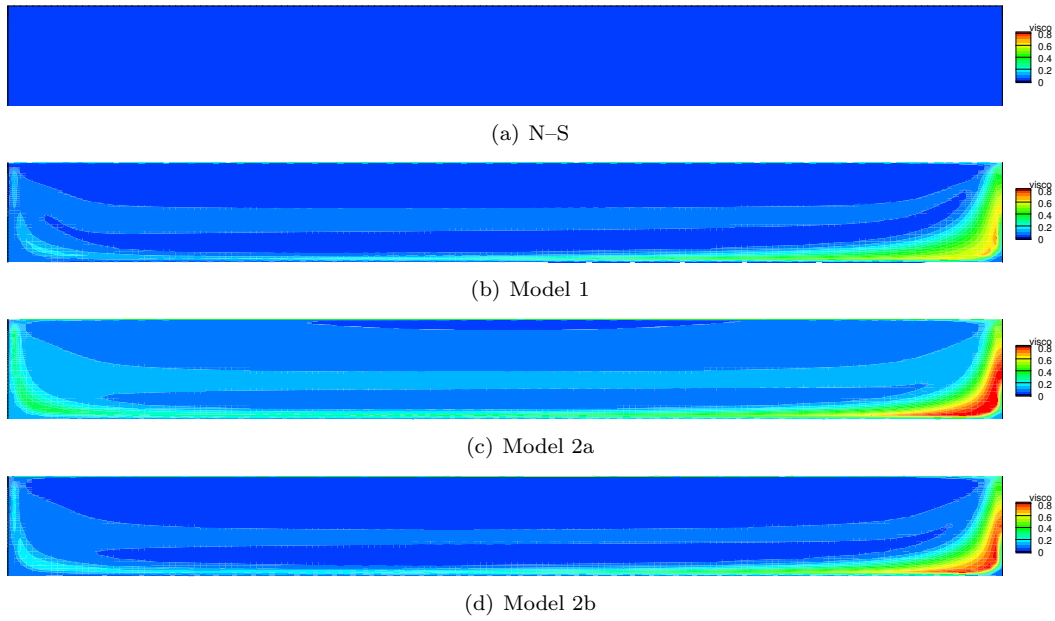
FIGURE 9.14. Viscosity for different models.

FIGURE 9.15. Viscosity profiles on vertical and horizontal cuts of the computational domain. Top: Horizontal, bottom: vertical cuts, left: whole profile on the specific cut, right: zoom at the left/bottom edge.

(a) Model 1

(b) Model 2a

(c) Model 2b

FIGURE 9.16. Shear–thinning index for different viscosity models.
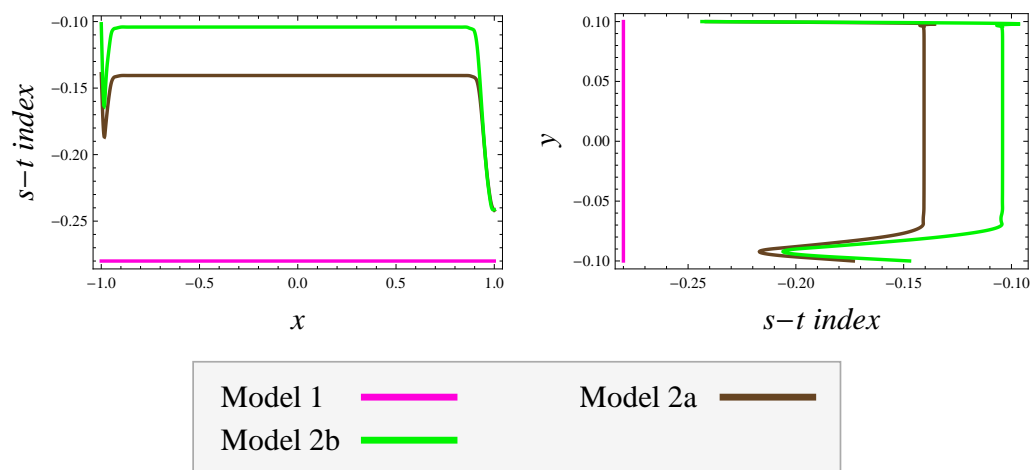
FIGURE 9.17. Shear–thinning index profiles on vertical and horizontal cuts of the computational domain. Left: shear–thinning index profile on horizontal cut, right: profile on vertical cut.

$$\Gamma_1$$

$$\Gamma_2 =\!= \Gamma_2$$

$$\Gamma_2$$
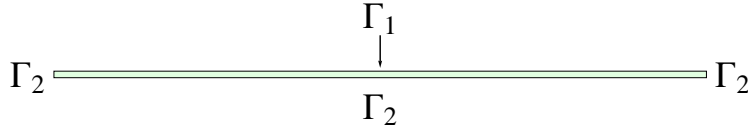
FIGURE 9.18. Domain Ω of tested problem with edge ratio $100 : 1$.

9.4. Geometry influence

In this section, we study the influence of the ratio of domain walls on the numerical solution, as the joint cavities are in reality very thin domains, see Fig. 2.1. For this reason, we change the computational domain geometry to a domain setting as depicted in Fig. 9.18, with an aspect ratio of $100 : 1$. The rest of the computational setting remains the same as in the previous section. Again, we present the same figure sets for concentration (Fig. 9.19 and 9.20), velocity (Fig. 9.21 and 9.22), viscosity (Fig. 9.23 and 9.24) and shear–thinning index (Fig. 9.25 and 9.26), presenting the whole area distributions and zooms at the right–hand side of the domain and the profiles of solutions on the same vertical and horizontal domain cuts as before, this time defined between the points $[0, -0.01] \leftrightarrow [0, 0.01]$ and $[-1, 0] \leftrightarrow [1, 0]$, respectively.

As we can see, the computational results exhibit less oscillatory behavior in comparison to the previous ones, which is caused by the gradual changes in the solution profiles. Nevertheless, the characteristic of profiles is similar to the computational results of setting with aspect ratio $10 : 1$. All the plots are presented for the results obtained by the SUPG stabilization method, however, the differences in numerical solutions obtained by the CIP and SUPG are of very small order. This is presented in Fig. 9.4 where the relative differences of numerical solutions of concentration, in a sense of $|c_{\mathrm{SUPG}} - c_{\mathrm{CIP}}|/c_{\mathrm{CIP}}$, are compared for SUPG and CIP and for two different mesh densities.

(a) N–S

(b) Model 1

(c) Model 2a

(d) Model 2b
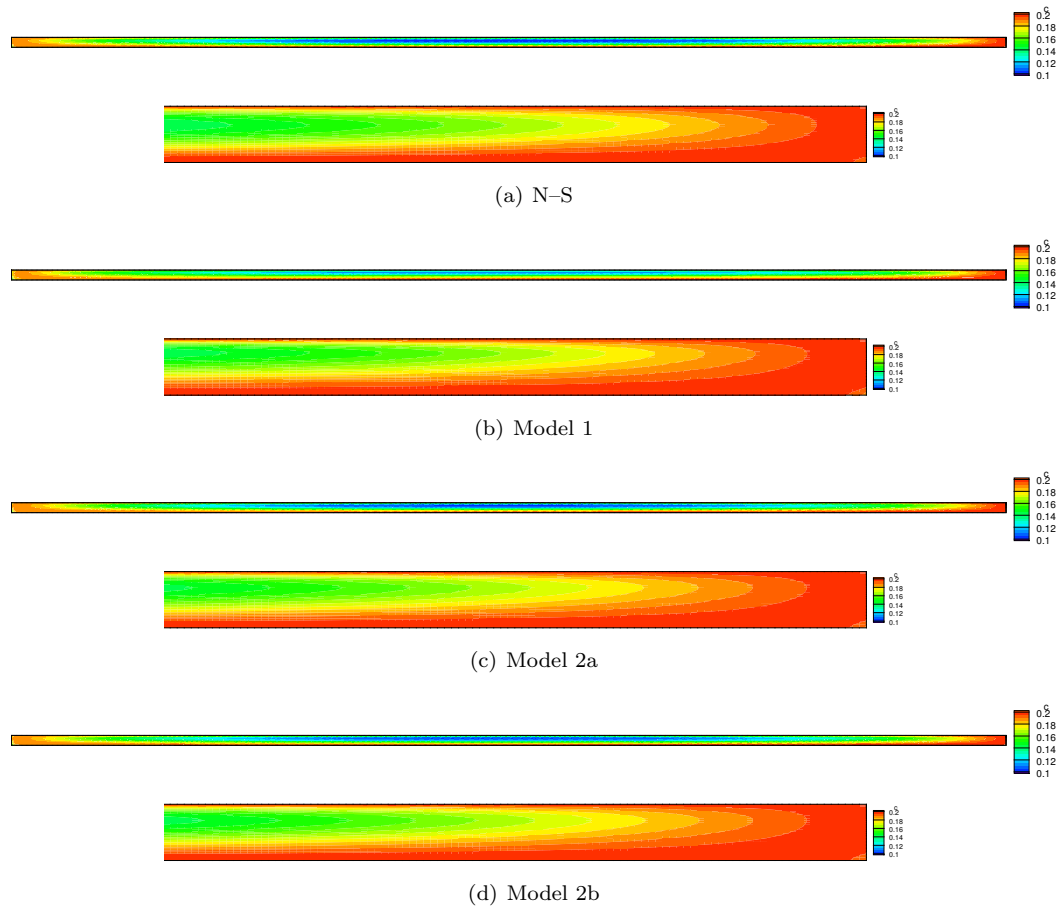
FIGURE 9.19. Concentration distribution for different viscosity models, the whole domain figures and zooms of figures at right–hand sided wall.
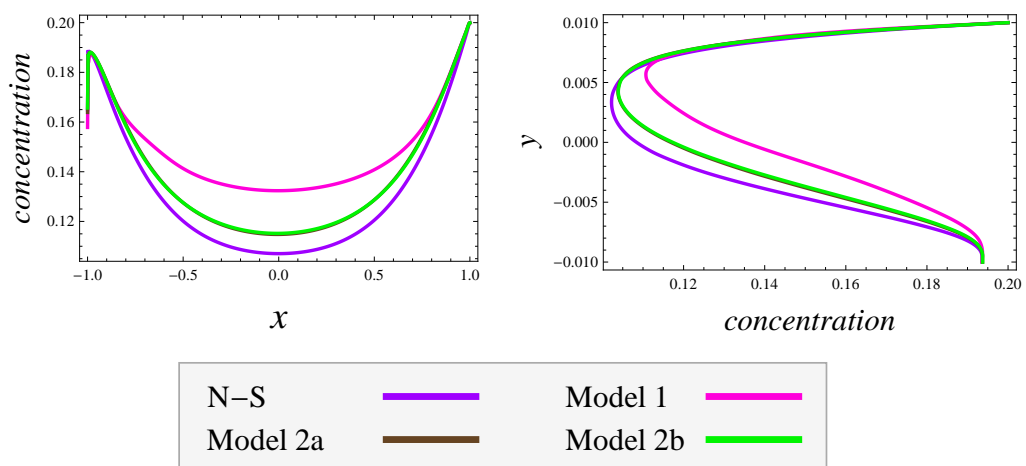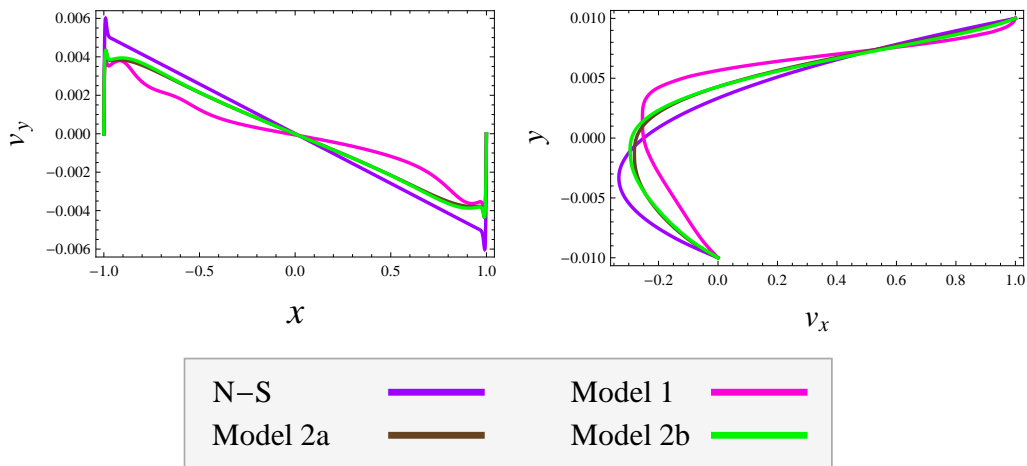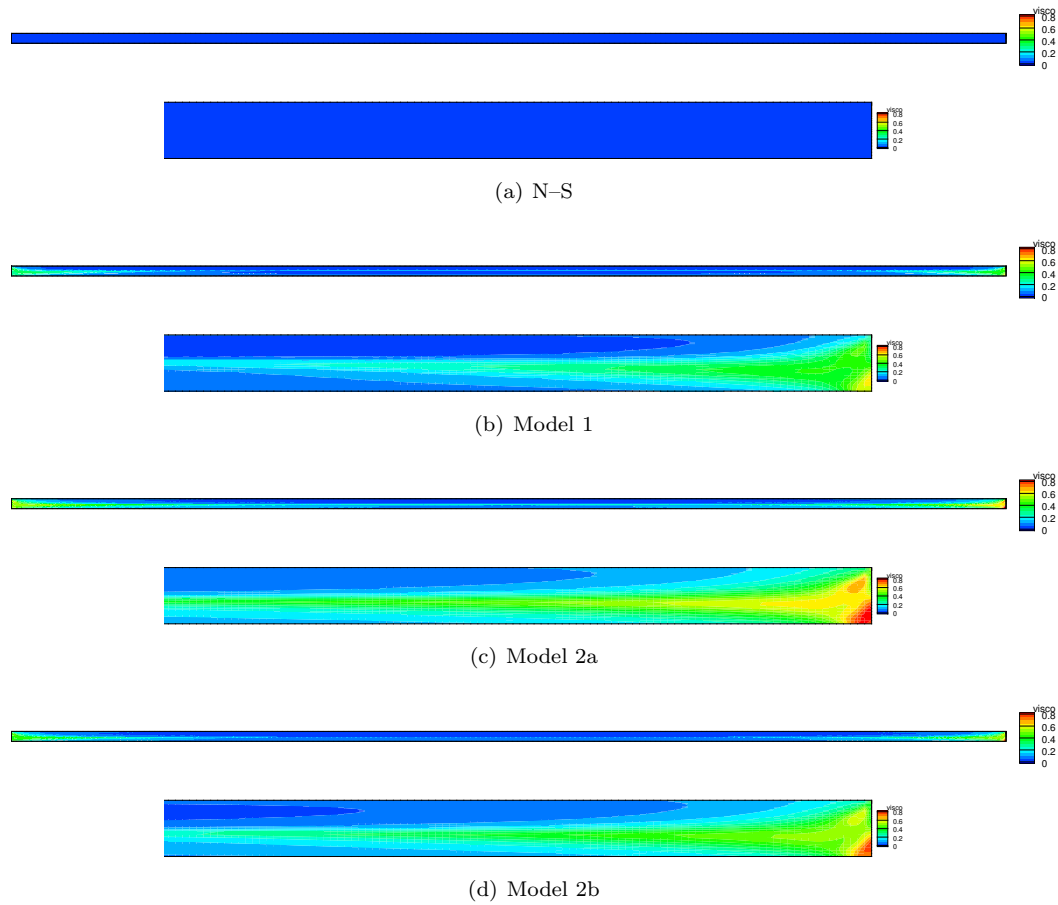

FIGURE 9.20. Concentration profiles on vertical and horizontal cuts of the computational domain.
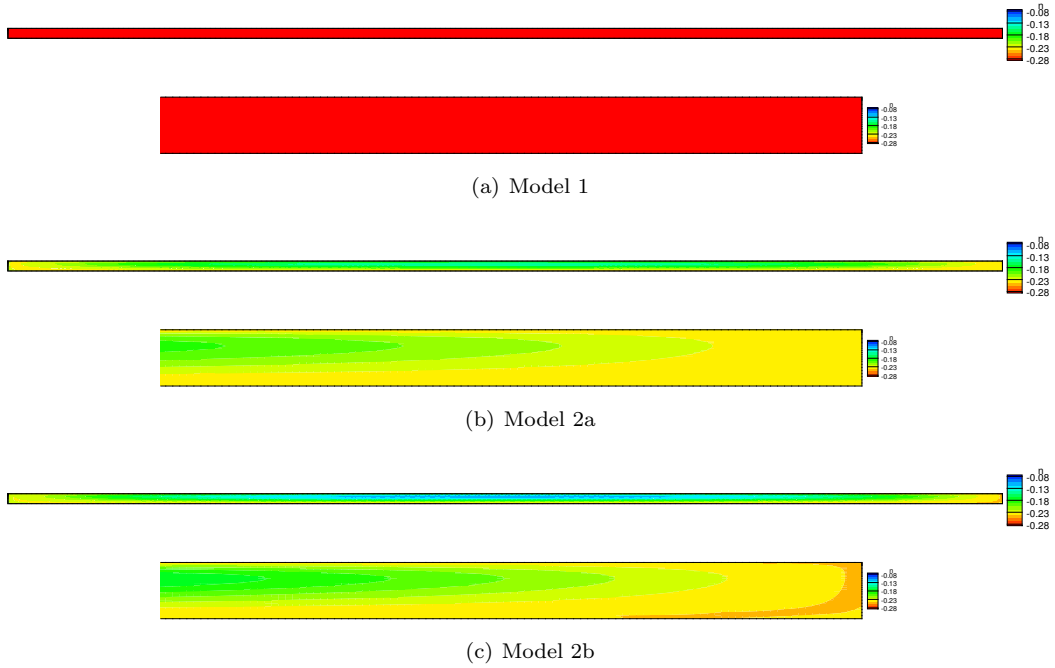
(a) N–S

(b) Model 1

(c) Model 2a

(d) Model 2b
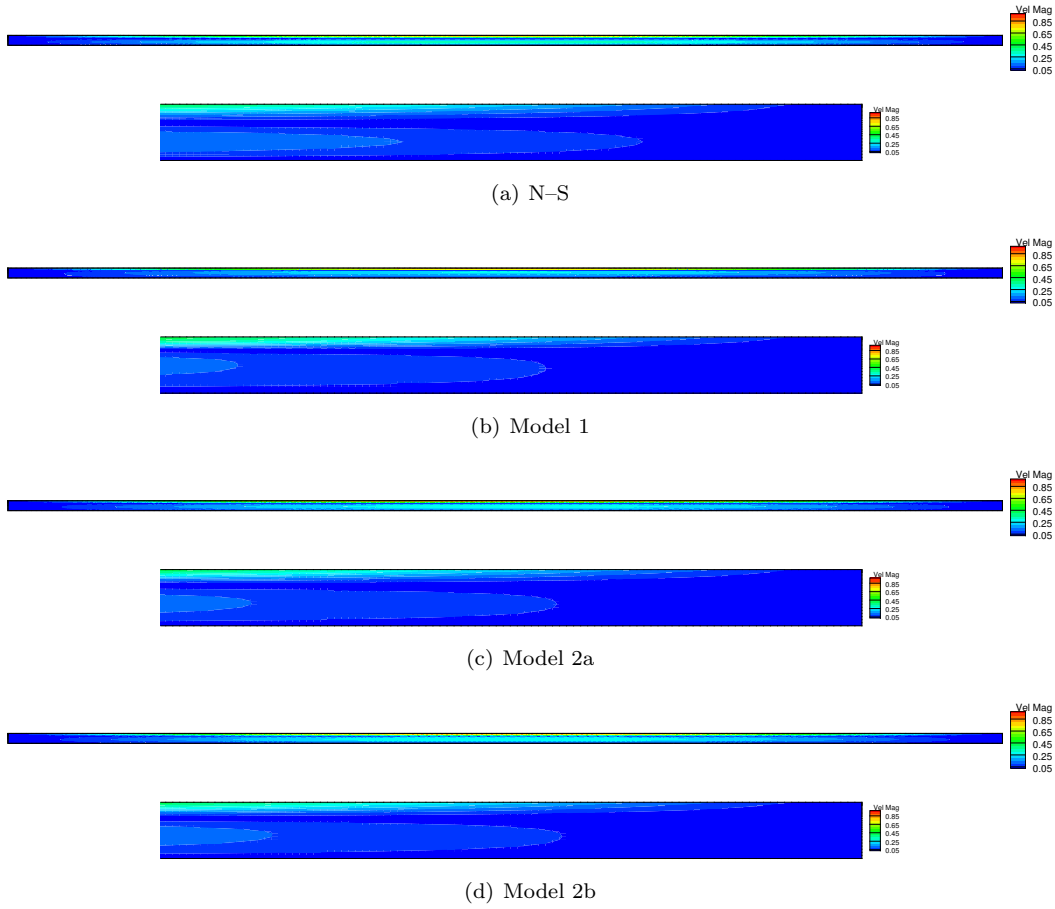
FIGURE 9.21. Magnitude of velocity distribution for different viscosity models, the whole domain figures and zooms of figures at right–hand sided wall.

FIGURE 9.22. Profiles of velocity vector components on vertical and horizontal cuts of the computational domain. Left: the v_y component on horizontal cut, right: the v_x component on vertical cut.

(a) N–S

(b) Model 1

(c) Model 2a

(d) Model 2b

FIGURE 9.23. Viscosity for different models, the whole domain figures and zooms of figures at right–hand sided wall.
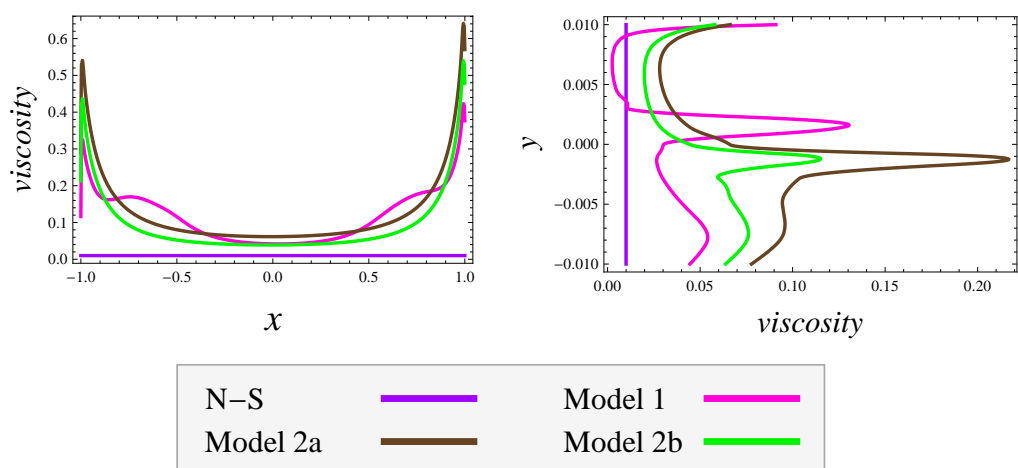
FIGURE 9.24. Concentration profiles on vertical and horizontal cuts of the computational domain.

(a) Model 1

(b) Model 2a

(c) Model 2b

FIGURE 9.25. Shear–thinning index distribution for different viscosity models, the whole domain figures and zooms of figures at right–hand sided wall.
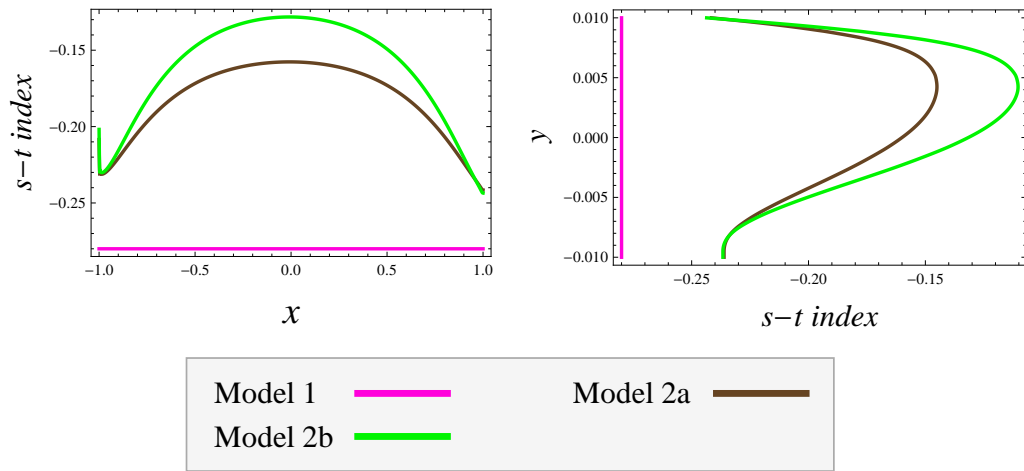
FIGURE 9.26. Profiles of shear–thinning index of different models on vertical and horizontal cuts of the computational domain.
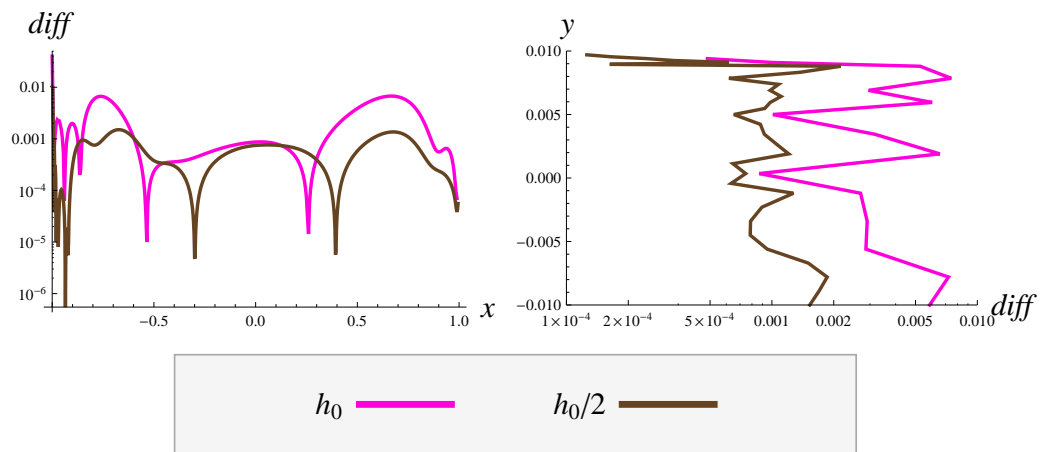
FIGURE 9.27. Relative differences between numerical solutions obtained by
the use of SUPG and CIP stabilizations; $diff = |c_{\mathrm{SUPG}} - c_{\mathrm{CIP}}|/c_{\mathrm{CIP}}$.

Chapter 10

Synovial membranes modeling

10.1. Introduction to membrane modeling

Membranes play an important role in many applications. For example, biological membranes act as selective barriers between or around living cells, artificial membranes are used for separation purposes in laboratory or in industry, like in dialysis, water purification, seawater desalinization or removing of microorganisms from dairy products. Their structure alters with the application, above all adapted to the chemical composition of the fluid mixture passing through. This indicates that modeling of membrane transport can not be unified in a general way, instead it has to be suited to the specific problem. In the case of synovial membrane, the solution is very diluted, i.e. the mass concentration of the solute is very low, and the molecules of hyaluronan are large with respect to the membrane pores and thus high amount of hyaluronan molecules is "reflected"[1] back to the joint cavity while the ultafiltrated plasma, the "volume background", can diffuse freely through the membrane. Moreover, the transport of the fluid is passive, no special active transport is involved in the process. Due to these reasons we shall study the flow of volume (solvent – the Newtonian plasma ultrafiltrate) and the diluted chemical (solute – the hyaluronan) in domains separated by a leaky semipermeable[2] membrane which can be modeled as an interface allowing solvent to go through, but rejecting high amount of solute.

The most commonly used driving forces of the flow through semipermeable membrane are pressure and concentration gradients. This process is known as filtration, and in the literature, see e.g. Kedem and Katchalsky (1958), Patlak et al. (1963), Cheng (1998), Kocherginsky (2010), is described by two equations, one for solute flux and one for volume flux (their explicit formulas shall be introduced later). They involve three parameters which model the membrane properties: the filtration coefficient or hydraulic conductivity of the membrane, the solute reflection coefficient (describing the property of the membrane to partly reject the solute), and the solute permeability of the membrane. Although general, this approach describing total volume fluxes through the membrane is limited due to the fact that the effects considered processes are taken in average. This might be sufficient, e.g. for experimental needs when one needs to predict approximative total flux through the membrane. However, if we want to model the flow of the solvent and transport of concentration in domains separated by a membrane, we need suitable transmission conditions at the membrane, which lead to well posed models. In the case of reaction–diffusion processes in domains separated by the membrane, the effective transmission conditions were derived in Neuss-Radu and Jäger (2008) and Neuss-Radu et al. (2010) by means of multi–scale techniques, starting from a microscopic model of the processes in the membrane, and letting the scale parameter (ratio between the thickness of the membrane and the dimension of the domain) tend to zero. The flow

---

[1] Reflection of the membrane is standard term used in the membrane classification, it describes the property of membrane to separate particular component(s) form the fluid mixture.

[2] The semipermeable membrane is a membrane that allows certain type of molecules or ions to pass through by diffusion while other molecules can not penetrate. The term "leaky" reflects that even the second type of molecules/ions can pass but only of some fraction which is being usually very small.

of miscible mixtures through membrane could be also studied in the context of the theory of mixtures, see e.g. Rajagopal et al. (1983), and Tao et al. (2001). In this concept, the processes inside the membrane are resolved starting from the balance of mass, momentum and energy. However, this approach has its own difficulties, namely the specification of boundary conditions.

For our application, we propose a new mathematical model for flow and transport processes in domains separated by a zero–thickness interface representing leaky semipermeable membrane. The model of the processes in the bulk domains consists of the the Navier–Stokes equations describing the flow of diluted solution, together with the convection–diffusion equation modeling the solute transport, as introduced in the Chapter 7. This system of non–dimensionalized governing equations takes the form

$$
(10.1) \qquad \frac{\partial \boldsymbol{v}}{\partial t} + [\operatorname{grad} \boldsymbol{v}]\boldsymbol{v} = -\operatorname{grad} p + 2\frac{1}{\mathrm{Re}}\operatorname{div}\left(\mu(c, |\boldsymbol{D}|^2)\right),
$$

$$
(10.2) \qquad \operatorname{div} \boldsymbol{v} = 0,
$$

$$
(10.3) \qquad \frac{\partial c}{\partial t} + (\operatorname{grad} c)\cdot \boldsymbol{v} = \frac{1}{\mathrm{Pe}}\operatorname{div}\left(D_c(c, |\boldsymbol{D}|^2)\operatorname{grad} c\right),
$$

where $\boldsymbol{v}$ is the velocity vector of the solvent, p hydrodynamical pressure, c concentration of the solute and $\boldsymbol{D}$ symmetric part of the velocity gradient. The system of governing equations (10.2)–(10.3) has to be complemented with initial conditions, boundary conditions at the outer boundaries, and, mainly, by transmission conditions at the separating membrane. These transmission conditions shall create the membrane model, formulated on the macroscopic scale, assuming the membrane to be fixed and rigid interface, separating the flow domains. Thus, the processes inside the membrane are not resolved, however, their effective contributions are included phenomenologically in the transmission conditions. We consider the membrane to be symmetric, i.e. the transmission properties of the membrane from both sides are the same, without the influence of its possible curvature on the flow of the solvent, which is however up to now an open question.

In the formulation of the transmission conditions across the membrane, the following aspects shall be taken into account: first, the separating properties of the membrane with respect to the solvent, which lead to the buffering of solute concentration at the membrane and second, connected with the first aspect, the influence of the concentration accumulation on the volume flow, known as osmotic effect. Such transmission model has similar features with other models existing in the literature, see e.g. Kedem and Katchalsky (1958). However, the important difference is that we shall not formulate equations only for the total volume fluxes across the membrane, as it is done in the existing literature, but we give transmission conditions which can be used to describe the influence of the membrane on the processes in the bulk regions.

The model, first derived for a Newtonian fluid, is introduced gradually, starting with the formulation of the transmission conditions for the situation when the osmotic effect is neglected, which means that, at the beginning, only the process of concentration buffering is modeled. Next, the general model including the osmotic effect is formulated. Via the osmotic pressure, which is a function of solute concentration, the flow equations for the solvent are also coupled with the transport equation for the solute, yielding a fully coupled model. This model is then applied on the synovial membrane case. Partial results of this chapter were already published in Hron et al. (2011).

10.2. Modeling of concentration buffering

At this point, the solution parameters – density, kinematic viscosity and diffusivity are considered to be constant as we aim to model the effects of the transport through the membrane, free of other rheological effects.

The effect of concentration buffering (sometimes called the concentration polarization) is caused by the free transport of the solvent through the membrane while the solute carried by the solvent to the membrane is partially rejected by the membrane and consequently accumulated in front of it.
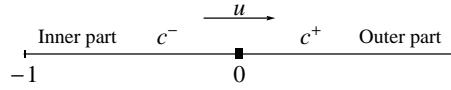
FIGURE 10.1. One–dimensional description of membrane surroundings. Membrane is placed at point $x = 0$.

Let us consider the one–dimensional stationary case, where we can find the analytic solution of the system and therefore identify the proper transmission conditions. Then, we shall generalize the model to higher dimensions.

10.2.1. 1D model. For the stationary case in one dimension, due to the incompressibility of the fluid, the system of the Navier–Stokes equations provides unique constant solution of the velocity, which we denote by u. The governing equation for the concentration reduces to the ordinary differential equation where enters the known constant velocity u. Our domain of interest is the interval $\langle -1, 1 \rangle$, where we place the membrane at position $x = 0$ as schematically depicted in Fig. 10.1. Since the solvent can go through the membrane freely, the velocity remains constant in the whole domain. We set the solvent velocity in the direction of the positive axis.

We denote by c^- the concentration on the interval $\langle -1, 0 \rangle$, and by c^+ the concentration on the interval $\langle 0, 1 \rangle$, in front and after the membrane, respectively. The governing model for concentrations c^- and c^+ together with outer boundary conditions can be written in the form

(10.4) $\qquad -1 \leq x \leq 0$ $\begin{cases} -\dfrac{1}{\mathrm{Pe}} \dfrac{\mathrm{d}^2 c^-}{\mathrm{d}x^2} + u \dfrac{\mathrm{d}c^-}{\mathrm{d}x} = 0, \\[2ex] c^-(-1) = c_{in}, \\[2ex] -\dfrac{1}{\mathrm{Pe}} \dfrac{\mathrm{d}c^-}{\mathrm{d}x}(0) + \sigma u c^-(0) = 0, \end{cases}$

(10.5) $\qquad 0 \leq x \leq 1$ $\begin{cases} -\dfrac{1}{\mathrm{Pe}} \dfrac{\mathrm{d}^2 c^+}{\mathrm{d}x^2} + u \dfrac{\mathrm{d}c^+}{\mathrm{d}x} = 0, \\[2ex] -\dfrac{1}{\mathrm{Pe}} \dfrac{\mathrm{d}c^+}{\mathrm{d}x}(1) = 0, \\[2ex] -\dfrac{1}{\mathrm{Pe}} \dfrac{\mathrm{d}c^+}{\mathrm{d}x}(0) + u c^+(0) = u(1-\sigma)c^-(0), \end{cases}$

where σ is called the membrane reflection coefficient, describing the property of the membrane to be leaky semipermeable. More precisely, the parameter σ takes the values between 0 and 1, and it specifies the fraction of the convective flux of the solute molecules which is rejected by the membrane. Accordingly, $(1 - \sigma)$ specifies the fraction being allowed to pass through the membrane. The ideal semipermeable membrane (i.e. membrane that perfectly separates solute from solvent) would be then described by the reflection coefficient $\sigma = 1$.

The conditions for concentrations on the membrane imply the natural assumption on the continuity of the solute fluxes $\frac{1}{\mathrm{Pe}} \frac{\mathrm{d}c^-}{\mathrm{d}x}(0) - u c^-(0) = \frac{1}{\mathrm{Pe}} \frac{\mathrm{d}c^+}{\mathrm{d}x}(0) - u c^+(0)$ across the membrane. The membrane condition for the "inflow" concentration c^- specifies that only σ fraction of the convective transport is rejected by the membrane, and thus only this part is active in the convection–diffusion balance. On the other hand, the rest, the $(1 - \sigma)$ fraction, is allowed to pass and thus this fraction is governing the total flux of the concentration c^+ on the right–hand side of the membrane.

The analytic solution of system (10.4)–(10.5) is

(10.6) $\qquad c^-(x) = -\dfrac{c_{in}(1 - \sigma + \sigma e^{x\, u\, \mathrm{Pe}})}{-1 + \sigma - \sigma e^{-u\, \mathrm{Pe}}}, \qquad c^+(x) = -\dfrac{c_{in}(1 - \sigma)}{-1 + \sigma - \sigma e^{-u\, \mathrm{Pe}}}.$

(a) $u = 1$, Pe $= 1$

(b) $u = 5$, Pe $= 1$
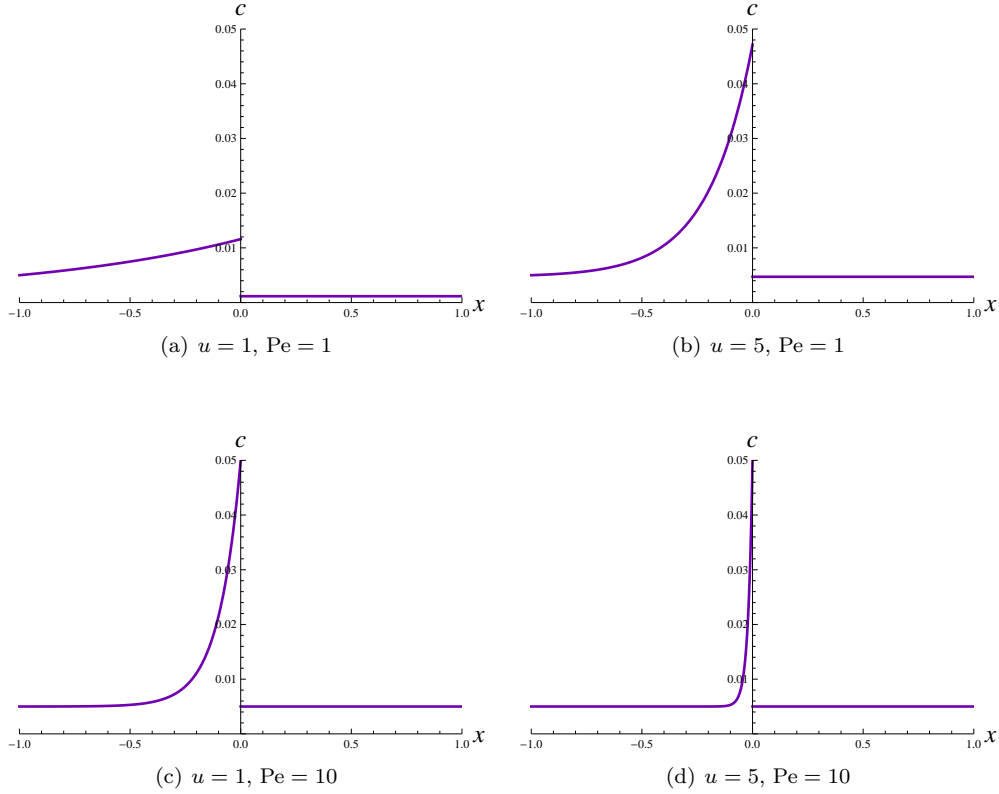
(c) $u = 1$, Pe $= 10$

(d) $u = 5$, Pe $= 10$

FIGURE 10.2. Profiles of concentration buffering; membrane is placed at position $x = 0$. Four plots for different velocity and Péclet number (diffusivity) setting. The Range of concentration corresponds to diluted solution of 1% mass concentration.

The plotted solutions for different parameter values are given in Fig. 10.2. We remark the formation of the concentration polarization layer, and the discontinuity in the solute concentration at the membrane. As one can see, the influence of velocity and diffusivity on the concentration polarization layer are of the similar effect, with higher velocity and lower diffusivity the boundary layer is more distinguishable and more steep. This behavior qualitatively agrees to the experimental results found for example in Scott et al. (2000a). In the next section, the transmission conditions for the concentration at the membrane are generalized to higher dimensional setting.

10.2.2. Generalization of the transmission conditions to higher dimensions. For higher dimensions, we consider domain Ω consisting of two subdomains Ω^+, and Ω^- in $\mathbb{R}^d$ separated by an interface Γ_m representing the membrane, see the two–dimensional configuration in Fig. 10.3. Thus, we have $\Omega = \Omega^+ \cup \Gamma_m \cup \Omega^-$. The restrictions of functions defined on Ω to the subdomains Ω^+, and Ω^- are denoted by the superscripts $+$ and $-$, respectively.

The transmission conditions for the solvent flow at the membrane now consist of the continuity of the normal component and no–slip condition in the tangential direction with the respect to the membrane interface for the velocity and of the continuity of normal stresses

$$(10.7) \qquad \boldsymbol{v_\tau}^+ = \boldsymbol{v_\tau}^- = \boldsymbol{0}, \qquad \boldsymbol{v}^+ \cdot \boldsymbol{n}^+ = -\boldsymbol{v}^- \cdot \boldsymbol{n}^- = \boldsymbol{v} \cdot \boldsymbol{n}^+,$$

$$(10.8) \qquad [-(p^- - p^+)\boldsymbol{I} + \frac{2}{\mathrm{Re}}(\boldsymbol{D}^- - \boldsymbol{D}^+)]\boldsymbol{n}^- = 0\boldsymbol{n}^-,$$

where $\boldsymbol{n}^+, \boldsymbol{n}^-$ are the outer unit normal vectors on Γ_m with respect to the domains Ω^+, Ω^- and vectors $\boldsymbol{v_\tau}^{+/-}$ represent the tangential components of velocity defined as $\boldsymbol{v_\tau}^{+/-} = \boldsymbol{v}^{+/-} - (\boldsymbol{v}^{+/-} \cdot \boldsymbol{n}^{+/-})\boldsymbol{n}^{+/-}$.
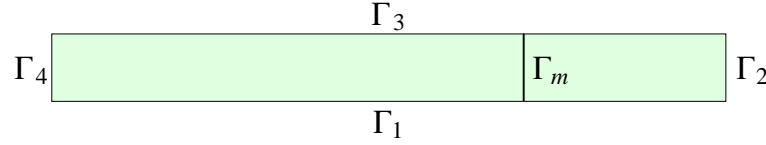
FIGURE 10.3. Two–dimensional computational domain with dimensions $\langle -5, 5 \rangle \times \langle 0, 1 \rangle$; boundaries Γ_1 and Γ_3 are impermeable walls, Γ_4 is the inlet and Γ_2 is the outlet. Γ_m is the inner boundary representing the zero–thickness membrane.

Concerning the transmission conditions for the solute concentration, we require the continuity of the normal fluxes across the membrane, and the condition modeling the partial rejection of the solute by the membrane. If we assume that the velocity $\boldsymbol{v}$ has the property $\boldsymbol{v} \cdot \boldsymbol{n}^- \geq 0$, then these conditions have the form

$$
\begin{aligned}
-\frac{1}{\text{Pe}} \operatorname{grad} c^- \cdot \boldsymbol{n}^- + \sigma c^- \boldsymbol{v} \cdot \boldsymbol{n}^- &= 0, \\
-\frac{1}{\text{Pe}} \operatorname{grad} c^+ \cdot \boldsymbol{n}^+ + c^+ \boldsymbol{v} \cdot \boldsymbol{n}^+ &= -(1-\sigma) c^- \boldsymbol{v} \cdot \boldsymbol{n}^-.
\end{aligned}
$$
(10.9)

The main disadvantage of this formulation is the directional dependence of the conditions for the concentration. Since the buffering occurs in the case of outflow while in the case of inflow the washout of concentration from the membrane is observed, we have to explicitly know the flow direction. One of the possible generalization of the transmission conditions for the concentration (10.9), assuming symmetric properties of the membrane from both sides, is

$$
\begin{aligned}
\frac{1}{\text{Pe}} \operatorname{grad} c^- \cdot \boldsymbol{n}^- &= (\sigma c^-) \boldsymbol{v} \cdot \boldsymbol{n}^- + (1-\sigma)(c^- - c^+) \min(0, \boldsymbol{v} \cdot \boldsymbol{n}^-), \\
\frac{1}{\text{Pe}} \operatorname{grad} c^+ \cdot \boldsymbol{n}^+ &= (\sigma c^+) \boldsymbol{v} \cdot \boldsymbol{n}^+ + (1-\sigma)(c^+ - c^-) \min(0, \boldsymbol{v} \cdot \boldsymbol{n}^+).
\end{aligned}
$$
(10.10)

It is easy to see that (10.10) reduces to (10.9) if $\boldsymbol{v} \cdot \boldsymbol{n}^- \geq 0$, and on the other hand, for the case $\boldsymbol{v} \cdot \boldsymbol{n}^- \leq 0$ we obtain analogous condition for outflow in opposite direction.

The complete model for higher dimensions thus consists of the equations (10.2)–(10.3), together with the boundary conditions at the outer boundary, and the transmission conditions (10.7), (10.8) and (10.10).

For the numerical simulation of the concentration buffering in two dimensions, we use the following computational setting. We consider the domain from Fig. 10.3, with the fixed and rigid membrane Γ_m. The domain Ω^- on the left from membrane is prolonged since there the most interesting accumulation of concentration occurs. We assume the pressure driven flow, for which the fluid of a given concentration enters the channel on boundary Γ_4, and the filtrate leaves the channel on boundary Γ_2. The walls of the channel Γ_1 and Γ_3 are impermeable for both, the concentration and velocity. The form of the boundary conditions on the outer boundaries is

$$
\Gamma_4: \quad [-p\boldsymbol{I} + 2\frac{1}{\text{Re}}\boldsymbol{D}]\boldsymbol{n} = -p_{in}\boldsymbol{n}, \qquad\qquad c = c_{in},
$$
(10.11)

$$
\Gamma_1, \Gamma_3: \quad \boldsymbol{v} = \boldsymbol{0}, \qquad\qquad \left(\frac{1}{\text{Pe}} \operatorname{grad} c + c\boldsymbol{v}\right) \cdot \boldsymbol{n} = 0,
$$
(10.12)

$$
\Gamma_2: \quad [-p\boldsymbol{I} + 2\frac{1}{\text{Re}}\boldsymbol{D}]\boldsymbol{n} = 0\boldsymbol{n}, \qquad\qquad \frac{1}{\text{Pe}} \operatorname{grad} c \cdot \boldsymbol{n} = 0,
$$
(10.13)

where c_{in} is a constant inlet concentration and p_{in} is a constant or a periodical function of time. The transmission conditions on the membrane are (10.7), (10.8), and (10.10). Since we solve the time–dependent problem, we set the initial conditions as a rest state ($\boldsymbol{v} = 0$ and $c = 0$).

The computational results are shown later, in section 10.5, for comparison with the results obtained for model extended by the osmotic effects.

10.3. Extension of the model by osmotic effect

In this section, we take into account the influence of the solute concentration on the volume flow, via the osmotic pressure. In the literature concerning the filtration problems, the flow through the membrane including the effects of the osmosis is usually described by the Kedem–Katchalsky equations (Kedem and Katchalsky (1958)). They describe the simultaneous trans–membrane volume J_v and solute J_s fluxes in the pressure–driven membrane processes by

$$(10.14) \qquad\qquad J_v = L_p(\Delta p - \sigma \Delta \pi),$$

$$(10.15) \qquad\qquad J_s = -P_s \Delta \pi / RT + (1 - \sigma) J_v \bar{c},$$

where Δp is the pressure difference and $\Delta \pi$ is the difference in osmotic pressures ($\Delta \pi = \pi(c^+) - \pi(c^-)$) across the membrane, R, T are the gas constant and temperature, respectively, and $\bar{c}$ is the average solute concentration. The membrane properties are described by three membrane parameters: the filtration coefficient or hydraulic conductivity L_p, the reflection coefficient σ and the solute permeability P_s. One should notice here, that the osmotic pressure in the formula (10.14) is scaled by factor σ.

This general yet simple approach describes the total fluxes in average, however, in our case, we are not interested only in the resulting outflows rather in the spatial distribution of particular physical quantities themselves. This means, we need to modify our current transmission model to include the osmotic effect in agreement with the common approach based on (10.14)–(10.15).

Due to the physical reasons, we prefer to include the osmotic pressure $\pi(c)$ into our model via the the normal stress of the fluid at the membrane. In that case, the transmission conditions for the flow are of the following form

$$(10.16) \qquad \boldsymbol{v_\tau}^+ = \boldsymbol{v_\tau}^- = \boldsymbol{0}, \quad \boldsymbol{v}^+ \cdot \boldsymbol{n}^+ = -\boldsymbol{v}^- \cdot \boldsymbol{n}^- = \boldsymbol{v} \cdot \boldsymbol{n}^+,$$

$$(10.17) \qquad [-(p^- - p^+)\boldsymbol{I} + 2\frac{1}{\mathrm{Re}}(\boldsymbol{D}^- - \boldsymbol{D}^+)]\boldsymbol{n}^- = -(\pi(c^-) - \pi(c^+))\boldsymbol{n}^-.$$

Here, we do not scale the osmotic pressure since the reflection effect is already included in the concentration profile, which generates the osmotic pressure profile, and thus, it is already incorporated in the model. In this work, we still assume the existence of the osmotic pressure only on/across the membrane but the approach of considering the osmotic pressure as a part of normal stress allows us to consider the existence of osmotic pressure in the whole space. This can be advantageous in the cases of the concentration shock waves or steep concentration gradients, which are, from our point of view, the typical cases where osmotic pressure can play an important role even for the membrane–free cases. The influence on the flow would then be via its gradient, as a complement of hydrodynamical pressure gradient in the Navier–Stokes equations.

For the osmotic pressure of the solution, we use the following representation

$$(10.18) \qquad\qquad \pi(c) = P_1 c + P_2 c^2.$$

This quadratic dependence is typical for polymeric solutions, in contrast to much more common linear dependence of solutions of ions or small molecules, for example. Here, parameters P_1 and P_2 are constants[3], reflecting characteristics of the solute–solvent interactions, see e.g. Cheng (1998) and Coleman et al. (1999) and are the first two of the virial coefficients of the osmotic pressure virial expansion. First parameter P_1 is dependent on the molecular weight of the polymer while P_2 reflects the energy of binary interactions between polymer chains and solvent molecules. This representation immediately suggests that the second parameter can not be neglected in the case of hyaluronan molecules diluted in synovial fluid due to their significant chain–solvent interactions.

The complete model describing the filtration problem in the domain Ω containing the membrane Γ_m thus consists of the equations (10.2)–(10.3) on the subdomains Ω^+, and Ω^-, together with the boundary conditions (10.11)–(10.13) at the outer boundary, the transmission conditions (10.10) for the solute concentration, and the transmission conditions

---

[3]Different constants for different solute–solvent constitution of the fluid.

(10.16), (10.17) for the flow. As one can see, the equations for the flow and the transport equation for the solvent are now fully coupled via the transmission condition (10.17).

For the numerical simulations of the model including osmotic effect, we consider the setting from Section 10.2.2. The results are compared for the transmission model without and with the osmotic pressure effect in Section 10.5.

10.4. Adaptation of numerical method

We use standard Galerkin finite element method to solve the PDE system consisting of equations (10.2)–(10.3) on the domain introduced in Fig. 10.3 and boundary conditions (10.11)–(10.13), as in greater detail described in Section 8. Beside standard assumptions on the mesh, we require that the membrane Γ_m coincides with edges of the mesh.

While the velocity is required to be continuous on the membrane and can be approximated by globally continuous functions, the concentration and the pressure are allowed to be discontinuous on the membrane. Since, for the pressure, we use approximation by piecewise linear but discontinuous functions and the membrane boundary coincides with the mesh edges, the discretization of the pressure does not need to be adapted. On the other hand, the concentration discontinuity has to be treated in a special way. Among many different ways, the simplest one is the splitting of c into two continuous variables c^+ and c^- defined on Ω^+ and Ω^-, respectively. The standard weak formulation of the system is thus derived separately on the two subdomains Ω^+ and Ω^-, where the mutual coupling is provided through the requirement of continuous velocity on the membrane and the transmission conditions (10.17) and (10.10). If we define the global concentration[4] variable as

$$(10.19) \qquad c(\mathbf{x}) = \begin{cases} c^+(\mathbf{x}) \text{ if } \mathbf{x} \in \Omega^+, \\ c^-(\mathbf{x}) \text{ if } \mathbf{x} \in \Omega^-, \end{cases}$$

with the spatial approximation from the space

$$(10.20) \qquad C_h = \{c_h \in C(\Omega^+) \cup C(\Omega^-), \ c_h|_T \in Q_2(T) \quad \forall T \in \mathcal{T}_h\},$$

then the global discretization remains almost unaltered.

10.5. Numerical simulations

In this section, we present numerical simulations giving an insight of the importance of osmotic pressure and the membrane parameter σ on the flow through membrane in pressure driven filtration processes. The numerical solutions of the transmission model are computed for the computational setting described in section 10.2.2, for Reynold's number Re = 1 and Péclet number Pe = 100, still for a Newtonian fluid. In each set of plots, we compare the model without the osmotic effect with the full transmission model. Hereby, we consider linear or quadratic osmotic pressure dependence on concentration, and two different values of the reflection coefficient σ. The following physical quantities are being plotted:

  – the distribution of solute concentration, hydrodynamical pressure and flux/velocity component v_x in the whole domain Ω, see Fig. 10.4, 10.5, 10.7 and 10.9,
  – the curve profiles of the concentration, hydrodynamical pressure and total flux on the central horizontal cutline $\langle -5, 5 \rangle \times [0, 0.5]$, see Fig. 10.6, 10.8 and 10.10,
  – the time evolution of the concentration, pressure, and total flux, at the middle point of the membrane $[0, 0.5]$, see Fig. 10.11–10.14.

Fig. 10.4 and 10.5 present the steady state of the concentration distribution in the whole domain, the Fig. 10.6 visualizes the profiles of concentration on the second half of horizontal cut (between points $[0, 0]$ and $[5, 0]$). As we can see, the shape of the concentration layer strongly differs. In the case of simulation without inclusion of osmotic pressure (case (a)), the concentration at the membrane is higher towards the walls than in the middle part. This is caused by the non–decelerated parabolic velocity profile. The velocity is higher in the middle part than close to the walls thus it carries away more of the concentration. This phenomena is not observed for the cases where the velocity at the membrane rapidly drops like in the settings of (b) and (d), as it can be seen in Fig. 10.13, and Fig. 10.14. For the setting (c)

---

[4]On the membrane boundary, we use similar notation even for the pressure.

and (d) with low reflection coefficient and quadratic osmotic pressure dependence, a small concentration layer is created compared to the setting with higher σ and linear dependence of osmotic pressure, setting (a) and (b).

Profiles of hydrodynamical pressure are presented in Fig. 10.7 and 10.8. In the case of computational setting without osmosis, the equations for velocity and concentration are not fully coupled and thus the hydrodynamical pressure is a solution of the classical Navier–Stokes equations, and thus, it has a linear profile. For the settings including osmosis the jumps in the pressure occur. In the case of small σ, the concentration layer at the membrane is not so significant, see Fig. 10.11, and thus it does not evoke high difference in the osmotic pressures which could act against the fluid pressure, see Fig. 10.12. In the case of the quadratic osmotic pressure dependence on the concentration, the compensation of the pressures occurs even though the drop in concentration was not so high as for the case in Fig. 10.11, (b).

Last set of pictures reflecting distributions at the steady state are Fig. 10.9 and 10.10, characterizing the x–component of the velocity vector $\boldsymbol{v}$, thus in some sense, the flux of the fluid. This clearly demonstrates the important role of the osmotic pressure and high reflection coefficient of the membrane for the fluid drainage.

Figures 10.11–10.13 present the time evolution of individual physical quantities in the middle point of the membrane. Since the values of the concentration and of the pressure are discontinuous at the membrane, we plot the traces of these functions from both sides of the membrane, the solvent flux is continuous across the membrane. At the beginning of the computation, there are no jumps since at that time no concentration layer at membrane has been created. During this time the solvent flux is constant and highest. After the creation of the concentration layer, the flux decreases corresponding to the induced hydrodynamical pressure drop. These sets of graphs illustrate, that even high pressures induced in the channels (cavities) can be apparently diminished behind the membrane, and thus, the channels boundaries are stable without the risk of rapture. Moreover, the flux through the membrane is controlled and thus no high drop in the volume is observed.

The last set of graphs in Fig. 10.14 shows the solution of computation with time periodic inlet pressure $p_{in} = p_0(1 + \sin(\varpi t))$. As we can see, after a short initial phase, the solution becomes periodic with the same frequency as the enforcing pressure condition. In this setting we can observe that the solvent flux changes its direction at the time when the forcing pressure is lowest. This is the manifestation of the osmotic effect, since the concentration on the left–hand side of the membrane is higher than the concentration on the right–hand side, which creates the pressure force acting against the inflow pressure.
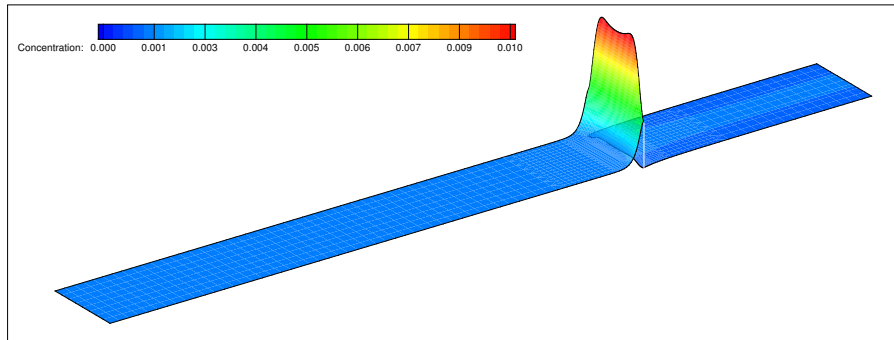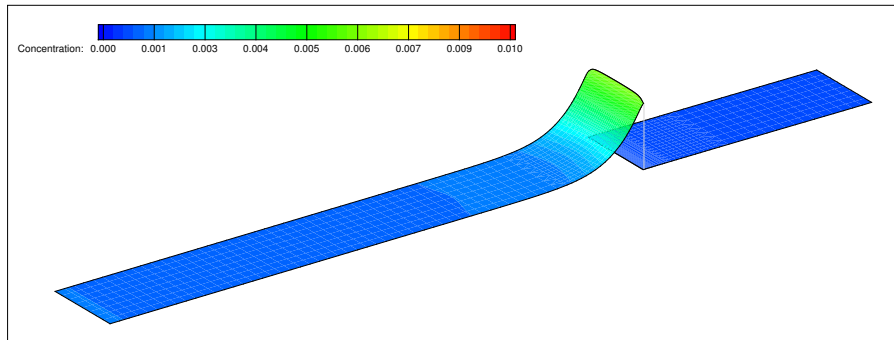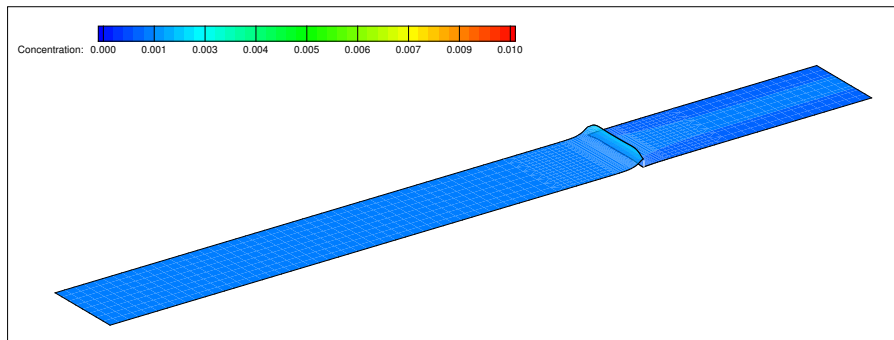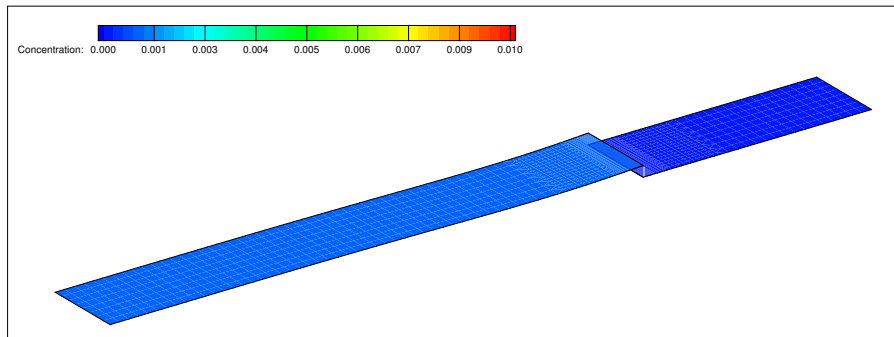
(a) $\sigma = 0.9$, $P_1 = P_2 = 0$

(b) $\sigma = 0.9$, $P_2 = 0$

(c) $\sigma = 0.5$, $P_2 = 0$

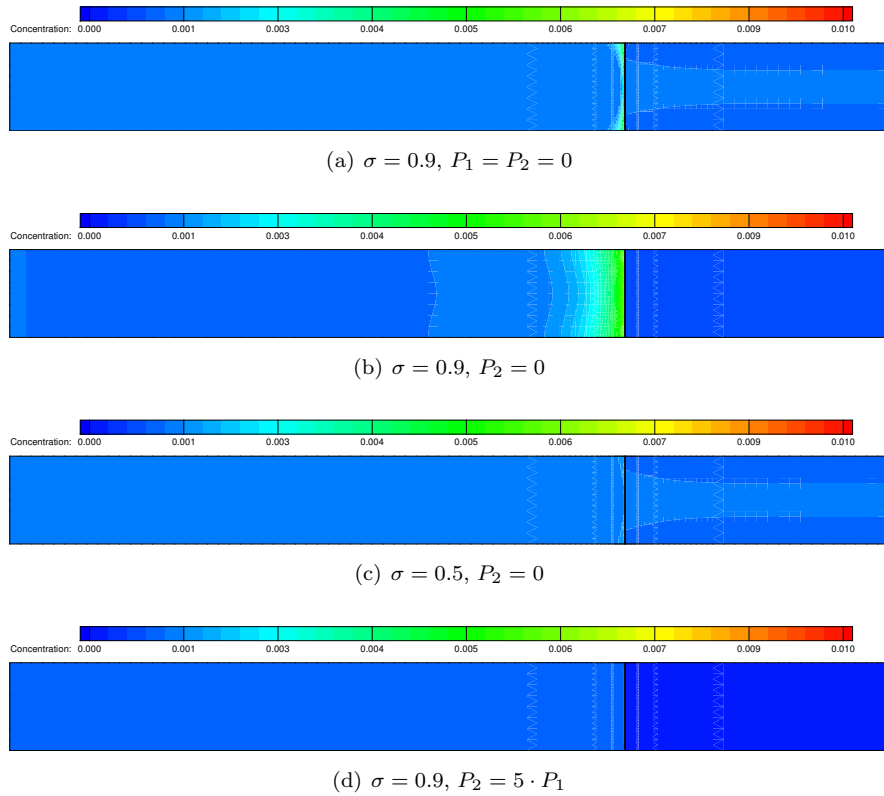(d) $\sigma = 0.9$, $P_2 = 5 \cdot P_1$

FIGURE 10.4. Concentration distribution at steady state. Four plots for different parameter setting; without osmotic pressure: (a) $\sigma = 0.9$, $P_1 = P_2 = 0$; with osmotic pressure: (b) $\sigma = 0.9$, $P_2 = 0$, (c) $\sigma = 0.5$, $P_2 = 0$, (d) $\sigma = 0.9$, $P_2 = 5 \cdot P_1$.
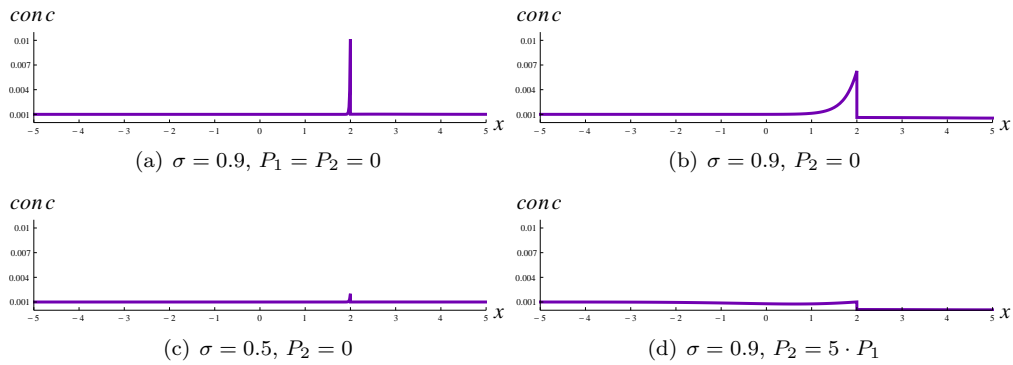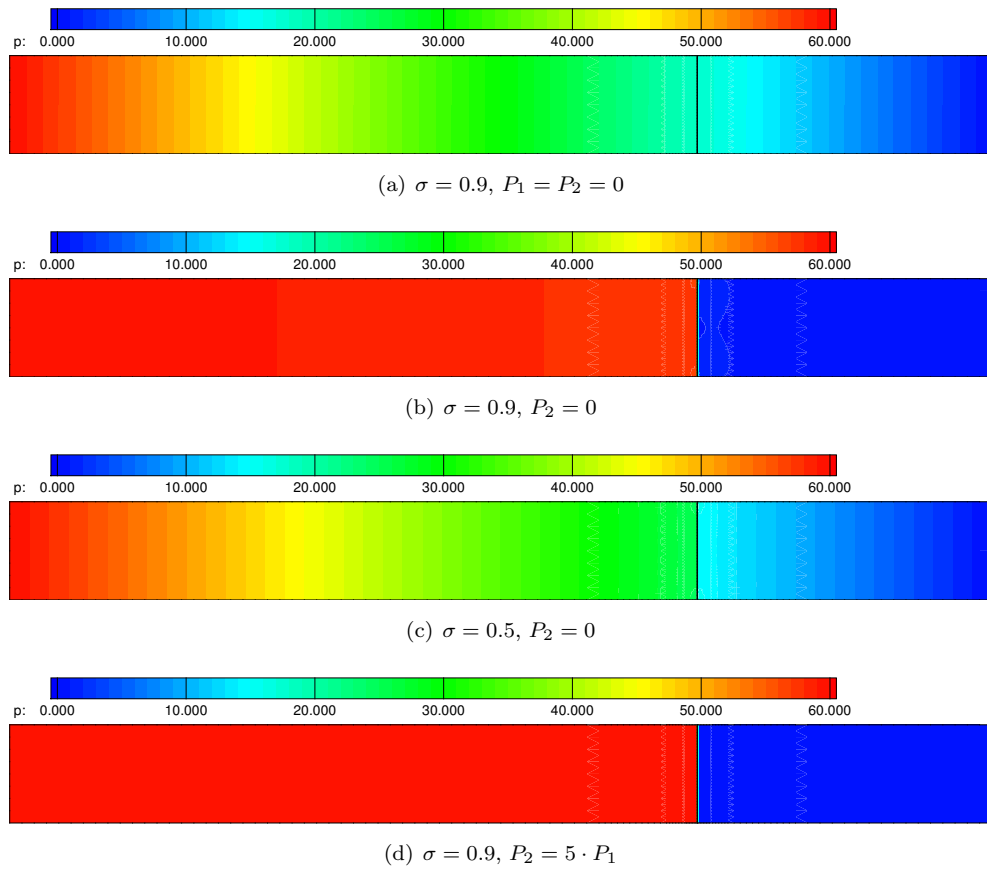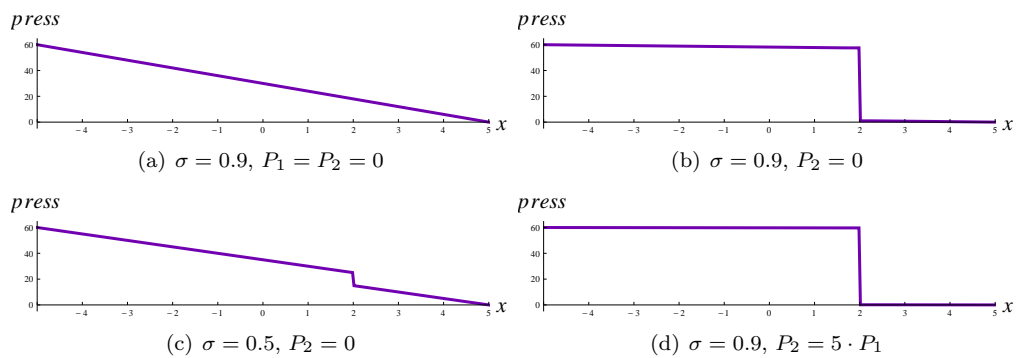
(a) $\sigma = 0.9$, $P_1 = P_2 = 0$

(b) $\sigma = 0.9$, $P_2 = 0$

(c) $\sigma = 0.5$, $P_2 = 0$

(d) $\sigma = 0.9$, $P_2 = 5 \cdot P_1$

FIGURE 10.5. Concentration distribution at steady state. Four plots for different parameter setting; without osmotic pressure: (a) $\sigma = 0.9$, $P_1 = P_2 = 0$; with osmotic pressure: (b) $\sigma = 0.9$, $P_2 = 0$, (c) $\sigma = 0.5$, $P_2 = 0$, (d) $\sigma = 0.9$, $P_2 = 5 \cdot P_1$.
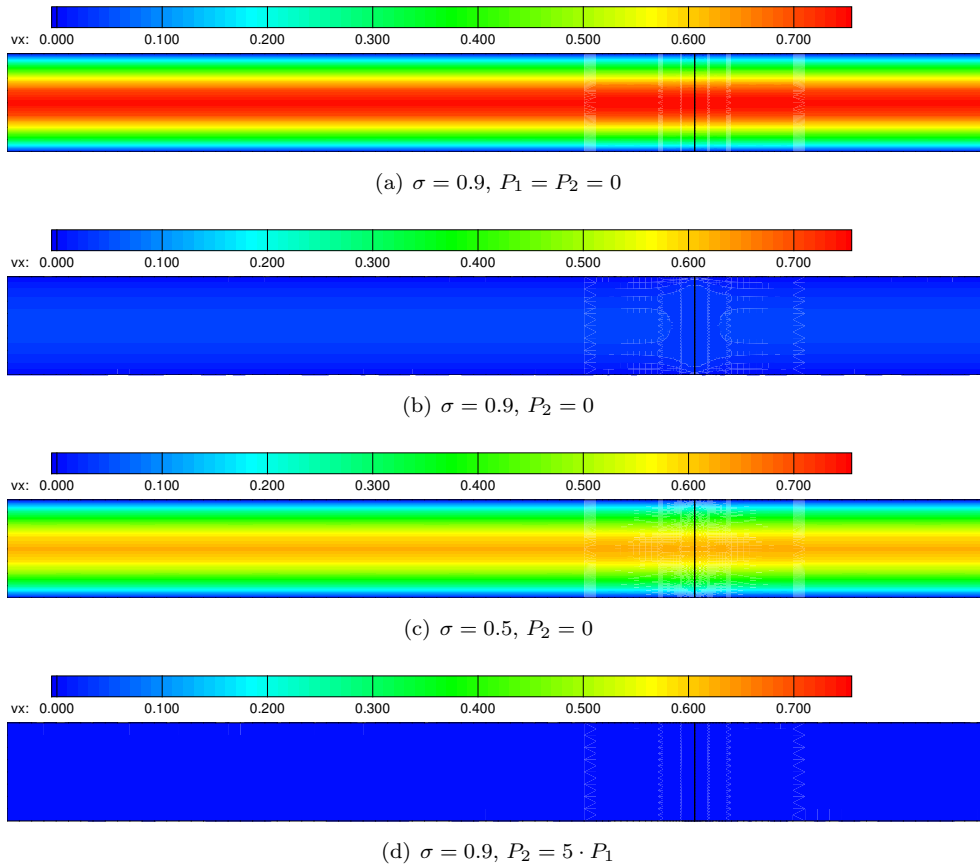

(a) $\sigma = 0.9$, $P_1 = P_2 = 0$

(b) $\sigma = 0.9$, $P_2 = 0$

(c) $\sigma = 0.5$, $P_2 = 0$

(d) $\sigma = 0.9$, $P_2 = 5 \cdot P_1$

FIGURE 10.6. Concentration profile on horizontal cutline at steady state. Four plots for different parameter setting; without osmotic pressure: (a) $\sigma = 0.9$, $P_1 = P_2 = 0$; with osmotic pressure: (b) $\sigma = 0.9$, $P_2 = 0$, (c) $\sigma = 0.5$, $P_2 = 0$, (d) $\sigma = 0.9$, $P_2 = 5 \cdot P_1$.
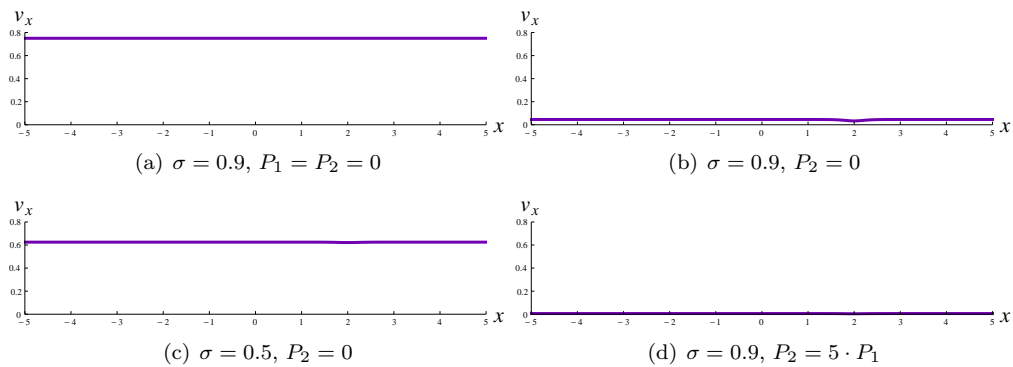
(a) $\sigma = 0.9$, $P_1 = P_2 = 0$

(b) $\sigma = 0.9$, $P_2 = 0$

(c) $\sigma = 0.5$, $P_2 = 0$

(d) $\sigma = 0.9$, $P_2 = 5 \cdot P_1$

FIGURE 10.7. Hydrodynamic pressure distribution at steady state. Four plots for different parameter setting; without osmotic pressure: (a) $\sigma = 0.9$, $P_1 = P_2 = 0$; with osmotic pressure: (b) $\sigma = 0.9$, $P_2 = 0$, (c) $\sigma = 0.5$, $P_2 = 0$, (d) $\sigma = 0.9$, $P_2 = 5 \cdot P_1$.

(a) $\sigma = 0.9$, $P_1 = P_2 = 0$

(b) $\sigma = 0.9$, $P_2 = 0$

(c) $\sigma = 0.5$, $P_2 = 0$

(d) $\sigma = 0.9$, $P_2 = 5 \cdot P_1$

FIGURE 10.8. Hydrodynamic pressure profile on horizontal cutline at steady state. Four plots for different parameter setting; without osmotic pressure: (a) $\sigma = 0.9$, $P_1 = P_2 = 0$; with osmotic pressure: (b) $\sigma = 0.9$, $P_2 = 0$, (c) $\sigma = 0.5$, $P_2 = 0$, (d) $\sigma = 0.9$, $P_2 = 5 \cdot P_1$.
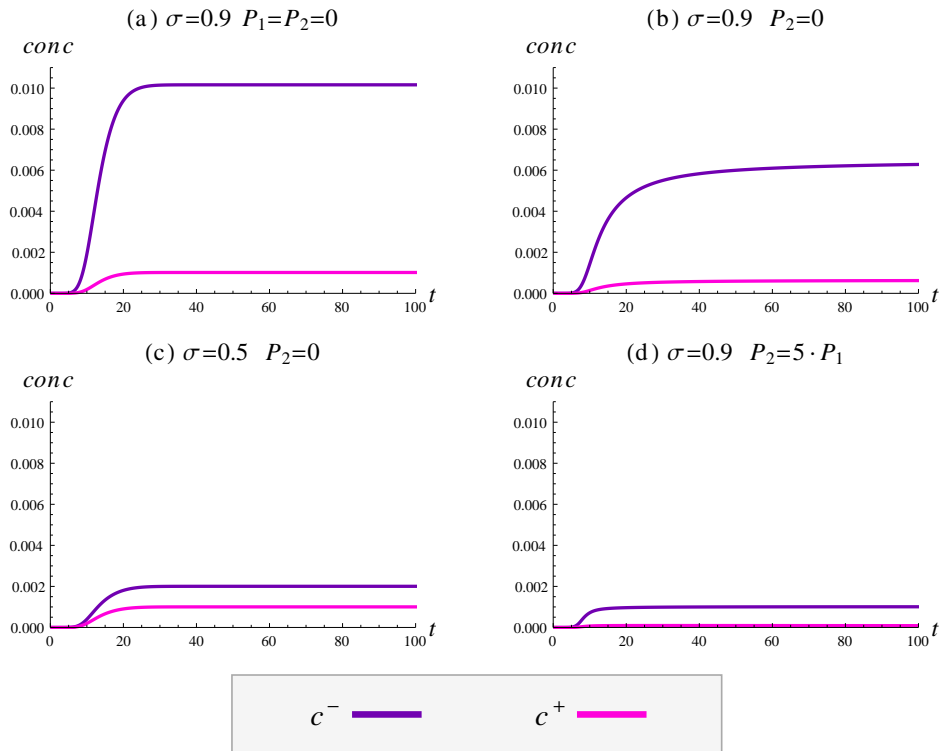
(a) $\sigma = 0.9$, $P_1 = P_2 = 0$

(b) $\sigma = 0.9$, $P_2 = 0$

(c) $\sigma = 0.5$, $P_2 = 0$

(d) $\sigma = 0.9$, $P_2 = 5 \cdot P_1$

FIGURE 10.9. Distribution of v_x velocity component at steady state. Four plots for different parameter setting; without osmotic pressure: (a) $\sigma = 0.9$, $P_1 = P_2 = 0$; with osmotic pressure: (b) $\sigma = 0.9$, $P_2 = 0$, (c) $\sigma = 0.5$, $P_2 = 0$, (d) $\sigma = 0.9$, $P_2 = 5 \cdot P_1$.

(a) $\sigma = 0.9$, $P_1 = P_2 = 0$

(b) $\sigma = 0.9$, $P_2 = 0$

(c) $\sigma = 0.5$, $P_2 = 0$

(d) $\sigma = 0.9$, $P_2 = 5 \cdot P_1$

FIGURE 10.10. Profile of v_x velocity component on horizontal cutline at steady state. Four plots for different parameter setting; without osmotic pressure: (a) $\sigma = 0.9$, $P_1 = P_2 = 0$; with osmotic pressure: (b) $\sigma = 0.9$, $P_2 = 0$, (c) $\sigma = 0.5$, $P_2 = 0$, (d) $\sigma = 0.9$, $P_2 = 5 \cdot P_1$.

FIGURE 10.11. Time evolution of concentration at midpoint of the membrane for different parameter combinations; without osmotic pressure: (a) $\sigma = 0.9$, $P_1 = P_2 = 0$; with osmotic pressure: (b) $\sigma = 0.9$, $P_2 = 0$, (c) $\sigma = 0.5$, $P_2 = 0$, (d) $\sigma = 0.9$, $P_2 = 5 \cdot P_1$.
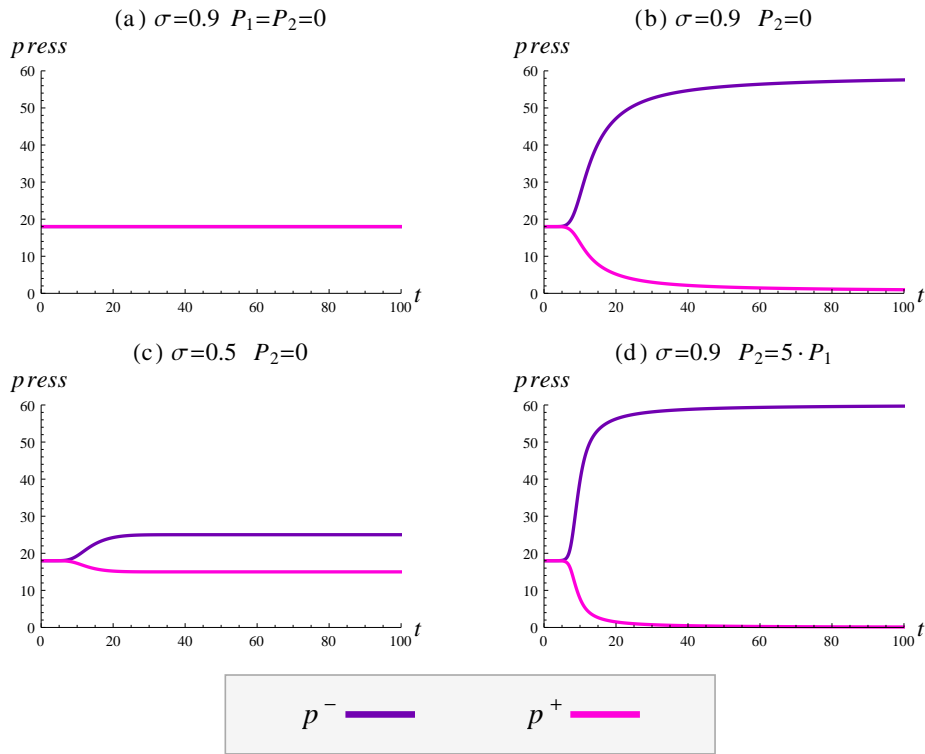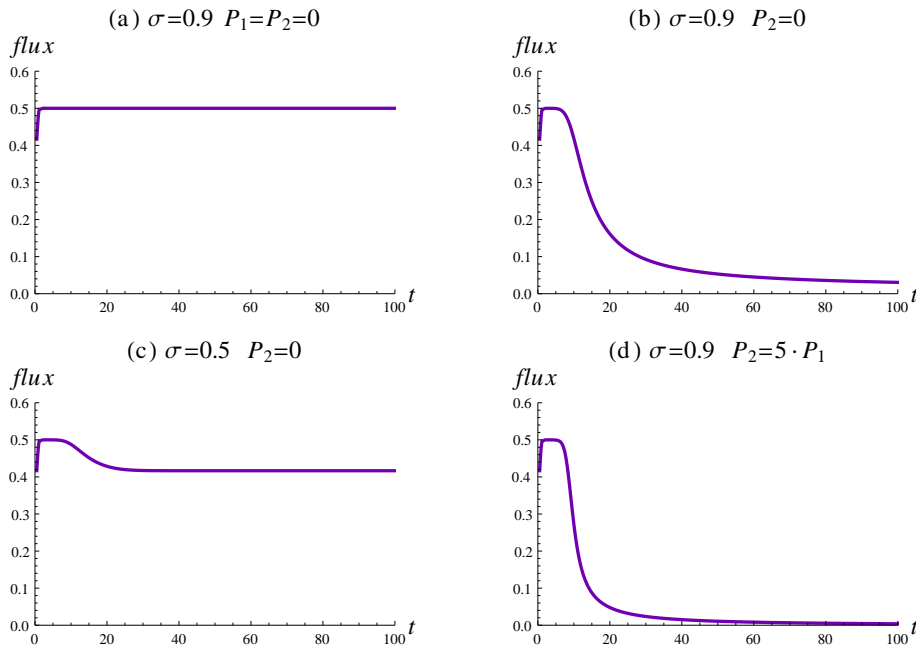
FIGURE 10.12. Time evolution of hydrodynamical pressure at midpoint of the membrane for different parameter combinations; without osmotic pressure: (a) $\sigma = 0.9, P_1 = P_2 = 0$; with osmotic pressure: (b) $\sigma = 0.9, P_2 = 0$, (c) $\sigma = 0.5, P_2 = 0$, (d) $\sigma = 0.9, P_2 = 5 \cdot P_1$.
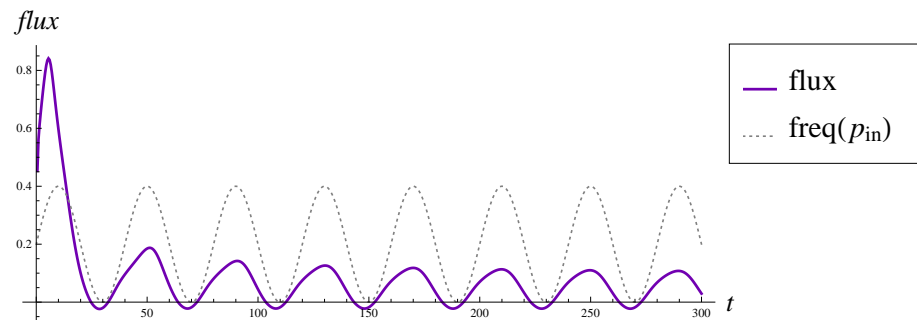

FIGURE 10.13. Time evolution of total solvent flux through Γ_m for different parameter combinations; without osmotic pressure: (a) $\sigma = 0.9, P_1 = P_2 = 0$; with osmotic pressure: (b) $\sigma = 0.9, P_2 = 0$, (c) $\sigma = 0.5, P_2 = 0$, (d) $\sigma = 0.9, P_2 = 5 \cdot P_1$.
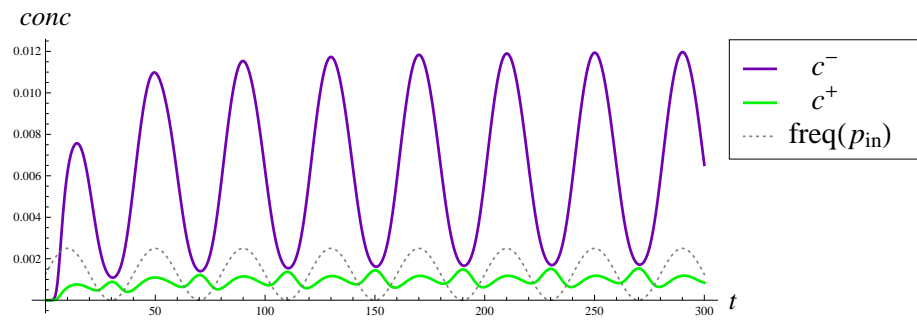
(a) concentration
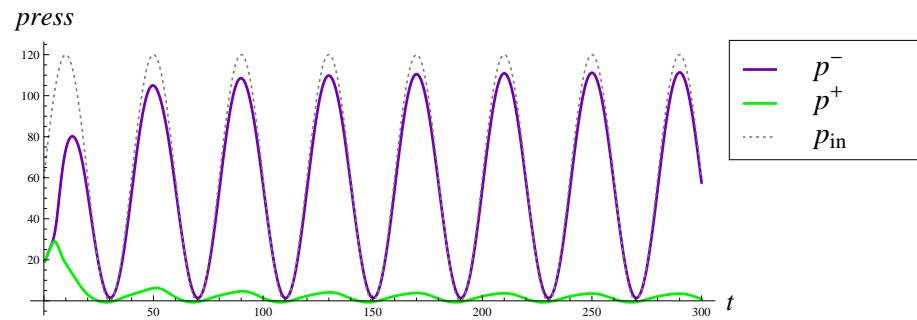
(b) pressure

(c) flux

FIGURE 10.14. Time evolution of various quantities for periodic pressure inlet, $\sigma = 0.9$, $P_2 = 0$; (a) concentration, (b) pressure, (c) total solvent flux through Γ_m, all plotted for the middle point of the membrane boundary. Dotted profiles represent the frequency of the pressure inlet oscillations.

(a) trans–synovial flow
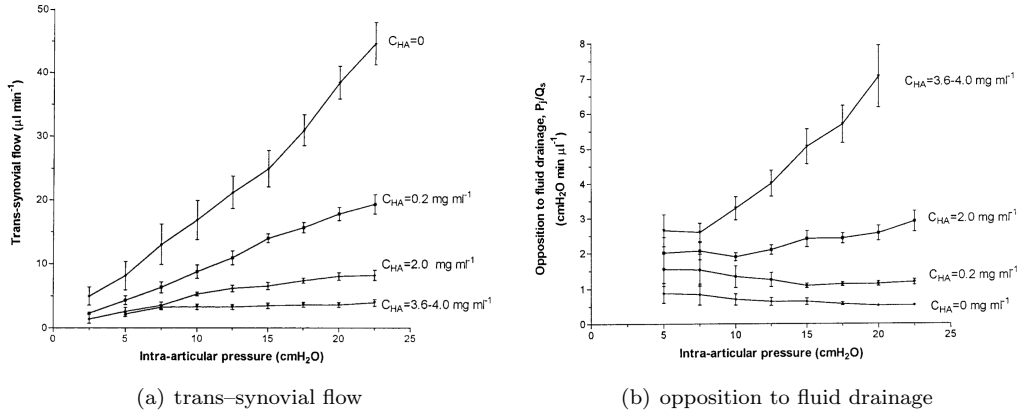

(b) opposition to fluid drainage

FIGURE 10.15. Effect of hyaluronan concentration on fluid drainage through synovial interstitium; (a) effect on pressure–flow relation, (b) effect of hyaluronan concentration on opposition to outflow; From Scott et al. (2000b).

10.6. Application of the transmission model to synovial membranes and synovial fluid

As it has been introduced in Chapter 2, the hyaluronan outflow buffering is important for the balance of joint fluid volume and composition of the fluid, which is, generally, important for the whole stability of synovial joint system. For these reasons, it is important to study the filtration processes of synovial fluid through the synovial membrane in relation to the hyaluronan concentration, which can vary with different physiological conditions of the joint. This motivates us to apply our membrane transmission model (developed for diluted polymeric solutions) to synovial fluid drainage.

In this section, we shall consider the transmission model for the membrane as introduced above in application to synovial membrane. Furthermore, we shall include into the model the effects of membrane resistivity to bulk flow, and, we shall consider the non–Newtonian characteristic of synovial fluid, in a manner of viscosity being concentration and shear rate dependent

$$(10.21) \qquad \mu = \mu_0 \left(\beta + \gamma |\boldsymbol{D}|^2 \right)^{n(c)},$$

where the shear–thinning index is of the form of

$$(10.22) \qquad n\left(c\right) = \omega \left(\frac{1}{\alpha c^2 + 1} - 1 \right),$$

as was closely described in Chapter 5. We start from experiments of Scott et al. (2000b) and Coleman et al. (1999), see Fig. 10.15, which were motivated to test the concentration polarization hypothesis, in particular the effect of hyaluronan concentration on pressure–driven flow across a synovial membrane *in vivo*. As it was described by Scott and Coleman, the hyaluronan concentration significantly reduces the outflow of synovial fluid from the synovial cavity, even for high intraarticular pressures. On the other hand the dilution of hyaluronan in synovial fluid, as in effusions, results facilitation of fluid drainage. Our aim is to reproduce such characteristic of synovial fluid membrane transport and obtain similar outflow properties/relations.

There can be many mechanisms playing a role during the synovial fluid drainage, for example the increase of intramembrane viscosity, the influence of molecular chain length on the critical concentration of molecular overlapping, the influence of inhibitors of chain–chain interactions, etc. We shall nevertheless focus on the concentration polarization due to the reflexivity of the synovial membrane, and newly, we include to the model the resistivity of the membrane to the bulk flow. In the previous section, we assumed such membrane properties that the zero reflexivity, $\sigma = 0$, led to a membrane–free model. This means that the flow
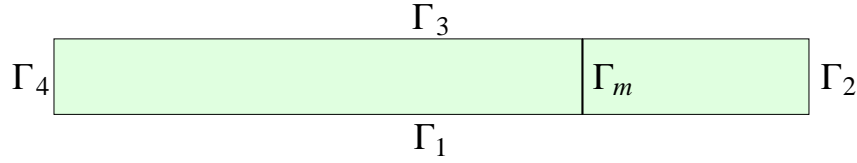
FIGURE 10.16. Two–dimensional computational domain with dimensions $\langle -5, 5 \rangle \times \langle 0, 1 \rangle$; boundaries Γ_1 and Γ_3 are impermeable walls, Γ_4 is the inlet and Γ_2 is the outlet. Γ_m is the inner boundary representing the zero–thickness membrane.
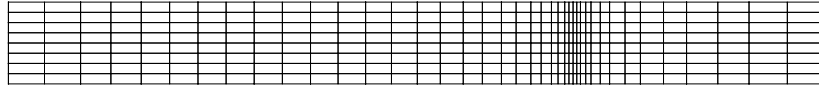

FIGURE 10.17. Computational mesh. From both horizontal directions the mesh is refined close the membrane.

through the membrane would not be slowed down, or in other words, the fluid would not "feel" the membrane presence, which is physically non–realistic. From the experiment of Scott, see Fig. 10.15 (a), it is visible that the relation between outflow and imposed intraarticular pressure exhibit linear relation for zero concentration solution of hyaluronan. This can be considered as a specification of the membrane resistivity to the bulk flow of the Newtonian fluid "background". We therefore, as the membrane is considered as zero–thickness interface, prescribe the resistance R through the normal stress as following

$$(10.23) \qquad [-(p^- - p^+)\boldsymbol{I} + 2\frac{1}{\mathrm{Re}}(\boldsymbol{D}^- - \boldsymbol{D}^+)]\boldsymbol{n}^- = -(\pi(c^-) - \pi(c^+))\boldsymbol{n}^- - R(v_n)\boldsymbol{n}^-,$$

where, as suggested from the experiment, we take linear relation for the resistance

$$(10.24) \qquad\qquad\qquad R(v_n) = \tilde{R}\, v_n,$$

with a constant resistivity $\tilde{R}$. All together, we assume the transmission conditions for velocity

$$(10.25) \qquad \boldsymbol{v_\tau}^+ = \boldsymbol{v_\tau}^- = \boldsymbol{0}, \quad \boldsymbol{v}^+ \cdot \boldsymbol{n}^+ = -\boldsymbol{v}^- \cdot \boldsymbol{n}^- = \boldsymbol{v} \cdot \boldsymbol{n}^+,$$

$$(10.26) \qquad [-(p^- - p^+)\boldsymbol{I} + 2\frac{1}{\mathrm{Re}}(\boldsymbol{D}^- - \boldsymbol{D}^+)]\boldsymbol{n}^- = -(\pi(c^-) - \pi(c^+))\boldsymbol{n}^- - R(v_n)\boldsymbol{n}^-$$

and for concentration

$$(10.27) \qquad \frac{1}{\mathrm{Pe}}\operatorname{grad} c^- \cdot \boldsymbol{n}^- = (\sigma c^-)\boldsymbol{v} \cdot \boldsymbol{n}^- + (1 - \sigma)(c^- - c^+)\min(0, \boldsymbol{v} \cdot \boldsymbol{n}^-),$$

$$(10.28) \qquad \frac{1}{\mathrm{Pe}}\operatorname{grad} c^+ \cdot \boldsymbol{n}^+ = (\sigma c^+)\boldsymbol{v} \cdot \boldsymbol{n}^+ + (1 - \sigma)(c^+ - c^-)\min(0, \boldsymbol{v} \cdot \boldsymbol{n}^+).$$

For the experiment reproduction, we consider the same two–dimensional test geometry as above with fixed and rigid interface Γ_m representing the membrane, see Fig. 10.16, with the mesh refined around the membrane, see Fig. 10.17. Moreover, since we assume diffusivity of order 10^{-6}, we solve the problem by the use of the numerical stabilization method, particularly by the continuous interior penalty (CIP) method, as described in Chapter 8, Section 8.8.

As in the experiment, we assume the pressure driven flow, for which the fluid of a given concentration enters the channel on boundary Γ_4, and the filtrate leaves the channel on boundary Γ_2. Here, we record the total flux of the fluid as a function of an imposed pressure on boundary Γ_1 and qualitatively compare it with the volume outflow relation from the experiment. We prescribe the walls of the channel Γ_1 and Γ_3 to be impermeable for both, the concentration and velocity. The form of the boundary conditions on the outer boundaries
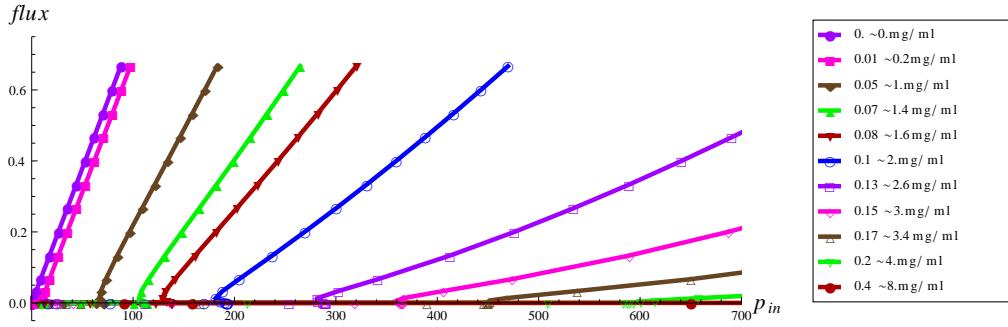
(a) trans–synovial flow – numerical result
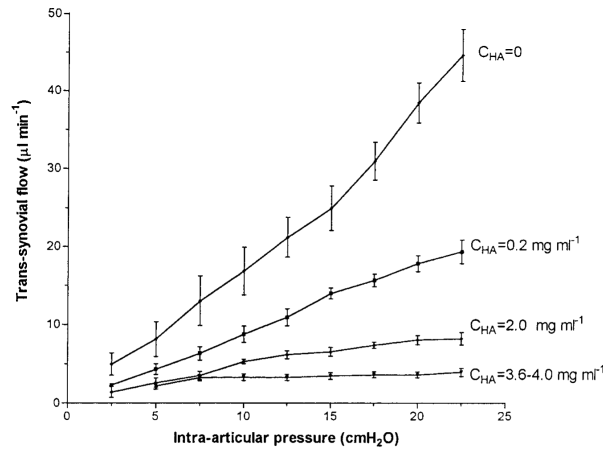
(b) trans–synovial flow – experimental result

FIGURE 10.18. Qualitative comparison of numerical results of pressure driven flow through the membrane (a), with the experimental results of Scott et al. (2000b), (b).

is then following

$$(10.29) \qquad \Gamma_4: \quad [-p\boldsymbol{I} + 2\frac{1}{\mathrm{Re}}\boldsymbol{D}]\boldsymbol{n} = -p_{in}\boldsymbol{n}, \qquad\qquad c = c_{in},$$

$$(10.30) \qquad \Gamma_1, \Gamma_3: \quad \boldsymbol{v} = \boldsymbol{0}, \qquad\qquad \left(\frac{1}{\mathrm{Pe}}\operatorname{grad} c + c\boldsymbol{v}\right)\cdot\boldsymbol{n} = 0,$$

$$(10.31) \qquad \Gamma_2: \quad [-p\boldsymbol{I} + 2\frac{1}{\mathrm{Re}}\boldsymbol{D}]\boldsymbol{n} = 0\boldsymbol{n}, \qquad\qquad \frac{1}{\mathrm{Pe}}\operatorname{grad} c \cdot \boldsymbol{n} = 0,$$

where c_{in} is a constant inlet concentration and p_{in} is a constant pressure inlet. During the simulations we cycle over the values of c_{in} and p_{in}, as we want to compare the results of Scott et al. (2000b). We set the initial conditions as a rest state ($\boldsymbol{v} = 0$ and $c = 0$).

The numerical results of the simulations are presented in the Fig. 10.18. As it is well distinctive, the model is able to capture the main outflow vs. imposed pressure characteristics which are their linear relationship and the rapid decrease of the outflow for the concentration around $0.13 \approx 2$ mg/ml and higher. Even though we consider the phenomenologically derived model, under the considered limitations it gives reasonable resulting properties of the filtration process.

Bibliography

Antontsev, S. and Rodrigues, J. (2006). On stationary thermo-rheological viscous flows. *Annali dell Universita di Ferrara*, 52(1):19–36.

Babuška, I. (1973). The finite element method with Lagrangian multipliers. *Numerische Mathematik*, 20(3):179–192.

Balazs, E. (1968). Viscoelastic properties of hyaluronic acid and biological lubrication. *University of Michigan Medical Center Journal*, 1968:255–259.

Balazs, E. and Gibbs, D. (1970). The rheological properties and biological function of hyaluronic acid. *Chemistry and Molecular Biology of the Intercellular Matrix*, 3:1241–1253.

Bensoussan, A. and Frehse, J. (2002). *Regularity results for nonlinear elliptic systems and applications*, volume 27. Springer.

Bochev, P. and Gunzburger, M. (2009). *Least-squares finite element methods*, volume 166. Springer Verlag, New York.

Boltzmann, L. (1874). Zur Theorie der elastischen Nachwirkung. *Mat Naturwiss. Kl. Kaiser. Akad. Wiss.*, 70:275–306.

Bothner, H. and Wik, K. (1987). Rheology of hyaluronate. *Acta oto-laryngologica. Supplementum*, 442:25–30.

Brezzi, F. and Fortin, M. (1991). *Mixed and hybrid finite element methods*. Springer-Verlag, New York.

Brooks, A. and Hughes, T. (1982). Streamline upwind/Petrov-Galerkin formulations for convection dominated flows with particular emphasis on the incompressible Navier-Stokes equations. *Computer Methods in Applied Mechanics and*, 32(1-3):199–259.

Bulíček, M., Málek, J., and Rajagopal, K. R. (2009). Mathematical Results Concerning Unsteady Flows of Chemically Reacting Incompressible Fluids. In Robinson, J. C. and Rodrigo, J. L., editors, *Partial Differential Equations and Fluid Mechanics*, volume 7, pages 26–53. Cambridge University Press, London, london mat edition.

Burman, E. and Ern, A. (2007). Continuous interior penalty hp-finite element methods for advection and advection-diffusion equations. *Mathematics of computation*, 76(259):1119–1140.

Burman, E. and Fernández, M. (2009). Finite element methods with symmetric stabilization for the transient convection–diffusion–reaction equation. *Computer Methods in Applied Mechanics and Engineering*, 198(33-36):2508–2519.

Burman, E. and Hansbo, P. (2004). Edge stabilization for Galerkin approximations of convection-diffusion-reaction problems. *Computer methods in applied mechanics and*, 193(15-16):1437–1453.

Cai, Z., Lazarov, R., Manteuffel, T., and McCormick, S. (1994). First-order system least squares for second-order partial differential equations: Part I. *SIAM Journal on Numerical Analysis*, 31(6):1785–1799.

Cai, Z., Manteuffel, T., and McCormick, S. (1997). First-order system least squares for second-order partial differential equations: Part II. *SIAM Journal on Numerical Analysis*, 34(2):425–454.

Cheng, T. (1998). Flux analysis by modified osmotic-pressure model for laminar ultrafiltration of macromolecular solutions. *Separation and Purification Technology*, 13(1):1–8.

Ciarlet, P. (1978). *The finite element method for elliptic problems*. North-Holland, Amsterdam.

Codina, R. (2000). On stabilized finite element methods for linear systems of convection-diffusion-reaction equations. *Computer Methods in Applied Mechanics and Engineering*, 188(1-3):61–82.

Coleman, B. and Noll, W. (1961). Foundations of linear viscoelasticity. *Reviews of Modern Physics*, 33(2):239–249.

Coleman, P., Scott, D., Mason, R., and Levick, J. (1999). Characterization of the effect of high molecular weight hyaluronan on trans-synovial flow in rabbit knees. *The Journal of physiology*, 514 (Pt 1:265–82.

Coleman, T. and Li, Y. (1996). An Interior, Trust Region Approach for Nonlinear Minimization Subject to Bounds. *SIAM Journal on Optimization*, 6:418–445.

Davies, D. (1946). Synovial membrane and synovial fluid of joints. *Lancet.*, 7(2):815–819.

Davies, D. and Palfrey, A. (1968). Some of the physical properties of normal and pathological synovial fluids. *Journal of biomechanics*, 1(2):79.

Davis, T. (2004). UMFPACK-an unsymmetric-pattern multifrontal method with a column pre-ordering strategy. *ACM Trans. Math. Software*, 30:196–199.

de Giorgi, E. (1957). Sulla differenziabilità e l'analiticità delle estremali degli integrali multipli regolari. *Mem. Accad. Sci. Torino. Cl. Sci. Fis. Mat. Nat.*, 3:25–43.

Deuflhard, P. (2004). *Newton methods for nonlinear problems: affine invariance and adaptive algorithms*, volume 35. Springer Verlag.

Diening, L. (2004). Riesz potential and Sobolev embeddings on generalized Lebesgue and Sobolev spaces $L^{p(\cdot)}$ and $W^{k,p(\cdot)}$. *Mathematische Nachrichten*, 268(1):31–43.

Diening, L., Harjulehto, P., Hästö, P., and Růžička, M. (2011). *Lebesgue and Sobolev spaces with variable exponents*, volume 2017. Springer Verlag.

Diening, L., Hästö, P., and Nekvinda, A. (2005). Open problems in variable exponent lebesgue and sobolev spaces. In Drabek and Rakosnik, editors, *FSDONA04 Proceedings*, pages 38–58.

Diening, L., Málek, J., and Steinhauer, M. (2008). On Lipschitz truncations of Sobolev functions (with variable exponent) and their selected applications. *Control, Optimisation and Calculus of Variations*, 14(2):211–232.

Diening, L., Růžička, M., and Schumacher, K. (2010a). A decomposition technique for John domains. *Annales Academiae Scientiarum Fennicae Mathematica*, 35:87–114.

Diening, L., Růžička, M., and Wolf, J. (2010b). Existence of weak solutions for unsteady motions of generalized Newtonian fluids. *Ann. Sc. Norm. Super. Pisa Cl. Sci.*, 9:1–46.

Douglas, J. and Dupont, T. (1976). Interior penalty procedures for elliptic and parabolic Galerkin methods. *Lecture Notes in Physics, Computing methods in applied sciences*, 58(x):207–216.

Douglas Jr, J., Dupont, T., and Douglas, J. (1970). Galerkin methods for parabolic equations. *SIAM Journal on Numerical Analysis*, 7(4):575–626.

Edmunds, D. and Rákosník, J. (1992). Density of smooth functions in $W^{k,p(x)}(\Omega)$. In *Proc. Roy. Soc. London Ser. A*, volume 437, pages 229–236.

Edmunds, D. and Rákosník, J. (2000). Sobolev embeddings with variable exponent. *Studia Math*, 143(3):267–293.

Edmunds, D. and Rákosník, J. (2002). Sobolev embeddings with variable exponent, II. *Mathematische Nachrichten*, 246(1):53–67.

Elman, H., Silvester, D., and Wathen, A. (2005). *Finite elements and fast iterative solvers: with applications in incompressible fluid dynamics*. Oxford University Press, USA.

Eriksson, K., Estep, D., Hansbo, P., and Johnson, C. (1996). *Computational differential equations*. Cambridge University Press.

Fan, X., Shen, J., and Zhao, D. (2001). Sobolev Embedding Theorems for Spaces $W^{k,p(x)}(\Omega)$. *Journal of Mathematical Analysis and*, 262(2):749–760.

Fan, X., Wang, S., and Zhao, D. (2006). Density of $C^{\infty}(\Omega)$ in $W^{1,p(x)}(\Omega)$ with discontinuous exponent $p(x)$. *Mathematische Nachrichten*, 279(1-2):142–149.

Fatou, P. (1906). Séries trigonométriques et séries de Taylor. *Acta Mathematica*, 30(1):335–400.

Feistauer, M., Felcman, J., and Straškraba, I. (2003). *Mathematical and Computational Methods for Compressible Flow (Numerical Mathematics and Scientific Computation).* Oxford University Press.

Ferry, J. D. (1980). *Viscoelastic properties of polymers.* John Wiley and Sons.

Fiard, J., Manteuffel, T., and McCormick, S. (1998). First-order system least squares (FOSLS) for convection-diffusion problems: Numerical results. *SIAM Journal on Scientific Computing*, 19(6):1958–1979.

Fiorenza, A. (2002). A mean continuity type result for certain Sobolev spaces with variable exponent. *Communications in Contemporary Mathematics*, 4(3):587–605.

Franca, L. and Valentin, F. (2000). On an improved unusual stabilized finite element method for the advective-reactive-diffusive equation. *Computer Methods in Applied Mechanics and Engineering*, 190(13):1785–1800.

Fraser, J. R., Laurent, T., and Laurent, U. (1997). Hyaluronan: its nature, distribution, functions and turnover. *Journal of internal Medicine*, 242(1):27–33.

Frehse, J., Málek, J., and Steinhauer, M. (1997). An Existence Result for Fluids with Shear Dependent Viscosity - Steady Flows. *Nonlinear Analysis: Theory, Methods & Applications*, 30(5):3041–3049.

Frehse, J., Málek, J., and Steinhauer, M. (2000). On existence results for fluids with shear dependent viscosity- unsteady flows. In *Partial diferential equations*, volume 406, pages 121–129. Chapman & Hall/CRC, Boca Raton, FL, Praha.

Frehse, J., Málek, J., and Steinhauer, M. (2003). On analysis of steady flows of fluids with shear-dependent viscosity based on the Lipschitz truncation method. *SIAM J. Math. Anal.*, 34(5):1064–1083.

Fries, T. and Matthies, H. (2006). A stabilized and coupled meshfree/meshbased method for the incompressible Navier–Stokes equations—Part II: Coupling. *Computer Methods in Applied Mechanics and Engineering*, 195(44-47):6191–6204.

Fung, Y. C. (1993). *Biomechanics: mechanical properties of living tissues.* Springer-Verlag.

Gibbs, D., Merrill, E., Smith, K., and Balazs, E. (1968). Rheology of hyaluronic acid. *Peptide Science*, 6(6):777–791.

Gomez, J. E. and Thurston, G. B. (1993). Comparisons of the oscillatory shear viscoelasticity and composition of pathological synovial fluids. *Biorheology*, 30(5-6):409–27.

Gribbon, P., Heng, B. C., and Hardingham, T. E. (1999). The molecular basis of the solution properties of hyaluronan investigated by confocal fluorescence recovery after photobleaching. *Biophysical Journal*, 77(4):2210–2216.

Hästö, P. (2005). Counter-examples of regularity in variable exponent Sobolev spaces.

Hron, J., Málek, J., Pustějovská, P., and Rajagopal, K. R. (2010). On the Modeling of the Synovial Fluid. *Advances in Tribology*, 2010(Art. No. 104957).

Hron, J., Neuss-Radu, M., and Pustějovská, P. (2011). Mathematical modeling and simulation of flow in domains separated by leaky semipermeable membrane including osmotic effect. *Applications of Mathematics*, 56(1):51–68.

Hughes, T. and Franca, L. (1989). A new finite element formulation for computational fluid dynamics: VIII. The galerkin/least-squares method for advective-diffusive equations. *Computer Methods in Applied*, 73(604912):173–189.

Iwanaga, T., Shikichi, M., Kitamura, H., Yanase, H., and Nozava-Inoue, K. (2000). Morphology and functional roles of synoviocytes in the joint. *Archives of histology and cytology*, 63(1):17–31.

Jiang, B.-n. (1998). *The Least-squares finite element method.* Springer.

Johnson, C. (1982). *Finite element methods for convection-diffusion problems.* North-Holland, Amsterdam.

Johnson, C. (1987). *Numerical solution of partial differential equations by the finite element method.* Cambridge University Press, Studentlitteratur, Lund.

Kedem, O. and Katchalsky, A. (1958). Thermodynamic analysis of the permeability of biological membranes to non-electrolytes. *Biochimica et biophysica Acta*, 27:229–246.

Kelley, C. (1995). *Iterative methods for linear and nonlinear equations.* Society for Industrial Mathematics, Philadelphia.

Kelley, C. (2003). *Solving nonlinear equations with Newton's method*, volume 1. Society for Industrial Mathematics, Philadelphia.

King, R. G. (1966). A rheological measurement of three synovial fluids. *Rheologica Acta*, 5(1):41–44.

Kobayashi, Y., Okamoto, A., and Nishinari, K. (1994). Viscoelasticity of hyaluronic acid with different molecular weights. *Biorheology*, 31(3):235.

Kocherginsky, N. (2010). Mass transport and membrane separations: Universal description in terms of physicochemical potential and Einstein's mobility. *Chemical Engineering Science*, 65(4):1474–1489.

Kováčik, O. and Rákosník, J. (1991). On spaces $L^{p(x)}$ and $W^{k,p(x)}$. *Czechoslovak Math. J*, 41(116):592–618.

Kühnel, W. (2003). *Color Atlas of Cytology, Histology and Microscopic Anatomy*. Thieme.

Ladyzhenskaya, O. (1967). On some new equations describing dynamics of incompressible fluids and on global solvability of boundary value problems to these equations. *Trudy Mat. Inst. Steklov*, 102:85–104.

Ladyzhenskaya, O. (1969). *The Mathematical Theory of Viscous Incompressible Flow*. Gordon and Breach, New York.

Ladyzhenskaya, O. and Ural'tseva, N. (1968). *Linear and quasilinear elliptic equations*. Translated from the Russian by Scripta Technica, Inc. Translation editor: Leon Ehrenpreis. Academic Press, New York.

Lai, W., Kuei, S., and Mow, V. (1978). Rheological equations for synovial fluids. *J. Biomech. Eng*, 100:169–186.

Laurent, T. and Fraser, J. R. (1992). Hyaluronan. *The FASEB journal*, 6(7):2397–2404.

Laurent, T., Laurent, U., and Fraser, J. R. (1995). Functions of hyaluronan. *Annals of the rheumatic diseases*, 54(5):429–32.

Lebesgue, H. (1909). Sur les integrales singulieres. *Ann. Fac. Sci. Univ. Toulouse*, 1:25–117.

Málek, J., Nečas, J., and Růžička, M. (1993). On the non-Newtonian incompressible fluids. *Mathematical models and methods in applied sciences*, 3(1):35–63.

Málek, J., Nečas, J., and Růžička, M. (2001). On weak solutions to a class of non–Newtonian incompressible fluids in bounded three–dimensional domains: the case $p \geq 2$. *Adv. Diff. Equ.*, 6:257–302.

Maxwell, J. (1867). On the dynamical theory of gases. *Philosophical Transactions of the Royal Society of London*, 157:49–88.

Meyer, K., Smyth, E., and Dawson, M. (1939). The isolation of a mucopolysaccharide from synovial fluid. *Journal of Biological Chemistry*, 128(1):319.

Morrey, C. (1966). *Multiple Integrals in the Calculus of Variations*. Springer Verlag.

Morris, E., Cutler, A. A., Ross-Murphy, S. S., Rees, D., and Price, J. (1981). Concentration and shear rate dependence of viscosity in random coil polysaccharide solutions. *Carbohydrate Polymers*, 1(5):5–21.

Morris, E., Rees, D., and Welsh, E. J. (1980). Conformation and dynamic interactions in hyaluronate solutions. *Journal of molecular biology*, 138(2):383–400.

Mow, V. and Lai, W. (1979). Mechanics of animal joints. *Annual Review in Fluid Mechanics*, 11:247–288.

Musielak, J. (1983). *Orlicz Spaces and Modular Spaces*. Springer-Verlag, Berlin.

Nakano, H. (1950). *Modulared semi-ordered linear spaces*, volume 1. Maruzen Co., tokyo math edition.

Nash, J. (1958). Continuity of solutions of parabolic and elliptic equations. *American Journal of Mathematics*, 80(4):931–954.

Neuss-Radu, M. and Jäger, W. (2008). Effective transmission conditions for reaction-diffusion processes in domains separated by an interface. *SIAM Journal on Mathematical*, 39(3):687–720.

Neuss-Radu, M., Ludwig, S., and Jäger, W. (2010). Multiscale analysis and simulation of a reaction–diffusion problem with transmission conditions. *Nonlinear Analysis: Real World Applications*, 11(6):4572–4585.

Ogston, A. and Stanier, J. (1950). On the state of hyaluronic acid in synovial fluid. *The Biochemical journal*, 46(3):364–76.

Ogston, A. and Stanier, J. (1953). The physiological function of hyaluronic acid in synovial fluid; viscous, elastic and lubricant properties. *The Journal of Physiology*, 119(2-3):244.

Oldroyd, J. (1950). On the formulation of rheological equations of state. *Proceedings of the Royal Society of London. Series A. Mathematical and Physical Sciences*, 200(1063):523.

Orlicz, W. (1931). Über konjugierte Exponentenfolgen. *Stud. Math.*, 3:200–211.

Patlak, C. S., Goldstein, D. a., and Hoffman, J. F. (1963). The flow of solute and solvent across a two-membrane system. *Journal of Theoretical Biology*, 5(3):426–442.

Poincaré, H. (1890). Sur les équations aux dérivées partielles de la physique mathématique. *American Journal of Mathematics*, 12(3):211–294.

Rajagopal, K. R. (1993). Mechanics of non-Newtonian fluids. In Galdi, G. P. and Necas, J., editors, *Recent Developments in Theoreical Fluid Mechanics*, volume 33, pages 129 – 162. Longman, Essex.

Rajagopal, K. R. and Srinivasa, A. (2000). A thermodynamic frame work for rate type fluid models. *Journal of Non-Newtonian Fluid Mechanics*, 88(3):207–227.

Rajagopal, K. R. and Srinivasa, A. (2011). A Gibbs-potential-based formulation for obtaining the response functions for a class of viscoelastic materials. *Proceedings of the Royal Society A*, 467(2125):39–58.

Rajagopal, K. R., Wineman, A., and Shi, J. (1983). The diffusion of a fluid through a highly elastic spherical membrane. *International Journal of Engineering Science*, 21:1171–1183.

Rigutti, A. (2000). *Atlante di anatomia*. Giunti.

Rijswijk, M. H. V. (1992). *Folia Rheumatologica*. Ciba-Geigy.

Rohen, J. W., Yokochi, C., and Lutjen-Drecoll, E. (1998). *Color Atlas of Anatomy: A Photographic Study of the Human Body*. Williams & Wilkins.

Roos, H. and Stynes, M. (1996). *Numerical methods for singularly perturbed differential equations*, volume 24. Springer Verlag, Berlin.

Ropes, M., Rossmeisl, E., and Bauer, W. (1940). The origin and nature of normal human synovial fluid. *J Clin Invest*, 50:795–799.

Rudraiah, N., Kasiviswanathan, S., and Kaloni, P. (1991). Generalized dispersion in a synovial fluid of human joints. *Biorheology*, 28(3-4):207.

Rwei, S., Chen, S., Mao, C., and Fang, H. (2008). Viscoelasticity and wearability of hyaluronate solutions. *Biochemical Engineering Journal*, 40:211–217.

Růžička, M. (1997). A note on steady flow of fluids with shear dependent viscosity. *Nonlinear Analysis: Theory, Methods & Applications*, 30(5):3029–3039.

Růžička, M. (2000). *Electrorheological fluids: modeling and mathematical theory*, volume 1748. Springer Verlag, lecture no edition.

Růžička, M. (2004). Modeling, mathematical and numerical analysis of electrorheological fluids. *Appl. Math*, 49:565–609.

Sabaratnam, S., Mason, R., and Levick, J. (2006). Hyaluronan molecular reflection by synovial lining is concentration dependent and reduced in dilute effusions in a rabbit model. *Arthritis & Rheumatism*, 54(5):1673–1681.

Samko, S. (2000). Denseness of $C_0^\infty(R^n)$ in the generalized Sobolev spaces $W^{m,p(x)}(R^n)$. *Direct and inverse problems of mathematical physics (Newark, DE, 1997), Int. Soc. Anal. Appl. Comput.*, 5:333–342.

Scott, D., Coleman, P., Mason, R., and Levick, J. (2000a). Action of polysaccharides of similar average mass but differing molecular volume and charge on fluid drainage through synovial interstitium in rabbit knees. *J Physiol.*, 528(3):609–618.

Scott, D., Coleman, P., Mason, R., and Levick, J. (2000b). Concentration dependence of interstitial flow buffering by hyaluronan in synovial joints. *Microvascular research*, 59(3):345–53.

Scott, J. E., Cummings, C., Brass, A., and Chen, Y. (1991). Secondary and tertiary structures of hyaluronan in aqueous solution, investigated by rotary shadowing-electron microscopy and computer simulation. Hyaluronan is a very efficient network-forming polymer. *The Biochemical journal*, 274:699–705.

Sharapudinov, I. (1978). On the topology of the space $L^{p(t)}([0,1])$. *Matem. Zametki*, 26:613–632.

Sunblad, L. (1953). Studies on hyaluronic acid in synovial fluids. *Acta Societatis Medicorum Upsaliensis*, 58(113).

Tao, L., Humphrey, J., and Rajagopal, K. R. (2001). A mixture theory for heat-induced alterations in hydration and mechanical properties in soft tissues. *International Journal of Engineering Science*, 39:1535–1556.

Thurston, G. B. and Greiling, H. (1978). Viscoelastic properties of pathological synovial fluids for a wide range of oscillatory shear rates and frequencies. *Rheologica Acta*, 17(4):433–445.

Truesdell, C. and Noll, W. (1965). *The Non-Linear Field Theories of Mechanics*. Springer-Verlag, Berlin-Heidelberg-New York, handbuch d edition.

Truesdell, C. and Rajagopal, K. R. (2000). *An introduction to the mechanics of fluids*. Springer.

Turek, S. and Ouazzi, A. (2007). Unified edge-oriented stabilization of nonconforming FEM for incompressible flow problems: Numerical investigations. *Journal of Numerical Mathematics*, 15(4):299–322.

Turek, S., Rivkind, L., Hron, J., and Glowinski, R. (2006). Numerical Study of a Modified Time-Stepping θ-Scheme for Incompressible Flow Simulations. *Journal of Scientific Computing*, 28(2-3):533–547.

Voet, D. and Voet, J. G. (2004). *Biochemistry, 3rd Edition*. Wiley.

Wineman, A. and Rajagopal, K. R. (2000). *Mechanical response of polymers: an introduction*. Cambridge University Press.

Wright, V. and Radin, E. L. (1993). *Mechanics of Human Joints*. Informa Healthcare.

Zhikov, V. (1987). Averaging of functionals of the calculus of variations and elasticity theory. *Izvestiya: Mathematics*, 29(1):33–66.